Templated syntheses towards new boron-based nanomaterials

Fernando Igoa Saldaña

SORBONNE UNIVERSITÉ
CRÉATEURS DE FUTURS
DEPUIS 1257

Sorbonne Université

Ecole doctorale de Physique et Chimie des Matériaux (ED397)

Laboratoire de Chimie de la Matière Condensée de Paris

Templated syntheses towards new boron-based nanomaterials

Par Fernando Igoa Saldaña

Thèse de doctorat de Physique et Chimie des Matériaux

Dirigée par David Portehault et Yann Le Godec

Présentée et soutenue publiquement le 28 novembre 2022

Devant un jury composé de :

Mme. Paula Abdala	Senior Scientist, ETH Zürich	Rapportrice
M. Alain Demourgues	Directeur de recherche, Université de Bordeaux	Rapporteur
M. Nicolas Pradeilles	Maître de conférences, Université de Limoges	Examinateur
M. Gilles Wallez	Professeur des universités, Sorbonne Université	Examinateur
M. David Portehault	Directeur de recherche, Sorbonne Université	Directeur de thèse
M. Yann Le Godec	Directeur de recherche, Sorbonne Université	Directeur de thèse

A mi eterna admiradora y admirada, Mamá

Acknowledgements

I would like to thank firstly the jury members, Dr. Paula Abdala, Dr. Alain Demourgues, Dr. Nicolas Pradeilles and Dr. Gilles Wallez, for serving as my jury members and providing very interesting and useful suggestions and discussions.

I would like to acknowledge both my supervisors David Portehault and Yann Le Godec, who have provided the aid needed to complete this thesis work.

Many thanks to all our research team members, current and former, for all the discussions (scientific and not so) and the moments shared. Specially to Edouard, Marzena, Anissa, Francisco, Emile and Simon. Very specially to Daniel, Isabel and Yang.

I would like to thank all the permanent LCMCP and IMPMC staff who have provided important training and who help keep the laboratories working. Specially to Corinne and Helene, whose ever impressive efficiency has made the sailing through the turbulent waters of bureaucracy, a rather smooth voyage.

I would like to thank all the scientific collaborators:

- Cristina C. -D. and Christel G. for all the NMR measurements and modelling.
- Sylvie L. F. and Thomas G. for training me and helping me using the spark-plasma sintering equipment.
- Gwenaëlle R. for helping me with my many diffractograms refinement and being always responsive to my various inquiries.
- Jonathan W. and Pierre-Olivier A. for providing enormous aid during the beamtimes at ID11.
- Laura H. and Nicolas G. also for their great help during the PSICHE beamtimes.
- Leopoldo S. for the many discussions and trainings on powder diffraction.

Finally, I want to thank those whose moral support have helped me keep my head up in moments of struggle. To my dear friends Martin E., Martin L., Julian, Diego K., Diego F., Ana, Pancho and Neno for their friendship, the anecdotes we have gathered and those that are yet to come, and specially trust we have built. To Caroline, whose infinite patience and comprehension towards me have only made me a better self, especially during some of my most difficult times throughout my PhD. And to her who's entire manuscript is dedicated to, but still cannot begin to compensate everything I owe her: Mamá.

List of abbreviations

ABF – STEM	Annular Bright Field – Scanning Transmission Electron Microscopy
AIMD	Ab-initio molecular dynamics
BET	Brunauer-Emmett-Teller Surface Area
BH	Berkovich's Hardness
CAESAR	Combined Angle- and Energy-dispersive Structural Analysis and Refinement
DFT	Density Functional Theory
EDS	Energy Dispersive X-ray Spectroscopy
FC	Force Constant
FFT	Fast Fourier Transform
FWHM	Full Width at Half Maximum
HEL	Hugoniot Elastic Limit
HER	Hydrogen Evolution Reaction
HP	High Pressure
HR-TEM	High Resolution Transmission Electron Microscopy
HV	Vicker's Hardness
MeOH	Methanol
PMMA	Polymethyl Methacrylate
RE	Rare Earth
SAED	Selected Area Electron Diffraction
SEM-FEG	Scanning electron microscopy Field Emission Gun Electron Source
SG	Space Group
SPS	Spark Plasma Sintering
SSD	Solid State Detector
SS-NMR	Solid State Nuclear Magnetic Resonance
XPS	X-ray Photoelectron Spectroscopy
XRD	X-ray Diffraction

Résumé

Les composés contenant du bore présentent plusieurs propriétés physiques exploitables pour les besoins industriels actuels, à savoir les propriétés catalytiques, magnétiques, de supercapacité, de stockage élevé du lithium et mécaniques. La plupart de ces propriétés peuvent être adaptées et optimisées en façonnant le matériau à l'échelle nanométrique. Cependant, la nature fortement covalente des liaisons chimiques impliquant le bore entrave la synthèse des nanostructures, car un apport d'énergie élevé est nécessaire pour former ces liaisons. Cela se traduit par des températures de synthèse élevées qui, en fin de compte, entraînent forcément la croissance des grains. La synthèse de sels fondus suscite un intérêt considérable en tant qu'outil de synthèse pour produire des nanostructures. Les sels fondus permettent d'effectuer des réactions chimiques dans un milieu liquide à des températures suffisamment élevées pour déclencher la cristallisation des matériaux riches en bore, mais suffisamment douces pour limiter leur croissance. Malgré le succès de ces synthèses, le contrôle de la morphologie du produit reste un défi important. Dans certains cas, ce problème peut être surmonté par des méthodes de transformation isomorphiques, c'est-à-dire en utilisant des nanoparticules comme précurseurs qui subissent une restructuration interne, de sorte qu'elles puissent également servir de nano-gabarits.

Dans ce travail de thèse, l'utilisation de nano-gabarits couplée à la synthèse de nanomatériaux par sels fondus a été explorée pour deux systèmes complexes à base de bore. Tout d'abord, des nanoparticules de carbure de bore ont été synthétisées à partir de gabarits de carbaborure de sodium, eux-mêmes synthétisés dans des sels fondus. L'intérêt de produire des nanostructures de carbure de bore a été largement reconnu dans la littérature comme un moyen d'améliorer sa dureté et son utilisation durable en tant que matériau de structure. La synthèse du gabarit a été réalisée grâce à la réaction entre une source de carbone polymère (polyéthylène) et un borohydrure dans du iodure de sodium fondu, ce qui a fourni des nanoparticules de ~ 5 nm. Ces nanoparticules ont alors pu être transformées avec succès en carbure de bore par décomposition thermique tout en conservant la morphologie nanométrique. En outre, la transformation du carbure de bore en monolithes denses a également été étudiée au moyen du frittage par plasma en courant pulsé. Une fois la densification et la consolidation réalisées, les propriétés mécaniques des nanostructures de carbure de bore ont été étudiées. Nous avons ainsi mis en évidence une dureté et une résistance à l'amorphisations significativement supérieures à celles de leur homologue massif.

En parallèle, un borure métallique lamellaire a également été étudié avec des procédures analogues. Le système en question est Fe_2AlB_2, constitué de couches de Fe_2B_2 intercalées par des couches d'Al. Cette phase suscite un énorme intérêt en tant que précurseur possible vers le matériaux bidimensionnel Fe_2B_2. La synthèse du Fe_2AlB_2 présente cependant plusieurs difficultés. Nous avons ici exploité l'approche du gabarit dans les sels fondus à partir d'un précurseur de FeB. Nous avons démontré que l'insertion d'Al dans des chlorures alcalins fondus fourni bien Fe_2AlB_2. La délamination de la phase Fe_2AlB_2 vers 2D-Fe_2B_2 a été étudiée par oxydation sélective des atomes d'Al. Bien que la délamination n'ait pas été atteinte, nous avons mis en évidence un comportement thermique anormal dans Fe_2AlB_2. Lorsqu'il est traité thermiquement, Fe_2AlB_2 expulse des atomes de Fe et de B de la structure, générant ainsi des lacunes. Ce mécanisme a été démontré par diffraction des rayons X *in-situ* et par des analyses *post mortem*.

Abstract

Boron-containing compounds exhibit several physical properties exploitable for current industrial needs, *i.e*. catalytic properties, magnetism, supercapacitance, high Li^+ storage capacity and excellent mechanical properties. Most of these behaviors can be tailored and optimized by shaping the material into nanostructured morphologies. However, the strong covalent nature of boron bonding hurdles the synthesis of nanostructures, as high energy input is needed to form such bonds. This translates in elevated synthesis temperatures, which ultimately also trigger grain growth. Molten-salts synthesis has gained considerable attention as a synthetic tool to yield nanostructures. Molten-salts permit to perform chemical reactions under a liquid media in a range of temperatures sufficiently large to trigger borides crystallization, but soft enough to limit their growth. Despite its success, the control over the product's morphology remains a significant challenge. In some cases, this can be overcome by isomorphic transformations, *i.e*., using nanoparticles as precursors, which undergo internal restructuration, so that they could also act as nanotemplates.

In this thesis work, the use of nanotemplates coupled to molten salts synthesis of nanomaterials has been explored for two challenging boron-based systems. Firstly, boron carbide nanostructures were synthesized from sodium carbaboride templates, themselves synthesized in molten salts. The interest behind producing boron carbide nanostructures has been largely recognized in the literature, as a way to ameliorate the hardness of this material and its durable use as a structural material. The template synthesis is achieved thanks to the reaction between a polymeric carbon source (polyethylene) and a borohydride in molten sodium iodide, which yields ~ 5 nm nanoparticles. These nanoparticles can be successfully transformed to boron carbide while maintaining the nanoscale morphology by thermal decomposition. Furthermore, the processing of boron carbide into dense monoliths was also studied by means of spark-plasma sintering. Once proper densification and consolidation were achieved, the mechanical properties of the boron carbide nanostructures were investigated. We then highlighted a significantly higher hardness and amorphization resistance than the bulk counterpart.

In parallel, a layered metal boride has also been investigated with analogous procedures. The system in question is Fe_2AlB_2, consisting of Fe_2B_2 layers intercalated by Al layers. This phase has raised enormous interest as a possible parent phase towards bidimensional Fe_2B_2. The synthesis of Fe_2AlB_2 presents several difficulties though. We have herein exploited the

templating approach in molten salts from a bulk FeB template, which we demonstrate that upon Al insertion in molten LiCl/KCl yields Fe_2AlB_2. The Fe_2AlB_2 phase delamination towards 2D-Fe_2B_2 was investigated by selective etching of the Al atoms. Although delamination did not occur, we evidenced an abnormal thermal behavior in Fe_2AlB_2. When thermally treated, Fe_2AlB_2 expulses Fe and B atoms out of the structure, generating vacancies. This mechanism was demonstrated by *in-situ* X-ray diffraction and *post mortem* analyses.

Table of Contents

Chapter I: General Introduction

Since the first claim of boron isolation by the English scientist Humphry Davy[1] and independently by the French Louis Joseph Gay-Lussac and Louis Jacques Thenard[2] in 1808, boron chemistry has evolved to be, arguably, one of the richest and most complex of the whole periodic table. Boron atom's most outstanding features include structural complexity, electron deficiency, presence of unusual binding situations and an extremely rich variety of compound's formation. All of these contribute to a very interesting, yet challenging chemistry. Boron compounds primarily exhibit extended covalent networks in which boron can be arranged on complex polyhedral clusters, such as octahedra, pentagonal bipyramids, trigonal dodecahedra, double-capped square antiprisms, cuboctahedra and icosahedra.[3] These covalent networks encompass a plethora of structures ranging from 1D chains to 2D sheets and 3D networks.[4]

Such a rich and diverse structural chemistry ultimately reflects on equally broad fields of applications. Among the most known commercial uses of boron, stands out the spread use of boron oxide in glass manufacturing and fibre glass insulation.[5] Furthermore, boron nitrides, whose hexagonal (*h*-BN) and cubic (*c*-BN) polymorphs are structurally related to graphite and diamond respectively, are used as solid lubricant at high temperatures for *h*-BN,[6] while *c*-BN is used as cutting tool for ferrous alloys where diamond would form iron carbides and thus dissolve.[7] Boron can form alloys or stoichiometric compounds with a large number of metals and lead to remarkable physical phenomena. Since as early as the 1960's, amorphous nickel borides have been used as catalysts for various organic reactions, most notably hydrogenation and reduction reactions.[8] Boron also forces the alignment of iron magnetic moments along the *c* crystallographic axis in the $Nd_2Fe_{14}B$ structure, which in turn makes it the strongest permanent magnet known.[9,10] The majority of metal borides are refractory. For instance, zirconium diboride combines an extremely high melting temperature (3230 °C), elevated elastic modulus and excellent oxidation resistance, making it a very robust structural material.[11] Finally, the superconductor MgB_2 stands until now as the type-I superconductor bearing the highest transition temperature (39 K).[12]

The control of nanodomains during the synthesis of borides is important due to several unique properties these domains can bring, like chemical stability, hardness and wear resistance, unique magnetic behavior, and enhanced biocompatibility compared to their bulk counterparts.[13,14] However, the exploration of boron-based nanomaterials still remains

scarce, mainly due to the synthetic challenge it represents, which is related to the high oxophilicity of boron and its tendency to form strong and directional covalent bonds in solids.[15] The use of solid state reactions has allowed the production of some transition metal borides, for instance VB_2[16] and Co_2B,[17] while the great reactivity of gaseous Mg has been employed to produce MgB_2 through different routes.[18–20] However, most spread synthetic routes (CVD, ball-milling, arc plasma, etc.) require sophisticated instruments that are extremely case sensitive and can hardly be extrapolated to further chemical systems. They also involve toxic reagents and/or by-products and are thus overall difficult to operate in a standard laboratory.[21]

The use of liquid phase synthesis, *i.e*. solution or colloidal reactions, instead of traditional solid-state reactions has proven to contribute meaningfully to the kinetic accessibility of the chemical space, including size and morphology control at the nanoscale.[22–24] One big challenge to overcome for the synthesis of boride nanostructures is the sensitive compromise between providing enough energy to crystallize the given compound and avoiding grain growth. In terms of temperature, this translates in the use of relatively mild conditions, ideally in the 500-900 °C window, under which regular organic solvents are unstable. The use of molten salts as solvent for liquid-phase reactions has been proposed and shown to lead to nanomaterials of a wide range of borides.[13] The principle is based on the reaction between metal salts and an alkali borohydride below 900 °C at atmospheric pressure in a eutectic mixture of alkali halides, leading to the production of hexaborides, tetraborides, diborides and lower borides of diverse metals like Ca, Ce, Mo, Nb, Hf, Fe and Mn.[13] The molten salt offers a thermally stable and oxygen-free solvent, whose post-synthetic removal can be easily achieved by water washing. The ability of this procedure to tailor the stoichiometry and morphology has been also demonstrated for nickel and yttrium borides.[25] The experimental implementation of such procedure consists in grinding the needed amount of salts along with the reagents. The temperature and atmosphere control is analogous to a solid-state reaction.

One of the challenges for nanomaterials design in molten salts though, is the control of the product's morphology at the nanoscale. In some cases, this can be overcome by topochemical methods, *i.e.*, using nanoparticles as precursors, so that they could also act as nanotemplates.[26] According to the Merriam-Webster's Dictionary, a template is a "gauge, pattern or mold used as a guide to the form of a piece being made".[27] In the frame of nanomaterial's synthesis, templated synthesis seeks to direct the size, shape and structure of a

desired nanomaterial by retaining certain characteristics of the initial template.[28] Templated metallic nanoparticles have greatly benefited from these strategies. For instance, Schaak *et al*. demonstrated the synthesis of M–Sn (M = Fe, Co, Ni, Pd) intermetallic nanocrystals by appropriately reducing metal salts and on β-Sn nanocrystals acting as templates.[29] The cubic template particles were transformed to different structures with predominantly hollow square features. The general route consists in **(i)** preparing the template, **(ii)** using the template to direct the synthesis and **(iii)** eliminating the template if necessary.

In this PhD work, we have aimed at exploiting the templating synthesis in molten salts described above, in order to seek for novel boron-based nanomaterials bearing potential interest either because of their structural or functional properties. Firstly, we explored the synthesis of boron carbide nanostructures as a reinforcement strategy towards enhanced mechanical properties. Boron carbide is a material that possesses a lot of potential for high performance mechanical applications, albeit hindered because of its relative low hardness (compared to other superhard materials) and its poor resistance to amorphization. Secondly, we have targeted the synthesis of the layered Fe_2AlB_2 phase.[30] This material belongs to the so-called MAB phases, composed of an early transition metal (M), a metal (A = Al, Ga, In in most cases) and boron, a family analogous to the more studied MAX phases, where X is either C or N. The latter consist of lamellar structures of space group *P6₃/mmc*[31] that can undergo topochemical deintercalation of the A atoms upon reaction with an adequate etchant. This results in the exfoliation into 2D nanosheets of MXenes, widely investigated for applications in supercapacitors, batteries and catalysis, to name a few.[32–34] Such full deintercalation process has been only achieved for selected MAB phases: Cr_2AlB_2,[35] and most recently $(Mo_{2/3}Y_{1/3})_2AlB_2$[36] and $(Mo_{2/3}Sc_{1/3})_2AlB_2$.[36]

The present manuscript is divided in two parts, each of which presents a chemical system: boron carbide nanostructures and layered Fe_2AlB_2 MAB phase. Each part begins by a review of the state-of-the-art revolving around the material and its context (**Chapters II** and **V** for boron carbide and Fe_2AlB_2 respectively). Later, a chapter is dedicated to the development of the corresponding template in each case, where its synthesis and structure are analysed, besides some physical properties when this is of interest. For boron carbide, the template developed is nanostructured NaB_5C, described in **Chapter III**, which leads to boron carbide by controlled thermal decomposition. For Fe_2AlB_2, the reaction was performed by Al insertion in molten salts of the template FeB, described in **Chapter VI**. Finally, a chapter is dedicated to each of the

targeted materials, describing its synthesis and structure in general, on top of the mechanical properties for boron carbide (**Chapter IV**) or delamination approaches for Fe_2AlB_2 (**Chapter VI**).

References for Chapter I

[1]: H. Davy, *Philos. Trans. R. Soc. London*, 1808, **98**, 333–370.
[2]: J. L. Gay-Lussac and L. J. Thenard, *Ann. Chim. Phys.*, 1808, **68**, 169–174.
[3]: B. Albert and H. Hillebrecht, *Angew. Chemie - Int. Ed.*, 2009, **48**, 8640–8668.
[4]: G. Akopov, M. T. Yeung and R. B. Kaner, *Adv. Mater.*, 2017, **29**, 1–29.
[5]: H. Huppertz and D. A. Keszler, *Encyclopedia of Inorganic and Bioinorganic Chemistry*, Wiley, 2014.
[6]: Y. Kimura, T. Wakabayashi, K. Okada, T. Wada and H. Nishikawa, *Wear*, 1999, **232**, 199–206.
[7]: V. L. Solozhenko, O. O. Kurakevych and Y. Le Godec, *Adv. Mater.*, 2012, **24**, 1540–1544.
[8]: B. Ganem and J. O. Osby, *Chem. Rev.*, 1986, **86**, 763–780.
[9]: J. J. Croat, J. F. Herbst, R. W. Lee and F. E. Pinkerton, *Appl. Phys. Lett.*, 1984, **44**, 148–149.
[10]: J. F. Herbst, J. J. Croat, F. E. Pinkerton and W. B. Yelon, *Phys. Rev. B*, 1984, **29**, 4176–4178.
[11]: K. I. Portnoi, V. M. Romashov and L. N. Burobina, *Sov. Powder Metall. Met. Ceram.*, 1970, **9**, 577–580.
[12]: C. Buzea and T. Yamashita, *Supercond. Sci. Technol.*, **14**, R115–R14.
[13]: D. Portehault, S. Devi, P. Beaunier, C. Gervais, C. Giordano, C. Sanchez and M. Antonietti, *Angew. Chemie - Int. Ed.*, 2011, **50**, 3262–3265.
[14]: S. Khoshsima, Z. Altıntaş, M. Schmidt, M. Bobnar, M. Somer and Ö. Balcı, *J. Alloys Compd.*, 2019, **805**, 471–482.
[15]: S. Carenco, D. Portehault, C. Boissière, N. Mézailles and C. Sanchez, *Chem. Rev.*, 2013, **113**, 7981–8065.
[16]: L. Shi, Y. Gu, L. Chen, Z. Yang, J. Ma and Y. Qian, *Mater. Lett.*, 2004, **58**, 2890–2892.
[17]: P. Cai, H. Wang, L. Liu and L. Zhang, *J. Ceram. Soc. Japan*, 2010, **118**, 1102–1104.
[18]: W. N. Kang, E. M. Choi, H. J. Kim, H. J. Kim and S. I. Lee, *Phys. C Supercond. Appl.*, 2003, **385**, 24–30.
[19]: S. H. Lai, S. C. Liu and M. D. Lan, *J. Cryst. Growth*, 2007, **304**, 460–463.
[20]: S. M. Zhou, P. Wang, S. Li, B. Zhang, H. C. Gong and X. T. Zhang, *Mater. Lett.*, 2009, **63**, 1680–1682.
[21]: J. L. Ma, N. Li, Q. Zhang, X. B. Zhang, J. Wang, K. Li, X. F. Hao and J. M. Yan, *Energy Environ. Sci.*, 2018, **11**, 2833–2838.
[22]: A. P. Alivisatos, D. J. Milliron, S. M. Hughes, Y. Cui, L. Manna, J. B. Li and L. W. Wang, *Nature*, 2004, **430**, 190–195.
[23]: C. J. Murphy, A. M. Gole, S. E. Hunyadi and C. J. Orendorff, *Inorg. Chem.*, 2006, **45**, 7544–7554.
[24]: D. Portehault, S. Cassaignon, E. Baudrin and J. P. Jolivet, *Chem. Mater.*, 2007, **19**, 5410–5417.
[25]: G. Gouget, P. Beaunier, D. Portehault and C. Sanchez, *Faraday Discuss.*, 2016, **191**, 511–525.
[26]: S. K. Gupta and Y. Mao, *J. Phys. Chem. C*, 2021, **125**, 6533.

[27]: www.merriam-webster.com. Revised on the 21/09/2022.
[28]: Y. Yin, D. Talapin, R. Article, Y. Liu and J. Goebl, *Chem. Soc. Rev*, 2013, **42**, 2610–2653.
[29]: H. C. Nam and R. E. Schaak, *J. Am. Chem. Soc.*, 2007, **129**, 7339–7345.
[30]: J. Liu, S. Li, B. Yao, S. Hu, J. Zhang, W. Yu and Y. Zhou, 2018, **766**, 488–497.
[31]: M. Barsoum and T. El-Raghy, *Am. Sci.*, 2001, **89**, 334.
[32]: B. Anasori, M. R. Lukatskaya and Y. Gogotsi, *Nat. Rev. Mater.*, 2017, **2**, 16098.
[33]: M. Naguib, M. Kurtoglu, V. Presser, J. Lu, J. Niu, M. Heon, L. Hultman, Y. Gogotsi and M. W. Barsoum, *Adv. Mater.*, 2011, **23**, 4248–4253.
[34]: M. Alhabeb, K. Maleski, T. S. Mathis, A. Sarycheva, C. B. Hatter, S. Uzun, A. Levitt and Y. Gogotsi, *Angew. Chemie - Int. Ed.*, 2018, **57**, 5444–5448.
[35]: H. Zhang, H. Xiang, F. zhi Dai, Z. Zhang and Y. Zhou, *J. Mater. Sci. Technol.*, 2018, **34**, 2022–2026.
[36]: J. Zhou, J. Palisaitis, J. Halim, M. Dahlqvist, Q. Tao, I. Persson, L. Hultman, P. O. Å. Persson. and J. Rosen, *Science.*, 2021, **373**, 801–805.

Part One:

Boron Carbide

Superhard Nanostructures

Chapter II: State of the art on boron carbide

II.1 Introduction

Boron carbide ($B_{4+\delta}C$, with $-0.2 < \delta < 7.1$) is among the most performing boron refractory compounds.[1] It exhibits an attractive combination of properties such as high hardness (38 GPa),[2,3] low density (2.52 $g \cdot cm^{-3}$),[4] high melting point (2720 °C),[5] elevated elastic modulus (448 GPa),[6] incompressibility (adiabatic bulk modulus of 241 GPa),[7] chemical inertness,[8] enormous neutron absorption cross-section (600 barns)[9] and high Seebeck coefficient (300 $\mu V \cdot K^{-1}$),[10] among many others. In terms of applications, boron carbide is suitable as an abrasive powder for lapping, polishing and water jet cutting of metals and ceramics.[11] In particular, $B_{4+\delta}C$ coated tools are employed for cutting various ferrous alloys, due to the lack of solubility in comparison to the most commonly used material for such purposes: diamond.[12] As sintered dense monoliths, boron carbide is used as blasting nozzles, ceramic bearings and wire drawing dies due to the good wear resistance.[13] The combination of low density, high hardness and impact resistance make it an ideal material for body and vehicle armours.[14] In the nuclear field, boron carbide is employed as a neutron capture material in detectors[15] and retaining walls[16] or even for cancer treatment through neutron capture therapy.[17] Finally, owing to its Seebeck coefficient, $B_{4+\delta}C$ is an established high temperature *p*-type thermoelectric material.[10]

II.2 Structure

Most properties in boron carbide, particularly the mechanical ones, arise from its composition and atomic structure. While it was a topic of argument and discordance in the past, nowadays it is widely accepted that the boron carbide crystalline network can accommodate at least between 9 % ($B_{11.1}C$) and 21 % *at.* ($B_{3.8}C$) of carbon content.[1] M. Beauvy proposed in 1983 the most widely spread $B_{4+\delta}C$ phase diagram, this is shown in **Figure II. 1** as adapted from the original report.[18] Ranges outside the solubility limit give amorphous boron or graphite as secondary phase in the lower and upper ends respectively.

The crystalline structure of boron carbide was firstly proposed in 1941 by Zhdanov and Sevastanov[19] and re-solved a year later by Clark and Hoard.[20] More contemporary structural studies combining neutron[21] and synchrotron light diffraction[22] have confirmed

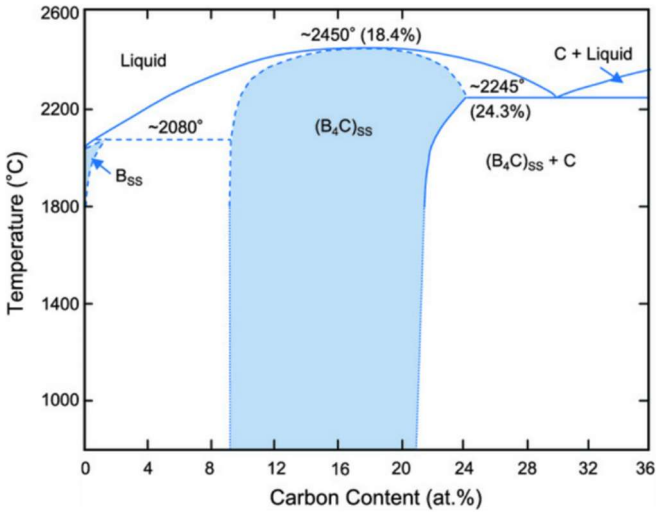

Figure II. 1. B-C phase diagram, as adapted from reference [18].

the accuracy of these early reports. The structure of boron carbide is closely related to that of *α-B*. Both compounds crystallize in the rhombohedral $R\bar{3}m$ space group and share a basic structural motif, *i.e.*, boron-based icosahedra. The primitive rhombohedral representation can be converted in the more intuitive hexagonal system. Transformed lattice parameters are a = 4.90, 5.60 Å and c = 12.56, 12.07 Å for *α-B* and B_4C respectively (the most common stoichiometry is taken as reference for boron carbide).[1,23,24] However, lattice parameters in boron carbide are dependent on the composition. In **Figure II. 2b**, a parallelism of both structures in the hexagonal settings is shown, while in **Figure II. 2c** the lattice parameter dependence to boron carbide's composition is shown with the available empirical data.[1]

In both structures, an icosahedron is placed at every corner of the unit cell. To be more precise, it is their mass-center actually that lies at the cell vertexes. Two more icosahedra are placed with their mass-center distributed along the body diagonal ($[\bar{1}101]$ direction) at 1/3 and 2/3 of its length each. Therefore, overall, *α-B* or $B_{4+\delta}C$ contain 3 boron-based icosahedra per unit cell, composed of 12 atoms each, thus 26 B(C) atoms per unit cell. The icosahedron as a platonic solid contains six 5-fold rotation axes passing between each pair of opposing vertexes. These are of course not compatible with the periodic crystalline structure and the polyhedron must become distorted in order to fit the lattice symmetry.

In the case of *α-B*, icosahedra are tilted such that three upper and three lower B atoms form classical intericosahedra B-B bonds. Although the remaining 6-atom middle fringe do not form covalent intericosahedra bonds, these are not formally uncoordinated either. As a matter of fact, the electron count per icosahedron yields 36 valence electrons in total, out of which 26 fill the

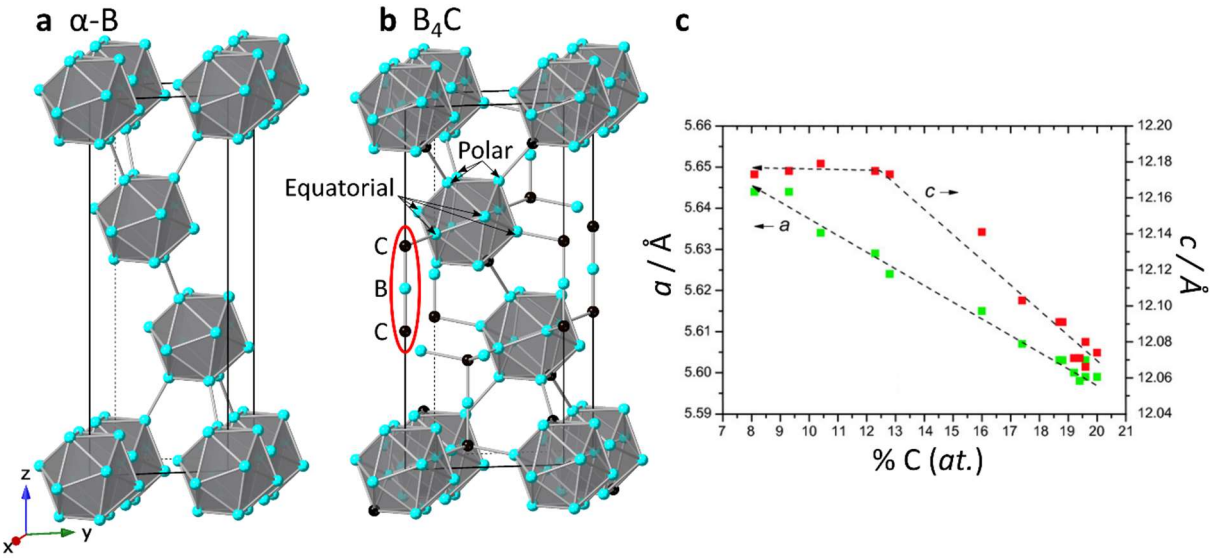

Figure II. 2. *α-B* **(a)** and $B_{4+\delta}C$ **(b)** structures. **(c)** Lattice parameters dependence of boron carbide with the carbon content as adapted from reference [1].

13 molecular orbitals that stabilize the internal bonding of the icosahedron, and 6 participate in covalent intericosahedra B-B bonds. It becomes evident that the remaining 4 electrons cannot provide classical 2-center-2-electron (2c2e) pair bonds for the six remaining B atoms per icosahedron.[24] Therefore, these electrons distribute among the undercoordinated atoms in a set of six 3-center-2-electron (3c2e) bonds between neighboring icosahedra. This is reflected in the bond distance, as the intericosahedra B-B bonds length is 1.669(3) Å in contrast with the 2.023(3) Å separation of adjacent 3c2e B atoms.[24] In summary, *α-B* intericosahedra skeleton is half formed by covalent bonds and half by electron-deficient 3c2e bonds. This bonding scheme determines the stability of the compound, which transforms to *β-B* at a temperature as low as 1200 °C.[25]

In the case of boron carbide, the icosahedra distortion discerns two unequal positions, namely the polar and equatorial sites; these are depicted in **Figure II. 2b**. Here, the orientation of each icosahedron is such that every polar site links to another polar atom of a neighboring icosahedron. On the other hand, equatorial atoms bridge to chains of three atoms, ideally CBC, although the nature of these chains will be further discussed in the **Local structure, defects, and disorder** section. There are 3 three-atom chains per cell (highlighted in **Figure II. 2b**), which lie parallel to the [0001] direction and bond in total 6 equatorial atoms from 6 different icosahedra each: 3 per chain-end. This saturates every equatorial position with pure covalent bonds. Moreover, and depending on the actual stoichiometry, C atoms provide further electrons to the network, thus avoiding the electron deficiency situation exposed for *α-B* and in many

cases, even providing excess of valence electrons. The result is a highly stable compound that does not present thermal decomposition and melts only at 2720 °C.[5]

Overall, four types of bonds can be identified for boron carbide in the $R\bar{3}m$ symmetry: **(i)** the *intrachain* bond, connecting each chain-end atom to the center of the three-atom chain, it has a strong π character; **(ii)** the *chain-icosahedron* bond, that serves to link the chain-ends to the equatorial atoms in the icosahedra; **(iii)** the *intericosahedral* bonds, connecting polar atoms of neighbouring icosahedra and originating from *sp* hybridized orbitals; and **(iv)** the highly delocalized *intraicosahedral* sp^2 bonds as the ones connecting atoms within each icosahedron unit.[1] Several authors have independently found that the intrachain bond has the shortest length followed by the chain-icosahedron bonds, the intericosahedral and finally the intraicosahedral bonds.[26–28] This finding is further supported by the available theoretical calculations of bond strength.[29–31] The relative order of bond strength has been the basis of Emini's classification of boron carbide as an *inverted molecular solid*.[32]

Local structure, defects, and disorder

Regarding the identity of each atom in the chain and icosahedra motifs, this is of course dependent on the actual stoichiometry of the compound. For the most common occurrence of 20 % *at*. in carbon (B_4C), the most classical claim proposes a $(B_{11}C)$CBC general formula. That is, icosahedra formed of 11 B atoms and a carbon one, linked by CBC chains. This possibility was initially evidenced by NMR spectroscopy, although doubt was raised at the time regarding the NMR peak assignment.[33,34] Later theoretical simulations of the NMR spectra on the frame of the density functional theory (DFT) helped resolve this issue.[35] It was found that the best fitting model consisted of all CBC chains and a mixture of B_{12}, $B_{11}C^p$ and $B_{10}C_2^p$ icosahedra (with C_p being a carbon atom located at the polar position of the icosahedra) in the ratio 2.5:95:2.5.[35] Modelling of the Raman and infrared spectra have reached similar conclusions.[36] Moreover, the presence of boron in the center of the atom chain has been observed from the scattering contrast in high-resolution X-rays[37] and neutron diffraction,[27] further supported from X-ray absorption[38] and scattering experiments.[39,40] Therefore, there is a generalized consensus that in the B_4C stoichiometry, the overall boron carbide solid exhibits the $(B_{11}C^p)$CBC configuration as depicted in **Figure II. 2b**.[1]

The thermodynamic average ($B_{11}C^{p}$)CBC structure is rarely if ever obtained though. When boron carbide samples are analyzed with local probes such as high resolution transmission electron microscopy (HR-TEM), plenty of different arrangements are observed, most notably regarding the three-atom chains.[37] By combining HR-TEM with DFT modelling of many possible local structures, Rasim and collaborators identified the presence of at least five different local arrangements in the chain region, including chains with vacancies in the center position (C□C) and 4-atom distorted rhombi-like chains (CB_2C).[37] The quantification of these point defects is quite a challenge, as they can only be probed locally. In the same work, Rasim proposes over 20 possible chain configurations from DFT calculations, out of which 8 are selected as the most likely ones, as their presence in a given ratio can explain the

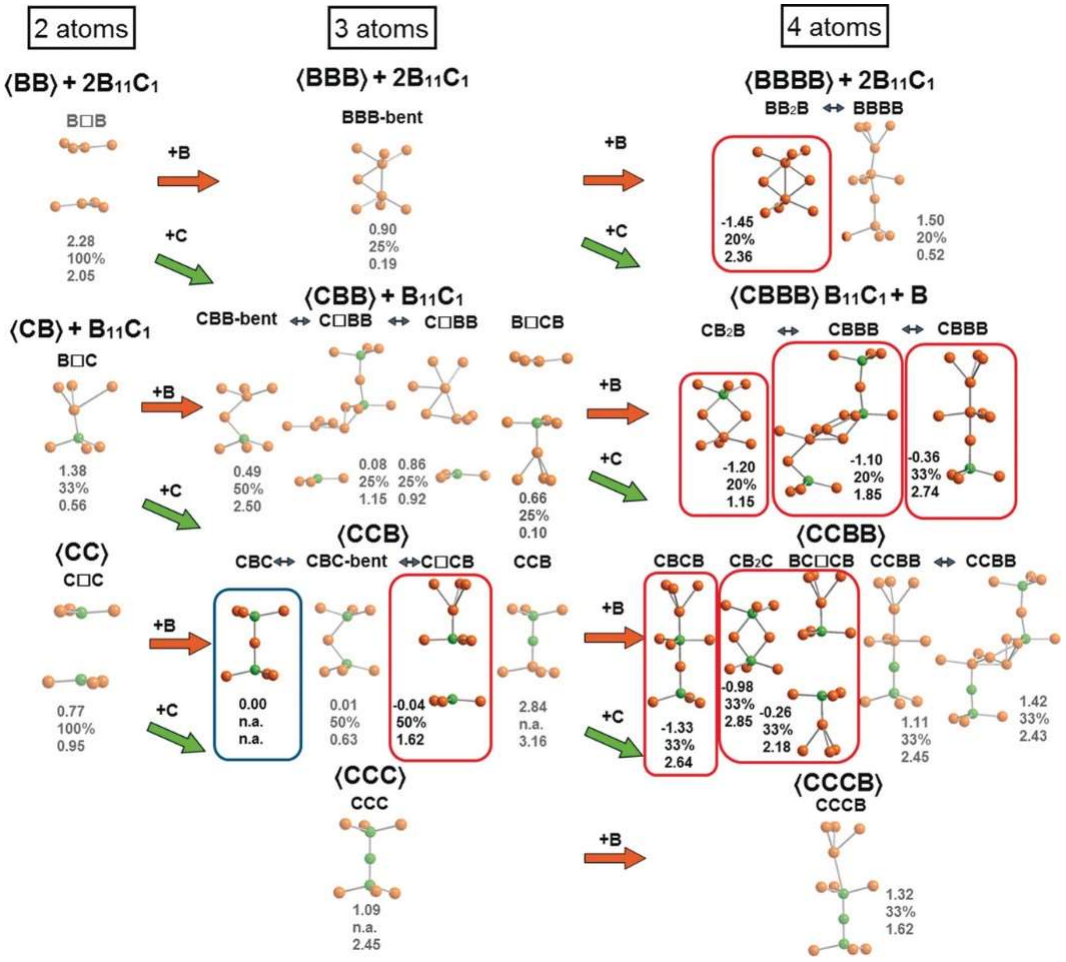

Figure II. 3. Local chain arrangements in boron carbide referenced to the regular CBC motif by energy of formation, threshold concentration in % sufficient for the metal-to-semiconductor transition and lowest electronic defect level above valence band maximum (top to bottom for each arrangement, energies in eV). The regular CBC arrangement is marked in blue, the energetically favorable arrangements are tagged in red. The image is reproduced from reference [37].

semiconducting properties of the sample. The proposed local arrangements are shown in **Figure II. 3**, with the most likely ones being highlighted.

Reaching thermodynamic equilibrium in boron carbide has proven a non-trivial task and has raised the question whether the presence of punctual defects is not constitutive of the structure. However, recent evidences indicate that disorder is not intrinsic to boron carbide. This was exposed in 2016, when a defect-free sample of stoichiometry $B_{13}C_2$ was reported. The use of high-pressures (8.5 – 9 GPa) was shown to be the key to achieve perfectly crystalline boron carbide-solids.[41] Beyond this case, the matter of structural defects in carbon poor samples is much less consensual than for B_4C.[1] Based on entropic and energetic considerations, Emin conjectured that as carbon content decreases, boron will preferentially substitute the chain sites.[42] According to the model, the number of CBB chains would increase until the totality of the material is comprised of (B_{11})CBB units. For even lower carbon contents, boron would take the place of the icosahedral carbon up to the idealized (B_{12})CBB stoichiometry. However, interpretation of the available X-ray diffraction data contraries this model and suggests rather that the icosahedral sites are replaced by boron in a first instance.[28,43] This view is also supported by DFT calculations, which indicate that the (B_{12})CBC configuration is more stable than the $(B_{11}C)$CBB one, both from the energetic considerations and from the lattice parameter correlation to the experimental data.[44–47] Fanchini *et al.* analyzed the energy landscape and structural parameters of various polytypes in a range of boron carbide stoichiometries.[46] It was observed that the free energy for the most common configurations fall within 0.2 eV of difference, matching typical temperature variations along boron carbide's synthesis.[46] In reality, polytypes probably coexist and most samples are likely a solid mixture of these.

II.3 Use of boron carbide as a structural material

Superhardness

For the sake of accurate comparison, several contemplations must be considered when discussing boron carbide's hardness. It should be firstly noted that due to the greater data availability, only Vicker's (VH) and Berkovich's hardness (BH) will be considered as micro- and nano-probes respectively. Both experiments consist in forcing the penetration of a diamond tip at the surface of the material, with a given force for a given time. The shape of the indenter tip is a 4 or 3-faced pyramid for the Vicker's and Berkovich's probe respectively. The experiment leaves a print or indentation on the surface of the material, as schematized in **Figure**

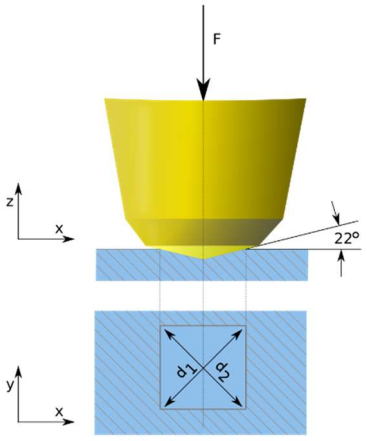

Figure II. 1. Vicker's indentation experiment scheme, reproduced from reference [50].

$$VH = \frac{2\sin(68°)\,F}{d^2} \qquad \textbf{Equation II. 1}$$

$$VH = 0.9261 \cdot BH \qquad \textbf{Equation II. 2}$$

II. 4. The dimensions of the indentation are the basis of the hardness' calculation. The hardness is then defined as the peak applied force divided by the contact area to the indenter, according to **Equation II. 1** for the Vicker's hardness. Berkovich's hardness can be transformed to Vicker's hardness upon geometrical correction through **Equation II. 2**.[48] The hardness value is in general dependent on the applied load. Such dependency is particularly high at low loads (0.1 – 5 N), which encumbers comparison of results. In this regime, small fluctuations from one equipment to another would render enormous hardness differences not representing actual changes in the sample's properties. When possible, it is generally advised to use higher loads (at least 10 N) until the hardness becomes asymptotically constant with the applied force.[49] As we will see, this ideal situation is not always feasible in superhard materials.

Several authors refer to the 1984 paper of Niihara[51] as the reference hardness of boron carbide, where a value as high as 47 GPa is reported as Vicker's hardness.[1,52] It should be clarified that this hardness was measured using a load of 0.98 N, which, as discussed above, corresponds to a regime of high dependence with the applied load, where the measure should not be taken as a reference. On the other hand, ideal asymptotic fall of the hardness of boron carbide towards high loads is not observed,[53,54] which is common in superhard materials.[55] Instead, hardness falls smoothly and linearly beyond 5 N loads.[54] Some authors have taken the initiative to consider the average among the hardness/load curve measured values as the reported hardness.[54] It should be stressed that there is no underlying physical meaning behind any of these values. The best hardness choice is the one that assures the comparability and limits the bias of the results. Averaging through an arbitrary load range that includes the non-linear regime is particularly susceptible to bias and incomparability.

Instead, during the course of this manuscript, the Vicker's hardness measured at 9.8 N ($VH_{9.8}$) and Berkovich's hardness at 1000 mN (BH_{1000}) will be taken at reference points, as per the ASTM-C1327 recommendations.[56] This choice is further justified because of the greater data availability and the fact that these loads lie well within the linear fall regime. When relevant, hardness/load curves will also be exposed for discussion.

The first important reference value to keep in mind when studying a compound's hardness is its intrinsic hardness. This is the hardness of the compound itself, without consideration of the morphology, defects, oxidation, surface states or any aspect other than the bulk crystalline structure. The intrinsic hardness can either be calculated on the basis of electronegativity and bond strength models or measured in single crystals, although in both cases it can still be dependent on the crystallographic facet, which should be specified. The computed $VH_{9.8}$ intrinsic hardness for the usual $B_{11}C^{p}$(CBC) configuration is of 38 GPa, without anisotropy considerations.[2] Empirically, Gogotsi initially studied the Berkovich hardness of zone-melt grown $B_{4.3}C$ single crystals.[3] Two crystallographic planes were analyzed: the (0001) and the $(10\bar{1}1)$ families. Both resulted in similar BH values: 40.5 and 41.5 GPa respectively. More recent results match very well these values.[57,58] Upon correction through **Equation II. 2**, VH would result in 37.5 and 38.4 GPa respectively, thus showing an excellent match with the theoretical predictions.

When polycrystalline samples are considered, numerous variables beyond the intrinsic hardness play a key role in the overall mechanical properties. Firstly, powders must be densified or sintered into dense monoliths for performing mechanical characterizations. The density or on the contrary, the presence of porosity, highly affects the hardness. Typically, densities over 99 % of the crystallographic density are preferred for accurate hardness testing. Even at a same compaction degree, the cohesion between grains has also shown strong influence.[59] Indeed, the bonding between the intergranular interface will modify the mobility of each grain under stress. Within this frame, a particular case withstands: nanotwins. Nanotwinning has been widely observed in B_4C.[60,61] The presence of twins has been shown to suppress the stress decrease as the B-C bond between icosahedral clusters breaks upon mechanical failure.[61,62] This in turn could increase the material's hardness up to a 12 %, which has been observed experimentally, although only with an increase of 2.3 %.[61] Hardness has also been shown to be strongly dependent on the composition, with an optimal stoichiometry of B_4C.[51] On the other hand, contrary to intuition, polytypes and the presence of defects are not expected to

exhibit major effect on the mechanical properties.[2] In contrast, the grain size has an enormous influence through the so-called Hall-Petch effect. This phenomenon will be further discussed in a following section, but roughly speaking, smaller crystallite sizes limit dislocation transport and thus enhance the resistance to plastic deformations.[63,64] Finally, the presence of secondary phases, most typically oxidized species,[65] carbon[66] or amorphous phases in general[1] have been shown to be detrimental to the mechanical properties, especially for nanopowders, where grain sliding is a major deformation mechanism.[67]

In **Table II. I**, the highest values reported for boron carbide $VH_{9.8}$ and BH_{1000} are summarized along with the main sample's characteristics. In all cases, these high values are obtained by combining high-purity ultrafine/nanosized samples and a throughout screening for the optimal sintering conditions. Interestingly, only the very best $VH_{9.8}$ report barely overpass the intrinsic hardness of boron carbide, which is a proof of the challenge raised by the processing of refractory materials as boron carbide. For the highest value reported, the role of high pressures was stressed in order to achieve optimal mechanical properties. For the same heat treatment, sintering at 3.5 or 4.5 GPa rendered an increase in hardness from 34.5 to 38 GPa, mainly associated to the enhancement of the density from 99.1 % to 99.6 %.[68] It should be noted that a report claiming an $VH_{9.8}$ of 42 GPa raises enormous doubts regarding the synthesis, processing and characterization of the compound and therefore will not be considered for the discussion.[69]

While the principle stands the same, Berkovich's hardness offers a probe with less contribution from the density/porosity and then more representative of the compound's intrinsic features.[73] For this reason, the hardness measured in the Berkovich setting tends to be higher than the one measured with a Vicker's probe, even after geometrical corrections. Still, no report

Table II. 1. Literature Vicker's and Berkovich's hardness for boron carbide sample along with the main sample characteristics.

Grain size (nm)	Density (%)	$VH_{9.8}$ (GPa)	Reference
2350	99.7	39 ± 1	[68]
690	100	34 ± 2	[53]
130	97	33 ± 3	[70]
300	99.2	32 ± 1	[54]
180	97.5	31 ± 3	[70]
27700	Not reported	30 ± 2	[71]
100	94.6	23 ± 3	[70]
Grain size (nm)	**Density (%)**	**BH_{1000} (GPa)**	**Reference**
5000	99.6	39 ± 2	[72]
40 – 150	92.8	20.5 ± 1.0	[66]

has overpassed boron carbide's intrinsic hardness. It is worth outstanding the case of the 20.5 GPa BH_{1000} measured by Reddy *et al.*[66] The authors prepared a compact monolith formed of nanograins with a significant amount of nanopores and graphite impurities located in the intergrain space. These are indeed at the origin of the reduced hardness, but do enhance other mechanical properties though. The authors show that nanopores and grain sliding lubricated by graphite hinders the nucleation of cracks and as a result, the fracture toughness is increased to 3.6 – 4.7 MPa $m^{1/2}$, that is a 75 % higher with respect to bulk B_4C.[74–77] This is a nice demonstration of a common occurrence in the study of structural materials, where optimizing one property often means compromising another.

Mechanical failure: shear amorphization bands

In spite of its diverse application ranges and outstanding properties, commercialization of boron carbide remains scarce, mainly due to its softening and fracture under *operando* conditions.[78] Boron carbide's brittle failure occurs under various loading environments such as hypervelocity impact,[79] indentation,[80] laser shock,[81] radiation[82] and mechanical scratching.[83] This feature prevents its use for long time periods and thus limits its engineering applications. The origin of such failure has been tracked down to the loss of crystallinity under stress and consequent formation of amorphization bands that serve as cavitation sites.[84] The amorphization bands are normally 2 – 3 nm of width and extend over 100 – 300 nm in length, an example can be seen in **Figure II. 5a** and **Figure II. 5b**.[85] Plenty of efforts have been

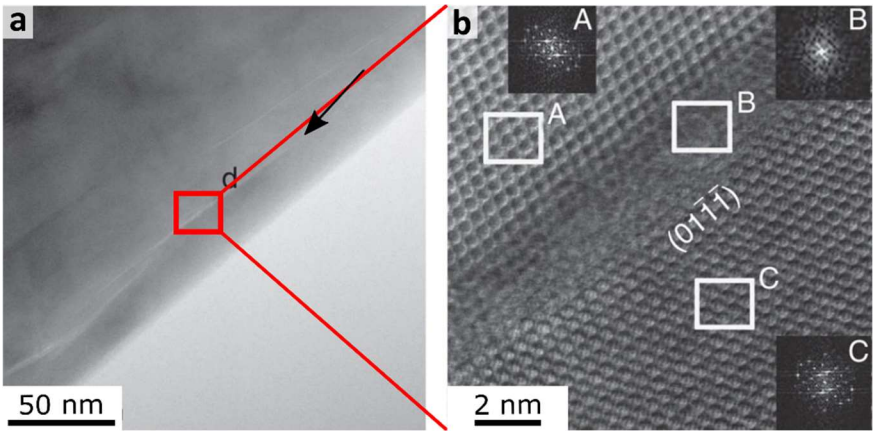

Figure II. 2. **(a)** Bright-field STEM image of a zoom-in shear band with a length of ~ 200 nm. The black arrowhead shows the tip of the shear band. **(b)** ABF-STEM image of the shear band taken from the red-box region in **(a)**. Inset: FFT patterns demonstrate the amorphous nature of the shear band. The image is adapted from reference [85].

devoted to the understanding of the amorphization mechanism and development of strengthening strategies to avoid it, but once again, the literature is overwhelmed with disputes.

A first mechanism **(i)** was proposed from *ab initio* molecular dynamics (AIMD) calculations that simulated the uniaxial compression of boron carbide.[86] It was concluded that B_4C deforms elastically up to 18.9 GPa and that further pressurization leads to a discontinuous volume reduction. Relaxed structures under these conditions (**Figure II. 6a**) revealed that the collapse arises in the bending of the C-B-C chains while the icosahedra remained intact. When the bending angle is large enough, the middle boron atom was observed to form bonds with neighboring atoms that later are not broken upon depressurization. Therefore, it was concluded that CBC bending triggered the deconstruction and subsequent amorphization of B_4C. Proposed mechanism **(ii)** comes from DFT calculations of the stress/strain curves through 11 possible slip planes. It was concluded that the $(01\bar{1}\bar{1})/<\bar{1}101>$ slip system presents the lower Hugoniot elastic limit (HEL) and thus is the most likely to fail first (see **Figure II. 6b**).[87] Stress drop

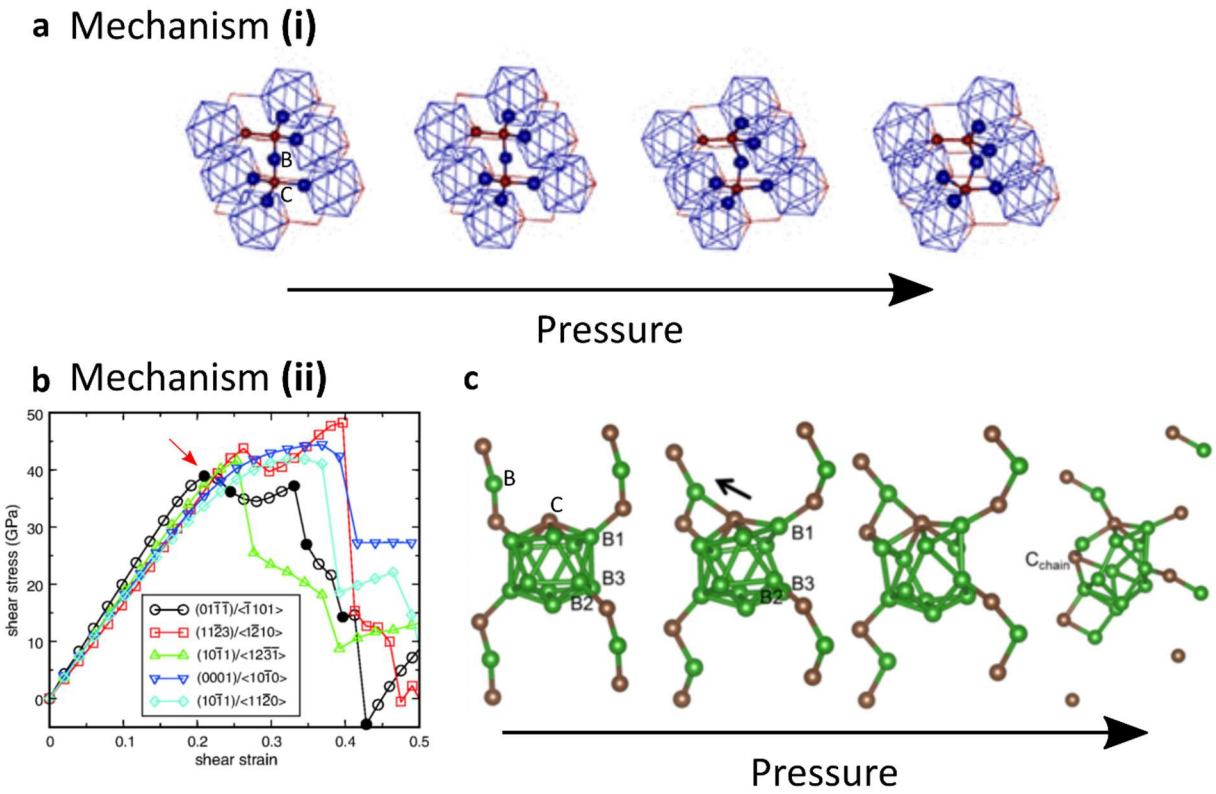

Figure II. 6. Possible amorphization mechanisms of boron carbide. **(a)** Chain-bending with pressure according to mechanism **(i)**. **(b)** Modelled stress/strain curves for the most plausible failure slip planes of boron carbide. The system failing at the lowest strain is marked with a red arrow: $(01\bar{1}\bar{1})/<\bar{1}101>$. **(c)** Structural visualization of the failure mechanism **(ii)**.

occurred beyond the HEL in two steps, interpreted as two different failure events. The simulations suggested that the first event corresponds to an intericosahedra C-B bond break, creating very reactive carbene species (**Figure II. 6c**). These are the ones that later react with the bended CBC chains as described previously, such reaction was not observed in mechanism **(i)** as the icosahedra were considered to contain all-B atoms instead of one polar carbon atom per icosahedra in mechanism **(ii)**.

Surprisingly, the same authors later suggested yet another amorphization mechanism **(iii)**.[88] Under the pretext that prior computations were limited to hundreds of atoms and that the actual amorphization band was not observed, they performed reactive molecular dynamics in a 200,000 atoms system. This time, it was found rather that the icosahedra fractured to give place to the denser amorphous phase. The higher density of the icosahedra was argued to lead to the tensile stress that causes cavitation, later crack opening and ultimately brittle failure. No structural local proof of the icosahedra collapse was shown though, and the conclusions were drawn from the analysis of calculated radial distribution functions, where no peak assignment was performed, hence raising questions on the veracity of the model. Other hypotheses suggesting a phase transition to an amorphous phase containing highly distorted, yet identifiable $B_{11}C$ icosahedra, have been highly questioned.[81] Calculations suggest that the energy barrier for such a transition is too high and so it must occur at pressures way beyond those at which amorphization bands are observed (168 GPa against the HEL of 17-20 GPa).[89] Raucoules *et al*. suggested that this barrier could be overcome if vacancies were formed within the structure, which at sufficiently high concentration could reduce the required pressure down to 28 GPa.[90]

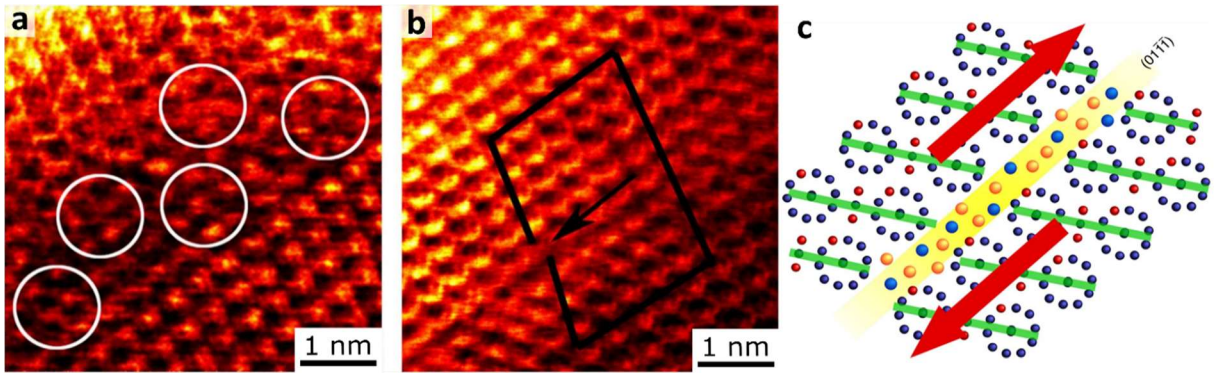

Figure II. 3. Amorphous band structure. **(a)** Retained icosahedra in the amorphous shear band imaged by on-axis ABF-STEM. The randomly distributed icosahedra in the amorphous band are denoted with white circles. **(b)** Shear displacement at the tip of the amorphous shear band, along with the Burger loop and Burger vector. **(c)** Visualization of the preferential slip plane shear-amorphization. The images are adapted from reference [85].

In the absence of *in-silico* consensus, models with the greater accordance to empirical evidence will be relied on. The local structure of the amorphous band has been directly imaged through annular bright-field scanning transmission electron microscopy (ABF-STEM), as shown in **Figure II. 7a**.[85] Amorphous bands were found to retain icosahedra motives, thus apparently discarding the view that amorphization originates from the collapse of icosahedra –mechanism **(iii)**–. However, it must be noted that the density of icosahedra is lower than in the crystalline compound, so these do partially collapse. Also matching with model **(ii)** is the fact that amorphization bands are indeed observed along the $(01\bar{1}\bar{1})$ plane, which is comprised of aligned three-atom chains (**Figure II. 7c**).

In **Figure II. 7b**, there is an evident lattice mismatch between the crystalline regions residing at both sides of the amorphous band. The Burger loop confirms a lattice displacement analogous to a partial dislocation, with a Burgers vector parallel to the shear band direction. This is interpreted as proof that amorphization of B_4C results from shear deformation analogous to dislocation deformation in ductile crystals. The Burgers vector magnitude is argued to be too large to allow for the extended propagation of dislocations or stacking faults, and thus deformation and eventual breaking of the structure must occur. In other words, dislocation plasticity is not expected in superhard materials like boron carbide due to the high lattice resistance and energy barrier.[91] In a recent report from the same group, it was experimentally found that dislocations do in fact mediate the amorphization of boron carbide.[80] This result

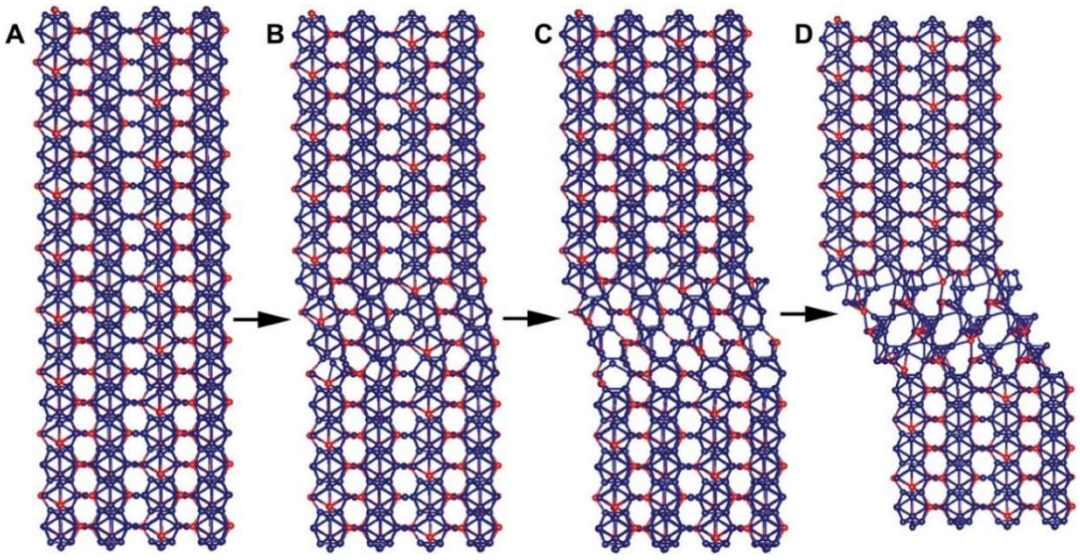

Figure II. 8. Schematic illustration shows the dislocation-mediated amorphization in B_4C. **(A)** Perfect crystal before deformation. **(B)** Shear deformation distorting the lattice. **(C)** Dislocation kink formation under shear deformation. **(D)** Amorphization under shear deformation, initiated from the dislocation. The image is reproduce from the reference [80].

was drawn from the stochastic analysis of pop-ins events (discontinuities) in the load/displacement curves, associated to abrupt volume changes from, in theory, the formation of dislocations. From the critical stress at the discontinuity, the activation volume (υ*), nucleation rate (η) and activation energy (E_a) of the hypothesized dislocations were determined. All these values are consistent with the fact that there is an initial step of dislocation formation. Further motion does not occur because of the lattice resistance and instead the structure breaks, probably according to mechanisms **(i)** and/or **(ii)**. The dislocation mediated amorphization mechanism is schematized in **Figure II. 8**.

Nanostructuration as a reinforcement strategy

Several reinforcement strategies have been proposed in order to both increase the hardness and the resistance to the amorphization of boron carbide.[92,93] A first avenue on this matter is the introduction of dopants in the structure. DFT calculations suggest that boron carbide leaves empty cages within the framework sufficiently large to host foreign atoms.[93] These cavities lie adjacent to the three-atoms chains, which have a higher susceptibility to bending and probably trigger the amorphization as it was discussed before. Filling this empty space with foreign atoms and forcing bonding with the linear chains may give structural support and hence ameliorate the mechanical properties. Among the large list of suggested dopants, Si,[94–96] Mg[97,98] and alkaline elements[99–102] outstand as the ones that have been experimentally achieved on top of theoretically studied. However, Si doping is the only case so far that has been empirically demonstrated to be beneficial to the mechanical properties.[96] While no major hardness enhancement was registered, it was demonstrated that even doping levels as low as 1 *at*. % in Si greatly mitigated amorphization.[96]

A second track that has proven way more fruitful is that of grain-boundary strengthening. Due to the lattice mismatch between adjacent grains and the higher disorder at the interface, grain boundaries act as pinning points for transporting dislocations and then impeding their propagation. Obstructing dislocation movement will hinder the onset of plasticity and hence increase the yield strength of the material. As a result, under an applied stress, dislocations pile

$$\sigma_y = \sigma_0 + \frac{k_y}{\sqrt{d}} \qquad \textbf{Equation II. 3}$$

σ_y Yield stress
σ_0 Material's constant (resistance of the lattice to dislocation motion)
k_y Strengthening coefficient
d Average grain diameter

up in the boundary and generate a repulsive stress field. These repulsive forces act as a driving force to reduce the energetic barrier for diffusion across the boundary, such that additional pile up will eventually trigger dislocation diffusion. Decreasing the grain size down to the nanometric range, will first limit the amount of dislocations that can fit and thus accumulate in a single grain, and second, increase the density of grain boundaries and so the frequency of encounters with propagating dislocations. A higher amount of applied stress will then be necessary to move dislocations, which in turn means that the material becomes stronger. The effect is governed by the Hall-Petch relationship (**Equation II. 3**)

The equation is valid until the optimal size that is usually about 10 nm. At this point, only one or two dislocations fit the grain. Because of the impossibility to transport dislocation, another regime of stress relief becomes operative, notably grains sliding. Below 10 nm, grains sliding is favored for the smallest grain size, so further decrease yields lower hardness, as shown in **Figure II. 9**. This range is known as the inverse Hall-Petch effect region.

The Hall-Petch effect has already proven to render superior mechanical properties in boron carbide, including but not limited to, hardness increase and amorphization resistance. A study comparing the properties of ultrafine 300 nm particles against a benchmark of 10 µm particle size showed that the hardness is increased from 28.4 GPa in the latter to 31.6 GPa in the ultrafine particles, along with a significant reduction of the amorphization extent as probed from Raman microscopy.[54] Smaller particle sizes have been probed by Moshtaghioun, who studied samples of 17.2 µm, 688 nm, 370 nm and 120 nm grain size. At first glance, the study seems to

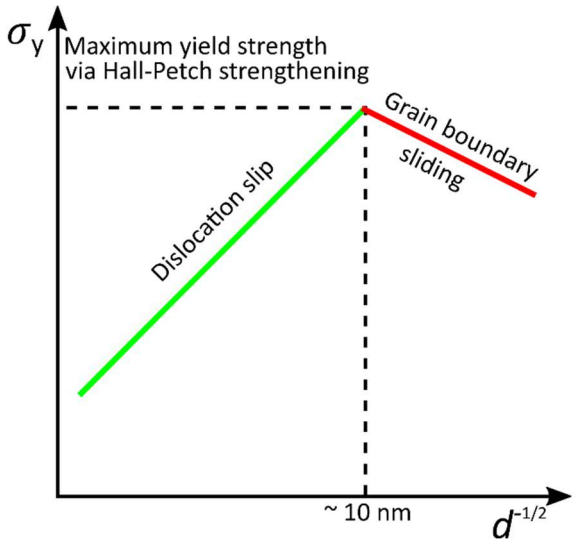

Figure II. 9. Yield stress needed to trigger dislocation transportation as a function of the grain size. The Hall-Petch relation governs for the grain sizes > 10 nm (green curve) and for smaller sizes the material is weakened through the inverse Hall-Petch effect (red curve).

show an optimal size for 688 nm, exhibiting a hardness of 34 GPa that decreases for smaller sizes. However, when these values are corrected for the porosity, the expected linear dependence of the hardness against $d^{-1/2}$ is retrieved, showing that grain's sliding is still not triggered. The smallest grain sizes hardness study on boron carbide corresponds to a report of Reddy *et al*., who reported a relatively low hardness (BH = 20.5 GPa) in (40 – 150) nm nanoparticles, probably due to the presence of carbon at the interfaces favoring grain's sliding.[66] This mechanism was observed by TEM. The case was analyzed from a theoretical point of view by the group of Qi An.[67] 5, 10 and 15 nm Voronoi polyhedra were built and joint together to model the B_4C nanostructures. It was found that indeed, upon a critical stress, grain interphases become amorphous and act as lubricant for grains sliding while engendering cavitation. This study showed for the first time the detrimental interplay between amorphization and hardness in boron carbide. There is no experimental report on such size range though, due to the synthetic challenge it represents.

II.4 Synthesis of Boron Carbide nano-objects

A major advantage of boron carbide against other refractory superhard materials is its relatively simple scalability and industriabillity. As superhardness arises in high valence electron concentration under an extended covalent framework, this phenomenon is almost exclusively exhibited in dense phases. The synthesis of dense compounds is favored under very high pressures, normally at least in the GPa order of magnitude. The textbook case is diamond, whose production from graphite is only achieved above 3.0 GPa.[103] This implies an enormous cost in the machinery needed to achieve such pressures and highly limits the production capacity. In this context, boron carbide outstands as one of the only superhard phases that can be obtained at room pressure. Moreover, boron carbide (or its polytype-mixture) is a thermodynamic product,[104] meaning that diverse boron and carbon sources can be used knowing that most likely, boron carbide will be obtained. The morphology and purity control are however the big challenges. In **Table II. 2**, the known fabrication processes along with the product's characteristics are summarized.

All the classical methods of fabrication of boron carbide (references [105–112]) use carbothermal reduction. This reaction employs the carbon source as reducing agent. Thanks to its simplicity, the production cost is very low, which is why this is the method of choice for industrial production of boron carbide. Although little to no microstructural control can be

achieved, the method has proven useful for delivering high purity bulk boron carbide. The carbothermal reduction between B_2O_3 and C achieves exceptionally small particles after sedimentation separation.[112]

The self-propagating thermal reduction method from reference [113] uses carbon black (or coke) and boric acid (or boric anhydride) as raw materials, active metal substance (usually Mg) as reducing agent or flux, and the heat generated by self-propagating combustion reaction of metal substance are used to synthesize boron carbide. Self-propagating thermal reduction has the advantages of low initial reaction temperature, energy saving, fast reaction, and simple equipment. However, as shown in the **Equation II. 4**, MgO is produced as by-product, which must be removed afterwards.

$$6\ Mg(s) + C(s) + 2\ B_2O_3(s) \rightarrow 6\ MgO(s) + B_4C(s) \qquad \textbf{Equation II. 4}$$

More recently, wet chemistry methods have shown their successful morphology control for boron carbide nanostructures. In particular, sol-gel reactions proved to be able to decrease the particle size down to the 50 – 90 nm range (references [114–117]). This type of reactions consists in dissolving the reagents in an aqueous media and let them jellify at low temperature. Posterior aging, evaporation and calcination triggers the crystallization of the targeted compound. This path allows to remarkably decrease the working temperature below 1000 °C, although carrying the disadvantage of low product crystallinity.[114] Superior product quality is obtained with a 1600 °C annealing step, although triggering the grain growth to 87 nm.[115] A second wet-chemical method used is solvothermal synthesis. This consists in dissolving the reagent amorphous boron in CCl_4 that acts as solvent and carbon source at the same time. The reaction is carried out in a sealed vessel such that upon temperature increase, pressure in the media will also increase. Crystallization is targeted at temperatures as low as 600 °C, with a resulting mean size of 60 nm, although again, at the expense of crystalline quality.[116]

Table II. 2. Summary of reported synthesis procedures towards boron carbide.

Reagents	Reaction parameters	Product size (dispersion)	Product purity	Year	Ref.
B_2O_3 + coke	2400 °C	Not reported	90 %	1933	[105]
H_3BO_3 + coke	1470 °C, 5h	(13 ± 10) μm	Not reported	2004	[106]
H_3BO_3 + charcoal	Charge melting temperature (arc furnace)	Not reported	15 % C impurities	1939	[107]
B_2O_3 + coke/active carbon	1470 °C, 1-5 h	(25 ± 20) μm	1 % C impurities	2006	[108]
B_2O_3 + carbon	1800 °C, 20	(10 ± 5) μm	C-free	2004	[109]
B_2O_3 + carbon black/graphite/activated charcoal	2227 °C	Not reported	98 % pure	1979	[110]
H_3BO_3 + acetylene carbon black	1580 °C, 3 min	(1.0 ± 0.8) μm	Not reported	1989	[111]
B_2O_3 + C	1400-1600 °C	(70 ± 50) nm	Unknown amorphous B_4C content	2006	[112]
H_3BO_3 + Mg + C	750 °C	(90 ± 50) nm	Unknown MgO content	2015	[113]
$B(OH)_3$ + phenil resin	1270 °C	(70 ± 30) nm	Unknown amorphous B_4C content	2012	[114]
$B(OH)_3$ + $(CH_2CHOH)_n$	1400 °C	(67 ± 20) nm	Unknown carbon content	2011	[115]
$B(OH)_3$ + $(CH_2CHOH)_n$	1600 °C	(87 ± 30) nm	99 %	2011	[115]
B(am) + Li + CCl_4	600 °C, 8 h	(60 ± 30) nm	Unknown amorphous B_4C content	2005	[116]

II.5 Sintering into dense monoliths

Sintering or consolidation refers to the densification process through which pores within a packed powder are shrinked upon heating and/or application of pressure. Traditionally, the interparticle pores are eliminated by atomic diffusion during the sintering, and the atomic diffusion may cause inevitable grain growth aside from contributing to the densification. Thus, the two competing mechanisms of densification and grain growth always coexist in sintering.[117] The large-scale application of boron carbide is limited in great deal due to the difficulty to process it into dense monoliths (density > 99 %). Many of the attributes of boron carbide that were listed as advantageous can actually become difficulties when it comes to the processing of the material. Consolidation of boron carbide is as a matter of fact complicated due to its high melting point (2720 °C),[5] low self-diffusion coefficient and high vapor pressure. Extreme high sintering temperatures are required to trigger densification due to the presence of predominantly covalent bonds in B_4C.

Pressureless sintering was initially explored as a cheap, easy and direct path towards dense monoliths of boron carbide. It was evidenced that at temperatures > 2000 °C, surface diffusion and evaporation condensation mechanisms occur, which result in mass transfer without densification. Densification is achieved only at temperatures above 2000 °C, by grain boundary and volume diffusion mechanisms. At higher temperature, exaggerated grain growth also takes place resulting in poor mechanical properties. Beyond this temperature, volatilization of non-stoichiometric boron carbide takes place, leaving carbon behind at the grain boundaries.[11] Without external force aid, it was concluded that proper densities above 90 % of the crystallographic density are only accessible past the 2300 °C. These compacts present a coarse grained microstructure of ~ 50 μm and high amounts of intragranular porosity.[11] For this reason, the focus will be rather put on pressure-assisted sintering processes.

Hot-Pressing

Pressure assisted consolidation/sintering involves heating a powder compact, with the simultaneous application of pressure. The powder compacts are typically heated externally using graphite heating elements and the pressure is applied hydraulically. It is worth stating that the melting point of boron carbide decreases with the pressure, so the maximal working temperature is reduced.[5] This remains a high limit though, as for 5 GPa the melting point is ~ 2650 °C and for 8 GPa ~ 2600 °C.[5] Inner lining of the graphite die with hexagonal boron

nitride (*h*-BN) is essential to prevent carbon migration to the boron carbide pellet. Fast heating rates and application of high pressures have been helpful in obtaining full densification at a lower temperature of 1900 °C.[118] Ostapengo *et al*. have found that the densification of boron carbide is governed by a process leading to non-linear creep, whose rate is a function on the square of the applied stress.[119] Later, Koval'chenko evidenced that dislocation climb is the responsible to the quadratic-dependent creep process.[120] This fact suggests that use of very high pressures may be instrumental in retaining a fine microstructure in boron carbide while targeting high densification. This was indeed recently shown by Liu and collaborators, who systematically studied the influence of pressure, temperature and time in the sintering of boron carbide. It was found that increasing the sintering pressure from 3.5 to 4.5 GPa yielded an augmented density of 99.7 % against the initial 99.2 %, which in turn increases the hardness from 34.5 to 37.5 GPa, although stagnation is observed for further pressurization.[68] The same asymptotic behavior was observed for temperatures beyond 1300 °C and dwell times beyond 5 min.[68]

Spark-Plasma Sintering

Spark-Plasma sintering was patented by Yoo in 1999 as an alternative to conventional hot-pressing sintering.[121] Instead of having the electrical current dissipated into heat by an external piece, it passes directly through the sample in a short-pulsed manner, while still applying an external pressure. The process is thus extremely sample-dependent, but in general terms, it should activate surface processes like evaporation of oxide films, impurities and moisture, all while heating only the grain's contact point and hence reducing the sintering temperature.[11] The main disadvantage in the particular case of boron carbide, is that lining with *h*-BN is no longer possible, as its isolating character would prevent current to go through the sample. Therefore, the sample must lay directly in contact with the graphite heater, which may lead to carbon migration into the sample. The group of Domínguez-Rodríguez explored this approach in 2015.[70] They did manage to produce dense monoliths in a two steps scheme, where a first treatment at low temperature was intended to clean the surface before actually triggering sintering at 1600 °C.[70] However, carbon traces were observed in the diffractograms and the achieved hardness of 32.5 GPa did not excel.[70]

II.6 Summary and strategy for the first experimental part

Boron carbide exhibits numerous properties that provide it with a high potential as a structural material for high performance applications. Two big bottlenecks are the impediments of its large-scale industrialization: its relatively low hardness (compared to other superhard materials) and its poor resistance to amorphization upon an external stress. A strategy that has proven fruitful to ameliorate both issues is the decrease of the grain size, which according to the Hall-Petch relation increases the hardness, and as it has been evidenced, the resistance to the amorphization at the same time. This avenue has not been extended to the optimal range of particle size of ~ 10 nm. The reason behind is the fact that no synthetic procedure has been developed to trigger the crystallization of the boron carbide phase in a sufficiently good quality while at the same time impeding grain growth. Also, the sintering procedures struggle to retain boron carbide's microstructure. If both bottlenecks were overcome, numerous applications could benefit from a resistant superhard and durable boron carbide.

A still unexplored track is the use of isomorphic transformations to prevent grain growth. That is the use of a compound with similar composition that could transition to boron carbide, but that at the same time can be manufactured with the desired nanoscale morphology in an easier manner than for the direct synthesis of boron carbide. This strategy relates to the templating method described earlier. The introduction of an extra-step in the synthesis, consisting in the synthesis of the template; would of course increase the complexity of the fabrication procedure. Therefore, an extensive investigation and characterization of the template itself must be performed in order to comprehend how to manipulate its latter transformation to ideally nanosized boron carbide.[122]

In the present work we have selected the compound NaB_5C as initial nanotemplate. This compound contains a B:C ratio well within the solubility range of these elements in the boron carbide structure. We explore its synthesis as nano-objects in molten salts, which is exposed in **Chapter III**. The key parameters involved in the synthesis are discussed, as well as the structure and microstructure of the compound, which are thoroughly investigated. Once the material's structure and morphological features are understood and controlled, we explore its transformation to boron carbide nanostructures in the frame of a nanotemplating synthesis. This is exposed in **Chapter IV**, where again the transformation parameters are discussed along with a deep structural characterization. The processing of the material was studied as well for

achieving dense monoliths. Finally, the performances were evaluated in terms of hardness and amorphization resistance, for which we correlate the properties to the structure and morphology of the nano-objects, hence ultimately bridging the original templating synthesis and the final properties. All in all, we show the advances possible by the proposed nanotemplating methodology.

Chapter III: Synthesis and structural analysis of the nanotemplate NaB_5C

III.1 Introduction

Metal hexaborides and isostructural carbaborides

NaB_5C is directly linked to the well-known metal hexaborides in terms of crystal and electronic structure (**Figure III. 1**). Metal hexaborides themselves have been the focus of renewed interest in recent years. Some of them are well known to exhibit field emission (rare earth hexaborides) and thermoelectric (alkaline earth hexaborides) properties, but new and unexpected behaviors have emerged within the last years: LaB_6 exhibits near-infrared surface plasmon resonance[123] while SmB_6 is a Kondo insulator coupled to a specific conductive surface state, which might be related to topological features.[124] Both examples show the importance of controlling the composition, but also the surface states and the surface-to-volume ratio of metal hexaborides in order to control optical and conduction properties, among others. Nanocrystal design provides interesting perspectives in this respect.

The theoretical frame explaining the stability and conduction properties of many metal hexaborides has been provided by Longuet-Higgins and de V. Roberts,[125] who have built an analogy between the octahedral B_6 clusters building the hexaboride framework (Error!

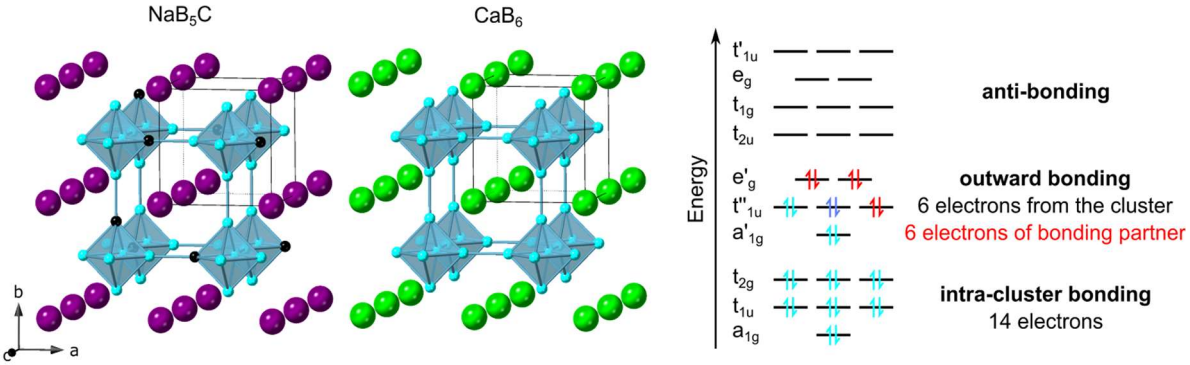

Figure III. 1. Crystal structures (cubic $Pm\bar{3}m$ space group) of NaB_5C and CaB_6. Boron, carbon, sodium and calcium atoms are in blue, black, purple and green, respectively. The octahedral clusters are represented in light blue. For NaB_5C, the carbon atoms are placed randomly in each unit cell. The molecular orbital diagram corresponds to one octahedral cluster, analogue to the molecular $B_6H_6^{2-}$ anion. Light blue arrows account for electrons provided by 6 boron atoms into a B_6 octahedral cluster. The 6 red arrows correspond to the bonding partners building 6 outward 2 center-2 electron bonds (B-H bonds in $B_6H_6^{2-}$ analogue, inter-cluster B-B bonds in the hexaboride). The remaining 2 blue arrows account for the two additional electrons needed for fully stabilizing the framework.

Reference source not found.) and the $B_6H_6^{2-}$ anion, thus referring to Wade's rules.[126–128] According to the molecular orbital diagram of a B_6 unit (**Figure III. 1**), the anion reaches a stable closed shell configuration and the B_6 extended framework is stable when each octahedron is provided with 20 electrons. These 20 electrons include 14 electrons filling the intra-octahedron bonding orbitals, and 6 electrons populating each of the 6 outwardly bonding orbitals at each corner of the octahedron to build 2 electrons-2 centers inter-octahedra bonds (or B-H bonds for the analog $B_6H_6^{2-}$ anion). The B_6 octahedron provides itself 18 electrons and the metal encaged between the octahedral units supplies 2 electrons in the formalism of the Zintl concept. Overall, with divalent metal cations, like alkaline earth, only the bonding states are filled, which yields semiconductors. In this model, an additional electron, provided with trivalent metal cations would yield metallic compounds, like LaB_6, although more complex effects such as strong electron correlation could change the outcome and yield bulk semiconductors, like in SmB_6. In this frame, replacing the metal with an alkali metal supplying only one electron would fail to provide full stabilization, which explains the near complete absence of alkali hexaboride[129,130] except Li_2B_6[131] and the notable exception of metal deficient KB_6, for which consensus has not been reached.[132]

To go beyond this restriction and in their effort to discover new boron-rich borides of alkali metals, B. Albert and K. Schmitt [133,134] have discovered ternary compounds with the hexaboride structure: alkali carbaborides NaB_5C and KB_5C, which are actually the only carbaborides of sodium and potassium.[130] In these compounds, the B_6 units in hexaborides are replaced by B_5C octahedra. Substituting one boron for one carbon atom in each octahedron provides the missing electron to fulfil the maximal stabilization conditions of the extended octahedral framework.[133,134] According to this model, one would expect that deviations from the ideal stoichiometry would destabilize the solids. These theoretical considerations have however been difficult to confirm experimentally up to now because of the absence of a local probe for investigating the boron/carbon local environment.

Besides, given the propensity of nanocrystals to accommodate larger strains and deviations to ideal stoichiometries,[135] the question arises as to whether stoichiometry deviation could occur or be facilitated in alkali carbaboride nanocrystals. In addition, the reactivity of NaB_5C and KB_5C is a virgin field, while other alkali-based compounds of *p*-block elements are known to exhibit interesting phase transformations when the alkali metal can be eliminated, as in the case of the evolution of sodium silicide Na_4Si_4 to silicon clathrates.[136] Overall, considering

the intrinsic carbon and boron mixing in a stoichiometry (16.7 % *at*. C) lying well within the solubility range in the boron carbide structure (9-20 % *at*. C) and the possible instability generated upon Na removal, we propose the hypothesis that NaB_5C nanocrystals could be used as boron carbide nano-objects precursor and template. The formation of NaB_5C nanocrystals from the molten salts procedure was initially evidenced by Simon Delacroix in the frame of his thesis work.[137] Initial synthesis conditions and partial characterizations (EDS, Raman, XPS, BET and ^{1}H-NMR) are reproduced from his thesis manuscript.[137] In the present chapter we further expand on the local and long-range structural characterization, particularly through powder XRD and solid state NMR as well as in the optimization of synthesis conditions.

III.2 Materials and methods

Sodium borohydride (98 %, Alfa Aesar), sodium iodide (> 99.5 %, Sigma Aldrich), polyethylene (M_w = 35000 g·mol^{-1}, Sigma Aldrich), ^{13}C-enriched polyethylene (CORTECNET, 99 %), methanol (VWR Normapur grade) were used as received and handled under argon atmosphere in a glovebox (H_2O < 0.5 ppm, O_2 < 0.5 ppm) and with standard Schlenk techniques.

To synthesize NaB_5C, 600 mg of sodium borohydride (15.9 mmol) were ground with 5 g of sodium iodide and initially 285 mg of polyethylene (20.4 mmol, C:B atomic ratio of 1:1.28) during two minutes at 20 Hz (Retsch MM400, 50 mL stainless steel bowls filled with one ball) to obtain an homogeneous finely ground powder. The protocol was later changed to use 185 mg of polyethylene (13.2 mmol, C:B atomic ratio of 1:0.83), the actual protocol used will be clarified for each sample. The mixture was heated at 900 °C under argon during two hours in a crucible, and then cooled down to room temperature. The synthesis was run in either molybdenum or *h*-BN crucibles. The reaction mixture was washed with methanol by ten cycles of centrifugation and redispersion. The powder was dried under vacuum at a 150 °C oil bath for 12 h before being stored under argon. 156 mg was typically recovered after synthesis, which corresponds to a yield of 55 % versus the boron precursor. The synthesis was reproduced at least 20 times to ensure reproducibility. The procedure for synthesizing ^{13}C-enriched NaB_5C used the C:B atomic ratio of 1:0.83 and *h*-BN crucible conditions, the rest of the parameters remained equal to the general procedure.

General characterizations are described in the **Appendix AI**.

III.3 Results and discussion

Synthesis and electron microscopy

NaB_5C nanoparticles were initially synthesized by using sodium borohydride and polyethylene as boron and carbon sources respectively. The reaction medium was molten sodium iodide (melting point 661 °C), which also acted as sodium source. Reaction temperature was set at 900 °C for 2 h. A large excess of carbon (B:C = 5:6.4) was used to compensate for carbon losses during the synthesis. The sample comprised exclusively slightly elongated cubic nanoparticles (**Figure III. 2**) with a size distribution centered at 7 nm, and edge lengths ranging from 2 to 14 nm (**Figure III. 2a**). Indexing from high resolution electron microscopy and electron diffraction Debye rings (**Figure III. 2b** inset) confirmed the expected NaB_5C structure in the localized regions. HRTEM also suggested the formation of single-crystalline domain particles that expose {100} facets.

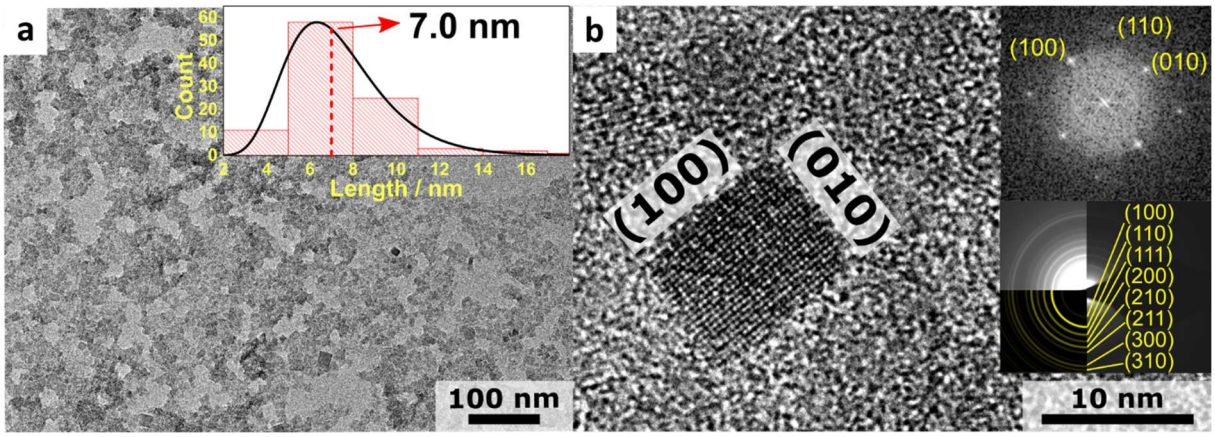

Figure III. 2. **(a)** TEM and **(b)** HR-TEM images of NaB_5C-related sodium carbaboride nanocrystals. The corresponding size distribution is shown as inset in **a**. The Fast Fourier Transform (FFT) of image **(b)** is shown as insert, together with the SAED pattern. They are fully indexed along the NaB_5C structure.

Powder X-ray diffraction

The powder X-ray diffraction (XRD) pattern (**Figure III. 3**) was fully indexed along the cubic $Pm\bar{3}m$ space group of the NaB_5C crystal structure. Rietveld refinement with this structure yields for the final model satisfactory conventional figures of merit (R_{wp} = 5.41, R_B = 0.66, χ^2 = 6.31). In a first step, the XRD pattern was fitted to the exact NaB_5C stoichiometry (see **Figure III. 3a**).[134] While this model seemed appropriate (R_{wp} = 7.42, R_B = 1.00, χ^2 = 11.18), discrepancies with the experimental and reported data motivated further analysis. Firstly, the adjustment failed to fully account for the intensity of the (100) reflection at about 21.6 ° (Cu

Kα), which represented the largest relative error according to the difference curve. Secondly, the refined cell parameter – 4.0878(2)Å – was slightly smaller than the reported one of 4.0925(1)Å.[134] We have then refined atomic occupancies in order to further improve the agreement with experimental data.

Three approaches were considered: refinement of only the B/C ratio (model **I**), refinement of only the Na occupancy (model **II**) and refinement of both the B/C ratio and the Na occupancy (model **III**). All three models coincide better with the experimental data (**Figure III. 3c**, **e** and **g** respectively), since they all influence the pattern by increasing the relative ratio of the (100) reflection, as compared in **Figure III. 3b**, **d**, **f** and **h** against the (200) and (210) reflections. However, model **I** yielded a negative B occupancy that is not chemically valid. On the other hand, model **II** leads to the stoichiometry $Na_{0.809}B_5C$, which deviates from the electron counting rules described above. Model **III** enabled to compensate possible Na vacancies with an increase in the carbon content to fulfil the overall electron counting rule in the B-C framework with 20 electrons per octahedral unit, provided the stoichiometry is constrained to $Na_{1-x}B_{5-x}C_{1+x}$. Accordingly, Rietveld refinement yielded the $Na_{0.816}B_{4.816}C_{1.184}$ composition, which does hint to the presence of Na vacancies and carbon over stoichiometry, but can only be taken as a semiquantitative result, the low *Z* character of all the elements involved do not allow to extract quantitative results from XRD in terms of composition.

The results from models **II** and **III** were indistinguishable in terms of figures of merit or visual inspection (**Figure III. 3**). However, model **III** satisfied the electron counting rule and was then privileged. The refinement was clearly in better agreement with the experimental diagram compared to the refinement from the ideal NaB_5C model (**Figure III. 3a**). The resulting stoichiometry corresponded to molar ratios Na:B and B:C of 0.17 and 4.07, respectively, *versus* 0.20 and 5.00 for the tabulated NaB_5C compound.[134] According to the final Rietveld refinement of the XRD pattern, the crystallite size is 5.0 nm in agreement with the particle size from TEM, confirming that each nanoparticle consisted in a single crystal domain. Full crystallographic data obtained from the final Rietveld refinement are summarised in the **Tables AII. 1** and **AII. 2** in **Appendix AII**. Aware of the limitations of X-ray diffraction for low *Z* elements, we further support our model by using solid-state Nuclear Magnetic Resonance (NMR) as probe, as shown in a following section.

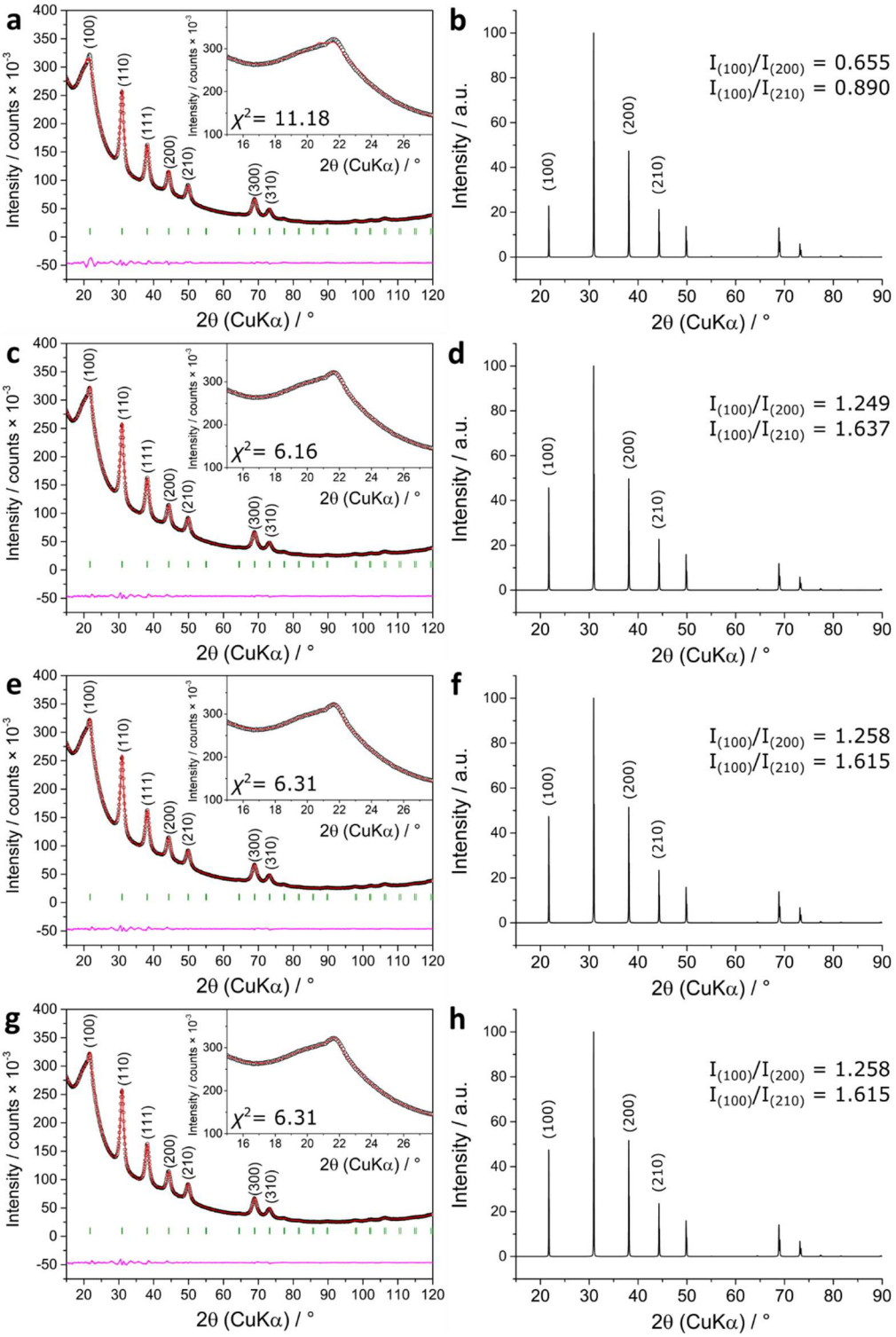

Figure III. 3. Consecutive Rietveld refinement of NaB_5C: experimental pattern (dotted black), calculated pattern (red) and difference curve (purple). The green vertical bars correspond to the Bragg peak positions according to the NaB_5C structure. The broad bump between 15 and 30° is due to beam scattering by the protective PMMA plastic dome used to maintain the powder under protective argon atmosphere. **(a)** No occupation refinement. **(b)** Simulated XRD powder diffractogram from model considered in **(a)**. **(c)** Model **I**, B to C ratio refinement. **d)** Simulated XRD powder diffractogram from model considered in **(c)**. **(e)** Model **II**, Na occupation refinement. **(f)** Simulated XRD powder diffractogram from model considered in **(f)**. **(g)** Model **III**, occupancies refined restrained to the $Na_{1-x}B_{5-x}C_{1+x}$. formula. **(h)** Simulated XRD powder diffractogram from model considered in **g**.

Determination of the composition

The composition of the material was confirmed by Energy dispersive X-ray spectroscopy (EDS), and X-ray photoelectron spectroscopy (XPS). Both techniques yield consistent molar Na:B ratios of 0.15 and 0.17, respectively, as compared to the ideal 0.2 ratio in NaB_5C. These values confirmed the sodium sub-stoichiometry inferred by XRD. The absence of any band characteristic of graphitic ordering on the Raman spectrum (**Figure III. 4**) suggested that the sample was exempt of layered carbonaceous by-products and of amorphous carbon, which usually exhibits a slight portion of staked graphitic layers, thus giving rise to a Raman signature. The presence of methanol at the surface of the nanocrystals was confirmed by ^1H solid-state nuclear magnetic resonance (SS-NMR, **Figure III. 5**), showing two peaks characteristic of methanol. The detectable amount of methanol is related to the high specific surface measured by nitrogen sorption around 300 $m^2 \cdot g^{-1}$ according to the BET method. This high surface area also resulted in surface carbonaceous contamination during analysis, which precludes any precise estimation of the carbon content.[134]

The surface states were still further probed by XPS (**Figure III. 6**). According to the deconvolution of C 1s spectrum, four carbon chemical states were detected. The lowest binding

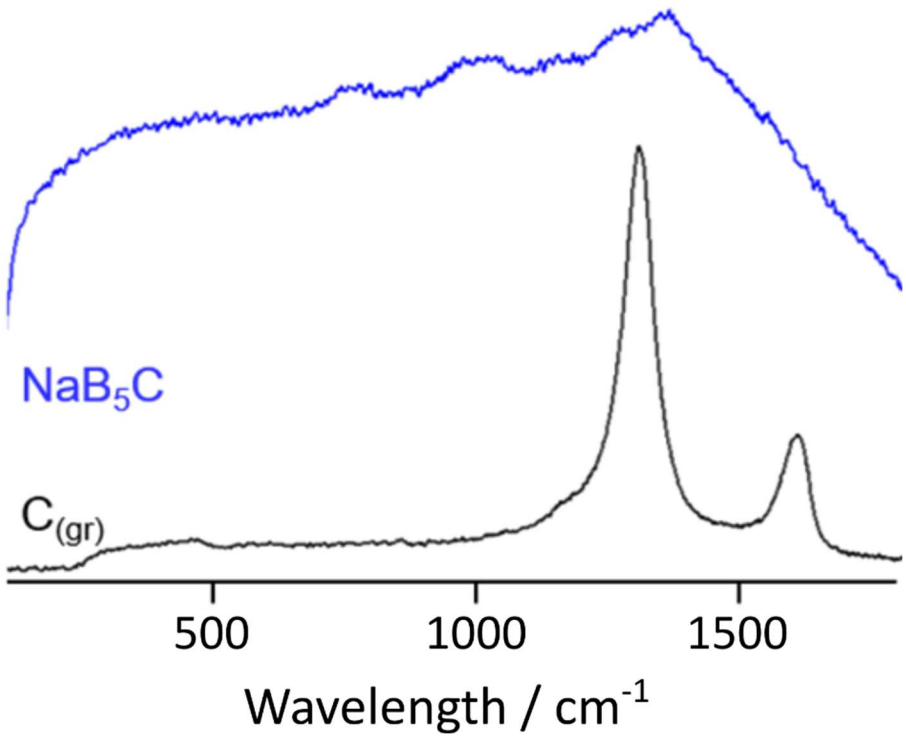

Figure III. 4. Raman spectra of sodium borocarbide nanocrystals (blue). The spectrum of glassy carbon is given as a reference (black), showing the two typical bands of disordered carbon with graphitic domains.

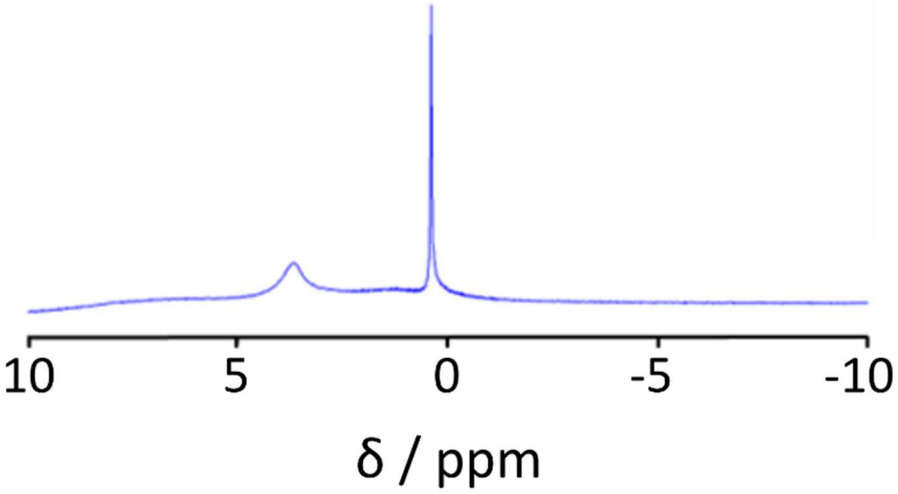

Figure III. 5. Solid state 1H NMR spectrum of sodium borocarbide nanocrystals.

energy peak at 283.06 eV was assigned to C-B bonds.[138] C-O bonds are also detected at 286.80 eV. They could arise from contamination and/or surface reactivity with methanol. The peaks at 284.81 eV and 289.04 eV come from adventitious carbon contamination. The B 1s spectrum was deconvoluted into three peaks. The component at 187.02 eV corresponded to B-B bonds.[139] The peak at 188.13 eV was assigned to B-C bonds.[139] Its relatively large FWHM indicated a distribution of boron chemical states round the B-C bonding boron, which could be explained by the various environments of boron atoms in the octahedra, with B atoms that can be linked to *e.g.* 3 B and 1 C, or 2 B and 2 C. The peak at 192.68 eV is characteristic of oxidized boron which could be ascribed to the high reactivity of the sample when exposed to air, during transfer to the XPS analysis chamber. This high reactivity, also observed by the pyrophoric nature of the dried samples when exposed a few seconds to air, was not reported for bulk sodium carbaboride[133,134] and is probably related to the small particle size and the very high surface-to-volume ratio. Despite surface oxidation and methanol adsorption, the particles were remarkably sodium borocarbide single nanocrystals. The consistency between the particle (TEM) and crystallite (XRD) sizes showed that oxidation impacts only the near surface of the nanocrystals when the samples are exposed only shortly to air. The quantitative deconvolution data from XPS is summarized in **Table AII. 3** of **Appendix II**.

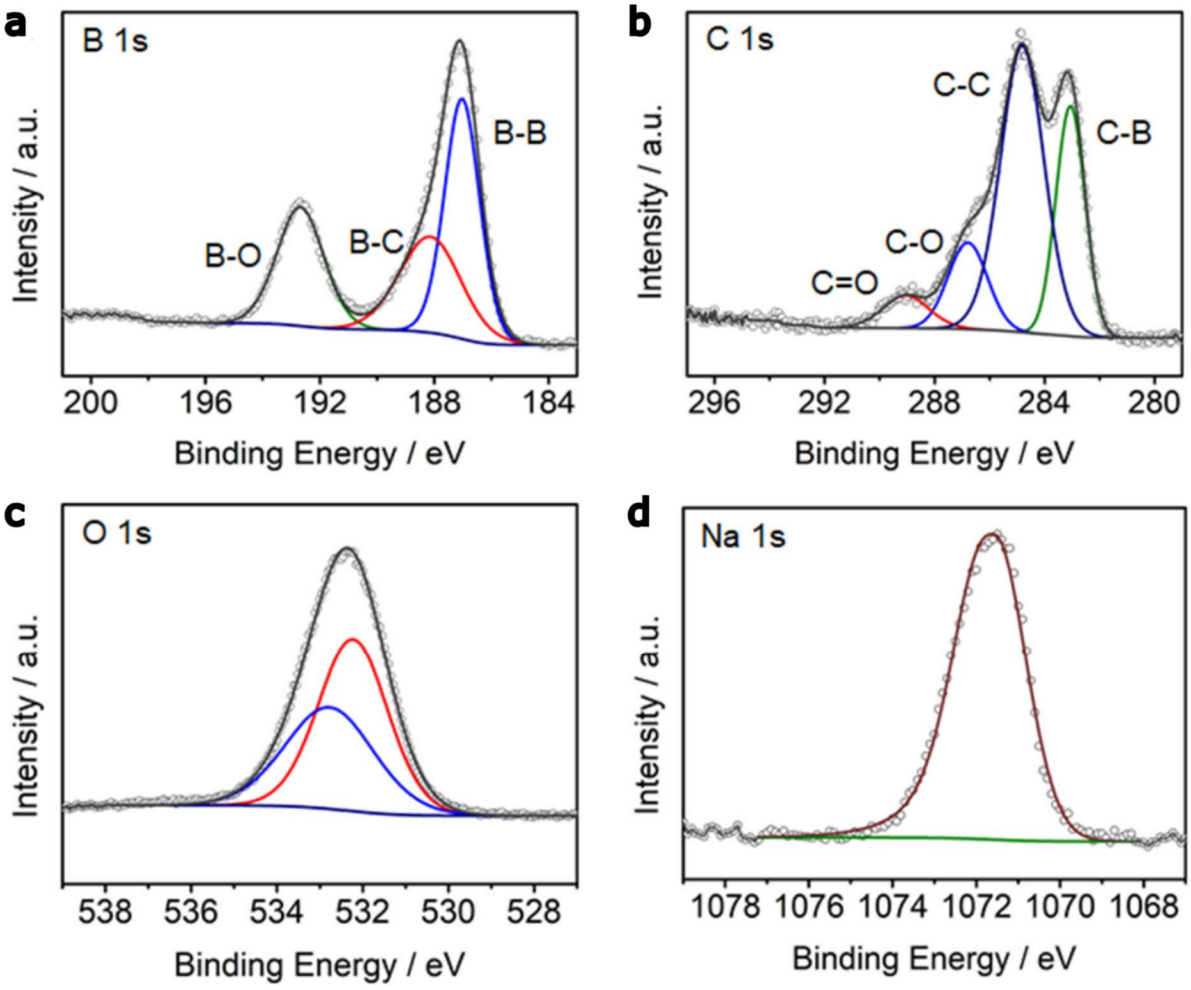

Figure III. 6. X ray photoelectron spectra of sodium carbaboride nanocrystals. **(a)** B 1s region. **(b)** C 1s region. **(c)** O 1s region. **(d)** Na 1s region.

Solid-state NMR

The sub-stoichiometry of sodium and the related carbon over-stoichiometry we propose for the sodium carbaboride nanocrystals are not in agreement with the ideal NaB_5C composition. Besides, addressing the validity of the electron counting rule in octahedra-based boron-rich compounds has been difficult to perform experimentally until now because of the absence of a local probe for investigating the boron/carbon local environment. For these reasons, we have embarked on assessing the composition of the octahedra within sodium borocarbide nanocrystals by using ^{11}B solid-state NMR.

The ^{11}B solid-state NMR spectrum of NaB_5C showd at least three broad signals centered around 15, 2 and -8 ppm (**Figure III. 7a**). For further assignment of these signals, the spectrum was compared to spectra calculated by DFT based on several structural models (**Figure III. 7a**). These models have been specifically designed in order to assess the composition of the

octahedral units $B_{5-x}C_{1+x}$ and the ordering between these units (details for the construction of these models are given in the **Appendix II**, **Tables AII. 4** – **AII. 8**). The first model named **1Crandom222** accounted for the NaB_5C composition and consisted in a 2×2×2 supercell with full Na occupancy with closed shell B_5C octahedra where the carbon atom is at a random position in all octahedra. The second model named **0C-2Crandom222** also accounted for the NaB_5C composition in a 2×2×2 supercell with full Na occupancy and built on octahedra, but with six of them being B_5C while the last two are one B_6 and one B_4C_2 octahedron, respectively. This model enabled assessing deviation from the electron counting rule, as B_6 octahedra in the presence of Na cannot exhibit a 20-electrons closed shell. The third model named **1Crandom333** again accounted for the NaB_5C composition. It is equivalent to the model **1Crandom222**, but extended through a 3×3×3 supercell, with full Na occupancy and closed shell B_5C clusters where the carbon atom is randomly positioned. The fourth and fifth models accounted for the sodium sub-stoichiometry and carbon over-stoichiometries described above, by considering B_5C and B_4C_2 octahedra together. Each B_4C_2 unit is surrounded by a Na vacancy to ensure a closed shell octahedron. The fourth and fifth models are named **1Na-1C-2Crandom222** and **3Na-1C-2Crandom333**, respectively. They correspond to 2×2×2 and 3×3×3 supercells, respectively. **1Na-1C-2Crandom222** bears seven B_5C octahedra and one B_4C_2 octahedron next to one Na vacancy. **3Na-1C-2Crandom333** encompasses 24 B_5C octahedra and 3 B_4C_2 octahedron next to 3 Na vacancies. The atomic coordinates for the five structures were first DFT-relaxed before calculation of the NMR parameters through the gauge including projector augmented wave method. For comparison, NMR parameters were also calculated on a **single cell** (**Figure III. 7**), corresponding to a NaB_5C composition that would be equivalent to a supercell with full Na occupancy and closed shell B_5C octahedra where the carbon atom is at the same position in all octahedra. All structural models are visually represented in **Figure III. 8.** The results of these calculations are given in **Figure III. 7** and **Tables AII. 9** – **AII. 14** in **Appendix II**.

The calculated NMR signals were then compared to the experimental ^{11}B NMR spectrum (**Figure III. 7a**). First, the discrepancy between the experimental spectrum and the one calculated for the single cell clearly showed that carbon atoms are not located in the same relative position in each octahedra. Second and overall, the best accuracy was reached for models **1-Na-1C-2Crandom222** and **3-Na-1C-2Crandom333**. This result confirmed the deviation from the ideal stoichiometry NaB_5C. It should be noticed that the calculated parameters were not able to reproduce very accurately the experimental spectrum but since ^{11}B

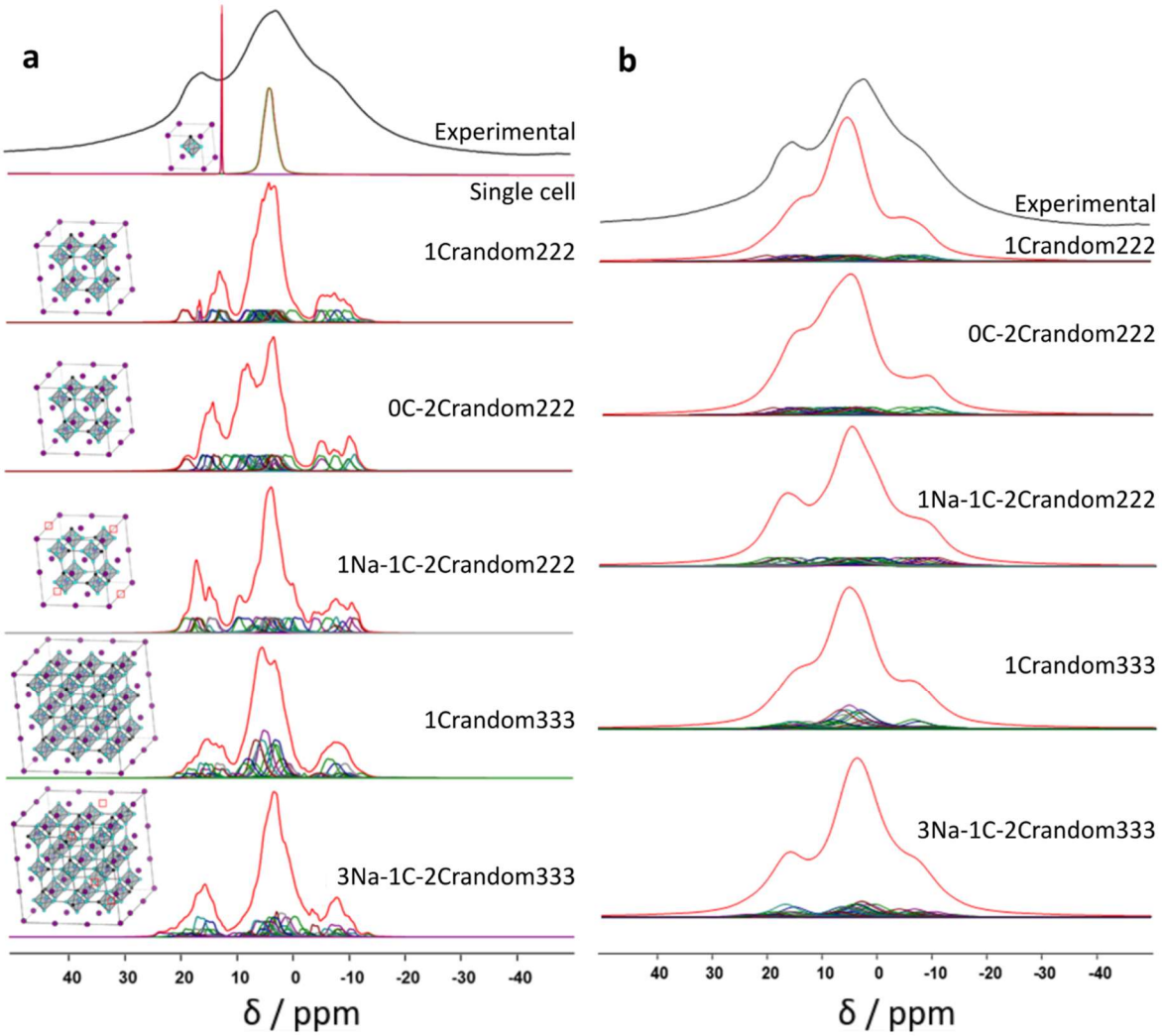

Figure III. 7. **(a)** ^{11}B experimental solid-state NMR spectrum of NaB_5C-related sodium carbaboride powder and calculated spectra for the different structural models, detailed in **Figure III. 8**. The single cell spectrum is calculated from the reported structure of NaB_5C, where the carbon atom in B_5C octahedra is always at the same position (equivalent of a 2×2×2 or a 3×3×3 supercell with iso-located carbon atoms in each octahedral cluster). **(b)** Calculated spectra for each model including a broadening Gaussian convolution to account for dipolar interactions.

calculated quadruplar coupling constants are relatively small while boron atoms are close in space, the spectrum shape is probably dominated by dipolar couplings, which were not considered by the calculation. To illustrate this point, broadened Gaussian shapes were used for all models keeping calculated chemical shifts. The corresponding calculated spectra are presented **Figure III. 7b**. As expected, the global agreement is more satisfactory.

In order to further confirm the presence of sodium vacancies and assess the existence of B_4C_2 units, the ^{23}Na MAS spectrum of NaB_5C was recorded. It showed a large signal centered around -6 ppm (**Figure III. 9**). This broadness could be either due to strong second-order quadrupolar

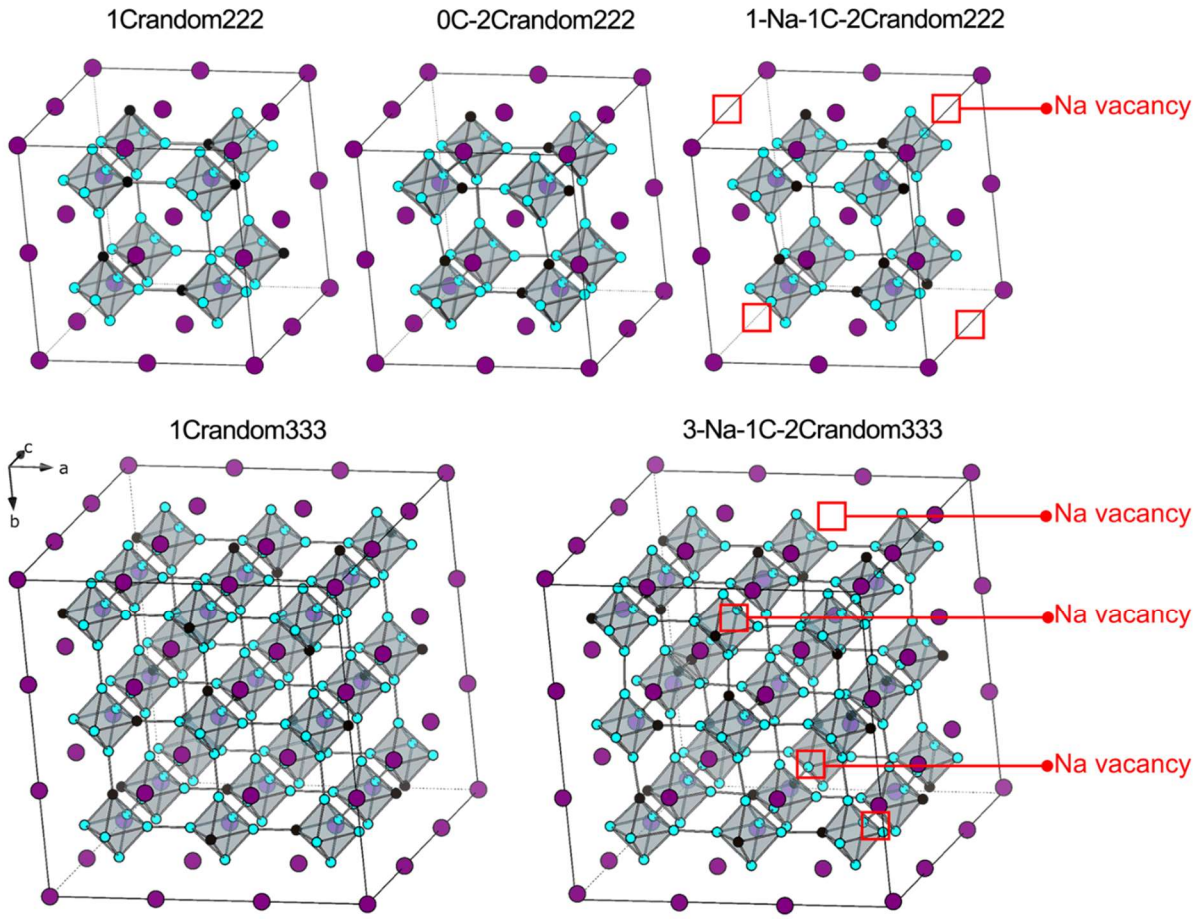

Figure III. 8. Structural models used to calculate the ^{11}B NMR spectra of sodium carbaborides. Boron, carbon and sodium atoms are in blue, black and purple, respectively. The octahedral clusters are represented in light grey. Sodium vacancies are represented with a red square.

effects or to a distribution of signals. To get clues on this question, the DFT calculated ^{23}Na spectra on the structural models previously described were compared to the experimental one (**Figure III. 9**). The calculated parameters are summarized in **Tables AII. 15** and **AII. 16 Appendix II**. It appears that second-order quadrupolar effects are relatively small with quadrupolar coupling constants calculated between 230 and 1140 kHz. Consequently, the width of the experimental line can only be reproduced with a distribution of chemical shift values as observed in random models. The agreement with the experimental spectrum could probably be improved with larger models that would possibly allow a larger distribution but this would render NMR calculations too difficult with the current calculators. It can nonetheless be noticed that the highest averaged quadrupolar coupling constant in absolute value (> 700 kHz), which favours the line broadening, is observed in **0C-2Crandom222**, **1Na-1C-2Crandom222** and **3Na-1C-2Crandom333** models. This strongly suggests the presence of B_4C_2 octahedral

clusters yielding an overall $Na_{1-x}B_{5-x}C_{1+x}$ formula, in agreement with the ^{11}B NMR and XRD results. When combining ^{11}B and ^{23}Na results, the presence of B_5C and B_4C_2 octahedral clusters with Na vacancies around the latter gives the best agreement between experimental and theoretical data. To the best of our knowledge, this type of structural motifs has not been observed so far in inorganic solids.

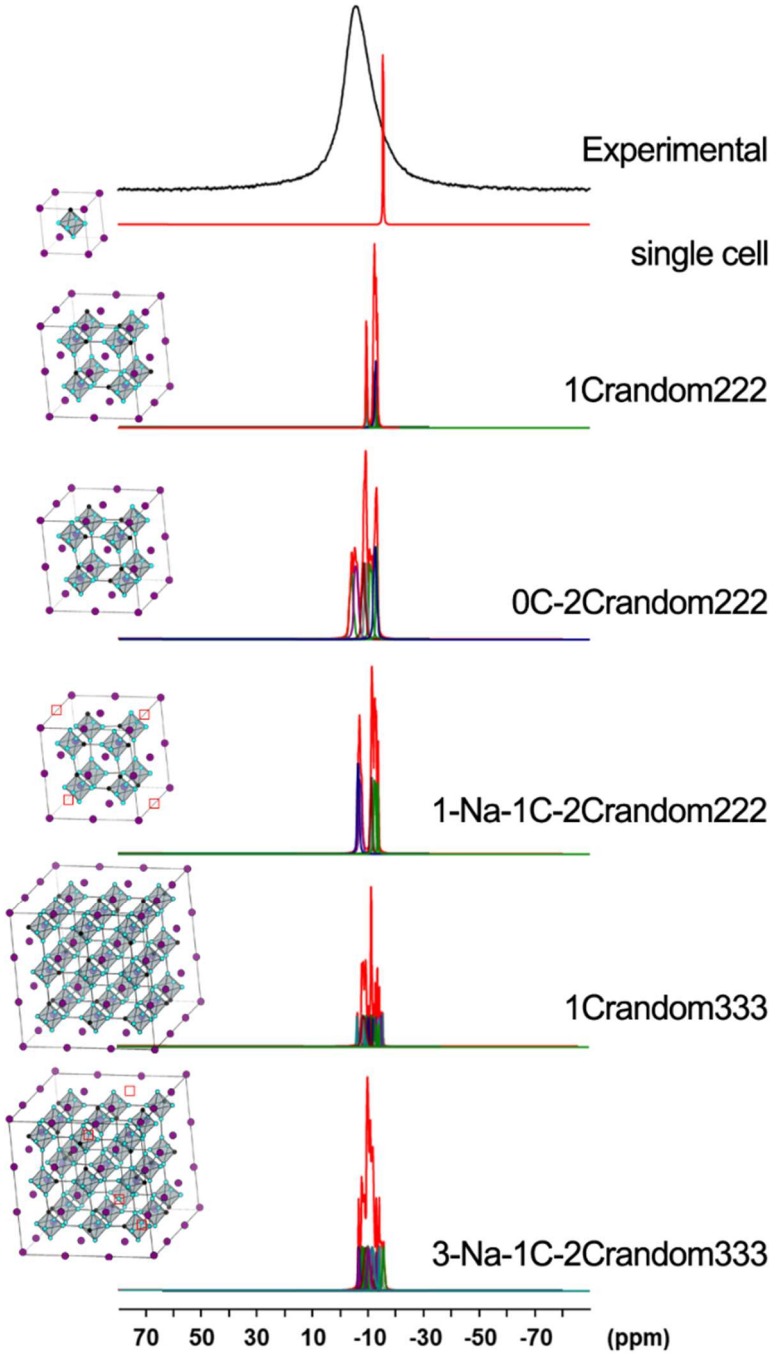

Figure III. 9. ^{23}Na experimental solid-state NMR spectrum of NaB_5C-related sodium carbaboride powder and calculated spectra for the different structural models, detailed in **Figure III. 8**. The single cell spectrum is calculated from the reported structure of NaB_5C, where the carbon atom in B_5C octahedra is always at the same position (equivalent of a 2×2×2 or a 3×3×3 supercell with iso-located carbon atoms in each octahedral cluster).

Carbon input screening

Motivated by the observed over-stoichiometry of carbon and posterior polydispersity problems when attempting the transformation of sodium borocarbide to boron carbide (see next chapter), we explored the possibility of reducing the carbon excess input. Beyond the initial B:C ratio of 5:6.4, ratios of 5:4, 5:2 and 5:1 were tested. XRD results, depicted in **Figure III. 10** showed in all cases a crystalline pure product of $Na_{1-x}B_{5-x}C_{1+x}$ without shifting of the lattice parameters whatsoever. While further carbon content in the crystalline network or Na vacancies presence could not be assessed for all the samples, this screening will be crucial in controlling the morphology of the boron carbide product in the next chapter. Finally, it must be noted also that KB_5C nanocrystals synthesis was attempted during this thesis work with analogous protocols, without success.

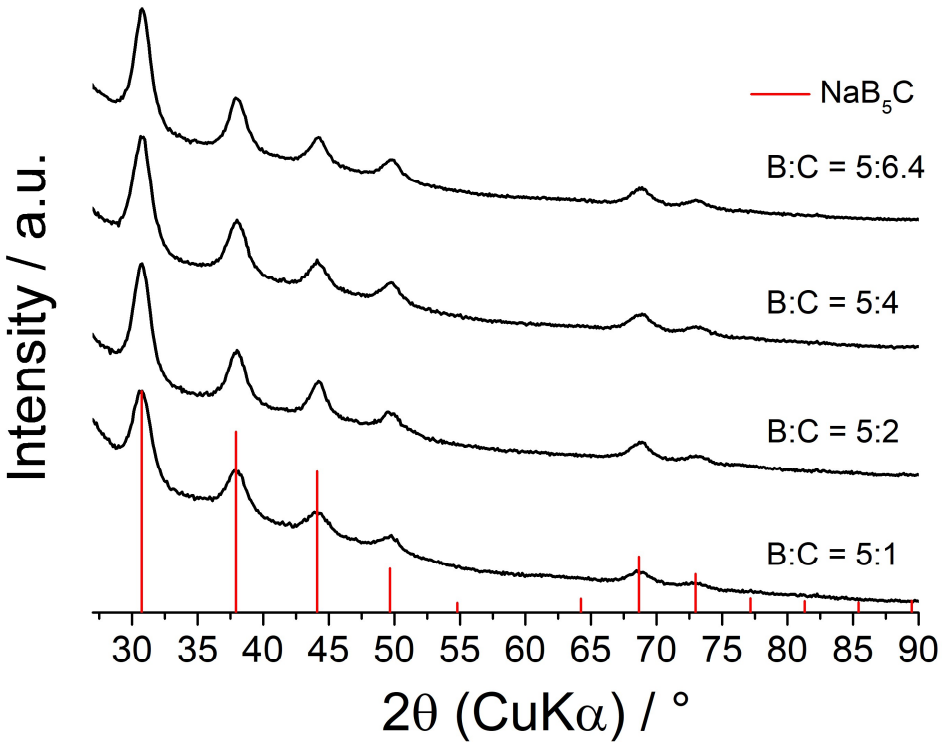

Figure III. 10. XRD diagrams of carbon input screening in the synthesis of $Na_{1-x}B_{5-x}C_{1+x}$. B:C ratios are specified for each sample.

III.4 Partial conclusions

Overall, we set a molten-salt based synthesis of $Na_{1-x}B_{5-x}C_{1+x}$ nanocrystals. We confirmed the obtained phase by X-ray diffraction and electron microscopy. Detailed analysis of the diffractograms by the Rietveld refinement method gave hints that an over stoichiometry of

carbon and consequently the formation of Na vacancies may take place in the structure. This was later confirmed by ^{11}B and ^{23}Na solid state NMR. Our results support a view where the as-synthesized sodium borocarbide nanocrystals encompass B_5C and B_4C_2 octahedral clusters. The former are surrounded by occupied Na sites, where Na provides one electron to yield formerly B_5C^- clusters, so that the solid obeys the stoichiometry NaB_5C in the local range. The environment of B_4C_2 octahedra is different as it contains Na vacancies, yielding the stoichiometry B_4C_2 at the short range. Both B_5C^- and B_4C_2 units meet the electron counting of 20 electrons for electronic stabilization of octahedral clusters. To our knowledge, B_4C_2 octahedral units or clusters have not been reported in fully inorganic structures, probably because of large strains to which they would be subjected. It is intriguing to note that B_4C_2 octahedral units might occur in nanocrystals. This could be related to the ability of nanocrystals to accommodate larger strains, and then to isolate such distorted structures, which are certainly metastable. Finally, the carbon input was explored in order to target possible variabilities for the upcoming transformation to boron carbide. The crystalline-phase pure $Na_{1-x}B_{5-x}C_{1+x}$ structure was confirmed for all carbon inputs studied. This completed the characterization of $Na_{1-x}B_{5-x}C_{1+x}$ as a template compound and left the road open to explore the transformation of sodium borocarbide to boron carbide.

Chapter IV: Superhard boron carbide nanostructures

IV. 1 Introduction

The previous chapter has shown how we could synthesize sodium carbaboride nanocrystals with a well specified composition. In this chapter we will discuss the use of this compound as template to produce boron carbide nanostructures. $Na_{1-x}B_{5-x}C_{1+x}$ is a very interesting precursor towards boron carbide as its carbon-to-boron ratio falls well within the B:C solid solubility range in boron carbide, as shown in **Figure IV. 1b** for the ideal NaB_5C stoichiometry. It is evident at first glance that Na atoms in the initial $Na_{1-x}B_{5-x}C_{1+x}$ compound are foreign to the $B_{4+\delta}C$ structure. An interesting approach would be to keep them throughout the reaction, as schematized in **Figure IV. 1a**, since, as it was discussed in **Chapter II**, filling the cavities of boron carbide with dopant atoms could ameliorate its mechanical properties. In particular, following the theoretical report of Q. An,[101] alkaline atoms could both fill these empty cages in the structure and inject valence electrons to the framework, which should strengthen the material by up to a 9.2 %.[101] Na is however a difficult atom to preserve given its high diffusion coefficient and high volatility, especially at the elevated temperatures where boron carbide crystallization occurs. For this reason, we formulated the hypothesis that high-pressure could prevent migration of Na outside the crystalline network. This first approach was explored by employing the Paris-Edinburg press at pressures up to 5 GPa. In a second avenue, one could try to eliminate Na and thus prevent any possible phase segregation problem. To assure Na

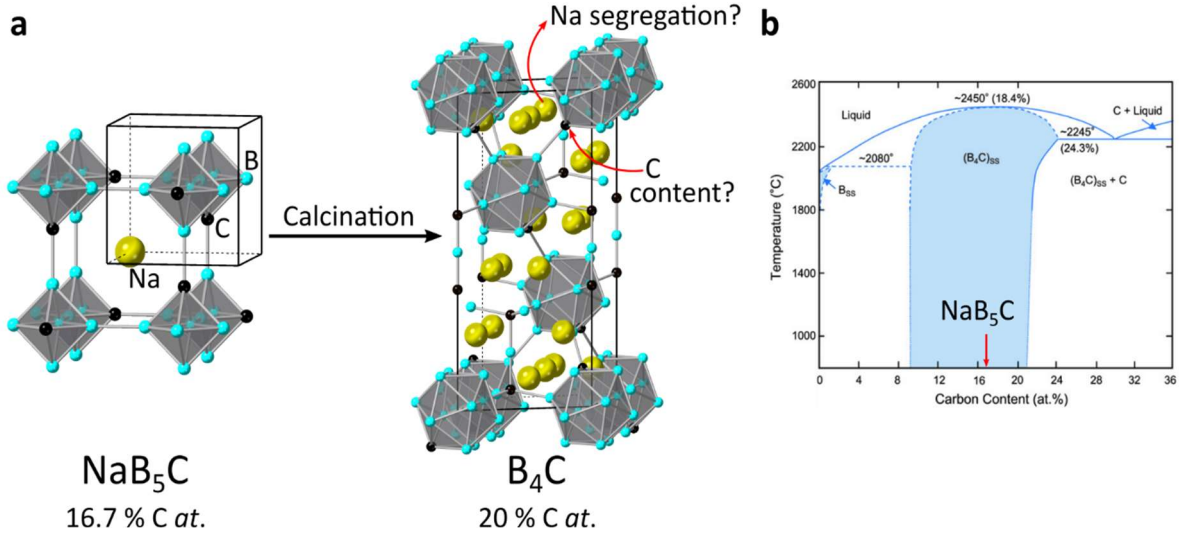

Figure IV. 1. **(a)** Scheme of the templating reaction proposed. **(b)** B:C phase diagram, highlighting the positioning of the NaB_5C stoichiometry within the solid solubility range of the boron carbide structure.

removal, room pressure and even vacuum reactions can be envisaged. Even under this frame, the stoichiometry control is not evident, as the thermodynamically most stable B_4C stoichiometry probably does not match that of the starting $Na_{1-x}B_{5-x}C_{1+x}$ compound (**Figure IV. 1a**). All these aspects of stoichiometry preservation and phase separation will be specially considered throughout this chapter.

IV.2 Experimental

Materials

All reagents were stored and handled in an argon-filled glove box. $Na_{1-x}B_{5-x}C_{1+x}$ starting material was obtained as described in the **Experimental** section of **Chapter III**. Methanol (VWR Normapur grade) was used for washing steps.

High-pressure transformation approach

Paris-Edinburg high-pressure experiments

Under an argon filled glove box, $Na_{1-x}B_{5-x}C_{1+x}$ powders were compacted and loaded into a Ø(3 mm external, 2.5 mm internal) × H 3 mm *h*-BN capsule, which was assembled inside a conventional 10×6.6 mm baked pyrophyllite high-pressure set-up and then placed into a Paris-Edinburgh anvils assembly as described by Le Godec and co-workers.[140] Briefly, the set-up was compressed between two tungsten carbide conical anvils with a specially designed bottom part to improve mechanical strength and compression.[140,141] The high-resistivity graphite inside the assembly was used as heater by injecting controlled electrical current from the anvils through the assembly. The samples were compressed at 2 or 5 GPa at a pressing ramp of 0.08 $bar \cdot s^{-1}$ in a 2 columns VX3 Paris-Edinburgh press. Once the desired pressure was reached, the samples were heated at the indicated targeted temperature at a *ca*. 50 $°C \cdot min^{-1}$ rate with a dwell time of 90 min before quenching. After cooling, the samples were decompressed at a rate of 0.02 $bar \cdot s^{-1}$. The assemblies were cut and open under air and the products recovered for further analysis.

PSICHÉ beamline *in-situ* X-ray diffraction at high pressure

In-situ energy dispersive X-ray diffraction scans at high-pressure were performed at the PSICHÉ (**P**ressure, **S**tructure and **I**maging by **C**ontrast at **H**igh **E**nergy) beamline of SOLEIL

synchrotron. The white beam mode (15 – 80 keV) was employed so that no detector rotation was required to explore the *q* space and thus X-ray diffraction patterns could be collected with satisfactory time resolution. A 4 columns V3 Paris-Edinburg press, installed in the optical hutch, was used in order to work at high pressure. Standard 10×6.6 mm X-rays transparent boron/epoxy setups were used as described previously for the *ex-situ* high pressure experiments. A rotating Ge solid-state detector (SSD) as a part of the CAESAR system was used to collect the diffracted intensity (detector energy resolution $\Delta E/E$ of ~ 10^{-2}). The detector was fixed throughout the *in-situ* scans at an angle 2θ of 8°. The beamline setup counts with tree pairs of collimating slits, where: one installed before the PE press two others placed between the PE press and the Ge SSD. These allow to select the sampling of the interior of the high-pressure assemblies and hence to exclude the signals from the sample environment. The pressure was slowly increased to 5 GPa (equivalent to a force of 50 tons on the anvils) by using a hydraulic hand pump. The temperature was increased and measured using a previously calibrated resistive heating system. The current was manually increased to yield powers of 0 – 700 W in steps such that it reproduced a 50 $°\cdot min^{-1}$ average heating ramp. Energy dispersive diagrams were measured after each step increase of temperature and while keeping it constant. In a first experiment (*in situ* 1), the temperature was continuously increased up to 2100 °C and then quenched. For the second experiment (*in situ* 2), the temperature was increased up to 1700 °C, then dwelled for 35 min before quenching. In both experiments, the pressure was slowly released once the temperature was completely quenched.

The CAESAR detection system (**C**ombined **A**ngle- and **E**nergy-dispersive **S**tructural **A**nalysis and **R**efinement) is based on Ge solid-state rotating detector. This allows to add to the intrinsic energy dispersive capacity of the Ge SSD, the advantages of the angular dispersive diffraction, at the expense of time resolution. The combined angular and energy dispersive diffraction detection yields a 2D map of intensity *vs*. 2θ and energy, where the typical artefacts of the measurement (Ge escape peaks, fluorescence and high background) can be better isolated and corrected according to algorithms described elsewhere.[142] The 2D map is then corrected and integrated in a single monodimensional diffractogram. Every CAESAR scan requires approximately 25 min to complete, for which it was only performed at selected points of interest where higher resolution and extended *q* range was needed, these will be specified in the **Results and Discussion** section.

Room-pressure transformation approach

The initial $Na_{1-x}B_{5-x}C_{1+x}$ powder was placed into an *h*-BN crucible inside an Ar filled glove box and sealed with parafilm. The crucible was transferred to a previously Ar purged (for 1 h) horizontal tubular oven, which was then further purged with Ar flow for 1 h before being heated under argon flow up to 1200 °C at a heating rate of 5 °C·min^{-1}. Then the temperature was dwelled for 12 h before stopping heating and letting the oven cool down naturally. The resulting powder was washed with methanol by cycles of centrifugation and redispersion until a conductivity of 4 μS·cm^{-1} in the supernatant was achieved. The sample was stored in air. The procedure was analogous for the different B:C input variations of the $Na_{1-x}B_{5-x}C_{1+x}$ precursor and for the ^{13}C enriched $Na_{1-x}B_{5-x}C_{1+x}$ calcination leading to ^{13}C enriched $B_{4+\delta}C$.

Spark-Plasma Sintering at high-pressure

The room-pressure produced boron carbide samples were sintered by using home-made spark plasma sintering (SPS) equipment coupled to a Paris-Edinburgh press.[143] All procedures related to the Paris-Edinburgh press were performed as described in the **Paris-Edinburg high-pressure experiments** section. Three experiments were performed in order to observe the effect of the temperature in the sintering behavior of B_4C nanopowders. Dwell temperatures of 2100 °C, 2300 °C and 2500 °C were tested following the same heating profile: pressurize the sample to 5 GPa – heat at a rate of 200 °C·min^{-1} up to dwell temperature – hold for 5 min – cool at 50 °C·min^{-1} down to 600 °C – quench heating by shut off the power supply – release the pressure. Heating was performed resistively through a graphite capsule where pulsed current was passed. The pulse pattern consisted of trains of eight 2 ms pulses with 1 ms lap time. The temperature was monitored from a previous calibration to the delivered power.

General characterizations are described in the **Appendix AI**.

IV.3 Results and discussion

High-pressure transformation approach

Our initial attempts to transform $Na_{1-x}B_{5-x}C_{1+x}$ nanopowders to boron carbide consisted in thermally treating a pressurized compact of the sample in a given set of conditions. Two initial pressures were explored, namely 2 and 5 GPa. For both treatments, the dwell temperature was set at 2000 °C during 90 min. The sample was recovered at ambient conditions and powder

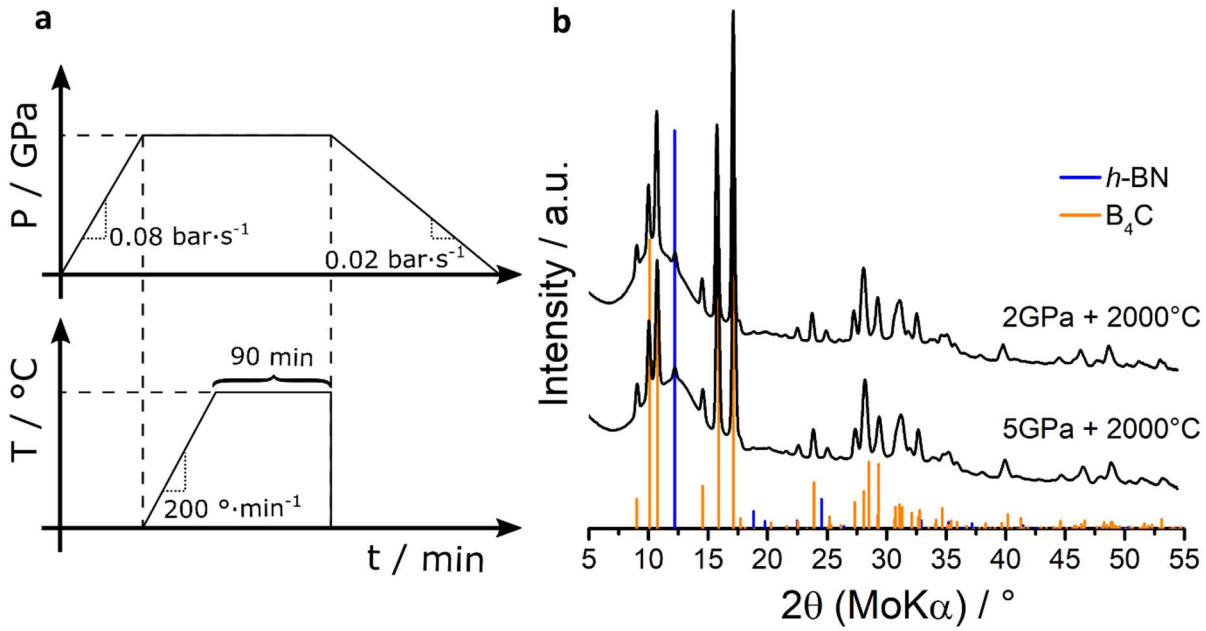

Figure IV. 1. **(a)** High-pressure transformation of $Na_{1-x}B_{5-x}C_{1+x}$ compacts. **(a)** Details of the pressure and temperature program used. **(b)** XRD results from the recovered pellets. *h*-BN impurities come from surface attaching of the high-pressure capsule.

XRD diffractograms were measured in a rotating Mo anode diffractometer as described in the **Appendix AI**. In **Figure IV. 2a**, details of the treatment program can be found, while in the **Figure IV. 2b**, XRD results are summarized.

Interestingly, crystalline phase pure $B_{4+\delta}C$ compounds were obtained in both cases, although the broad bump at low angles seemed to indicate the presence of an amorphous phase. This was confirmed by SEM-FEG analysis as shown in **Figure IV. 3**, where well faceted crystals are embedded in an amorphous matrix. EDX local analysis showed that the crystals corresponded to boron carbide free of Na while the amorphous phase contained Na, B and C in variable ratios. The detrimental role of the secondary phase became evident in the hardness measurement, where Vicker's hardness of (12 ± 1) and (11 ± 1) GPa were measured for the 2 and 5 GPa transformations respectively at applied load of 9.8 N –in contrast with the intrinsic hardness of B_4C of 38 GPa–.[2,3] This proved that the chosen conditions were too harsh and triggered phase segregation, although they do succeeded in providing transformation towards boron carbide.

In light of this result, a temperature screening for a chosen pressure of 5 GPa was performed. XRD results are depicted in **Figure IV. 4**. While no complete crystallization was observed for the lowest temperatures of 1400 and 1600 °C, a transformation was clearly observed at 1800 °C. However, due to broad peaks and possible multiple phase peaks superposition, phase

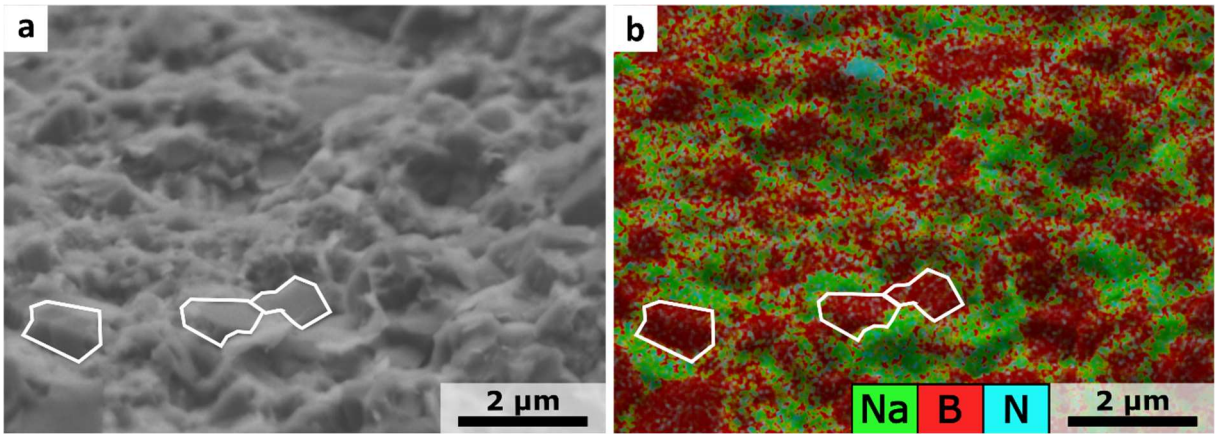

Figure IV. 3. **(a)** SEM-FEG image of $Na_{1-x}B_{5-x}C_{1+x}$ treated at 5 GPa and 2000 °C. **(b)** EDX mapping of the same sample and region than **(a)**.

identification for this pattern was not possible and the screening could not be conclusive. The phase mixing could come either from the coexistence of intermediates during the $Na_{1-x}B_{5-x}C_{1+x}$ to $B_{4+\delta}C$ transformation or because the opening of the assemblies at room conditions perturbed the product, notably by reaction with moisture or oxygen. For this reason, it was decided to perform an *in-situ* study to observe the transformation mechanism and at the same time retrieve optimized conditions to trigger $B_{4+\delta}C$ crystallization while avoiding the segregation of a Na-rich phase.

The *in-situ* study was performed at the PSICHÉ beamline of Soleil synchrotron. The evolution of the sample was monitored *in situ* through energy-dispersive X-ray diffraction. The average heating ramps were reproduced from *ex-situ* experiments, although a stepwise increase was used instead of a continuous rate in order to maintain a constant temperature during the ~ 30 s acquisition per scan. Angular and energy dispersive CAESAR scans were recorded at selected conditions for better clarification of the present phases.

A first study (*in situ* 1) was performed by pressurizing the sample at 5 GPa and screening the temperature in the heat treatment up to 2100 °C (**Figure IV. 5a**). Direct phase transition was observed at 1700 °C, thus revoking the hypothesis of multiple intermediate phases in the analysis of *ex-situ* XRD patterns in **Figure IV. 4**. Boron carbide was the only crystalline phase detected at high temperature, although the high background signal may cover amorphous components. When returning to room conditions (**Figure IV. 5b**), it was observed that a new phase crystallized upon cooling down. Unfortunately, due to the restrained *q* range that the white beam provides, only five peaks of this phase were measurable, one of which is later hidden by the iodine fluorescence peak and another lost in the background when the sample

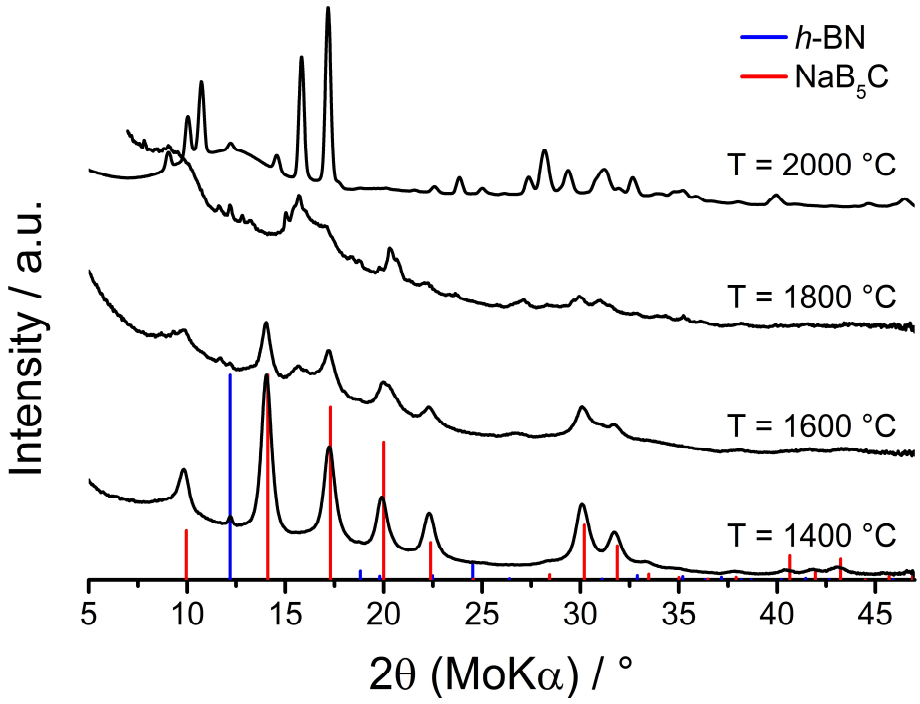

Figure IV. 4. XRD results of $Na_{1-x}B_{5-x}C_{1+x}$ heat treatment screening at constant applied pressure of 5 GPa.

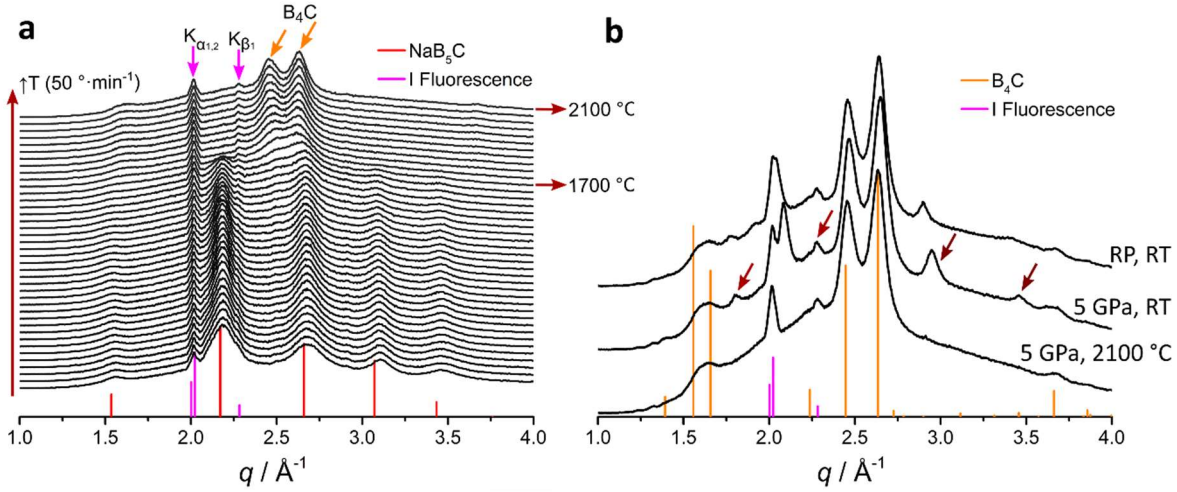

Figure IV. 5. **(a)** Energy dispersive diffractograms following the *in situ* 1 heating scan of $Na_{1-x}B_{5-x}C_{1+x}$ at 5 GPa. **(b)** Selected diffractograms recorded during the return to room conditions showing the appearance of a new phase when the temperature was quenched.

was depressurized. Let it be noted that the iodine fluorescence signal comes from surface iodine atoms from the of $Na_{1-x}B_{5-x}C_{1+x}$ synthesis in molten NaI. At this point a CAESAR scan was performed in order to cover a broader q –$q = 4\pi\sin(\theta)/\lambda$– range and allow the correction of the multiple artefacts of the measurement (iodine fluorescence peaks, Ge escape peaks, incident intensity distribution, among others). The CAESAR scan consists in taking energy dispersive diagrams for each of the available detector angle positions (3 – 28 °). This way, the origin of

the peaks could be deciphered. In **Figure IV. 6a** and **6b**, the bidimensional CAESAR scan is plotted as a function of energy and *q* respectively. In the former one, fluorescence peaks become evident as they appear at constant energy regardless of the angular position of the detector, while Ge escape peaks can be easily identified in the momentum transfer plot (*q*), as they physically appear with a constant energy difference to Bragg reflections, meaning a linearly variable *q* shift as opposed to Bragg peaks, which lie at fixed *q*. When the overall 2D diagram is integrated and corrected, a more resolved diffractogram is recovered, as compared in **Figure IV. 6c**. With this procedure, we could index the new diffraction peaks to $NaBH_4$. This result showed not only that under these conditions, phase segregation still takes place, but also that the sample contained a significant amount of hydride, probably originated in the surface adsorbed methanol.

In a second experiment (*in situ* 2), we attempted to maintain the conditions as soft as possible. Therefore, the temperature was scanned up to the minimal crystallization temperature at a given pressure, that is 1700 °C, and was maintained until no further change was observed (35 min), as shown in **Figure IV. 7a**. No $NaBH_4$ crystallization was observed upon cooling and depressurizing (**Figure IV. 7b**), which seemed to indicate that under these conditions phase

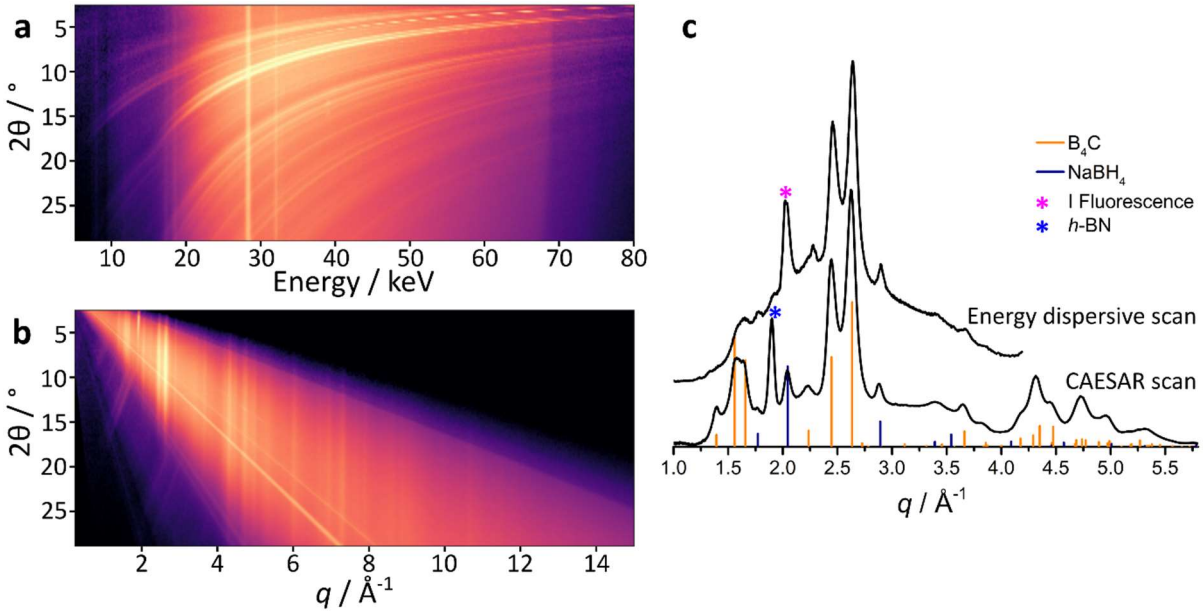

Figure IV. 6. CAESAR scan of recovered sample of heat treated NaB_5C at 5 GPa according to the *in situ* 1 experimental conditions. **(a)** Detected intensity against 2θ and energy. **(b)** Detected intensity against 2θ and *q*. **(c)** Integrated and corrected CAESAR scan at room conditions compared to the standard energy dispersive diffractogram. The higher quality permitted to assign the observed phase recovered after cooling to $NaBH_4$. It revealed the segregation of Na outside the boron carbide structure for these conditions.

segregation was avoided. However, after the setup was opened and a diffractogram of the recovered sample measured under air, $HNa_3(CO_3)_2 \cdot 2H_2O$ and $Na_2B_4O_7 \cdot 5H_2O$ phases were detected, as shown in **Figure IV. 8**. This evidences that phase segregation could still not be avoided and instead, Na and B would segregate in amorphous compounds undetected during the *in-situ* scan but reactive to moisture and oxygen once in the open air. Further efforts were concentrated in removing all the Na during the transformation, *ergo* in performing room pressure reactions.

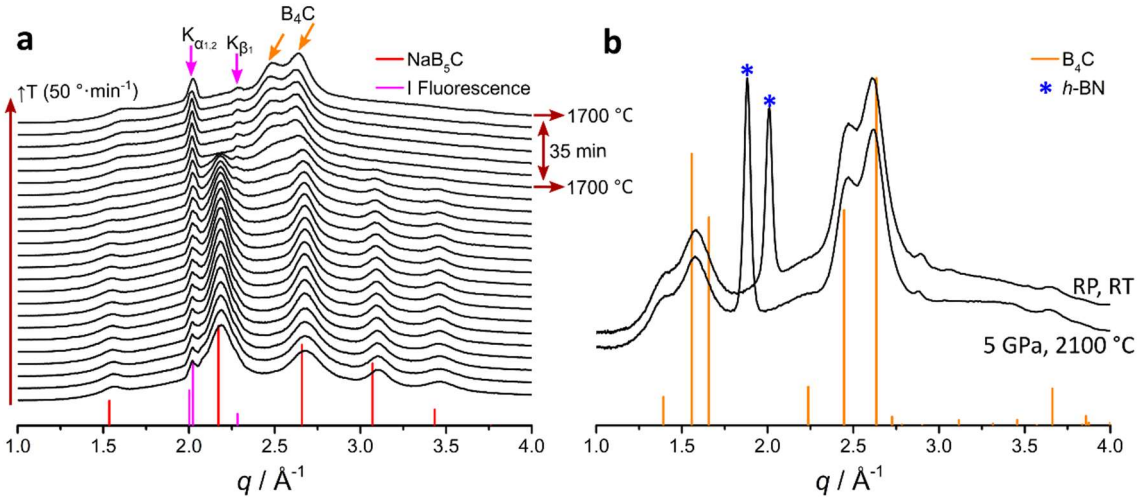

Figure IV. 7. **(a)** Energy dispersive diffractograms following the *in situ* 2 heating scan of $Na_{1-x}B_{5-x}C_{1+x}$ at 5 GPa. **(b)** Selected CAESAR scans during the return to room conditions showing no appearance of further crystalline phases other than boron carbide.

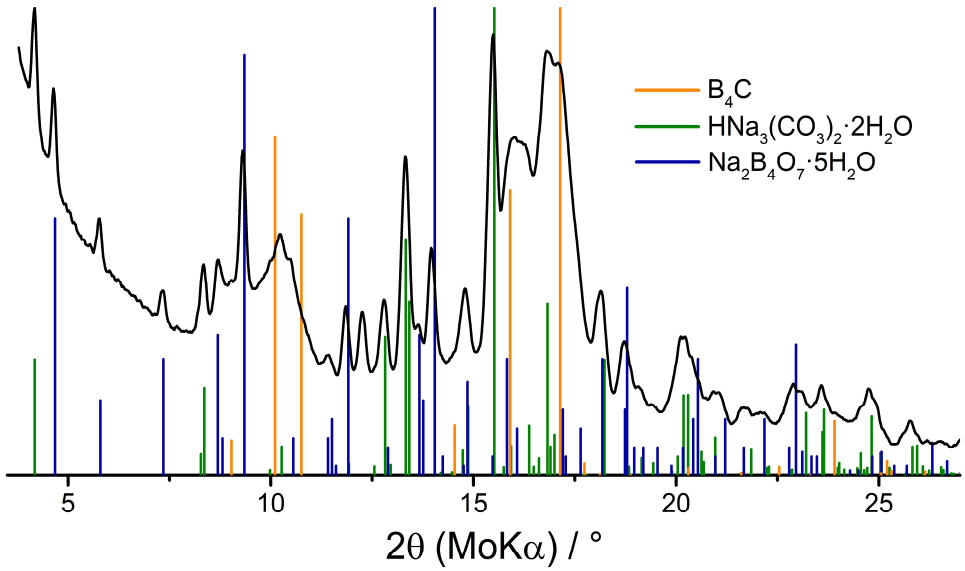

Figure IV. 8. *Ex-situ* XRD diagram in the open air of the recovered sample from the *in situ* 2 treatment. The appearance oxidized and carbonated species of Na and B evidence the phase segregation upon the heat treatment into amorphous compounds that later reacted with moisture and oxygen from the atmosphere once the setup was opened.

Room-pressure transformation approach

Preliminary data on the room temperature transformation of $Na_{1-x}B_{5-x}C_{1+x}$ had been recorded by Simon Delacroix in the frame of his thesis work.[137] At the time, the reaction temperature and dwelling time were optimized to 1200 °C and 12 h respectively in order to achieve good quality crystals, although phase pure product was not retrieved. During the first experimental attempts to reproduce such results, it became clear that the crucible material played a key role in the final purity. Typical alumina crucibles proved reactive to $Na_{1-x}B_{5-x}C_{1+x}$ and yielded aluminate impurities in the final product. The use of *h*-BN crucible then appeared essential to assure the inertness, although depending on the grade of the material, *h*-BN impurities could be recovered in the boron carbide sample, which are of course detrimental to the mechanical properties of boron carbide.

Even after eliminating the impurities originating from the crucible, it became clear that $Na_{1-x}B_{5-x}C_{1+x}$ oxidation had to be avoided at all cost in order to render the desired product. The fact that the calcination had to be performed in a horizontal furnace because of the elevated targeted temperature, meant that when transferring the sample from the glovebox to the furnace, the sample was subject to certain oxygen exposure. As a matter of fact, when the calcination was performed in slightly oxidized $Na_{1-x}B_{5-x}C_{1+x}$ samples from air exposure during transferring, a glass was recovered upon calcination, probably due to the vitrification of the borate groups formed. To assure an inert transfer, a strict protocol was developed as described in the **Experimental** section.

If sample transfer is performed under adequate inert conditions, then a brownish powder is recovered after calcination under argon flow. The powder XRD diagram recorded under inert atmosphere revealed the recovery of the $B_{4+\delta}C$ phase along with some unindexed peaks. If the powder is exposed to air for at least 11 h, these unindexed peaks grow in intensity, in principle at the expense of an amorphous component in the original product, as the boron carbide peaks do not widen. The growth of these peaks allowed to identify the named phase to H_3BO_3, which can be easily washed with methanol for instance. Upon washing, the pure boron carbide phase was recovered. To assure that H_3BO_3 originated from an amorphous component and not from the decomposition of the boron carbide, the washed boron carbide diffractogram was re-measured 24 h later, where no change is observed, hence confirming the hypothesis that an amorphous by-product resulted in boric acid upon contact with air. The amorphous component is most likely amorphous boron formed *in situ* from the boron over-stoichiometry compensation

during the transformation of $Na_{1-x}B_{5-x}C_{1+x}$ to $B_{4+\delta}C$. The sequential diffractograms and indexations can be seen in **Figure IV. 9**.

Le Bail refinement of the final product is shown in **Figure IV. 10**, where most importantly, the lattice parameter and average crystallite size were retrieved. The latter is 10 nm, which indicated a very good retention of the original size in $Na_{1-x}B_{5-x}C_{1+x}$ and indeed a success in templating the morphology of $B_{4+\delta}C$. This in turn is associated to the high covalency of both the reagent and final product, which implies only short-range atomic movements during the transformation. This average crystallite size is very promising as it corresponds to the theoretical maximum of Hall-Petch strengthening. The retrieved lattice parameters ($a = b = 5.6008$ Å, $c = 12.0803$ Å) can be correlated to the stoichiometry of the phase, as the dependence according to Vegard's law has been well studied for boron carbide.[1] The linear interpolation is shown on the inset of **Figure IV. 10**, according to which the final stoichiometry was $B_{4.1}C$, very close to the ideal B_4C. No traces of Na have been detected neither by XRD nor by EDX analysis, showing that Na was completely volatized from the structure.

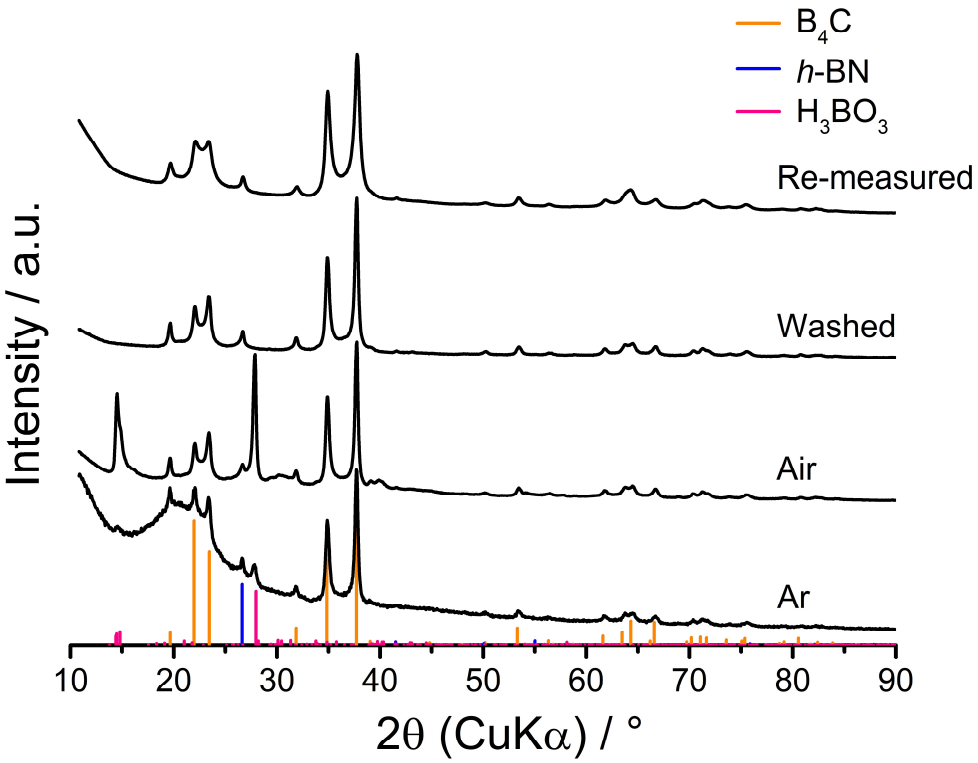

Figure IV. 9. Powder XRD diagrams of B_4C products as obtained from calcination of $Na_{1-x}B_{5-x}C_{1+x}$ and measured under different conditions: argon atmosphere, air exposure, subsequent washing with methanol followed by drying, and finally a re-measurement of the methanol washed sample 24 h later. In the diagram measured under argon, the broad bump centered at $2\theta(CuK_\alpha) \approx 21$ ° corresponds to the polymer dome used to keep the argon atmosphere during measurement.

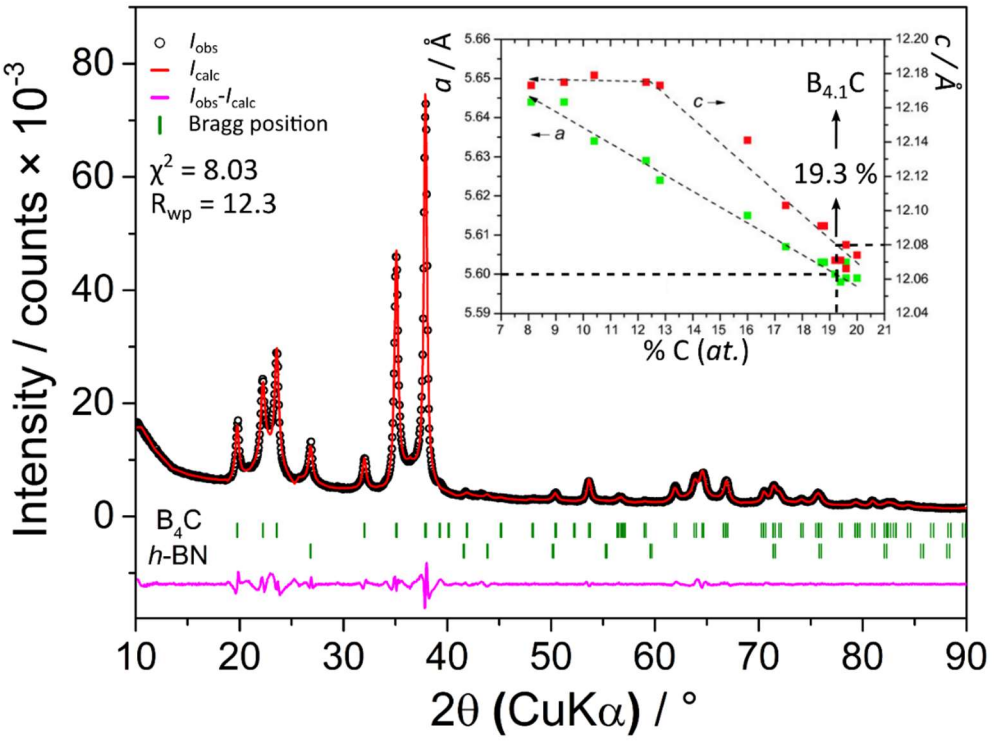

Figure IV. 10. Le Bail refinement of the boron carbide product obtained from $Na_{1-x}B_{5-x}C_{1+x}$ calcination. Inset: Vegard's law relationship between boron carbide's lattice parameter and its carbon content, as adapted from reference [1]. The interpolation from the refined lattice parameters yields a $B_{4.1}C$ stoichiometry (19.3 % C *at.*).

Even though XRD showed a small apparent crystallite size, electron microscopy revealed that the actual sample was not monodisperse, and grains were found with sizes ranging from 5 to over 100 nm as shown in **Figure IV. 11a** and **b**. The overall size distribution was still highly centered at 10 nm, which could then be ascribed to one population in a bimodal fashion, where the second population extended in a largely polydisperse size distribution up to 200 nm. This bimodal distribution suggested that two reactions could be taking place throughout the calcination, both leading to the formation of boron carbide but in different particle sizes. The first path would be the direct transformation of $Na_{1-x}B_{5-x}C_{1+x}$ to $B_{4.1}C$ leading to the small 10 nm particles of boron carbide through the templating effect (**Equation IV. 1**). While the second path may come from the fact that, as previously discussed, the excess of boron must be expelled from the NaB_5C structure (**Equation IV. 1**). Considering that a large carbon excess was used in the initial $Na_{1-x}B_{5-x}C_{1+x}$ synthesis (B:C ratio of 5:6.4) and that not all this carbon excess was fitted into the crystalline network, the NaB_5C precursor should contain carbon excess as a secondary phase, which was indeed suggested by XPS. In this case, at high temperature, boron and carbon excess could coexists, which could lead to large boron carbide particles as previously reported (**Equation IV. 2**).[144,145] This hypothesis was drawn from the ideal

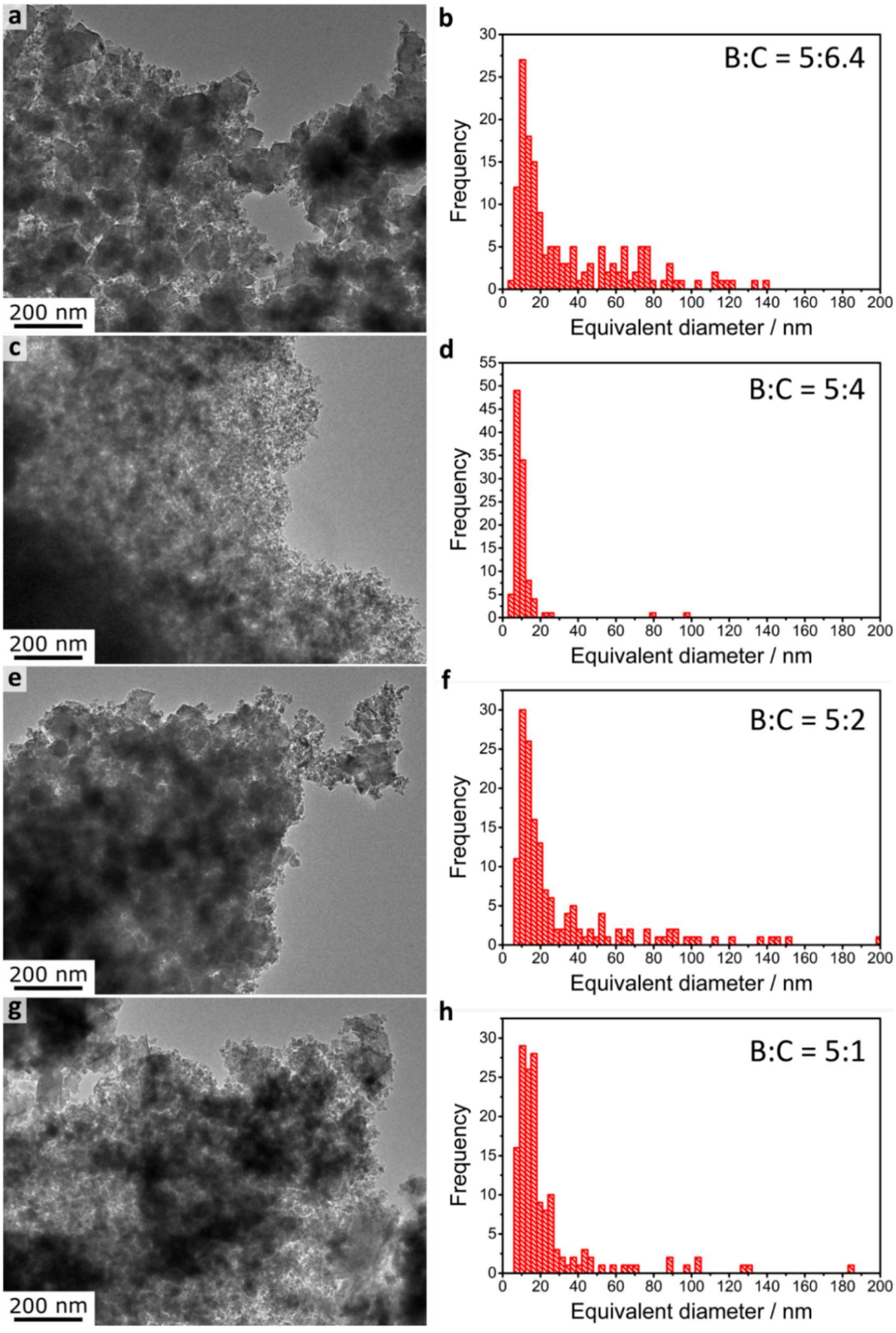

Figure IV. 11. TEM images and size distribution from counting 100 particles for boron carbide samples synthesized from different B:C inputs in the $Na_{1-x}B_{5-x}C_{1+x}$ precursor: **(a)** and **(b)** for B:C = 5:6.4, **(c)** and **(d)** for B:C = 5:4, **(e)** and **(f)** for B:C = 5:2 and **(g)** and **(h)** for B:C = 5:1.

NaB_5C stoichiometry, which contains an excess of 0.9 equivalents of boron per formula unit when compared to the experimentally obtained $B_{4.1}C$ stoichiometry in boron carbide. As it was discussed, deviations from the ideal NaB_5C stoichiometry are expected in the $Na_{1-x}B_{5-x}C_{1+x}$ formula, which would contribute to a different but still present B excess.

$$NaB_5C(s) \rightarrow B_4C(s) + Na(g) + B(s) \qquad \textbf{Equation IV. 1}$$

$$4\,B(s) + C(s) \rightarrow B_4C(s) \qquad \textbf{Equation IV. 2}$$

In order to test the hypothesis of boron and carbon excess contributing to form large boron carbide particles, the ratio of carbon source for synthesizing $Na_{1-x}B_{5-x}C_{1+x}$ was screened (B:C = 5:6.4, 5:4, 5:2 and 5:1). These experiments were described in the **Carbon Input Screening** section of the previous chapter. Then, each of the $Na_{1-x}B_{5-x}C_{1+x}$ samples were calcined following the protocol described above and the products were analyzed by transmission electron microscopy (**Figure IV. 11**). The NaB_5C stoichiometric ratio B:C = 5:1 did not lead to a monodisperse boron carbide sample, contrary to the ratio B:C = 5:4. We propose that this slight carbon excess is necessary to compensate for carbon losses during the sodium borocarbide synthesis and the corresponding polymer decomposition. Besides, the initial B:C = 5:4 ratio is the closest to the stoichiometry of the final $B_{4.1}C$ product. All in all, the initial B:C = 5:4 ratio may yield a $Na_{1-x}B_{5-x}C_{1+x}$ sample with the composition the closest to the final boron carbide. Therefore, screening the initial B:C ratio enabled yielding monodisperse nanocrystalline boron carbide. Note that although traces of large particles could still be detected in the B:C = 5:4 product, they are in significantly lower proportion than for the other initial carbon ratios. A larger magnification TEM image is depicted in **Figure IV. 12a** along with the average particle size (**Figure IV. 12a**) from the lognormal fitting of the size distribution histogram performed

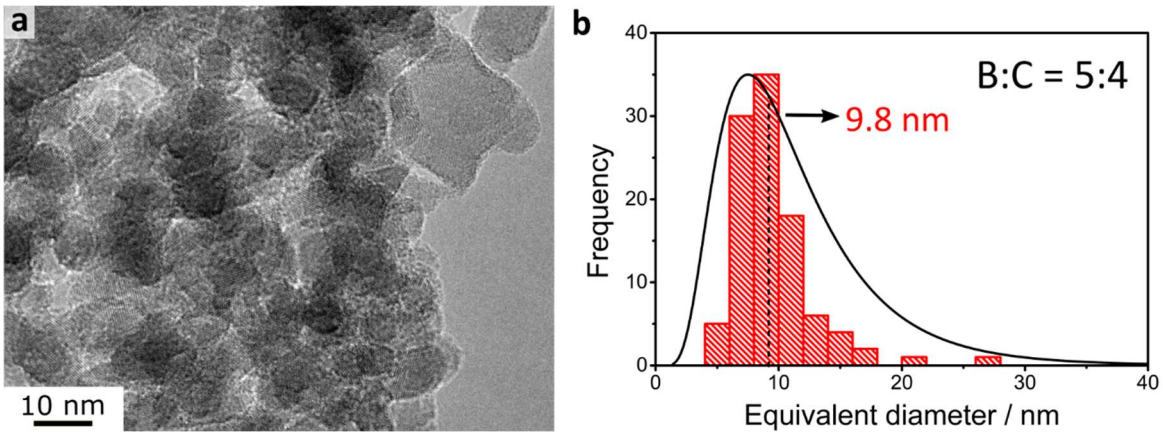

Figure IV. 12. (a) Higher magnification TEM image of the monodisperse boron carbide product as synthesized from $Na_{1-x}B_{5-x}C_{1+x}$ with B:C input of 5:4. (b) size distribution from counting 100 particles

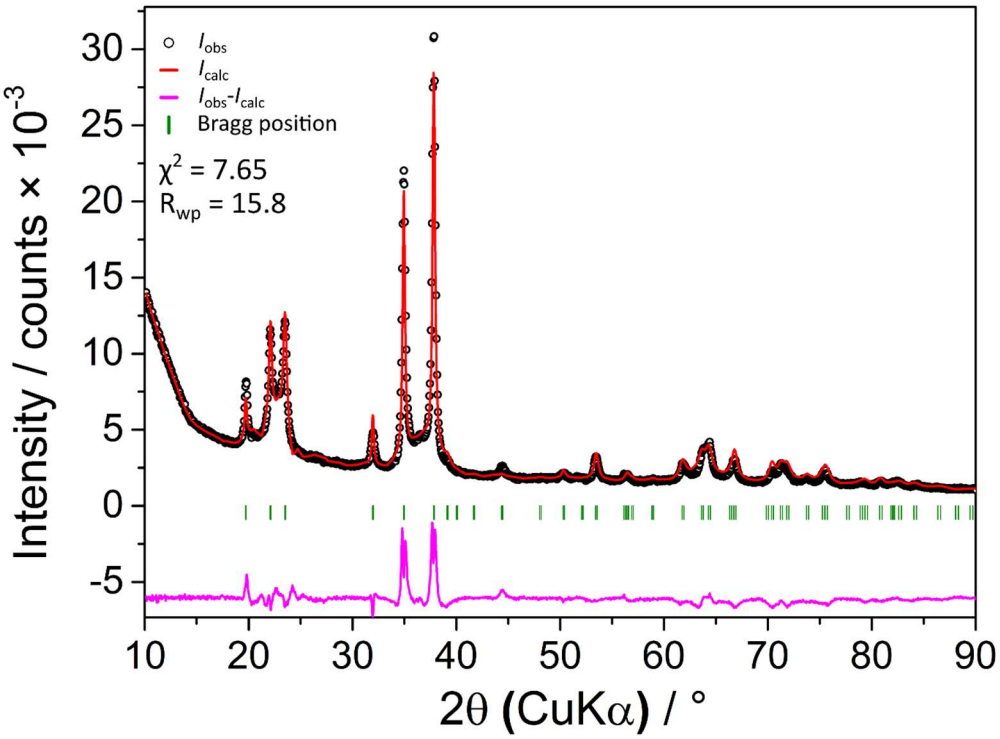

Figure IV. 13. Powder XRD pattern and corresponding Le Bail refinement of the monodisperse boron carbide product as synthesized from $Na_{1-x}B_{5-x}C_{1+x}$ with B:C input of 5:4.

over 100 particles.

At this point, the *h*-BN impurities present in the previous compound (**Figure IV. 8**) could also be avoided by using a crucible made of *h*-BN grown by CVD that hindered *h*-BN exfoliation. The powder XRD pattern and corresponding Le Bail refinement for the pure and monodisperse boron carbide product is shown in **Figure IV. 13**. The Le Bail refinement of the final product shows results very similar to previous ones, with an average crystallite size of 14 nm and lattice parameters $a = b = 5.6012$ Å, $c = 12.0792$ Å. All the upcoming characterization refer to this sample or other batches synthesized under the same protocol.

Local structure from solid-state NMR

It is consensually agreed that the average structure of B_4C can be described in a first approximation as $(B_{11}C^p)CBC$ units (with C^p being a carbon atom sited at the polar position of the icosahedra), as depicted in **Figure IV. 1**.[1,33–36,38–40] This thermodynamic equilibrium structure is rarely if ever obtained though. Local defects, notably within the linear C-B-C chains are a common occurrence. Through high-resolution transmission electron microscopy, Rasim and collaborators identified at least five different local arrangements in the chain region.[37] In

the same report, DFT calculations pointed at four defective local arrangements as the most likely ones yielding ~ 1 eV lower energies per group with respect to standard CBC chains.[37] These are the rhombi-like CB_2C, BB_2B, CB_2B and the 4-atom chain CBCB moieties. Furthermore, the defective geometries yield localized density of states below the conduction band and hence lower the band-gap from that of theoretical defect-free B_4C (3.59 eV).[37] It was proposed that a defect concentration of up to 25 % (16.6 % BB_2B and 8.3 % CBCB) could explain the empirical band-gap of boron carbide of 2.09 eV.[37] No experimental quantification of such defects nor confirmation of their identity has been provided so far.

Nuclear magnetic resonance has been recognized as a very useful tool for probing localized states in boron carbides.[1] ^{11}B-SS-NMR exhibits a main broad signal around -5 ppm, mostly linked to icosahedral boron atoms. Data analysis from crystalline B_4C suggested that beyond the equilibrium $(B_{11}C^p)$CBC arrangement, B_{12} and $B_{10}C_2^p$ motifs are also present in a $B_{11}C^p$:B_{12}:$B_{10}C_2^p$ ratio of 95:2.5:2.5.[35] However, no signs of chain defects were identified in this instance. In contrast, a ^{11}B-SS-NMR study in amorphous boron carbide of formula $B_{2.5}C$ recognized extra features at 25 and 50 ppm, ascribed to isotropic shifts of icosahedral boron and trigonal B environments (CBC chains), respectively.[146] Extra signals at -30 ppm are also observed in this report, which are not discussed.[146] This suggests that the chain defect concentration and consequently its detection threshold by solid-state NMR are crystallinity dependent. ^{13}C is a very interesting probe isotope to complement ^{11}B NMR, but it presents the main disadvantage of having a very low natural abundance of 1.11 %, against 98.89 % of the NMR inactive ^{12}C isotope. That is probably why not many ^{13}C NMR studies have been performed in boron carbide. The few records of ^{13}C-SS-NMR studies in boron carbide all show two main signals at ~ -0.6 and 79 ppm, assigned to the end-chain (**C**B**C**) atoms and to the icosahedra carbon atoms (B_{11}**C**^{p}) respectively.[147]

In the present work, we have studied the local structure of the as-synthesized nano-B_4C by means of ^{11}B and ^{13}C-SS-NMR. ^{13}C measurements were performed on an isotopically enriched sample. To do so, we prepared a $Na_{1-x}B_{5-x}C_{1+x}$ precursor from ^{13}C-enriched polyethylene, which was then calcined towards ^{13}C-enriched boron carbide. All NMR spectra shown were then performed in the ^{13}C-enriched sample, including the ^{11}B-NMR spectra. In order to interpret the results, DFT calculations of the NMR spectra were performed. Two initial models were considered for the average structure: $(B_{11}C^p)$CBC and $(B_{11}C^e)$CBC as depicted in **Figure IV. 14a** and **b** respectively (C^p = icosahedral carbon atom in polar position, C^e = icosahedral carbon

atom in equatorial position). The ^{11}B-SS-NMR spectrum is shown in **Figure IV. 14c**, along with that of a reference bulk-B_4C and the results of both spectra modelling. Similarly, ^{13}C-SS-NMR results are depicted in **Figure IV. 14d**, without the bulk reference this time as this is not ^{13}C-enriched. Both models fit well the major signals of the ^{11}B-SS-NMR spectra, but the overall structure can be discerned from the ^{13}C-SS-NMR, as the equatorial carbon model should render an extra band at ~ 20 ppm that is not empirically observed. Therefore, as expected, the average structure is concluded to consist of ($B_{11}C^p$)CBC. However, satellite signals in both the ^{11}B and the ^{13}C spectra were recognized (marked with arrows in **Figure IV. 14**), similar to those reported for amorphous-$B_{2.5}C$ in the case of the ^{11}B spectrum. These signals are not explained by the overall structure and could then probably be assigned to localized defects. Rotation bands, marked with * in **Figure IV. 14** were identified from performing the measurement at different rotation speeds (not shown).

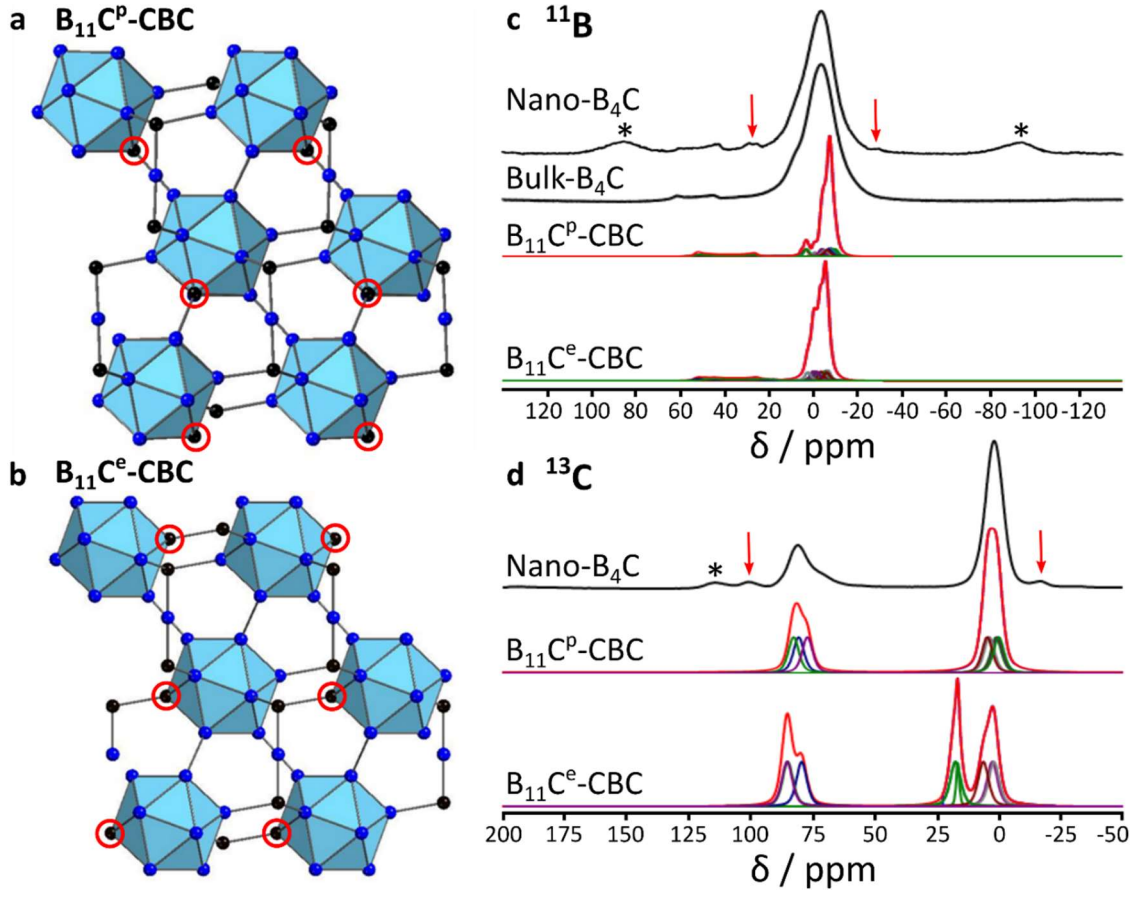

Figure IV. 14. SS-NMR study on Nano-$B_{4.1}C$. **(a)** Model structures are depicted for the ($B_{11}C^p$)CBC **(a)** and ($B_{11}C^e$)CBC **(b)** models, where the icosahedral C atoms in either the polar or equatorial positions are marked in red circles. SS-NMR spectra and models for ^{11}B **(c)** and ^{13}C **(d)** probes. Satellite signals not ascribed to the average structure are marked in red arrows and rotation bands with an *.

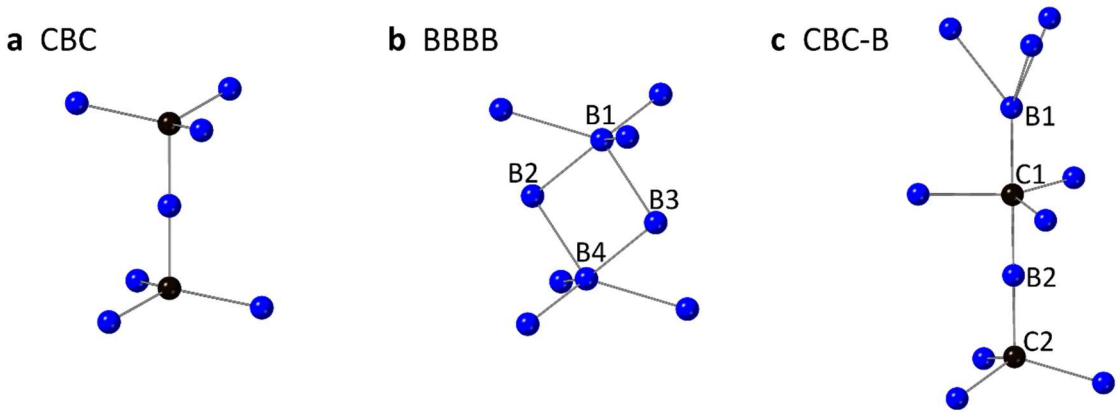

Figure IV. 15. Chain geometries variations assigned to NMR signal. **(a)** Standard CBC chains in the classical average $(B_{11}C^{p})CBC$ structure. **(b)** Rhombi-like BBBB defect chain. **(c)** 4-atom linear CBC-B defect chain.

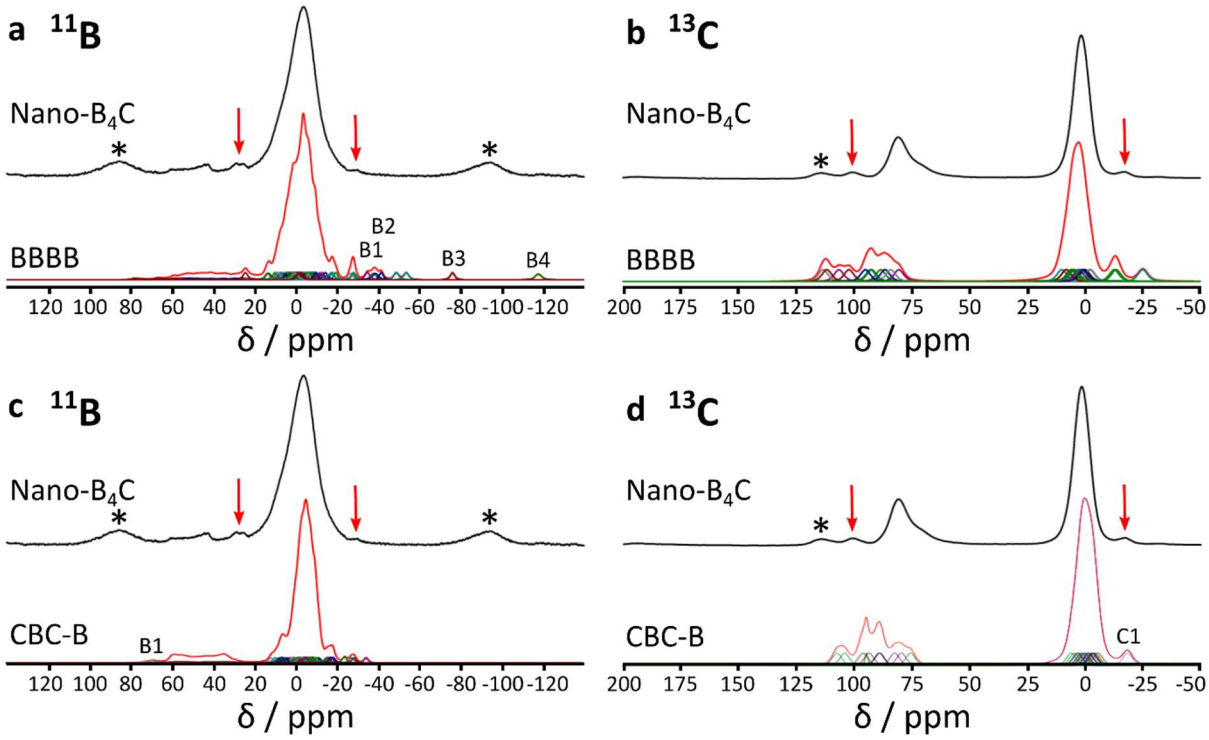

Figure IV. 16. DFT modelling of SS-NMR spectra considering defects in the linear chain. The rhombi-like BBBB chain defect is modelled and compared against the experimental data in **(a)** for the ^{11}B-NMR and in **(b)** for the ^{13}C-NMR. The 4-atom linear CBC-B chain defect is modelled and compared against the experimental data in **(c)** for the ^{11}B-NMR and in **(d)** for the ^{13}C-NMR. Red arrows indicate the satellite signals attributed to chain-defects.

For the upcoming calculations on defective structures, special care was taken on choosing the boron-to-carbon stoichiometry that reproduced the semiconducting behavior of boron carbide. That is because the addition of defects modifies the electron filling of the valence states.[37] This is compensated with adding carbons until all valence states are filled, which does not

necessarily renders the $B_{4.1}C$ empirical stoichiometry, but is still more representative as it reproduces the semiconducting behavior of boron carbide. These additional carbon atoms were introduced in the polar position of the icosahedra, since, as it was shown before, this matches the experimental data. Out of the 15 energetically favorable local defects that were evaluated, two kinds of defects remarkably reproduced the satellite signals in the NMR spectra: the rhombi-like BBBB and the linear chain CBC-B. These groups are the two most stable configurations according to DFT calculations.[37] These three local structures are depicted in **Figure IV. 15b** and **c** respectively, along with the classical CBC chain local structure in **Figure IV. 15a** for comparison. The calculated and experimental NMR spectra are shown in **Figure IV. 16a/b** and **c/d** for the BBBB and CBC-B structures respectively.

Most notably, the BBBB model reproduced all the observed signals while presenting certain not observed signals. On the other hand, the CBC-B motives reproduced very well the ^{13}C-NMR and the satellite signal of the 11B-NMR at -25 ppm, although it does not show the satellites at 20 ppm. This suggests that a linear combination analysis could reproduce the overall NMR profile, analysis in this direction are currently underway.

Sintering into dense monoliths

Once the purity, stoichiometry and monodispersity of boron carbide were optimized, the following stage was to sinter the powder into a dense monolith, ideally keeping the nanostructure intact. Sintering experiments were performed in a first instance by hot-pressing in a Paris-Edinburgh press. Standard assemblies described in the **Experimental** section were used. Resistive heating from continuous current dissipation in a graphite element was used for the annealing. The external pressure was fixed at 5 GPa and the temperature profile was chosen based on literature reports. Particularly, a fast heating ramp of 200 °C·min^{-1} and a dwell time of 5 min were used, as reported by Liu and collaborators in similar conditions of boron carbide sintering.[68] A slow cooling rate of 50 °C·min^{-1} was applied down to 600 °C before abrupt quenching according to the Léna Roumiguier's thesis work.[148] A slow cooling was shown to prevent the appearance of dislocations. XRD diagrams were recorded on the processed pellets. The pellets were later embedded in an acrylic resin and polished for recording of the Vicker's hardness. Details of the heating and pressurizing programs can be found in **Figure IV. 17a**, whereas the corresponding X-ray diffractograms are shown in **Figure IV. 17b**. It must be highlighted that the *h*-BN impurities detected by XRD come from the contact with the *h*-BN

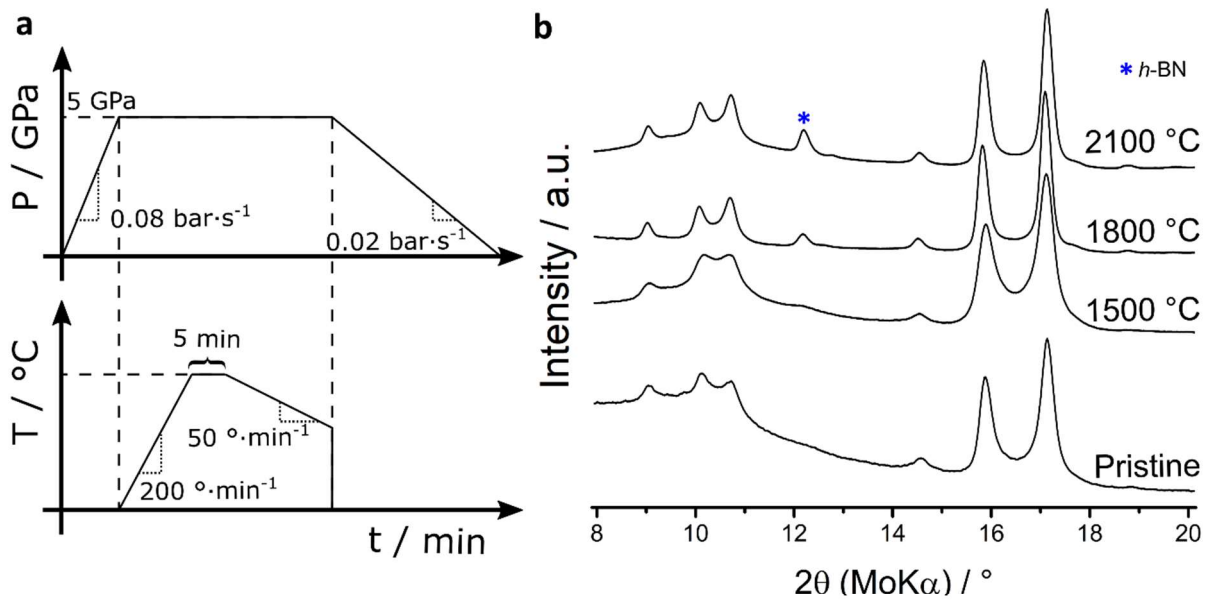

Figure IV. 17. Sintering experiment results in Paris-Edinburgh press. **(a)** Scheme of the pressurization and heating program. **(b)** XRD results from the dwell temperature screening.

capsule during sintering. It remains superficial and does not threaten the mechanical properties of the material, as confirmed below by Raman microscopy.

The measured $HV_{9.8}$ hardness values were (10 ± 1), (18 ± 1) and (31 ± 2) GPa for the samples sintered at 1500, 1800 and 2100 °C respectively. These results were already very promising as we succeeded in reproducing the typical hardness of boron carbide. Albeit, these results suggested that optimal sintering conditions were not achieved, since no great grain growth were observed according to the diffraction peak's width, while the hardness kept increasing with the sintering pressure. However, the limits of the Paris-Edinburgh press in terms of delivered current had been topped. For this reason, further sintering experiments were performed in a prototype Paris-Edinburgh press coupled to a spark plasma device at the Institut Lumière et Matière of the University Claude Bernard at Lyon. Here, differently to conventional spark plasma sintering, the current was not passed through the sample, so that an insulating *h*-BN capsule could still be used to keep carbon in the graphite oven from migrating inside the sample. The overall heating profile was reproduced from the initial hot-pressing experiments (**Figure IV. 2a**) and the dwell temperature was screened at the nominal temperatures of 2100 °C, 2300 °C and 2500 °C. The power, resistance and anvils displacements were recorded throughout the procedure in order to shed light on the sintering process, these can be found in **Figure IV. 18** for each of the studied temperatures.

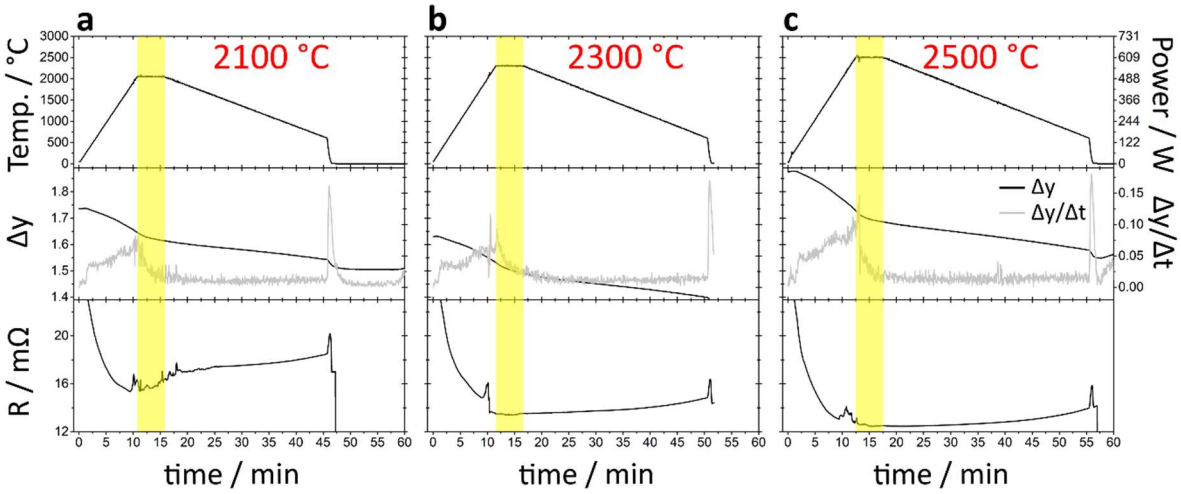

Figure IV. 18. Experimental heating profile (temperature or power vs. time), displacement and displacement derivative of the anvils position over time and resistance over time for the three sintering experiments performed at 5 GPa and **(a)** 2100 °C, **(b)** 2300 °C and **(c)** 2500 °C.

Changes in the resistance and in the derivative of the anvils displacement (displacement speed) are good indicators of sintering processes.[149] For our studies, we observed that at least one major event occurs at 2000 °C. This is observed as a peak in the displacement speed and the resistance, the latter being more evident. This fact confirms the previous observation, where no consolidation was achieved below this temperature. We also observe that this sintering event lasts about 5 min in all cases as the displacement speed decays to a constant value. This supports the choice of the dwell time. The sharp peak in the displacement speed curve corresponds to the change of heating slope (from heating ramp to dwell), which causes a sharp variation in the displacement rate. Further spikes in the resistance curve can be ascribed to imperfect contacts in the setup assembly.

After the sintering treatments were performed, we attempted to measure the densities of the monoliths in order to evaluate the actual densification. Densities were measured using the Archimedes method as described in **Appendix I**, yielding values of (97 ± 5) %, (99 ± 4) % and (96 ± 6) %, for the T = 2100 °C, 2300 °C and 2500 °C samples respectively. Although the results show a high degree of densification, the large uncertainties do not allow to conclude on a tendency of densification as a function of the sintering temperature. These large uncertainties arise from the small mass obtained for each compound, around 7 mg each.

Consequently, we evaluated first the X-ray diffraction patterns and secondly, the Vicker's hardness for each of the samples in order to identify the optimal conditions. The highest targeted

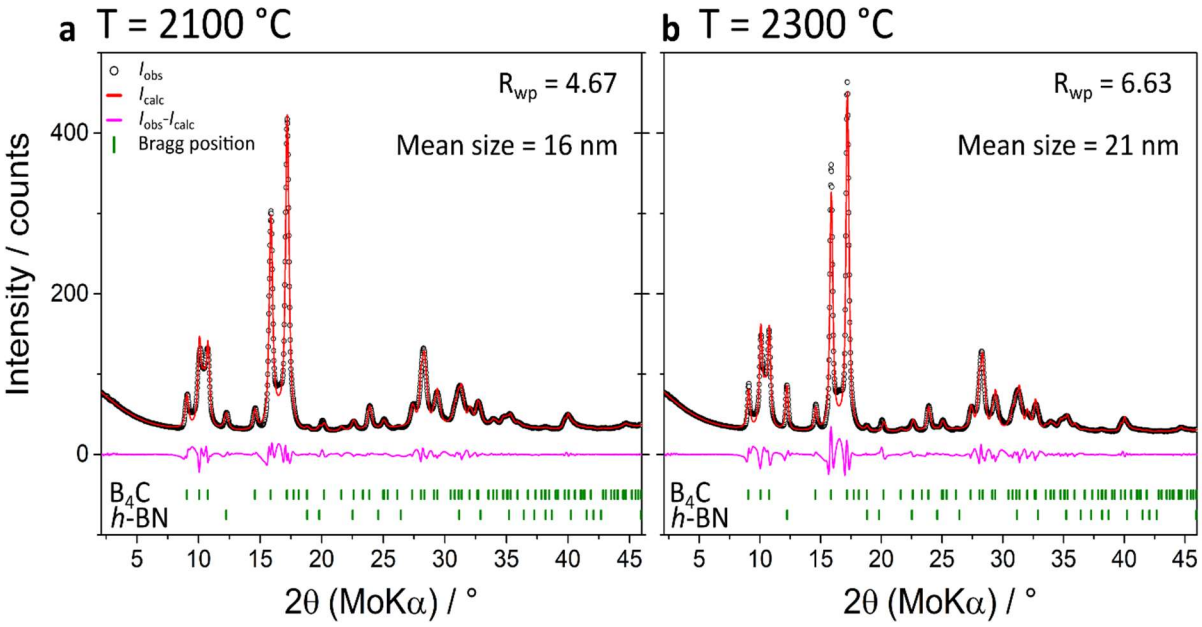

Figure IV. 19. XRD results and Le Bail analysis of samples of nano-$B_{4.1}C$ sintered compounds at 5 GPa and **(a)** 2100 °C and **(b)** 2300 °C.

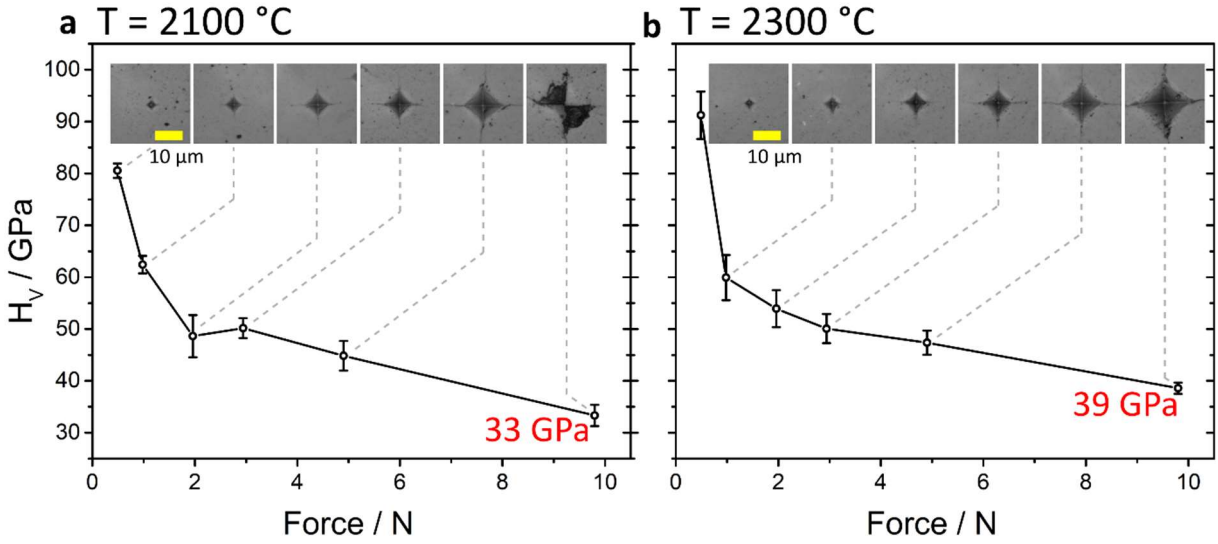

Figure IV. 20. Vicker's hardness curves in the 0.98 – 9.8 N load range, for samples of nano-B_4C sintered compounds at **(a)** 2100 °C and **(b)** 2300 °C.

temperature of 2500 °C triggered large grain growth towards the bulk state according to XRD (not shown). We have then not performed further analysis on this sample. The remaining two samples sintered at 2100 and 2300 °C showed retention of the nanodomains size according to Le Bail analysis of the XRD patterns shown in **Figure IV. 19**, with average crystallite sizes of 16 and 21 nm respectively. Full Vicker's microhardness curves were recorded for both samples, the results are depicted in **Figure IV. 20**. Both samples exhibit a remarkably high $HV_{9.8}$ hardness of (33 ± 2) and (39 ± 1) GPa respectively, the latter being a value that has never been measured in sintered compacts of boron carbide, to our knowledge. This value is compared to

Table IV. 1. Highest values of Vicker's hardness reported for boron carbide.

Grain size (nm)	Density (%)	$VH_{9.8}$ (GPa)	Reference
21	99	39 ± 1	This work
2350	99.7	39 ± 1	[68]
690	100	34 ± 2	[53]
130	97	33 ± 3	[70]
300	99.2	32 ± 1	[54]
180	97.5	31 ± 3	[70]
27700	Not reported	30 ± 2	[71]
100	94.6	23 ± 3	[70]

literature Vicker's hardnesses of boron carbide in **Table IV. 1**. The fracture toughness was also evaluated by using the extent of the cracks originated at the indentation vertexes. (1.29 ± 0.08) and (1.21 ± 0.06) $MPa \cdot m^{1/2}$ values are obtained at applied loads of 9.8 N for the 2100 and 2300 °C samples, respectively. Both values are smaller than those usually reported for boron carbide (2.5 – 3.0 $MPa \cdot m^{1/2}$), which actually is in line with the higher hardness, as harder materials tend to be more fragile, as particularly observed for boron carbide.[53]

We then produced a reference sample for comparison. Boron carbide powders from Sigma (5 μm < particle size < 10 μm, 98 %) were used as starting powders. The starting powder was analyzed by XRD and SEM-EDX, both confirming the declared granulometry and purity (not shown). The sample was sintered under the same conditions than the SPS T = 2300 °C sintered sample. We measured an $HV_{9.8}$ hardness of (20 ± 2) GPa, indeed much smaller than those of the herein produced nano-$B_{4.1}C$ thus confirming the role of the nanostructuration according the Hall-Petch relation.[63,64]

Beyond the hardness optimization, a further target underlying the synthesis of boron carbide nanoparticles was that nanostructuration would diminish the tendency towards amorphization upon stress, in order to enhance the long-term duration of this structural material. Raman microscopy was chosen as the main probe to characterize the amorphization, as the Raman spectrum of amorphized $B_{4+\delta}C$ presents well-recognized broad bands above 1200 cm^{-1}.[66,85] Only the most promising sample was chosen for this study, that is, the one sintered at 2300 °C, along with the reference sample for comparison. The 9.8 N indented regions were measured as they correspond to the reference load for hardness reporting. Raman spectra (**Figure IV. 21a** and **b**) were recorded in the pristine and indented region (points 1 and 2 respectively schematized in **Figure IV. 21c**). While prominent broad amorphization bands rise in the indented region for the reference-B_4C, no major amorphization was observed in the measured nano-$B_{4.1}C$ sample. The Raman spectrum of the nanostructured sample also confirmed the

absence of graphite or hexagonal boron nitride in the core of the monolith, as the corresponding D (1350 cm^{-1}) and G (1580 cm^{-1}) bands are absent.[150]

These first Raman spectra were recorded with low spatial resolution resulting from a large incident beam of 4×4 μm^2 as shown in **Figure IV. 21d**), which did not allow accurate probing inside the indentation (see **Figure IV. 21e**). To probe the spatial homogeneity of amorphization, we then performed Raman mapping with a 785 nm laser source and a 2.2×2.2 μm^2 spatial resolution and allows to scan the sample in a bidimensional mesh. In order to extract quantitative information, Gaussian deconvolutions were performed for each Raman spectrum of the map. The area of the peaks associated to the amorphized phase ($A_{am.}$) were then evaluated with respect to the crystalline $B_{4.1}C$ Raman bands area ($A_{cr.}$). The relative peak area percentage $A_{am.}/(A_{am.} + A_{cr.})$ is represented in **Figure IV. 22**. It can be observed that while certain degree of amorphization is observed in nano-$B_{4.1}C$, notably for the highest loading of 19.6 N, the proportion of amorphous component is much weaker than for the reference B_4C material.

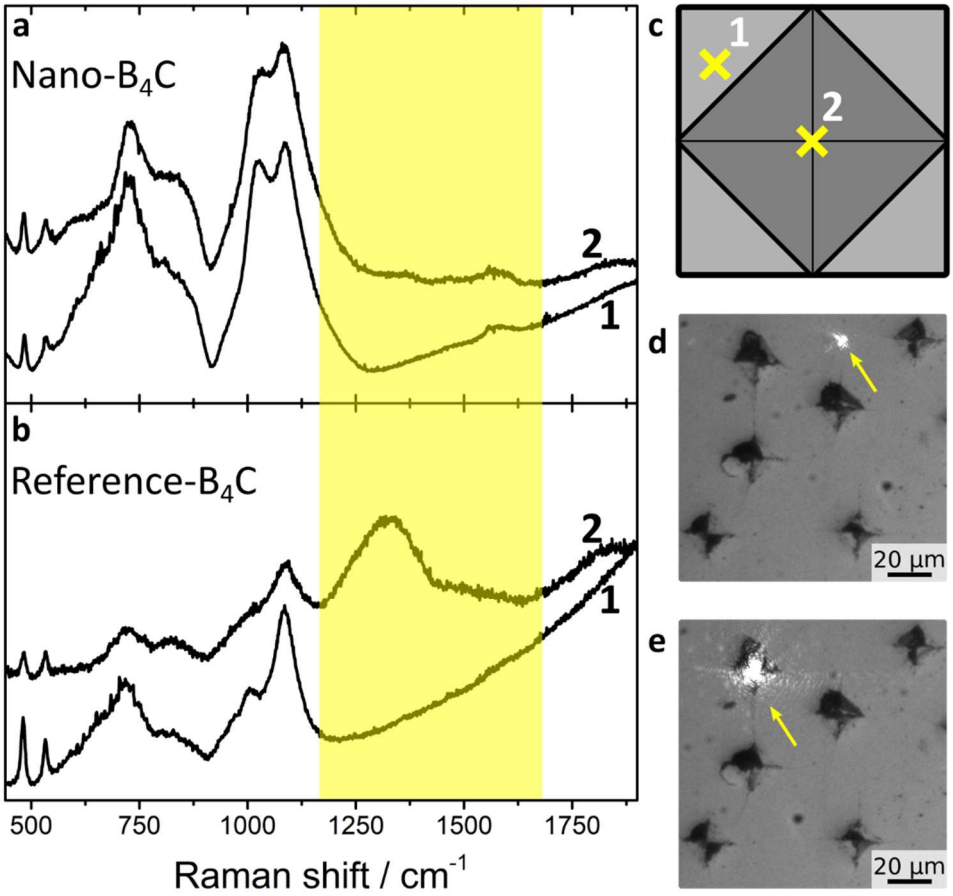

Figure IV. 21. Raman spectra in pristine (1) and indented with a load of 9.8 N (2) zones for nano-B_4C **(a)** and for the reference-B_4C **(b)**, both sintered at 2300 °C and 5 GPa. **(c)** Indentation scheme and selected spots for acquiring Raman spectra. The actual probed spots are exemplified in **(d)** for the pristine region and **(e)** for the indented region, showing in the latter the imprecision and lack of resolution of the targeted position.

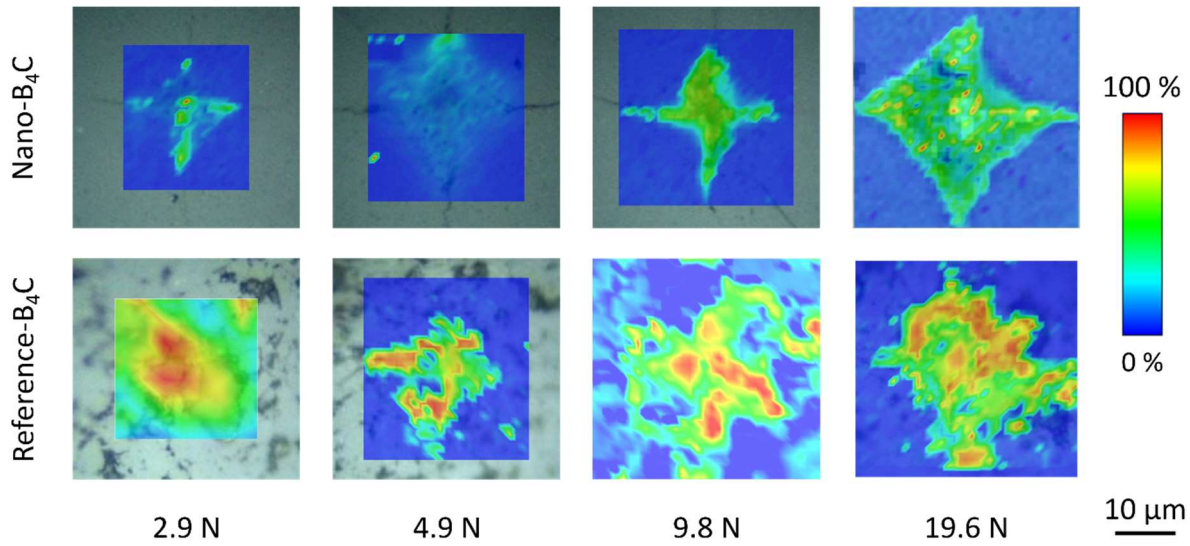

Figure IV. 22. Raman cartography at different indentation loads for nano-B_4C **(a)** and for the reference-B_4C **(b)**, both sintered at 2300 °C and 5 GPa.

IV.4 Partial conclusions

The synthesis of boron carbide nanostructures as a structural material was explored by the templated transformation of $Na_{1-x}B_{5-x}C_{1+x}$ nanostructures. Initial attempts to perform the transformation while avoiding phase segregation of Na were unsuccessful, as in the high-pressure conditions studied, Na atoms segregated out of the boron carbide structure and later reacted with air/moisture to yield sodium carbonates and borates, both detrimental to the mechanical properties of boron carbide. Instead, room-pressure transformation at 1200 °C allowed to eliminate Na by evaporation. Boron also segregates out of the structure, which under air exposure transformed to H_3BO_3 that could be easily removed by washing with methanol. The particle size was fairly conserved from the initial 5 nm $Na_{1-x}B_{5-x}C_{1+x}$ nanoparticles to 10 nm $B_{4.1}C$, although in the latter, a second population of large crystals (< 100 nm) were also identified. Monodispersity at 10 nm of the boron carbide product was achieved by screening the B:C input in the synthesis of the $Na_{1-x}B_{5-x}C_{1+x}$ precursor, resulting in the optimal input of B:C = 5:4 reagents ratio. The precise stoichiometry of the synthesized boron carbide nanocrystals was evaluated at $B_{4.1}C$ from the lattice parameters extracted by Le Bail fitting of the XRD diagram.

The local structure of the boron carbide nanocrystals was then investigated by means of solid state ^{11}B and ^{13}C-NMR. The expected distribution of carbon atoms in the polar icosahedra position $(B_{11}C^{p})CBC$ was evidenced. We could attribute the low intensity satellite signals in

both isotopes NMR to local defects in the CBC chain region. Two main defect geometries match the experimental signal: rhombi-like BBBB and linear chain CBC-B. These defects also correspond to the most likely and favorable chain defects according to recent modelling reports.[37]

In order to study the mechanical properties of the synthesized boron carbide nanostructure, its densification by hot pressing and high-pressure spark-plasma sintering at 5 GPa of pressure was explored. The latter showed the best results at a sintering temperature of 2300 °C, where a densification of 99 % was achieved without major grain growth (21 nm). The compound showed excellent mechanical properties, with an $HV_{9.8}$ hardness of 39 ± 1 GPa and a fracture toughness of 1.21 ± 0.06 $MPa \cdot m^{1/2}$. It also exhibited a significantly higher resistance to amorphization upon stress as evidenced by Raman spectroscopy in comparison to a standard microsized Boron Carbide reference. All in all, this study showed for the first time the synthesis of boron carbide nanostructures and opens the gates to its use for mechanical reinforcement and structural additives.

References for Part One

[1]: V. Domnich, S. Reynaud, R. A. Haber and M. Chhowalla, *J. Am. Ceram. Soc.*, 2011, **94**, 3605–3628.
[2]: A. A. Cheenady, A. Awasthi and G. Subhash, *J. Am. Ceram. Soc.*, 2020, **103**, 7127–7134.
[3]: V. Domnich, Y. Gogotsi, M. Trenary and T. Tanaka, *Appl. Phys. Lett.*, 2002, **81**, 3783.
[4]: H. K. Clark and J. L. Hoard, *J. Am. Chem. Soc.*, 1943, **65**, 2115–2119.
[5]: V. A. Mukhanov, P. S. Sokolov and V. L. Solozhenko, *J. Superhard Mater. 2012 343*, 2012, **34**, 211–213.
[6]: S. Ramana Murthy, *J. Mater. Sci. Lett.*, 1985, **4**, 603–605.
[7]: S. P. Dodd, G. A. Saunders and B. James, *J. Mater. Sci.*, 2002, **37**, 2731–2736.
[8]: A. O. Sezer and J. I. Brand, *Mater. Sci. Eng. B*, 2001, **79**, 191–202.
[9]: P. W. May, K. N. Rosser, N. A. Fox, C. M. Younes and G. Beardmore, *Diam. Relat. Mater.*, 1997, **6**, 450–455.
[10]: M. Bouchacourt, *J. Mater. Sci.*, 1985, **20**, 1237–1247.
[11]: A. K. Suri, C. Subramanian, J. K. Sonber and T. S. R. Ch. Murthy, *Int. Mater. Rev.*, 2013, **55**, 4–40.
[12]: P. W. May, *Science*, 2008, **319**, 1490–1491.
[13]: D. Jianxin, *Mater. Sci. Eng. A*, 2005, **408**, 227–233.
[14]: M. P. Dariel and N. Frage, *Adv. Appl. Ceram.*, 2012, **111**, 301–310.
[15]: D. Emin and T. L. Aselage, *J. Appl. Phys*, 2005, **97**, 13529.
[16]: P. Dijnner, H.-J. Heuvel and M. Horle, *J. Nucl. Mater.*, 1984, **124**, 185–194.
[17]: M. W. Mortensen, P. G. Sørensen, O. Björkdahl, M. R. Jensen, H. J. G. Gundersen and T. Bjørnholm, *Appl. Radiat. Isot.*, 2006, **64**, 315–324.
[18]: M. Beauvy, *J. Less-Common Met.*, 1983, **90**, 169–175.
[19]: G. S. Zhdanov and N. G. Sevast'yanov, *Compt. rend. acad. sci. U.R.S.S.*, 1941, **32**, 432–434.
[20]: H. . K. Clark and J. L. Hoard, *J. Am. Ceram. Soc.*, 1942, **65**, 2115–2119.
[21]: B. Morosin, G. H. Kwei, A. C. Lawson, T. L. Aselage and D. Emin, *J. Alloys Compd.*, 1995, **226**, 121–125.
[22]: P. Dera, M. H. Manghnani, A. Hushur, Y. Hu and S. Tkachev, *J. Solid State Chem.*, 2014, **215**, 85–93.
[23]: E. Nishibori, H. Hyodo, K. Kimura and M. Takata, *Solid State Sci.*, 2015, **47**, 27–31.
[24]: D. W. Bullett, *J. Phys. C Solid State Phys.*, 1982, **15**, 415–426.
[25]: G. Will, *Zeitschrift fur Anorg. und Allg. Chemie*, 2001, **627**, 2100–2104.
[26]: H. L. Yakel, *Acta Crystallogr. Sect. B*, 1975, **31**, 1797–1806.
[27]: G. H. Kwei and B. Morosin, *J. Phys. Chem.* **100**, 8031-8039.
[28]: A. Kirfel, A. Gupta and G. Will, *Acta Crystallogr. Sect. B*, 1979, **35**, 1052–1059.
[29]: D. R. Armstrong, J. Bolland, P. G. Perkins, G. Will and A. Kirfel, *Acta Crystallogr. Sect. B*, 1983, **39**, 324–329.
[30]: X. Guo, J. He, Z. Liu, Y. Tian, J. Sun and H.-T. Wang, *Phys. Rev. B*, 2006, **73**, 1–7.
[31]: S. Aydin and M. Simsek, *Phys. status solidi*, 2009, **246**, 62–70.
[32]: D. Emin, *Phys. Today*, 1987, **40**, 55–62.
[33]: T. V Hynes and M. N. Alexander, *J. Chem. Phys*, 1971, **54**, 5296.
[34]: L. Donghoon, J. B. Phillip and T. L. Aselage, *J. Phys. Condens. Matter*, 1999, **11**, 4435.
[35]: F. Mauri, N. Vast and C. J. Pickard, *Phys. Rev. Lett.*, 2001, **87**, 855061–855064.
[36]: R. Lazzari, N. Vast, J. M. Besson, S. Baroni and A. D. Corso, *Phys. Rev. Lett.*, 1999, **83**, 3230–3233.

[37]: K. Rasim, R. Ramlau, A. Leithe-Jasper, T. Mori, U. Burkhardt, H. Borrmann, W. Schnelle, C. Carbogno, M. Scheffler and Y. Grin, *Angew. Chemie Int. Ed.*, 2018, **130**, 6238–6243.
[38]: I. Jimé Nez, D. G. J. Sutherland, T. Van Buuren, J. A. Carlisle, L. J. Terminello and F. J. Himpsel, *Phys. Rev. B*, 1998, **57**, 13167–13174.
[39]: Y. Feng, G. T. Seidler, J. O. Cross, A. T. Macrander and J. J. Rehr, *Phys. Rev. B*, 2004, **69**, 1–8.
[40]: R. S. Kumar, D. Dandekar, A. Leithe-Jasper, T. Tanaka, Y. Xiao, P. Chow, M. F. Nicol and A. L. Cornelius, *Diam. Relat. Mater.*, 2010, **19**, 530–532.
[41]: S. Mondal, E. Bykova, S. Dey, S. I. Ali, N. Dubrovinskaia, L. Dubrovinsky, G. Parakhonskiy and S. Van Smaalen, *Sci. Rep.*, 2016, **6**, 11–16.
[42]: D. Emin, *Phys. Rev. B*, 1988, **38**, 6041–6055.
[43]: T. L. Aselage and R. G. Tissot, *J. Am. Ceram. Soc.*, 1992, **75**, 2207–2212.
[44]: N. Vast, J. Sjakste and E. Betranhandy, *J. Phys. Conf. Ser.*, 2009, **176**, 1–18.
[45]: D. M. Bylander and L. Kleinman, *Phys. Rev. B*, 1991, **43**, 1487–1491.
[46]: G. Fanchini, J. W. Mccauley and M. Chhowalla, *Phys. Rev. Lett.*, 2006, **97**, 1–4.
[47]: J. E. Saal, S. Shang and Z.-K. Liu, *Appl. Phys. Lett*, 2007, **91**, 231915-1-231915–3.
[48]: A. K. Kampouris and A. A. Konstantinidis, *J. Mech. Behav. Mater.*, 2016, **25**, 161–164.
[49]: Herrmann, K. (Ed.). (2011). Hardness testing: principles and applications. ASM international.
[50]: es.wikipedia.org/wiki/Dureza_Vickers (Revised on the 10/08/2022).
[51]: K. Niihara, A. Nakahira and T. Hirai, *Commun. Am. Ceram. Soc.*, 1984, **67**, C13–C14.
[52]: F. Thevenot, *J. Eur. Ceram. Soc.*, 1990, **6**, 205–225.
[53]: B. M. Moshtaghioun, D. Gomez-Garcia, A. Dominguez-Rodriguez and R. I. Todd, *J. Eur. Ceram. Soc.*, 2016, **36**, 1829–1834.
[54]: M. DeVries, J. Pittari, G. Subhash, K. Mills, C. Haines, J. Q. Zheng and F. Zok, *J. Am. Ceram. Soc.*, 2016, **99**, 3398–3405.
[55]: H. Tang, M. Wang, D. He, Q. Zou, Y. Ke and Y. Zhao, *Carbon N. Y.*, 2016, **108**, 1–6.
[56]: ASTM Standard, "C1327, Standard Test Method for Vickers Indentation Hardness of Advanced Ceramics"; ASTM International, West Conshohocken, PA, 2008.
[57]: M. Straker, A. Chauhan, M. Sinha, W. A. Phelan, M. V. S. Chandrashekhar, K. J. Hemker, C. Marvel and M. Spencer, *J. Cryst. Growth*, 2020, **543**, 125700.
[58]: X. Q. Yan, W. J. Li, T. Goto and M. W. Chen, *Appl. Phys. Lett.*, 2006, **88**, 67–70.
[59]: A. K. Vijh, *Wear*, 1975, **35**, 205–209.
[60]: K. Y. Xie, Q. An, M. F. Toksoy, J. W. McCauley, R. A. Haber, W. A. Goddard and K. J. Hemker, *Phys. Rev. Lett.*, 2015, **115**, 175501.
[61]: Q. An, W. A. Goddard, K. Y. Xie, G. D. Sim, K. J. Hemker, T. Munhollon, M. Fatih Toksoy and R. A. Haber, *Nano Lett.*, 2016, **16**, 7573–7579.
[62]: Q. An and W. A. Goddard, *Appl. Phys. Lett.*, 2017, **110**, 111902.
[63]: N. J. Petch, *J. Iron Steel Inst.*, 1953, **174**, 25–28.
[64]: E. O. Hall, *Proc. Phys. Soc. Sect. B*, 1951, **64**, 747–753.
[65]: L. Roumiguier, A. Jankowiak, N. Pradeilles, G. Antou and A. Maître, *Ceram. Int.*, 2019, **8**, 9912–9918.
[66]: K. Madhav Reddy, J. J. Guo, Y. Shinoda, T. Fujita, A. Hirata, J. P. Singh, J. W. McCauley and M. W. Chen, *Nat. Commun.*, 2012, **3**, 1–7.
[67]: D. Guo, S. Song, R. Luo, W. A. Goddard, M. Chen, K. M. Reddy and Q. An, *Phys. Rev. Lett.*, 2018, **121**, 1–6.
[68]: L. Liu, X. Li, Q. He, L. Xu, X. Cao, X. Peng, C. Meng, W. Wang, W. Zhu and Y. Wang, *J. Am. Ceram. Soc.*, 2018, **101**, 1289–1297.
[69]: C. C. Wang and L. Le Song, *Chinese Phys. B*, 2019, **28**, 1–4.

[70]: B. M. Moshtaghioun, A. L. Ortiz, D. Gómez-García and A. Domínguez-Rodríguez, *J. Eur. Ceram. Soc.*, 2015, **35**, 1991–1998.
[71]: C. Cheng, K. M. Reddy, A. Hirata, T. Fujita and M. Chen, *J. Eur. Ceram. Soc.*, 2017, **37**, 4514–4523.
[72]: L. Farbaniec, J. Hogan, J. McCauley and K. Ramesh, *Int. J. Appl. Ceram. Technol.*, 2016, **13**, 1008–1016.
[73]: C. A. Schuh, *Mater. Today*, 2006, **9**, 32–40.
[74]: D. Ghosh, G. Subhash, T. S. Sudarshan, R. Radhakrishnan and X. L. Gao, *J. Am. Ceram. Soc.*, 2007, **90**, 1850–1857.
[75]: G. W. Hollenberg and G. Walther, *J. Am. Ceram. Soc.*, 1980, **63**, 610–613.
[76]: M. W. Chen, J. W. McCauley, J. C. LaSalvia and K. J. Hemker, *J. Am. Ceram. Soc.*, 2005, **88**, 1935–1942.
[77]: H. Lee and R. F. Speyer, *J. Am. Ceram. Soc.*, 2002, **85**, 1291–1293.
[78]: T. Mashimo and M. Uchino, *J. Appl. Phys.*, 1997, **81**, 7064.
[79]: L. Farbaniec, J. D. Hogan, K. Y. Xie, M. Shaeffer, K. J. Hemker and K. T. Ramesh, *Int. J. Impact Eng.*, 2017, **99**, 75–84.
[80]: K. M. Reddy, D. Guo, S. Song, C. Cheng, J. Han, X. Wang, Q. An and M. Chen, *Sci. Adv.*, 2021, **7**, 1–7.
[81]: M. A. M. Z. Designed Research; S, *Proc. Natl. Acad. Sci.*, 2016, **113**, 12088–12093.
[82]: D. Gosset, S. Miro, S. Doriot, G. Victor and V. Motte, *Nucl. Instruments Methods Phys. Res. B*, 2015, **365**, 300–304.
[83]: M. Chen and J. W. Mccauley, *J. Appl. Phys*, 2006, **100**, 1–5.
[84]: M. Chen, J. W. Mccauley and K. J. Hemker, *Science*, 2003, **299**, 1563–1566.
[85]: K. M. Reddy, P. Liu, A. Hirata, T. Fujita and M. W. Chen, *Nat. Commun.*, 2013, **4**, 1–5.
[86]: X. Q. Yan, Z. Tang, L. Zhang, J. J. Guo, C. Q. Jin, Y. Zhang, T. Goto, J. W. McCauley and M. W. Chen, *Phys. Rev. Lett.*, 2009, **102**, 075505.
[87]: Q. An, W. Goddard and T. Cheng, *Phys. Rev. Lett.*, 2014, **113**, 1–5.
[88]: Q. An and W. A. Goddard, *Phys. Rev. Lett.*, 2015, **115**, 1–5.
[89]: E. Betranhandy, N. Vast and J. Sjakste, *Solid State Sci.*, 2012, **14**, 1683–1687.
[90]: R. Raucoules, N. Vast, E. Betranhandy and J. Sjakste, *Phys. Rev. B*, 2011, **84**, 14112.
[91]: R. B. Kaner, J. J. Gilman and S. H. Tolbert, *Science*, 2005, **308**, 1268–1269.
[92]: Y. Shen, J. Fuller and Q. An, *J. Appl. Phys*, 2021, **129**, 140902.
[93]: G. Subhash, A. P. Awasthi, C. Kunka, P. Jannotti and M. DeVries, *Scr. Mater.*, 2016, **123**, 158–162.
[94]: A. U. Khan, A. M. Etzold, X. Yang, V. Domnich, K. Y. Xie, C. Hwang, K. D. Behler, M. Chen, Q. An, J. C. LaSalvia, K. J. Hemker, W. A. Goddard and R. A. Haber, *Acta Mater.*, 2018, **157**, 106–113.
[95]: Q. An and W. A. Goddard, *J. Phys. Chem. Lett.*, 2014, **5**, 4169–4174.
[96]: S. Xiang, L. Ma, B. Yang, Y. Dieudonne, G. M. Pharr, J. Lu, D. Yadav, C. Hwang, J. C. Lasalvia, R. A. Haber, K. J. Hemker and K. Y. Xie, *Sci. Adv.*, 2019, **5**, 1–6.
[97]: V. Adasch, M. Schroeder, D. Kotzott, T. Ludwig, N. Vojteer and H. Hillebrecht, *J. Am. Chem. Soc.*, 2010, **132**, 13723–13732.
[98]: B. Tang, Y. He, W. A. Goddard and Q. An, *J. Am. Ceram. Soc.*, 2019, **102**, 5514–5523.
[99]: H. Hillebrecht, N. Vojteer, V. Sagawe, K. Hofmann and B. Albert, *Zeitschrift für Anorg. und Allg. Chemie*, 2019, **645**, 362–369.
[100]: N. Vojteer, H. Hillebrecht, D.-C. N. Vojteer and H. Hillebrecht, *Angew. Chemie Int. Ed.*, 2006, **45**, 165–168.
[101]: Y. He, Y. Shen, B. Tang and Q. An, *J. Am. Ceram. Soc.*, 2020, **103**, 2012–2023.
[102]: Z. Yuan, W. Hu and D. Yu, *J. Alloys Compd.*, 2022, **893**, 162320.
[103]: R. Abbaschian, H. Zhu and C. Clarke, *Diam. Relat. Mater.*, 2005, **14**, 1916–1919.

[104]: V. I. Berdnikov, Y. A. Gudim and M. I. Karteleva, *Steel Transl.*, 2011, **41**, 85–88.
[105]: R. Raymond Ronald, Raymond Ronald, R. Boron carbide and method of making the same. 1930. US1897214A.
[106]: A. Alizadeh, E. Taheri-Nassaj and N. Ehsani, *J. Eur. Ceram. Soc.*, 2004, **24**, 3227–3234.
[107]: F. Schroll and A. Vogt, Schroll, F., Vogt, A. Electrothermic production of boron carbide. 1939. US2163293A.
[108]: A. Alizadeh, E. Taheri-Nassaj, N. Ehsani and H. R. Baharvandi, *Adv. Appl. Ceram.*, 2006, **105**, 291–296.
[109]: C. H. Jung, M. J. Lee and C. J. Kim, *Mater. Lett.*, 2004, **58**, 609–614.
[110]: Y. N. Tumanov, *J. Less-Common Met.*, 1979, **67**, 529.
[111]: W. Rafaniello and W. G. Moore, Rafaniello, W., Moore, W. G. Producing boron carbide. 1987. US4804525A.
[112]: S. Herth, W. J. Joost, R. H. Doremus and R. W. Siegel, *J. Nanosci. Nanotechnol.*, 2006, **6**, 954–959.
[113]: F. Farzaneh, F. Golestanifard, M. S. Sheikhaleslami and A. A. Nourbakhsh, *Ceram. Int.*, 2015, **41**, 13658–13662.
[114]: A. Najafi, F. Golestani-Fard, H. R. Rezaie and N. Ehsani, *Ceram. Int.*, 2012, **38**, 3583–3589.
[115]: A. Fathi, N. Ehsani, M. Rashidzadeh, H. Baharvandi and A. Rahimnejad, *Ceram. - Silikaty*, 2012, **56**, 32–35.
[116]: Y. Gu, L. Chen, Y. Qian, W. Zhang and J. Ma, *J. Am. Ceram. Soc.*, 2005, **88**, 225–227.
[117]: G. Bernard-Granger, N. Monchalin and C. Guizard, *Scr. Mater.*, 2007, **57**, 137–140.
[118]: S. L. Dole, S. Prochazka and R. H. Doremu, *J. Am. Ceram. Soc.*, 1989, **72**, 958–966.
[119]: I. T. Ostapenko, V. V Slezov, R. V Tarasov, N. Le Kartsev and V. P. Podtykan, *Sov. Powder Metall. Met. Ceram.*, 1979, **18**, 312–316.
[120]: M. S. Koval'chenko, Y. G. Tkachenko, L. F. Ochkas, D. Z. Yurchenko and V. B. Vinokurov, *Sov. Powder Metall. Met. Ceram.*, 1987, **26**, 881–884.
[121]: Yoo, S. H., Sethuram, K. M., Sudarshan, T. S. Apparatus for bonding a particle material to near theoretical density. 1999. US5989487A.
[122]: Y. Yin, D. Talapin, R. Article, Y. Liu and J. Goebl, *Chem. Soc. Rev*, 2013, **42**, 2610–2653.
[123]: T. M. Mattox, A. Agrawal and D. J. Milliron, *Chem. Mater.*, 2015, **27**, 6620–6624.
[124]: L. Li, K. Sun, C. Kurdak and J. W. Allen, *Nat. Rev. Phys. 2020 29*, 2020, **2**, 463–479.
[125]: H. C. Longuet-Higgins and V. Roberts, *Proc. R. Soc. A*, 1954, **224**, 336–347.
[126]: K. Wade, *Chem. Commun.*, 1971, **10**, 792–793.
[127]: R. W. Rudolph, *Inorg. Chem*, 1976, **76**, 446–452.
[128]: E. D. Jemmis, M. M. Balakrishnarajan and P. D. Pancharatna, *J. Am. Chem. Soc.*, 2001, **123**, 4313–4323.
[129]: K. Schmitt, C. Stückl, H. Ripplinger and B. Albert, *Solid State Sci.*, 2001, **3**, 321–327.
[130]: B. Albert and H. Hillebrecht, *Angew. Chemie - Int. Ed.*, 2009, **48**, 8640–8668.
[131]: G. Mair, H. Georg Von Schnering, M. Wörle and R. Nesper, *Zeitschrift für Anorg. und Allg. Chemie*, 1999, **625**, 1207–1211.
[132]: A. Ammar, M. Ménétrier, A. Villesuzanne, S. Matar, B. Chevalier, J. Etourneau, G. Villeneuve, J. Rodríguez-Carvajal, H. J. Koo, A. I. Smirnov and M. H. Whangbo, *Inorg. Chem.*, 2004, **43**, 4974–4987.
[133]: B. Albert and K. Schmitt, *Chem. Commun*, 1998, **21**, 2373–2374.
[134]: B. Albert and K. Schmitt, *Cemistry Mater.*, 1999, **11**, 3406–3409.
[135]: R. B. Soriano, I. U. Arachchige, C. D. Malliakas, J. Wu and M. G. Kanatzidis, *J. Am. Chem. Soc.*, 2013, **135**, 768–774.
[136]: Y. Song, I. Gómez-Recio, R. Kumar, C. Coelho Diogo, S. Casale, I. Génois and D.

Portehault, *Dalt. Trans.*, 2021, **50**, 16703–16710.
[137]: Simon Delacroix. Synthèse de nanomatériaux riches en bore. Sorbonne Université - Paris VI, 2019. France.
[138]: S. Zhang, W. Lu, C. Wang, Q. Shen and L. Zhang, *Appl. Phys. Lett.*, 2012, **101**, 1416021–1416024.
[139]: A. Mishra, R. K. Sahoo, S. K. Singh and B. K. Mishra, *J. Asian Ceram. Soc.*, 2018, **3**, 373–376.
[140]: Y. Le Godec, M. T. Dove, S. A. T. Redfern, M. G. Tucker, W. G. Marshall, G. Syfosse and J.-M. Besson, *High Press. Res.*, 2007, **21**, 263–280.
[141]: J. M. Besson and R. J. Nelmes, *Phys. B Condens. Matter*, 1995, **213**, 31–36.
[142]: A. King, N. Guignot, L. Henry, G. Morard, A. Clark, Y. Le Godec and J. P. Itié, *J. Appl. Crystallogr.*, 2022, **55**, 218–227.
[143]: Le Godec, Y., Le Floch, S., Pailhes, S., Combes, J.-M. Device for sintering by pulsating current and associated method. 2022. US11247267.
[144]: S. Roszeitis, B. Feng, H. P. Martin and A. Michaelis, *J. Eur. Ceram. Soc.*, 2014, **34**, 327–336.
[145]: C. B. Wang, S. Zhang, Q. Shen and L. M. Zhang, *Mater. Sci. Technol.*, 2009, **25**, 809–812.
[146]: C. Pallier, J. M. Leyssale, L. A. Truflandier, A. T. Bui, P. Weisbecker, C. Gervais, H. E. Fischer, F. Sirotti, F. Teyssandier and G. Chollon, *Chem. Mater.*, 2013, **25**, 2618–2629.
[147]: T. Harazono, Y. Hiroyama and T. Watanabe, *Bull. Chem. Soc. Jpn.*, 1996, 69, 2419–2423.
[148]: Léna Roumiguier. Frittage par Spark Plasma Sintering de céramiques de carbure de bore. Université de Limoges. 2019.
[149]: A. Verchère, S. Cottrino, G. Fantozzi, S. Mishra, T. Gaudisson, N. Blanchard, S. Pailhès, S. Daniele and S. Le Floch, *Ceramics*, 2020, **3**, 507–520.
[150]: F. Tunistra and J. L. Koenig, *J. Chem. Phys.*, 1970, **53**, 1126–1130.

Part Two:

Towards the delamination

of MAB phases

Chapter V: State of the art on MAB phases

V.1 MAX *vs*. MAB phases

Composition and structure

MAB phases are layered borides that have emerged recently as analogues of their carbon or nitrogen containing counterparts: MAX phases. The term "MAX phases" was coined in the late 1990's by Barsoum.[1–3] These solids bear the general formula $M_{n+1}AX_n$ (n = 1 – 4) with M being an early transition metal, A any 13 – 16 periodic table group element and X carbon or nitrogen. They consist of layered hexagonal structures with space group *P6₃/mmc* (*No*. 194), formed by alternating near-close-packed layers of XM_6 octahedra interleafed with layers of pure A atoms.[4] These materials possess enormous interest given the combination of metallic properties, such as good electrical and thermal conductivity, machinability, thermal shock resistance and damage tolerance, with those of ceramics, like elevated elastic moduli, high temperature strength and oxidation resistance.[4]

The interest of the scientific community for the MAX phases is well reflected in the explosive growth of the number of known structures in the family. Barsoum summarized the already known MAX phases by the year 2000, which amounted to 49.[5] In 2019, Barsoum reviewed once again the number of MAX entries, which then scaled to 83.[6] According to the latest reports, this number now raises as high as 150.[6–8] Currently, there exists four basic $M_{n+1}AX_n$ stoichiometries, named 211, 312, 413 and 514 hereafter for n = 1, 2, 3 or 4 respectively. The four stoichiometries crystallize in the same space group (*P6₃/mmc*) and share the same structural motif for the M–X coordination environment, *i.e.*, edge-sharing M-X octahedra, as depicted in **Figure V. 1**. These units extend along the *a* and *b* crystallographic directions to form the $M_{n+1}X_n$ layers that are separated from each other by A layers. The difference between the four structure-types is in the number of continuous XM_6 layers. Specifically, it is two in the 211 phases, three in the 312 phases, four in the 413 phases, and five in the 514 phases. The A layers acts as mirror plane and thus give rise to "zig-zag" structures along the *c*-axis.[9]

Although not formally considered a MAX-phase, layered compounds slightly deviating from the $M_{n+1}AX_n$ formula have also been reported. A family of these compounds are the $M_{n+2}A_2X_n$

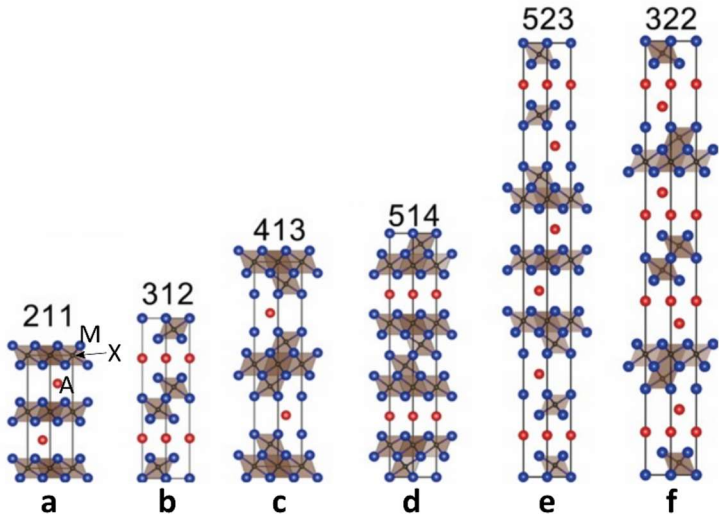

Figure V. 1. MAX phases structure for the different stoichiometries 211 **(a)**, 312 **(b)**, 413 **(c)** and 514 **(d)**. MAX-like structures are also included for the 523 **(e)** and 322 **(f)** stoichiometries. Blue, red and black balls denote the M, A and X atoms, respectively. The image is adapted from reference [158].

stoichiometries, *e.g.*, $Ti_5Al_2C_3$, which can be described as a combination of half a unit cell of Ti_2AlC and half that of Ti_3AlC_2 (**Figure V. 1e**).[10] Similarly, $Ti_7Si_2C_5$ can be conceived as two half unit cells of Ti_3SiC_2 and Ti_4SiC_3, with alternating three and four Ti–C layers between the Si layers.[11] Other MAX-like phases not adjusting any of the former stoichiometries have also been reported: Mo_2Ga_2C,[12] $Ti_3Au_2C_2$,[13] $Nb_{12}Al_3C_8$[14] or $V_{12}Al_3C_8$[15] for instance. All the MAB phases belong to the latter group, namely MAX-related phases, as they never crystallize in the *$P6_3/mmc$* space group nor do they respect the MAX-phase stoichiometry.[8]

The diversification of the MAX family is also noticeable in the identities of the M and A elements. While the original set of M elements were restricted to early transition metals –mainly Ti, Nb, Ze, Hf, V, Mo, Ta and Cr–, nowadays it extends all the way up to rare-earth (RE) elements.[7] Teo *et al.* published a class of quaternary MAX phases of general formula $(M^1_{2/3},M^2_{1/3})_2AlC$, where M^1 is Mo and M^2 is a RE element.[16] These have shown exotic magnetic behaviors such as incommensurate magnetic structures and magnetization plateaus.[16]

The A-site element has also expanded from the most common group IIIA or IVA elements to late transition metals such as Au, Cu and Zn.[7] Fashandi and coworkers reported the synthesis of Ti_3AuC_2 and $Ti_3Au_2C_2$ by a substitution reaction from Ti_3SiC_2; the latter Au-MAX phases can be further substituted to yield $Ti_3Ir_2C_2$.[13] Li *et al.* developed a general approach to synthesize a series of Zn-based MAX phases through a molten-salt replacement reaction of Al.

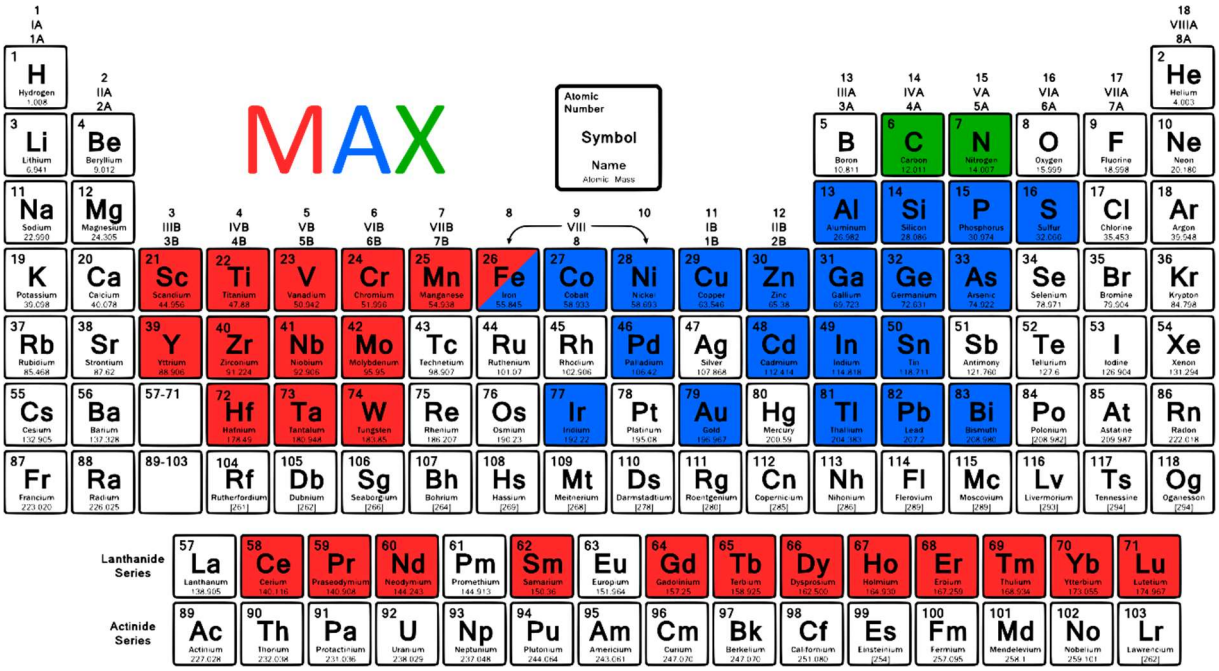

Figure V. 2. Constitutive elements of MAX phases in the periodic table.[6–8]

Ti_3AlC_2, Ti_2AlC, Ti_2AlN and V_2AlC were all transformed to their Zn analogues.[17] Al partial replacement with Cu to yield $Ti_3(Al_{1/3}Cu_{2/3})C_2$ has also been recently demonstrated by a similar method.[18] In 2020, Li and collaborators opened the doors to high-entropy MAX phases, since they prepared a series of $V_2(Sn,A)C$ (A = Fe, Co, Ni, Mn) solid solutions and $V_2(Mn_xFe_yCo_zNi_nSn_{1-x-y-z-n})C$ high–entropy MAX phase.[19] In **Figure V. 2**, the updated MAX-phase periodic table of elements is shown, summarizing the elements that have been accommodated in a MAX structure for each metallic site.[6–8]

As a matter of fact, the substitution of elements to yield quaternary phases results, in some cases, structural ordering. This has been separated in two types: out-of-plane ordered MAX phases (*o*-MAX) and in-plane ordered MAX phases (*i*-MAX). *o*-MAX phases have a general formula of $(M^1,M^2)_{n+1}AlC_n$, with n being 2 or 3. As the name suggests, the substitutional ordering takes place perpendicularly to the layers, where two M^1 layers "sandwich" either one or two layers of M^2 within each M layers. The first *o*-MAX phase was reported by Liu *et al*.,[20] who showed from neutron and X-ray diffraction refinement that the Cr and Ti atoms in $(Cr_{2/3}Ti_{1/3})_3AlC_2$ are ordered out of plane, and occupying the *2a* and *4f* Wyckoff sites, respectively. The ordering was ascribed to the distinct differences in electronegativity and covalent radius of Ti and Cr atoms,[20] which made it difficult to form solid solutions. In contrast, the in-plane ordering is only found in 211 MAX phases and the atomic ratio between the two M site alloying elements (M^1 and M^2) is always 2: $(M^1_{2/3},M^2_{1/3})_2AX$. The in-plane

ordering breaks the hexagonal symmetry and *i*-MAX phases are found to crystallize in either the *C2/c* monoclinic or the *Cmcm* orthorhombic space groups.[6,21]

Since 2015, the boron containing analogues to MAX phases, MAB, have emerged with renewed attractiveness.[22] The Cr-Al-B and Mo-Al-B are the two systems that, chronologically speaking, firstly called the attention and will serve to illustrate the most common MAB structures.[22] The Cr-Al-B system offers the largest amount of structure-types: Cr_2AlB_2, Cr_3AlB_4 and Cr_4AlB_6. Fe_2AlB_2 also belongs to the early MAB-phases group and matches the structure of Cr_2AlB_2, but this case will be discussed in a separate section as it is the phase investigated in the present manuscript.

The variety of Cr-Al-B phases is in accordance with that of the binary Cr borides. They can all be grouped in the $(CrB_2)_nCrAl$ formula, their structure being depicted in **Figure V. 3a**, **b** and **c** for n = 1, 2 and 3, respectively. The compounds $(CrB_2)_nCrAl$ are ternary variants of the binary borides in relation to the motifs of the boron subunits. They exhibit the same structural units for n = 1 as to CrB (zigzag chains), for n = 2 as to Cr_3B_4 (double chain of hexagons) and for n = 3 as to Cr_2B_3 (double chain of hexagons). While the structure differs significantly to that of MAX phases, certain parallelisms can be drawn. In both cases, the M-B layers are sandwiched by A layers. Also, the metal atoms are the ones exposed to the A atoms, meaning that they will be the surface atoms in an eventual exfoliation. On the opposite, the B coordination environment differs from X in MAX phases, as it consists of trigonal BM_6 units, which share faces. Also, the B substructure is unique, as it is made of zigzag chains or hexagons of covalent B-B bonds, instead of the linear topology of the X sublattice in MAX phases. According to the

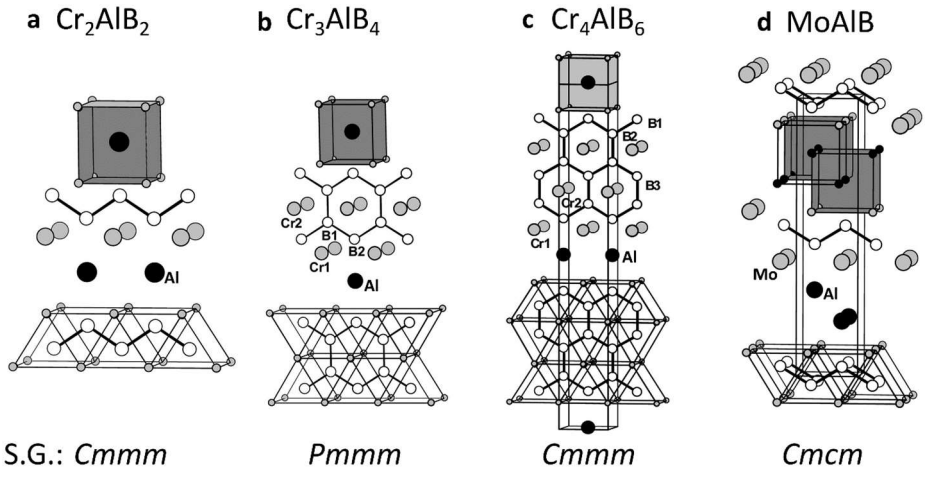

Figure V. 3. Most common MAB-phase structures: Cr_2AlB_2 **(a)**, Cr_3AlB_4 **(b)**, Cr_4AlB_6 **(c)** and MoAlB **(d)**. The image is adapted from reference [22].

catenation of the boron chains, there are two space group types. When *n* is an even number, the space group is *Pmmm* while an odd value of *n* leads to space group *Cmmm*. The Cr_2AlB_2 phase attracted considerably more attention as it is the key precursor to bidimensional CrB. Hence its synthesis has been scaled and optimized through various methods.[23,24]

For M = Mo, MoAlB is the most accessible MAB phase from a synthetic point of view, as this is achieved by reaction of the elements in an Al flux (Mo:Al:B = 1:53.3:1) at 1400 °C. Its structure is shown in **Figure V. 3d**.[25] The structure is analogous to the M_2AB_2 structure-type (**Figure V. 3a**), but with a double Al layer between the M_2B_2 layers. Considerable effort was made to conceive the Mo_2AlB_2 phase, as it contains a single interleaved Al sheet instead of a double one in MoAlB, which could facilitate exfoliation to 2D-MoB. Alameda and co-workers firstly evidenced that the basic or acidic treatment of MoAlB led to periodic etching of the Al layers every 50 – 300 nm. This in turn resulted in a series of local structures that could be identified, including $Mo_6Al_5B_6$, $Mo_4Al_3B_4$, $Mo_3Al_2B_3$ and the so-pursued Mo_2AlB_2.[25] In a latter report of the same group, the topochemical 2 MoAlB → Mo_2AlB_2 + Al transformation was successfully controlled.[26] The optimization of the MoAlB particle size and a subsequent thermal treatment at 600 °C followed by a rapid quenching were key in controlling the transformation, which albeit also yielded AlO_x impurities.[26]

Beyond the basic and original structures of MAB phases, a large and diverse set of compounds has been discovered. These include: Ru_2ZnB_2 (S.G.: *I4₁/amd*),[27] $Ru_3Al_2B_2$ (S.G.: *Cmmm*),[28] $Ru_4Al_3B_2$ (S.G.: *P4/mmm*),[28] Y_2SiB_8 (S.G.: *P4/mbm*),[29] Cr_5Si_3B (S.G.: *P6₃/mcm*),[30] Hf_5Si_3B (S.G.: *P6₃/mcm*),[30] $Ni_{n+1}ZnB_n$ (S.G.: *C2/m* for *n* = 1 and 2),[31] NiLiB (RT polymorph S.G.: *Cmc2₁,* HT polymorph S.G.: *P2₁/m*),[32] Ti_2InB_2 (S.G.: $P\bar{6}m2$),[33], WAlB (S.G.: *Cmcm*),[22] Mn_2AlB_2 (S.G.: *Cmmm*),[22] Mo_2FeB_2 (S.G.: *P4/mbm*).[34] Quaternary MAB phases have also been reported, in both in-plane –$(Mo_{2/3}Y_{1/3})_2AlB_2$ and $(Mo_{2/3}Sc_{1/3})_2AlB_2$ S.G.: $R\bar{3}m$–[35] and out of plane –Ti_4MoSiB_2 S.G.: *I4/mcm*–[36] ordered structures. The periodic table summarizing the elements that have been accommodated in a MAB-like structure is shown in **Figure V. 4**.

The significant structural difference between MAB and MAX phases is defined by the boron subnetwork which varies from dumbbells, to zigzag B_4 fragments, zigzag boron chains, chains of boron hexagons and chains of boron double hexagons.[22] In MAX phases however, no bond

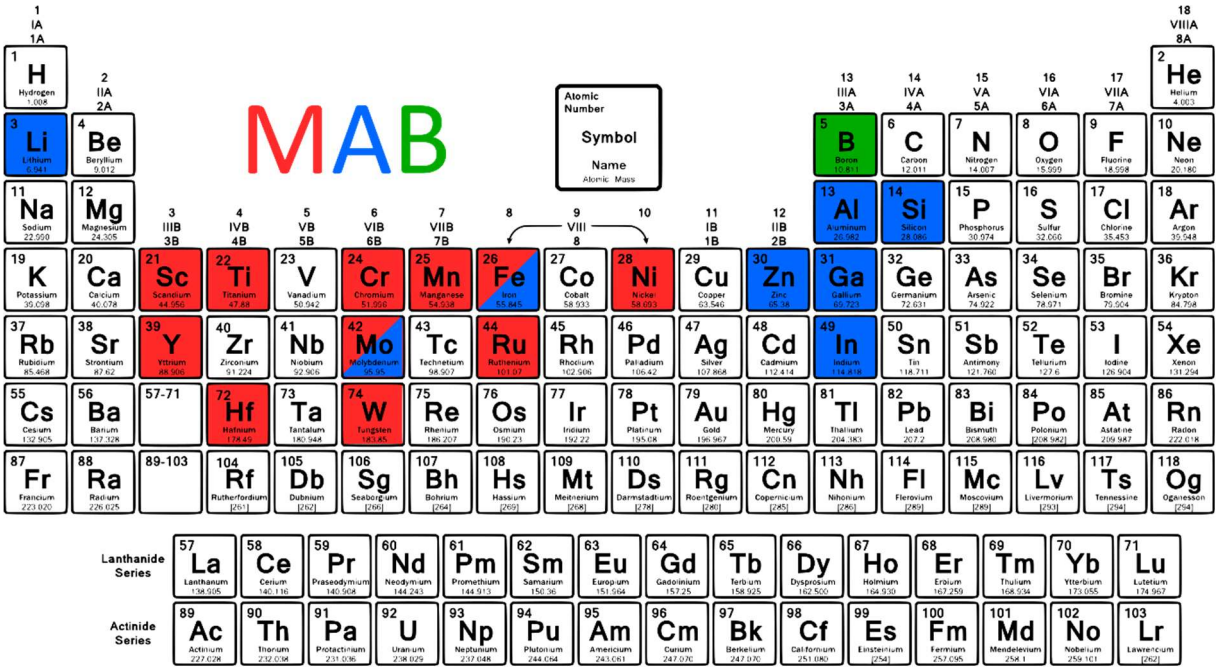

Figure V. 4. Constitutive elements of MAB phases in the periodic table.

exists between the X (C, N) atoms. In addition, significant bonding interactions exist between boron and the M atoms in MAB structures, while no significant interaction exist between X and M in MAX structures.[37] Fulfilling all these bonding constraints forces distinct atomic arrangement and hence do not allow for a common MAB structure. In such a diverse structural context, imposing a generalized rationale is unviable, and instead we will focus on those structure more relevant for the concerned MAB phase of this thesis: Fe_2AlB_2. Before focusing on this compound, it is instructive to discuss the efforts that have been put in the delamination of MAX phases.

Delamination of MAX phases

In 2011, M. Naguib reported the exfoliation of Ti_3AlC_2 leading to the 2D material $Ti_3C_2T_x$, with T being a surface termination group.[38] This discovery further increased the interest in MAX phases and opened the door to the so-called MXenes, one of the latest incorporations to the group of 2D materials, well known for their unusual electronic, mechanical and optical properties.[39] MXenes are produced by selective etching of the intercalating atoms “A” in controlled corrosive conditions as schematized in **Figure V. 5**, followed by exfoliation. The early reports of MAX to MXene transformations consisted in modifications of an HF-based washing. Etching conditions in HF have to be modified for each specific composition, as bond strengths vary for the different M elements. Besides Ti_3AlC_2, numerous MAX phases were

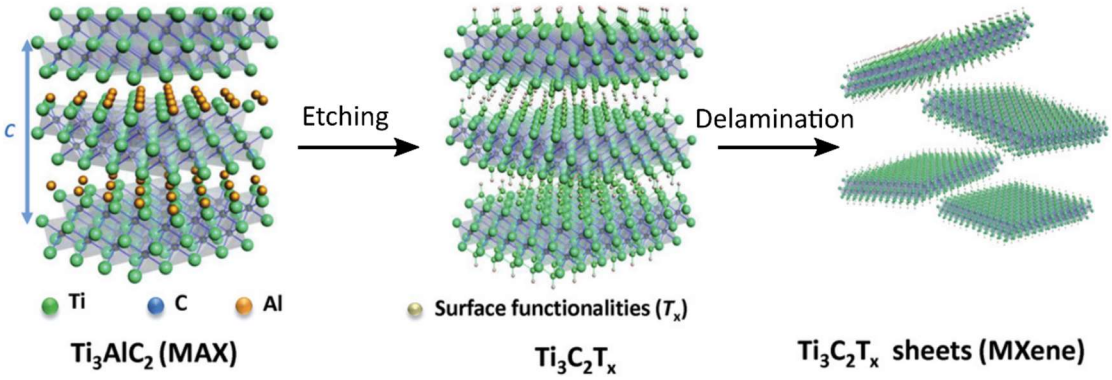

Figure V. 5. Etching and delamination process scheme for the Ti_3AlC_2 MAX phase. The image is adapted from reference [159].

delaminated this way: Ti_2AlC, V_2AlC, Nb_2AlC, Nb_4AlC_3, Ta_4AlC_3, $Ti_3Al(C_{0.5}N_{0.5})_2$, $(Ti_{0.5}Nb_{0.5})_2AlC$, $(V_{0.5}Cr_{0.5})_3AlC_2$, $(Ti_{0.5}V_{0.5})_2AlC$, $(Ti_{0.5}V_{0.5})_3AlC_2$, $(Nb_{0.5}V_{0.5})_4AlC_3$, etc.[40–42]

As the synthesis is carried out in an aqueous solution of HF, the resulting MXene contains mostly O, OH and F atoms as surface terminations (T).[43,44] The resulting morphology typically consists of multilayers held together by hydrogen bonds and Van der Waals interactions.[45] These bonds are weak enough to permit the intercalation of solvent molecules between the layers to further separate each individual sheet. Considering the negative surface charge of the T groups, intercalating large cations has been a successful technique to achieve separation. Tetrabutylammonium hydroxide (TBAOH), choline hydroxide and *n*-butylamine are among the most widely spread MXenes intercalators.[46]

The use of HF is a dangerous procedure requiring strict security protocols. When in 2014 it was discovered that the delamination could be achieved by combining LiF and HCl that would form *in situ* HF in diluted quantities, this came as a major boost to the field.[47] This implied that now laboratories prescinding the facilities needed for HF handling could also embark in MXenes research. Ammonium bifluoride (NH_4HF_2) was also used as an etchant for Al from Ti_3AlC_2 in both water[35] and, much more recently, in polar organic solvents.[36] Molten fluoride salts have also demonstrated fruitful to etch Al this time from Ti_4AlN_3.[48]

Fluoride could be avoided for the first time by electrochemical etching of Ti_2AlC in HCl, although this rendered only partial etching.[49] So did the hydrothermal treatment of Ti_3AlC_2 in 27.5 M NaOH at 270 °C.[50] Electrochemical etching was taken to completion in an aqueous electrolyte of 1.0 M ammonium chloride and 0.2 M tetramethylammonium.[51] Also iodine

dissolved in anhydrous acetonitrile at 100 °C proved an effective etchant to yield $Ti_3C_2I_2$ from Ti_3AlC_2.[52]

In 2019, M. Li and collaborators published the delamination of the MAX phase Ti_3AlC_2 by using molten $ZnCl_2$, which performed a selective redox reaction with the intercalating Al atoms according to **Equation V. I**.[17] This approach was generalized in 2020 by Y. Li *et al*, who performed an analogous procedure in Ti_3SiC_2 using molten $CuCl_2$ (**Equation V. II**) and offered guidelines on the choice of the molten redox couple with respect to the intercalating atom in terms of their redox potentials against their metallic state or molten chloride counterpart respectively.[53] These are summarized in the **Figure V. 6** as reproduced form the original report.

$$Ti_3AlC_2(s) + 1.5\ ZnCl_2(l) \rightarrow Ti_3C_2(s) + 1.5\ Zn(s) + AlCl_3(g)\uparrow \qquad \textbf{Equation V. I}$$

$$Ti_3SiC_2(s) + 2\ CuCl_2(l) \rightarrow Ti_3C_2(s) + 2\ Cu(s) + SiCl_4(g)\uparrow \qquad \textbf{Equation V. II}$$

The latest efforts are concentrated in tuning the MAX phase composition to alter the exfoliation easiness. For example, adding a small amount of Sc to the precursors of V_2AlC results in formation of a solid solution of V-Sc that reduces significantly the etching time needed to make $V_{2-y}CT_x$ ($y < 0.05$) as traces of Sc change the stability of the MAX phase.[54] Having a solid solution at the A sites in the MAX phase, like in the case of $Ti_3(Si_{0.75}Al_{0.25})C_2$ and $Ti_3(Si_{0.1}Al_{0.9})C_2$, weakens the bonding between the carbide sheets through the A layers and therefore allows for exfoliating these materials with the aid of ultrasonication, which is not

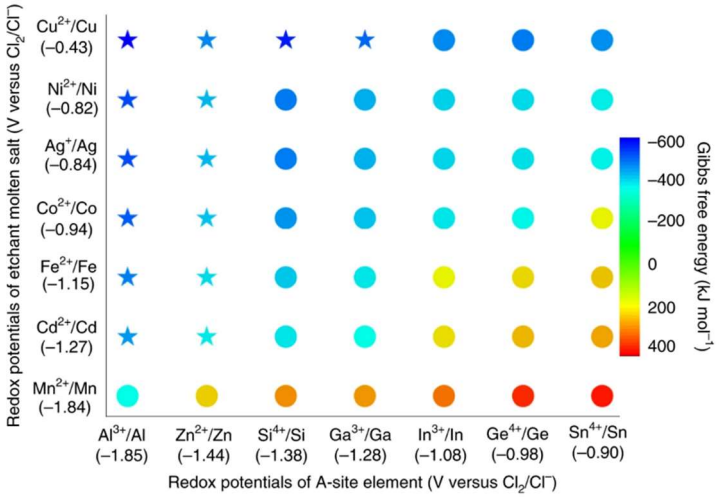

Figure V. 6. Calculated redox potentials of the molten salt etchant and A site element in MAX phases. The Gibbs free energy of each possible reaction is also shown in colour codes. The image is adapted from refence [53]. (Stars mark the corresponding MXenes demonstrated in [53])

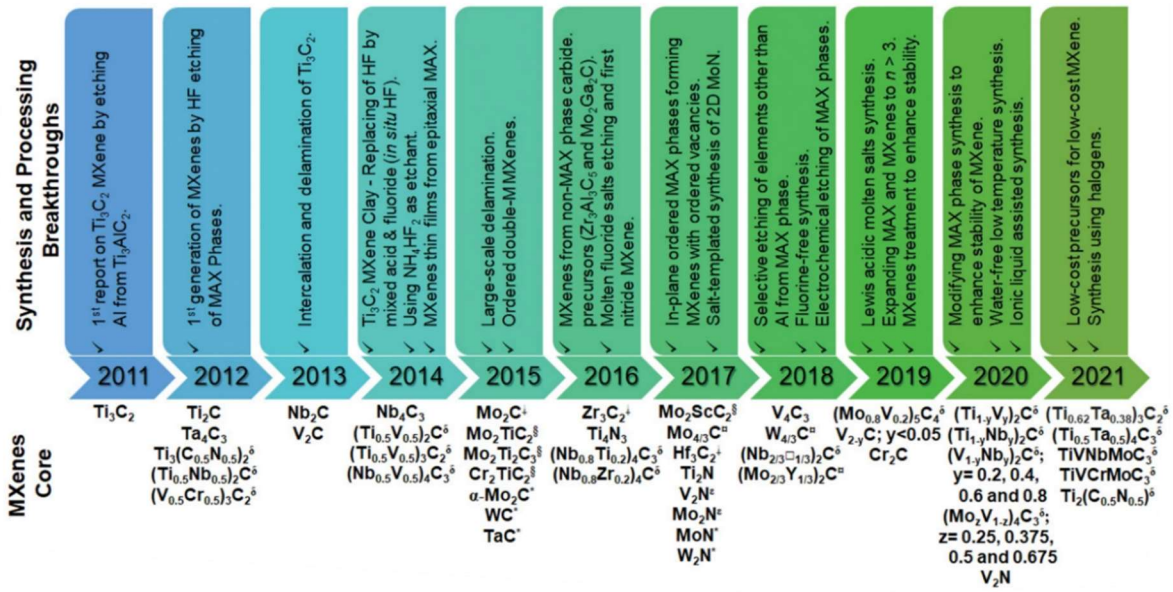

Figure V. 7. List of the main synthesis and processing breakthroughs over the first 10 years of MXenes' research. The image is adapted from reference [56].

possible for either Ti_3SiC_2 nor Ti_3AlC_2.[55] The milestones in the MAX phases delamination are summarized in **Figure V. 7**, as extracted from a recent review by M. Naguib *et al*.[56]

Delamination of MAB phases

The relative feasibility of the exfoliation of MAX phases contrasts with the difficulty of the process in MAB phases. This difference originates from the difference between M-X and M-bond energies. It has been theoretically calculated and experimentally evidenced that M-X or M-B bonds are more energetic than M-A ones, which is the whole reason why the A atom can be etched in the first place.[22,57–59] However, the precise difference between these quantities seems to drive the easiness of exfoliation, as discussed by Z. Guo[58] and M. Khazaei[59]. Z. Guo showed in the reproduced **Figure V. 8a**, a direct comparison between M_2AlB_2 (M = Cr, Mo, W or Fe) and M_2AlC (M = V or Nb), these last two MAX phases being successful cases of 2D delamination.[60] Here it is evident that for carbides, not only is the M-X bond is stronger but also the M-Al bond is less energetic, both supporting an easier exfoliation for carbides than for borides.[58] On the other hand, Khazaei and collaborators rather focused on the internal comparison between MAB phases of the most common M_2AlB_2 family.[59] In their work, they calculated the sum of all the force constants (FC) acting on every atom and from the analysis of the evolution with the atomic number (**Figure V. 8b**). There is a maximum of the $[(FC_M+FC_B) - FC_{Al}]$ energy difference for Cr, which later decays in the Cr → Ni direction.[59]

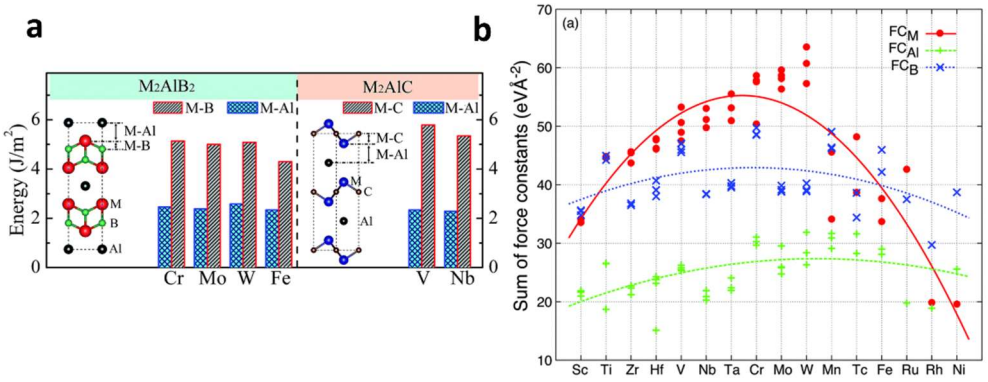

Figure V. 8. **(a)** Bonding energy comparison between MAB and similar MAX phases. The image is reproduced from reference [58]. **(b)** Force constants (FC) for M, Al and B in a series of 3d metals for M_2AlB_2 phases. The image is reproduced from reference [59].

Such calculations remarkably correspond with experimental observations, given that Cr_2AlB_2 has been fully exfoliated as previously mentioned under mild conditions.[23,61] Mo_2AlB_2 has only been partially delaminated (exfoliation over a length scale of 10 nm) to MoB.[62] Lastly, Fe_2AlB_2 has not been delaminated at all so far. In **Table V. 1**, all the reported attempts of delamination for MAB phases are summarized, including the etching conditions and resulting morphologies.

The Cr_2AlB_2 phase was the first MAB-phase from which all Al atoms could be completely removed. The first hints of delamination came in 2018, where Zhang *et al.* soaked Cr_2AlB_2 in 1.25 M HCl and observed the appearance of new Bragg peaks that were ascribed to Cr_2B_2 with different -OH termination groups arrangements as calculated by DFT.[63] The group later achieved full delamination with a more diluted and longer treatment, although the layers are completely re-stacked so the bidimensional structure is not accessible.[23]

Aqueous treatment also leads only to partial delamination in the $Ni_{n+1}ZnB_n$ system. The lack of satisfactory results by this method is what lead to explore unconventional strategy. The Ti_2InB_2 phase for instance was satisfactorily delaminated by sublimation of indium at 1050 °C under high vacuum (10^{-9} bar).[33] This is associated to the low melting point of In (157 °C) and its high vapor pressure, and then cannot be extrapolated for compounds where A = Al, Si, etc. Still, the layers did restack in this case and a secondary phase of TiB_2 appeared. [33] The only attempt to employ the molten salts strategy, successful in MAX-phases, was made for Ti_4MoSiB_2. It enabled oxidation and deintercalation of the Si atoms, but it also completely oxidized the Ti-B framework to TiO_xCl_y, which turned out to form a bidimensional structure, but not comprising a boride anymore.[36] Full delamination and isolation of a single metal boride layer was

Table V. 1. Delamination attempts, conditions and results for MAB phases.

MAB phase	Delamination conditions	Results	Ref.
Cr_2AlB_2	1.25 M HCl, RT, 6 h	Partial delamination and re-stacking	[63]
Cr_2AlB_2	0.5 M HCl, RT, 7 days	Complete delamination and re-stacking	[23]
MoAlB	10 % NaOH, RT, 24 h	Partial, periodic etching every 50 – 300 m	[62]
MoAlB	2 M LiF in 6 M HCl, RT, 24 h	Partial, periodic etching every 50 – 300 m, considerable corrosion	[25]
MoAlB	Direct during magnetron sputtering synthesis	Localized delamination surrounded by AlO_x matrix.	[64]
Ni_2ZnB	1.0 M HCl, RT, 72 h	Superficial pores formation and layer openings	[31]
Ni_3ZnB_2	1.0 M HCl, RT, 72 h	Superficial pores formation and layer openings	[31]
RT-NiLiB	Air exposure	Partial delamination and re-stacking to RT-$Li_{0.6}NiB$	[65]
HT-NiLiB	Air exposure	Partial delamination and re-stacking to HT-$Li_{0.4}NiB$	[65]
Ti_2InB_2	Thermal treatment at 1050 °C for 6 days under vacuum ($1 \cdot 10^{-9}$ bar)	Exfoliation to 2D-TiB with re-stacking and bulk TiB_2 as impurities	[33]
Ti_4MoSiB_2	Molten $ZnCl_2$, 600 °C, 8h + 0.5 M HCl washing + TBAOH delamination	Formation of bidimensional TiO_xCl_y	[36]
$(Mo_{2/3}Y_{1/3})_2AlB_2$	40 % HF, 35 °C, 3.5 h + 20 % *wt*. TBAOH delamination	Single-layer $Mo_{4/3}B_{2-x}$	[35]
$(Mo_{2/3}Sc_{1/3})_2AlB_2$	40 % HF, 35 °C, 3.5 h + 20 % *wt*. TBAOH delamination	Single-layer $Mo_{4/3}B_{2-x}$	[35]

achieved for the $(Mo_{2/3}Y_{1/3})_2AlB_2$ and $(Mo_{2/3}Sc_{1/3})_2AlB_2$ phases.[35] In this case, the acidic treatment dissolved not only the intercalating Al but also the doping rare earth elements, whose in-plane ordering was retained for the vacancies subsequently formed. The delaminated layers were isolated by tetrabutylammonium hydroxide (TBAOH) intercalation, which separated the layers thanks to the big size of the TBA ions.

V.2 The case of Fe_2AlB_2

This work will be focused on the less explored (regarding its possible transition to a MB phase) Fe_2AlB_2 system, so it is worth expanding on its specific literature. The structure of Fe_2AlB_2 was solved in the early work by W. Jetschko[66] and separately by Y. Kuzma[67], with samples prepared by induction melting of elemental reagents. Little attention was paid to such structure until the raising enthusiasm for MAX phases and MXenes. The crystal structure of the compound was re-solved from scratch by M. Ade and H. Hillebrecht from single crystals synthesized by Al flux reaction of the elements.[22] All three authors agree that the phase crystallizes in the space group *Cmmm*, with a = 2.9217(4) Å, b = 10.991(15) Å and c = 2.8563(5) Å. The atomic arrangement is completely isostructural to Cr_2AlB_2, whose structure was already discussed in **Section V. 1**. Fe_2AlB_2 exhibits a paramagnetic-to-ferromagnetic transition at T_C = 280 – 320K.[68] Its magnetic structure was characterized in 2016 by J. Cedervall *et al.*, who concluded that a ferromagnetic alignment in the *a* axis with the Shubnikov group *Cmm'm'* explains the observed magnetic behavior.[69] The closeness of T_C to room temperature endows Fe_2AlB_2 with a magnetic entropy change as high as 4.4 $J \cdot kg^{-1} \cdot K^{-1}$ (at applied field of 2 T), relevant for magnetic cooling from a material entirely made of Earth-abundant elements.[68]

Cedervall[69–71] as well as several other authors[57,68,72–81] followed the arc melting sample preparation procedure (or slight variations) suggested by M. El Massalami to synthesize Fe_2AlB_2.[82] As described by El Massalami, an excess of Al is needed in order to prevent the formation of FeB, even though this leads to $Al_{13}Fe_4$ impurities formation, which still are easily removable by acidic washing.[82] Other reactive sintering procedures have been suggested such as furnace heating and spark plasma,[73] Ga flux as reactive media was proposed by Tan in 2013,[68] and more recently its synthesis has been achieved in molten salts.[83] In general, elemental sources of Fe, Al and B were used to yield Fe_2AlB_2 in the reported synthesis. Despite this broad pallet of synthetic methods, a major hurdle in the investigation of Fe_2AlB_2 remains

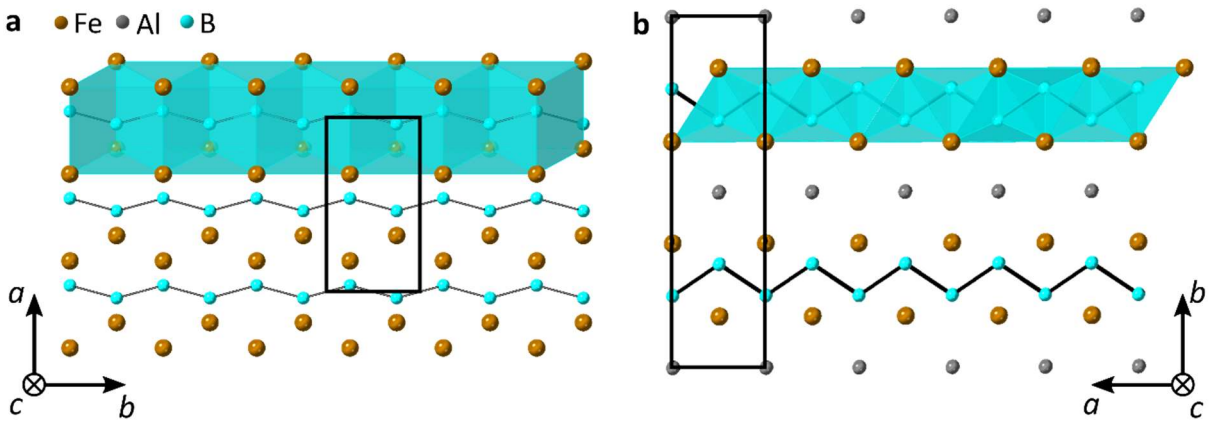

Figure V. 9. Structures of β-FeB **(a)** and Fe_2AlB_2 **(b)**.

its high synthesis temperature (> 1000 °C), long reaction times (> 24 h), but still with poor reproducibility. Liu and collaborators performed a comparative study between the Fe + Al + B and the β-FeB + Al reactions towards Fe_2AlB_2.[84] The conclusion of the study is that the latter leads to higher purity and reproducibility of the reaction. This is understandable considering the structural similarities between the β-FeB and Fe_2AlB_2. β-FeB already accommodates Fe and B in a single compound and thus requires only Al insertion in a single step. B atoms in β-FeB already form the B zig-zag chains characteristic of Fe_2AlB_2 and their coordination environment coincides in both structures, as shown in **Figure V. 9**.

The associated 2D MBene of Fe_2AlB_2 (Fe_2B_2 hereafter) has been proposed as Li battery electrode material and hydrogen evolution catalyst. DFT calculations reveal a negative adsorption energy of -1.12 eV for Li, preferentially in the B site (**Figure V. 10a**), indicative of a strong interaction between the species. Yet, the energy barrier to transport Li remains small (0.24 – 0.27 eV) in perpendicular directions towards the next B neighbors (Path I and II in **Figure V. 10a** and **Figure V. 10b**), hence offering an omnidirectional platform for Li^+ transport.[58] The theoretical specific capacity also outperforms that of common MXenes and of calculated MBenes: Fe_2B_2 (665 $mA{\cdot}h{\cdot}g^{-1}$),[58] Mo_2B_2 (444 $mA{\cdot}h{\cdot}g^{-1}$),[58] Ti_3C_2 (320 $mA{\cdot}h{\cdot}g^{-1}$),[85] Ca_2N (320 $mA{\cdot}h{\cdot}g^{-1}$).[86] The potential of Fe_2B_2 as a catalyst for hydrogen evolution (HER) has also been assessed from a theoretical point of view. The most spread descriptor in this case is the Gibbs free energy of the intermediate ($|\Delta G_{H^*}|$) H* species (adsorbed H atom) in the HER mechanism: H^+ (aq) + e^- → H* → 0.5H_2 (g).[87,88] Basically, if ΔG_{H^*} is too positive, H will not get adsorbed, if it is too negative it will not react towards H_2, so the closer $|\Delta G_{H^*}|$ is to 0, the better the performance of the material. The benchmark Pt shows a value of -0.09 eV.[89] Fe_2B_2 in a ¼ and 1/8 H* coverage, renders energies lower than 0.02 in

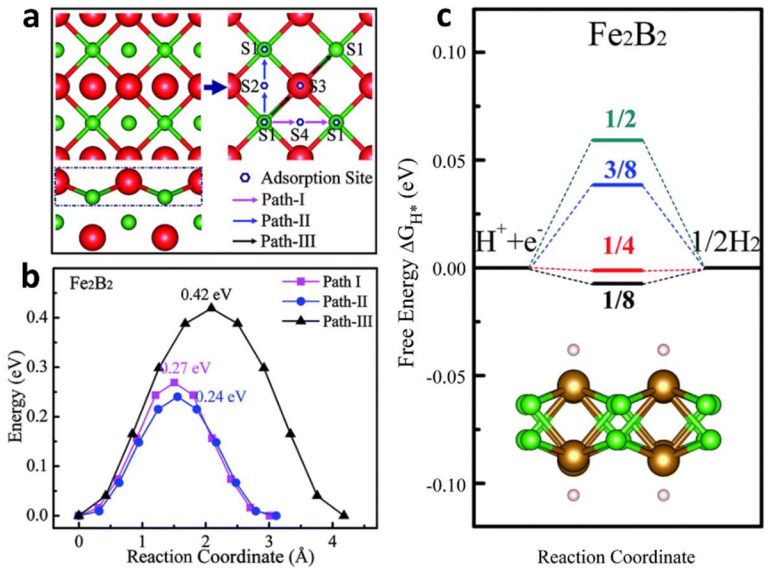

Figure V. 10. **(a)** Considered adsorption sites and diffusion pathways for Li atoms on MBenes, where the red, and green balls represent M and B atoms, respectively. **(b)** The diffusion energy curves for Li atoms on Fe_2B_2. **(c)** The calculated free–energy diagram of the HER at the equilibrium potential on the surface of Fe_2B_2 under different hydrogen coverage (1/8, 1/4, 3/8 and 1/2) conditions. The insets are the atomic structures of Fe_2B_2 at 1/2 hydrogen coverage. The image is adapted from reference [58].

absolute values, as depicted in **Figure V. 10c**, hence theoretically outperforming Pt.[58] Despite the enormous interest behind the delamination of Fe_2AlB_2, this is still to be achieved.

The case of Fe_2AlB_2 delamination was specifically studied against that of $(Mo_{2/3}Y_{1/3})_2AlB_2$ by the group of J. Rosen.[35] In this report, the chemical bonding was quantitatively analyzed on the basis of a Crystal Orbital Hamilton Population analysis to evaluate the partial contribution of each bonds to the cohesion of the solid. In general, B-B bonds are the strongest, followed by in-plane Al-Al and then out-of-plane M-B bonds. However, when the amount of each bond per atom is considered, the dominating force is actually the M-B bonding. For $(Mo_{2/3}Y_{1/3})_2AlB_2$, the Mo-B interaction is 2.7 times as strong as that of M-Al, while this ratio decreases to 2.1 in the Fe_2AlB_2 case (**Figure V. 11**). Moreover, if the Al-B bond is also considered (which is often neglected in theoretical studies as in that of Guo[58]), the bonding difference becomes very narrow, as depicted in the right-hand bars in **Figure V. 11**. This fact suggests that if exfoliation is to be achieved in Fe_2AlB_2, a very subtle compromise should be sought after in order to trigger the cleavage of the Fe-A bond uniquely.

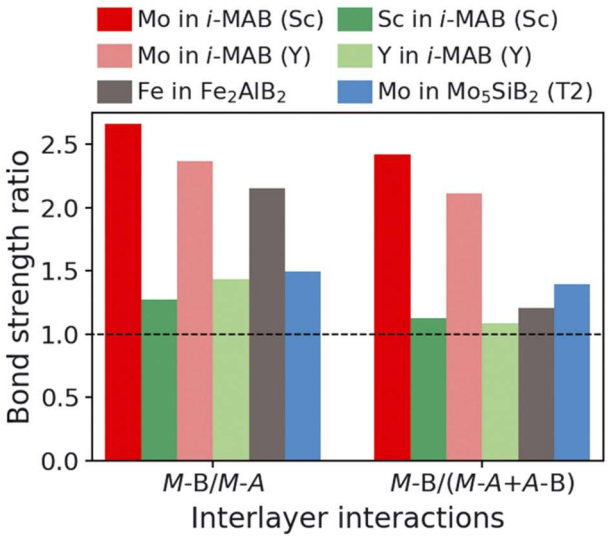

Figure V. 11. Bonding strength ratios for various interactions in $(Mo_{2/3}Y_{1/3})_2AlB_2$, $(Mo_{2/3}Y_{1/3})_2AlB_2$, Fe_2AlB_2, and Mo_5SiB_2. The image is reproduced from reference [35].

V.3 Summary and strategy

The synthesis and exfoliation of MAX phases has been largely developed for over 20 and 10 years now, respectively. MAB phases have emerged recently as interesting analogues. Their processing is evidently more challenging than in the case of MAX phases. This is due to the lower contrast of bonding energy between the in-plane metal boride bonds and the out-of-plane metal-metal and boron-metal interaction. This fact determines the difficulty of selectively etching the intercalating A atoms without destroying the remaining framework. The expected physical properties of 2D-metal borides largely justify the efforts to achieve chemical exfoliation of MAB faces despite these challenges. The particular case of Fe_2B_2 has been predicted to possess a high Li^+ storage capacity with an omnidirectional platform for its transportation. Also, it has been predicted to have a close to null adsorption energy for the HER intermediate H*, thus a high potential for HER electrocatalysis. To achieve this material, a very soft delamination of Fe_2AlB_2 must be performed. During the course of this part of the manuscript, we will expose our approaches towards this goal. As a first objective, the synthesis of Fe_2AlB_2 must be performed. To do so, we adopted a templating reaction scheme. We will show how Al insertion in the FeB structure leads to Fe_2AlB_2. As in the previous part, we will begin by exposing the synthesis and in-depth characterization of the template prior to its transformation. Once achieved a pure phase Fe_2AlB_2 compound, we will show our attempts towards delamination by molten salts selective oxidation and by direct sublimation.

Chapter VI: FeB synthesis, polymorphism and properties

VI.1 Introduction

In an analogous approach to the transformation from NaB_5C to B_4C, we have designed the synthesis of the ternary compound Fe_2AlB_2 as a reaction from the binary iron monoboride as a starting material according to **Equation VI. I**.

$$2\ FeB\ (s) + Al\ (s) \rightarrow Fe_2AlB_2\ (s) \qquad \textbf{Equation VI. I}$$

Iron borides themselves have been extensively investigated for their structural[90,91] and functional[92–94] properties. When manufactured at the nanoscale, iron borides exhibit distinct properties: FeB_2 nanoparticles are bifunctional electrocatalysts for overall water splitting, surpassing the Pt/RuO_2 benchmark.[95] Similarly, low-temperature wet chemical procedures have been used to produce FeB nanoparticles, which are harder magnets than their bulk analogues.[96,97] For FeB, an extra hurdle arises in the rationalization of structure-properties relationships as it exhibits *a priori* two polymorphs α- and β-FeB, at low and high temperatures, respectively. In the conditions of nano-objects synthesis, at low temperature, FeB crystallizes exclusively in the so-called α-FeB form,[94,96–100] a structural modification that is not currently understood.[96] Bulk α-FeB has not been evidenced, nor has nanosized β-FeB.[94,96–100] Hence, α-FeB is strongly related the nanoscale, but its structure remains unknown. In the present chapter, we will show the synthesis of bulk and nanosized FeB in the β- and α- modification respectively. We will focus on the elucidation and rationalization of both structures and their impact in catalytic properties for electrolytic water splitting. We will also discuss how to the optimize purity and morphology, in order to use the compound for the Fe_2AlB_2 synthesis in the next chapter.

VI.2 Materials and methods

All reagents were stored and handed under an argon flow glove box. $NaBH_4$ (98 % min., Alfa Aesar), and $FeCl_2$ (99.5%, Alfa Aesar) were used as element sources. NaH (90 %, Aldrich) was used as reducing agent. All reagents were used as received without further purification. A eutectic mixture of LiCl(99.9% Alfa Aesar)/KCl (99.9% Sigma Aldrich) was used as a solvent.

Deionized H_2O or Methanol (VWR Normapur grade) were used for the washing steps as it will be indicated in each case.

To synthesize FeB, 850 mg (6.71 mmol) of $FeCl_2$ and 254 mg (6.71 mmol) of $NaBH_4$ were mixed with 5.1 g of the eutectic LiCl/KCl mixture. All solids were finely ground together at 20 Hz for 2 min in a Retsch MM400 ball miller (airtight vials of 50 mL, one steel ball of 62.3 g and a diameter of 23 mm). The solid mixture was later placed in a Mo crucible (Ø15 mm × H200 mm), which was placed into a sealed quartz tube. The quartz tube was connected to a Schlenk line under Ar flow and placed inside a vertical oven. A heating ramp of 10 °C·min^{-1} was used up to 600 °C for α-FeB and 1100 °C for β-FeB, followed by a dwell time of 3 h. After dwelling, the sample was let to cool down naturally and subsequently washed by sequences of redispersion, sonication (1 min) and magnetic separation of the solid, until the conductivity of the supernatant dropped below 50 µS·cm^{-1}. Methanol-washed samples required preliminary grinding of the solidified mixture in order to extract the product due to the low solubility of the salt in the solvent. The powders were dried under vacuum at room temperature until the pressure dropped below $1.0 \cdot 10^{-3}$ mbar and were then heated to 150 °C with an oil bath (still under vacuum) overnight.

General characterizations are described in the **Appendix AI**.

VI.3 Results and discussion

Synthesis of FeB: α- and β-modifications

FeB was synthesized by adapting a previously reported synthesis in molten salts:[101,102] iron chloride acts as metal precursor and $NaBH_4$ as both reducing agent and boron source, according to **Equation VI. 2**. The eutectic LiCl/KCl mixture was chosen as a cheap, sustainable, water soluble and low-melting point solvent (347 °C) to trigger reactions in the liquid state. The powders were mixed at room temperature and heated under argon flow. After cooling, the powders were washed with methanol (MeOH). X-ray diffraction patterns (**Figure VI. 1**) indicated that α- and β-FeB are obtained for syntheses at 600 and 1100 °C, respectively. Especially, we recognized the XRD pattern of α-FeB from the typical absences of the $(101)_\beta$, $(201)_\beta$, $(111)_\beta$, $(211)_\beta$ and $(301)_\beta$ reflections (shown in red indexes) with respect to the β-FeB pattern, as well as the broad diffuse scattering bump at 2θ (CuK_α) ≈ 41°.[96] No crystalline oxidized species could be detected by XRD (**Figure VI. 1a**) in the corresponding products,

which contain mostly α/β-FeB as crystalline phases. No amorphous oxides were observed by TEM either (**Figure VI. 1b-c**). The characteristic parallel stripes of α-FeB are recognized, as shown in **Figure VI. 2**. Note however that β-FeB contains traces of Fe_2B impurities, probably coming from a slightly uncomplete reaction with boron species.

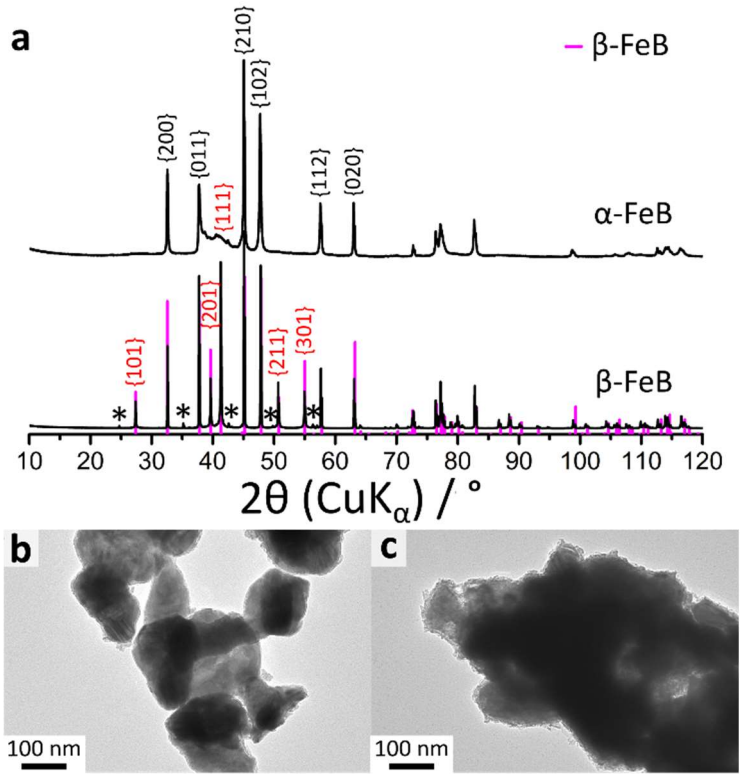

Figure VI. 1. α-FeB and β-FeB products synthesized from molten salts washed with methanol. **(a)** Powder XRD diffractograms showing the indexation of β-FeB peaks, and the characteristic reflection absences in α-FeB indexed in red. Fe_2B impurity traces are marked with *. **(b, c)** TEM images of α- and β-FeB, respectively, washed with MeOH.

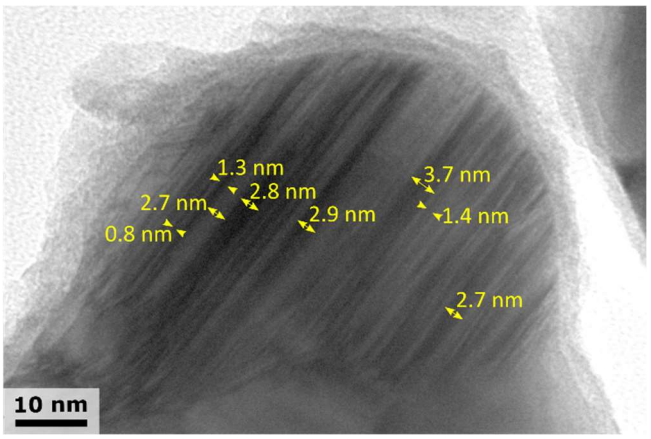

Figure VI. 1. TEM micrograph of a α-FeB nanoparticle that highlights streaks with varying contrasts and an average thickness of ~ 2 nm. These features are characteristic of the α-FeB structure.[97]

$$FeCl_2(s) + NaBH_4(s) \rightarrow FeB(s) + 1.5\ H_2(g) + NaCl(s) + HCl(g) \qquad \textbf{Equation VI. 2}$$

β-FeB crystallizes in the orthorhombic *Pnma* space group (*No*. 62), with lattice parameters a = 5.495 Å, b = 2.941 Å, c = 4.048 Å, as depicted in **Figure VI. 3**.[103] Its most prominent structural features are the BFe_6 trigonal prismatic units (**Figure VI. 3a** inset), which share faces with each other. These units form boron chains in trans configuration, as commonly observed for many other B-rich compounds.[104,105] The ensemble of the B-chains and its coordinated Fe atoms (named trigonal chains hereafter) extend along the [010] direction (**Figure VI. 3a**). The trigonal chains are packed along the [100] direction by sharing edges (**Figure VI. 3b**). All units are tilted by alternating angles of ± 21.2 ° *versus* the *a* axis (**Figure VI. 3b**) in order to fill

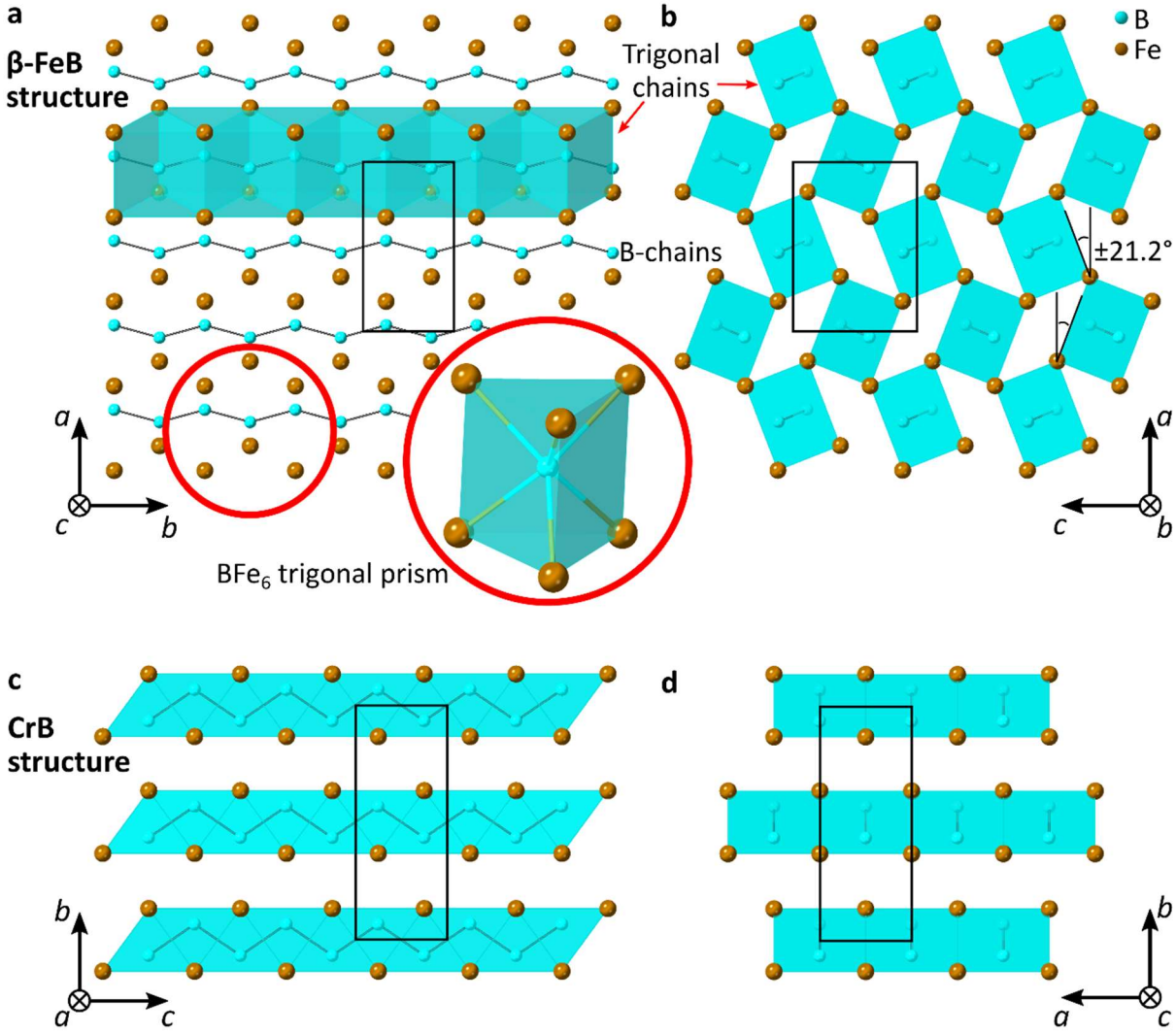

Figure VI. 3. **(a)** Structure of β-FeB projected along the *ab* plane, main structural features are highlighted: BFe_6 trigonal prisms, B-chains and trigonal chains. **(b)** Structure of β-FeB projected along the *ac* plane showing the edge-sharing piling of the trigonal chain. **(c)** Structure of α-FeB in the CrB-type structure, suggested by Barinov *et al*, projected along the *bc* plane. **(d)** Structure of α-FeB in the CrB-type structure projected along the *ab* plane.

the otherwise empty voids, and thus decrease the overall energy of the system, as observed in distorted perovskites for instance.[106] The structure of α-FeB is believed to be related to β-FeB due to the similarities of the powder patterns, but no conclusive evidence has been provided on the actual crystal structure. Therefore, we decided to analyze the different structural hypotheses proposed in the literature.

Structure analysis of α-FeB

Hypothesis (i): Fe/B exchange

Fruchart proposed partial substitutions of Fe and B, resulting in mixed occupations of the Fe and B positions.[107] This hypothesis has been considered physically unreliable as the Fe-Fe distance would drop below that of elemental iron (2.15 Å against 2.84 Å respectively) and boron covalent chains would be broken.[96,99,108] Such extreme structural rearrangements should be reflected in the Curie temperature, yet this remains unchanged.[108] Still, we have tested the model to assess its impact on the diffraction pattern. Symmetric Fe/B substitutions were modelled every 10 % exchange (**Figure VI. 4a**). None of the structural models enabled reproducing the experimental diffractogram. Moreover, Rietveld refinement was also performed by also allowing asymmetric substitutions and the presence of vacancies. The best adjustment achieved (**Figure VI. 4b** and **Table AII. 19**) could not reach satisfactory agreement with the experimental pattern. All in all, we could discard the hypothesis of Fe/B substitution.

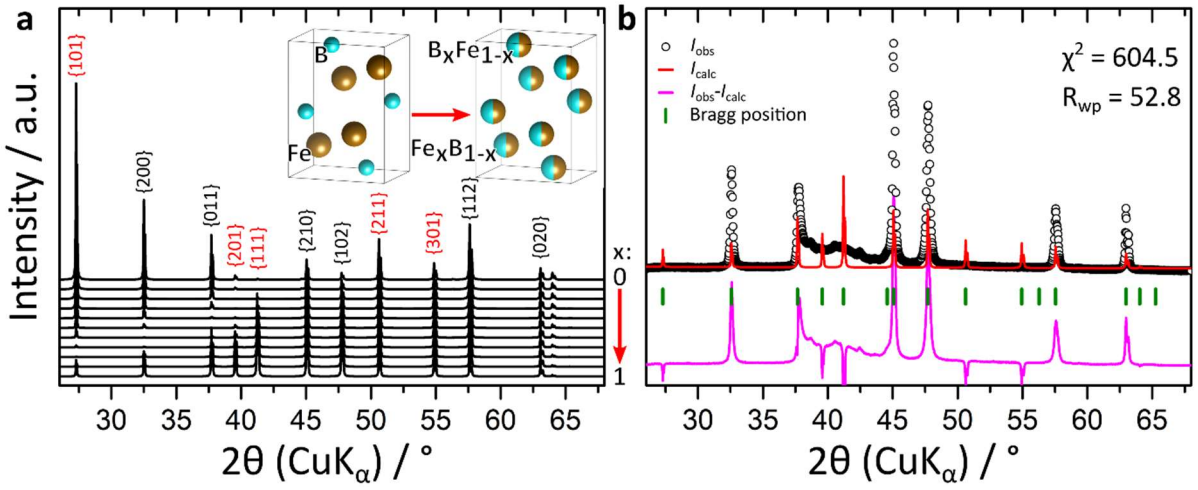

Figure VI. 4. **(a)** Simulations of powder X-ray diffractograms at various Fe/B substitutions x (B_xFe_{1-x} and Fe_xB_{1-x} respectively) in β-FeB. Inset: structural model used in the simulations. **(b)** Rietveld refinement of the experimental α-FeB diffractogram by using the β-FeB structural model with refinable B and Fe site occupancies.

Hypothesis (ii): Crystallization in the CrB-type structure (S.G. *Cmcm*)

Barinov *et al.* proposed that the higher symmetry space group *Cmcm* was responsible for imposing systematic absences in α-FeB compared to the ideal β-FeB structure (S.G. *Pnma*).[109] The *Cmcm* and the *Pnma* space groups are linked by a group-subgroup relation, for which the axis in *Cmcm* relate to those of *Pnma* as: $a_{Cmcm} = b_{Pnma}$, $b_{Cmcm} = c_{Pnma}$ and $c_{Cmcm} = a_{Pnma}$. This allows to compare the lattice parameters, which remain almost unaltered for b_{Pnma} (2.9408 Å *vs*. 2.954 Å in a_{Cmcm}), while c_{Pnma} expands from 4.0477 Å to 7.564 Å in b_{Cmcm}, as in the latter it corresponds to the stacking direction of the trigonal layers. This expansion is compensated by the contraction of the a_{Pnma} by approximately the same amount, which in turn yields similar cell volumes: V_{Pnma} = 65.414 Å *vs*. V_{Cmcm} = 65.982 Å. This increase in symmetry would yield the CrB-type structure, shown in **Figure VI. 5c-d**.[109] This model is indeed close to β-FeB structure and made of the same building units: BFe_6 trigonal prismatic units. In the CrB-type structure, the trigonal chains extend along the $[001]_{CrB}$ direction and exhibit a face-sharing planar packing in the $[100]_{CrB}$ direction, thus forming bidimensional layers that are then piled along the $[010]_{CrB}$ direction.

For their analysis, Barinov *et al.* relied on a highly strained sample, as suggested by the large width of the diffraction peaks.[109] Our synthesis procedure yields samples with higher crystallinity, which provides thinner diffraction peaks and then better resolved experimental data to test the hypothesis. Rietveld refinement using the cell previously proposed as starting model (a = 2.954 Å, b = 7.564 Å, c = 2.953 Å) does not yield a satisfactory fit, neither did manual increasing nor decreasing of the lattice parameters. The best fit, yielding lattice parameters a = 2.9460(4) Å, b = 7.6100(3) Å, c = 2.9491(2) Å, is shown in **Figure VI. 5a** and **Table AII. 19**.

By extending the proposition of Barinov *et al.*, we raised the question whether another space group could explain the reflection absences. For this reason, we have attempted to determine the unit cell and space group of α-FeB *ab initio*. We employed the EXPO2014 software for these purposes, which is highly performant in overall structure determination and refinement process from powder data.[110] The most plausible model found was an orthorhombic cell of space group *Pnca* (*No*. 60), with cell parameters: a = 5.498 Å, b = 2.951 Å, c = 4.062 Å. This model is very close to the β-FeB structure (S.G. *Pnma*, a = 5.495 Å, b = 2.941 Å, c = 4.048 Å), with the main difference being a *c* glide plane substituting the *m* mirror perpendicular to the *b* axis. The glide plane imposes the extra systematic absence of *h0l*: $l = 2n$, which in turn forbids

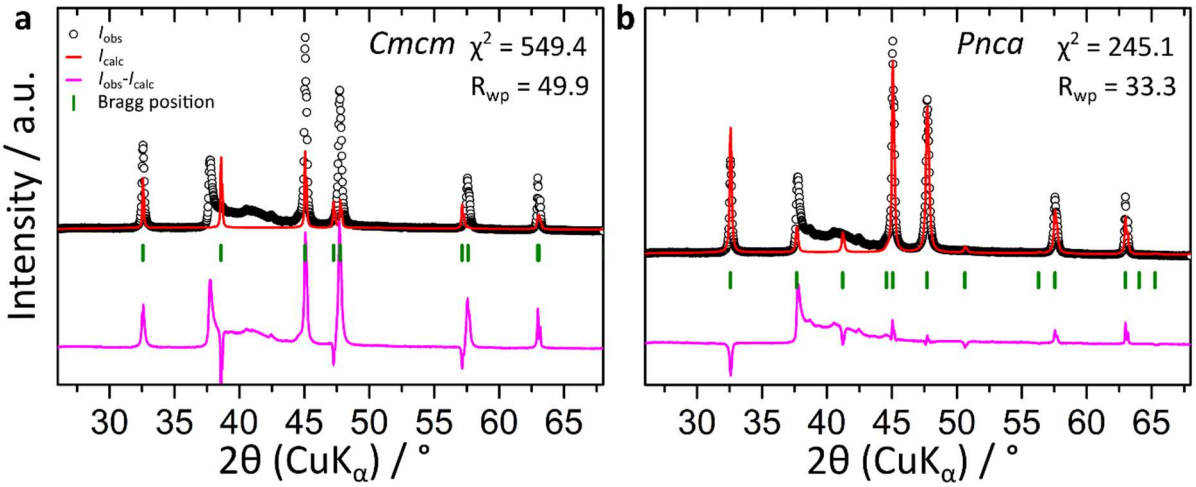

Figure VI. 5. **(a)** Rietveld refinement of the experimental α-FeB diffractogram by using the CrB-type structure (S.G. *Cmcm*) as model. **(b)** Rietveld refinement of the experimental α-FeB diffractogram by using the *Pnca* S.G. and leaving the Fe and B positions as refinable parameters in general positions.

the $(101)_\beta$, $(201)_\beta$ and $(301)_\beta$ reflections. To further account for the remaining experimental absences, we attempted to solve the structure in this space group by direct methods. We could not reach any plausible result, probably due to the arbitrary intensity integration in the diffuse scattering area. Alternatively, we assumed the atoms would lie in the same positions than in β-FeB provided the similarity of the cell metrics and the fact that α-FeB transitions to β-FeB. In turn, placing Fe and B atoms in the original β-FeB positions does extinguish the remaining $(111)_\beta$ and $(211)_\beta$ peaks. However, that is also true for the experimentally observed $(011)_\beta$ reflection, which discards this atomic positioning. Refinement in general positions does not yield a plausible model nor does it reproduce the diffraction pattern (best fit shown in **Figure VI. 5b** and **Table AII. 19**). No other S.G. proposed by EXPO2014 could account for the observed and missing reflections of α-FeB. Consequently, we discard hypothesis **(ii)**.

Hypothesis (iii): Faulted intergrowth of the β-FeB and the CrB-type structures.

In 1982, Kanaizuka suggested a recursive intergrowth between the CrB-type and β-FeB structures to model α-FeB.[108] The author relied on the earlier discoveries by Parthé and collaborators[111–115] that **(a)** several rare earth-metalloid alloys (DySi, HoSi, ErSi and PrGe) crystallized in the CrB structure at low temperature, which transitioned to the β-FeB structure upon heating, and that **(b)** CrB- and β-FeB-type structures were intermixed in periodically faulted stacks in YNi and GdNi-DyNi. On these bases, Kanaizuka built a 4-layers model, whose binary intermixing renders either pure CrB-type, pure β-FeB or a mixed β-FeB/CrB structure

(**Figure VI. 6**).[108] The layers A-D (**Figure VI. 6a**) are made from the unit cell of the original β-FeB structure with origin shifts in the *ab* plane such that they fit one of top of the other while keeping bond distances reasonable. **Figure VI. 6b** indicates the resulting structures from the binary mixtures of these layers stacked along the $[100]_\beta$ axis.

Kanaizuka then computed the interferences of the scattered waves from each layer by considering the possibility of existence of each. The probabilities obtained from these calculations were $P_A = 0.55$, $P_B = P_C = P_D = 0.15$,[108] which yield a decrease of the relative intensity of the $(101)_\beta$, $(201)_\beta$, $(111)_\beta$, $(211)_\beta$ and $(301)_\beta$ β-FeB reflections. Also, the model explains qualitatively the differences observed in the ^{57}Fe-Mössbauer spectra of α-FeB and β-FeB,[116] highlighting two distinct crystallographic Fe positions in α-FeB. However, the calculated diffractogram was still far from reproducing the experimental profile. Recent attempts to quantitatively account for the stacking faults in the modelling of the diffractogram have also proven unsuccessful.[117]

Conventional Rietveld refinement cannot account for stochastic stacking faults, as it only considers periodic structures. However, following the original idea of Kanaizuka, the powder diffractogram can be simulated and refined based on the explicit interference from the scattering of each layer. The FAULTS software has been developed for this purpose[118,119] and has shown high reliability for several types of materials.[120–123] FAULTS models the

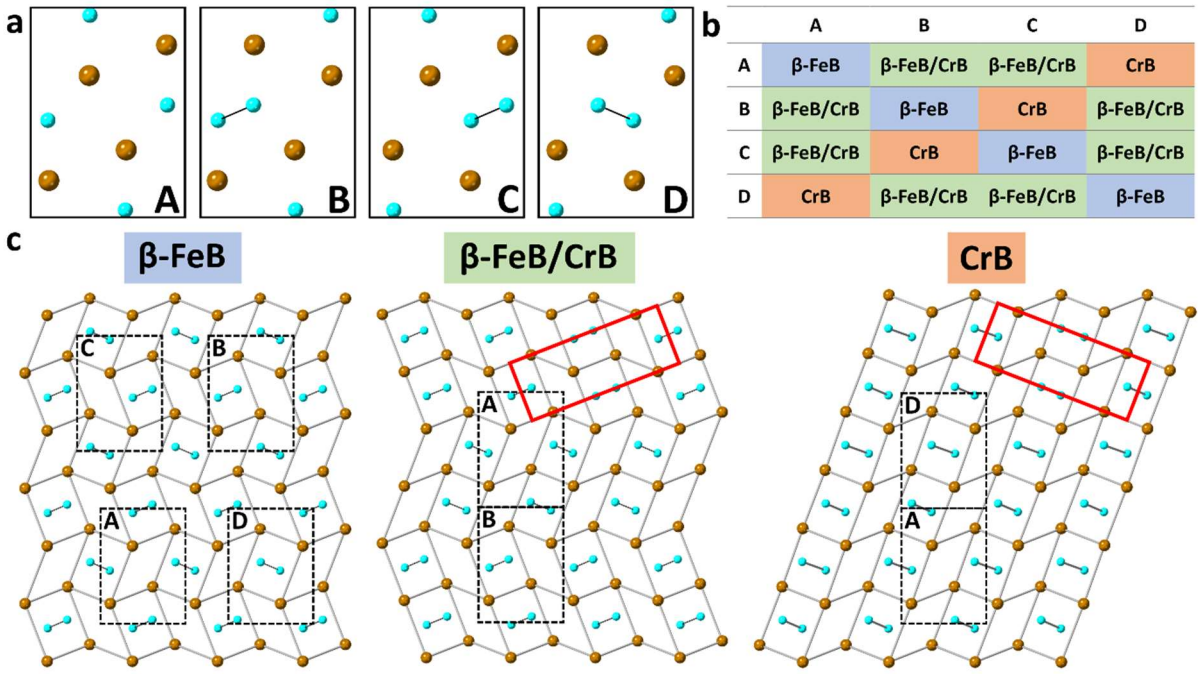

Figure VI. 6. **(a)** The four possible layer-types according to Kanaizuka's model. **(b)** Possible binary combinations outcome. **(c)** Visualization of binary outcomes.

diffractogram by considering a probabilistic assembly of layers along defined stacking vectors. We define the structure from A, B, C and D layers as building blocks stacked along the $[100]_\beta$ vector, with probabilities α_{ji} to transition from a layer *j* to *i* (where *j* and *i* are A, B, C or D), the atomic coordinates and crystallographic data used to build the layers can be found in the **Table AII. 17** of the **Appendix AII**. The probabilities of transition relate to the probabilities of existence P_i through **Equations VI. 3** and **VI. 4** below.[124] All symmetry elements but the identity are dropped to build this model as periodicity is no longer mandatory. Other factors typically important in a Rietveld refinement can also be accounted for, such as size broadening, occupations, Debye-Waller factors, atomic positions and unit cell variations, among others. This approach allows to describe bidimensional defects and disorder. Since the transition probabilities are refinable parameters, the method can quantify the amount of each layer.

$$P_i = \sum_{j=1}^{N} P_j \alpha_{ji} \qquad \textbf{Equation VI. 3}$$

$$\sum_{i=1}^{N} P_i = 1 \qquad \textbf{Equation VI. 4}$$

For a first set of simulations and for the sake of simplicity, only two sets of binary combinations were considered, that is A/B and B/C, as they suffice to explore all binary outcomes (see **Figure VI. 6b**). Transition probabilities were initially fixed to be equal for every arrival layer – $\alpha_{Ai} = \alpha_{Bi}$ or $\alpha_{Bi} = \alpha_{Ci}$ for *i* = A or B and B or C, respectively – and thus equal to the existence probability ($\alpha_{ji} = P_i$). Increments of 0.1 in existence probabilities were probed, the results can be seen in **Figure VI. 7a** and **Figure VI. 7b** for the A/B and B/C binary combinations, respectively. One can readily observe that some combinations significantly reduce the intensities of the reflections missing in α-FeB. The case where $P_B = P_C = 0.5$ (marked in red in **Figure VI. 7b**) stands out as all the $(101)_\beta$, $(201)_\beta$, $(111)_\beta$, $(211)_\beta$ and $(301)_\beta$ reflections vanish, in agreement with the experimental diagram. This strongly supports the hypothesis of CrB-type/β-FeB intergrowth by stacking faults along the $[100]_\beta$ axis, although the diffuse scattering is still not well modelled. Further simulations (**Figure VI. 7d**) were carried out by fixing the existence probability $P_B = P_C = 0.5$ and by varying the transition probabilities α_{ji}, under the simplification hypothesis that transition probabilities are symmetric ($\alpha_{ji} = \alpha_{ij}$). The main effect observed is the modification of the diffuse scattering profile with α_{BB}, which at the limit of $\alpha_{BB} = \alpha_{CC} = 0$ and $\alpha_{BC} = \alpha_{CB} = 1$ transforms in the characteristic Bragg peaks of the CrB-type structure. Similar α_{ji} screening simulations were carried out for the A/B mixing system for

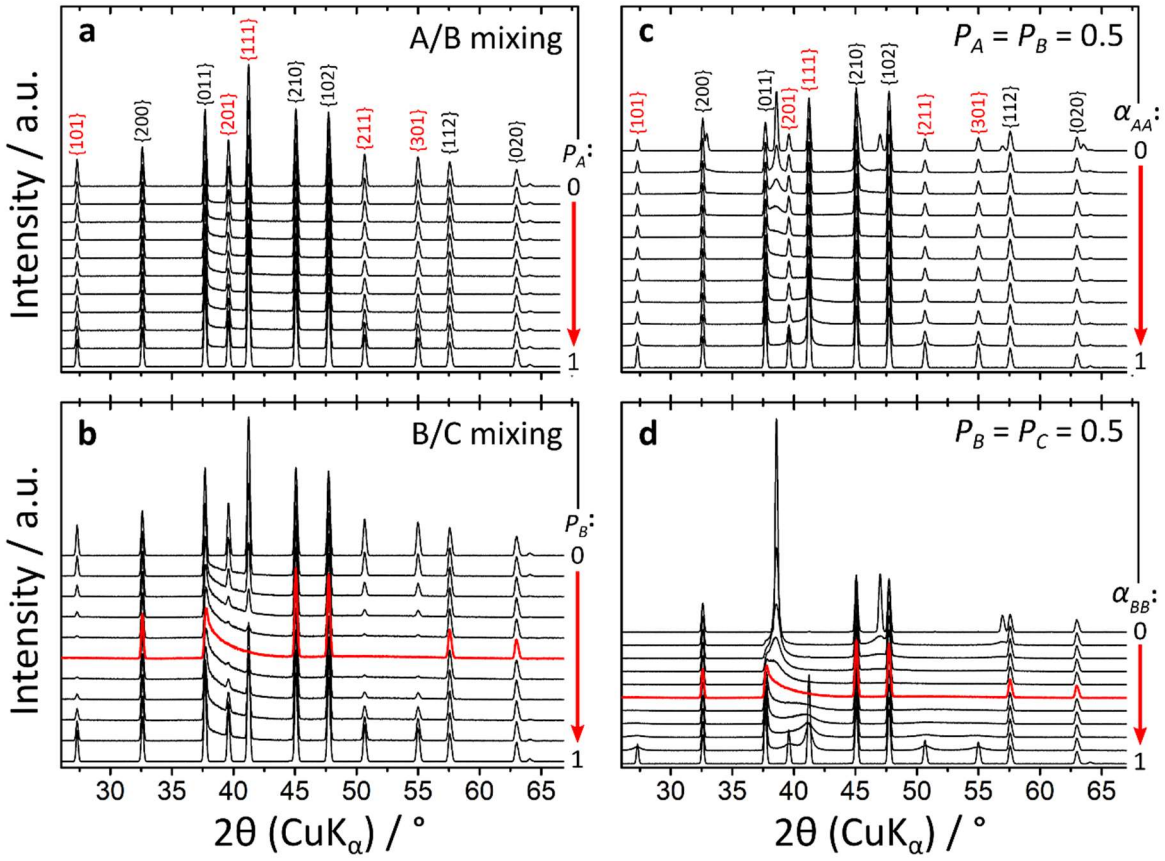

Figure VI. 7. Simulations of the diffraction pattern of α-FeB as an intergrowth between the β-FeB and the CrB-type structures:

(a) Simulations for binary mixing of A/B layers as a function of P_A, while fixing $\alpha_{Ai} = \alpha_{Bi}$; one parameter suffices to explore the system due to the constrains: $\alpha_{ji} = P_i$ and $P_B = 1 - P_A$.

(b) Simulations for binary mixing of B/C layers as a function of P_B, while fixing $\alpha_{Bi} = \alpha_{Ci}$; one parameter suffices to explore the system due to the constrains: $\alpha_{ji} = P_i$ and $P_C = 1 - P_B$. The pattern marked in red corresponds to $P_B = P_C = 0.5$, where the typical Bragg absences of α-FeB are reproduced.

(c) Simulations for binary mixing of A/B layers as a function of α_{AA}, while fixing $\alpha_{ji} = \alpha_{ij}$; note that one parameter suffices to explore the system due to the constrains: $1 - \alpha_{BB} = \alpha_{BA} = \alpha_{AB} = 1 - \alpha_{AA}$.

(d) Simulations for binary mixing of A/B layers as a function of α_{BB}, while fixing $\alpha_{ji} = \alpha_{ij}$; note that one parameter suffices to explore the system due to the constrains: $1 - \alpha_{CC} = \alpha_{CB} = \alpha_{BC} = 1 - \alpha_{BB}$. The pattern marked in red corresponds to the same conditions of the pattern marked in red in **(b)**.

comparison purposes (**Figure VI. 7c**), where an analogous trend is observed. These simulations were crucial in fixing a plausible initial input model for the following refinements. The complete values of probabilities employed for the simulations, as well as starting numeric values for refinements can be found in **Table AII. 18** of the **Appendix AII.**

In order to reproduce the diffuse scattering and reach an overall satisfactory fit of the experimental pattern, we had to include all four layers and asymmetrical transition probabilities ($\alpha_{ji} \neq \alpha_{ij}$) throughout the FAULTS refinement. The final refinement is depicted in **Figure VI. 8a** for a restricted 2θ range for clarity. The recovered transition probabilities are summarized in the A_{ji} tensor in **Table VI. 1**. Full refinement results are listed in **Table VI. 2**. A representation of the complete 2θ range can be found in **Figure AII. 1** of the **Appendix AII**. The powder diffractogram is very well reproduced, achieving figures of merits of R_{wp} = 7.3 % and χ^2 = 18.7. *Ergo*, our results confirm that *α*-FeB is an intergrowth of CrB-type and β-FeB structures stacked faults along the $[100]_\beta$ axis. This quantitative refinement permits to calculate the existence probabilities for the four types of layers: P_A = 0.20, P_B = 0.33, P_C = 0.33 and P_D = 0.14. Noteworthy, these values highly deviate from those proposed by Kanaizuka.[108]

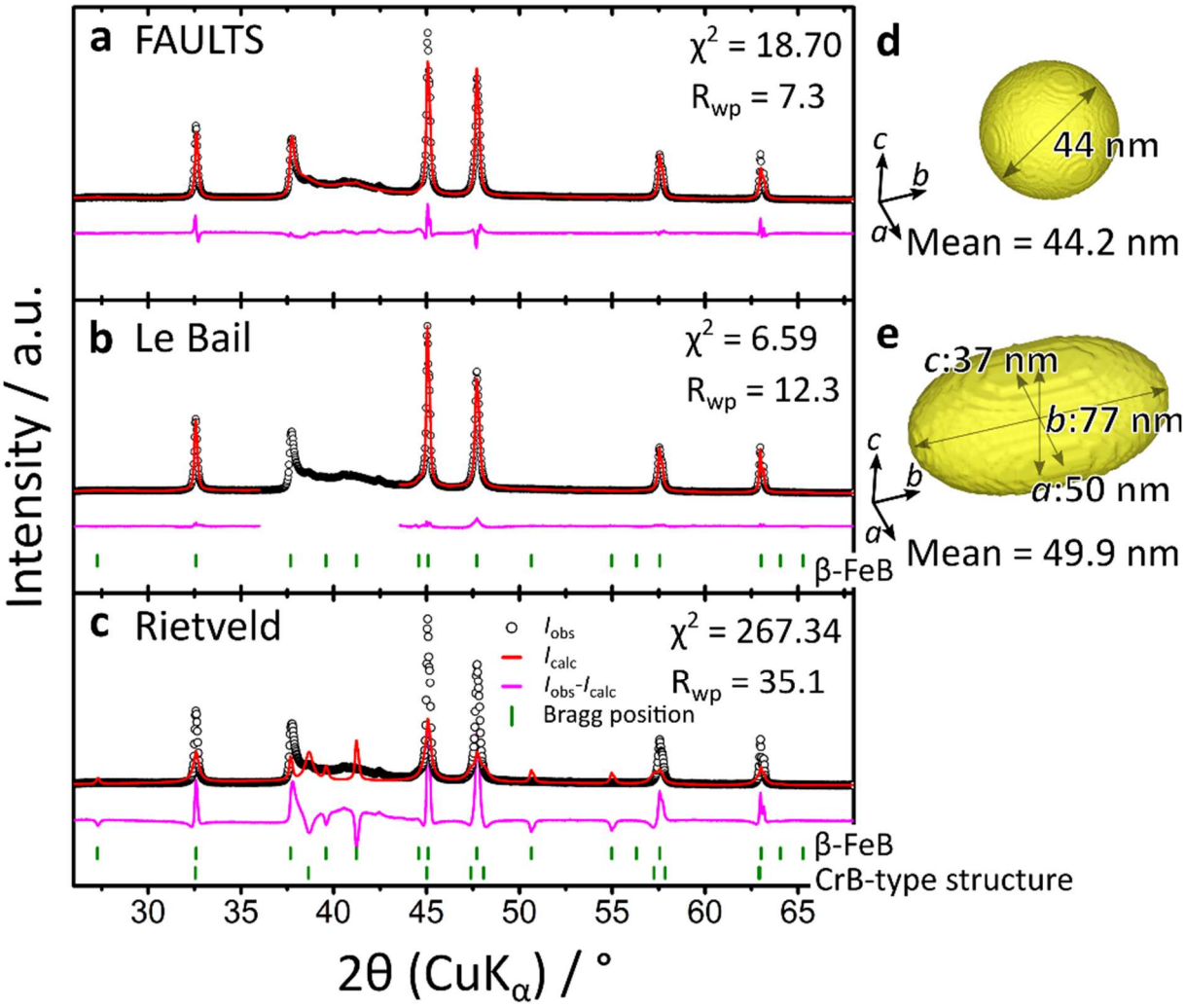

Figure VI. 8. Different refinement approaches to model α-FeB. **(a)** FAULTS refinement with the 4-layers model proposed by Kanaizuka.[160] **(b)** Le Bail refinement assessing the anisotropic particle size. **(c)** Rietveld refinement of a phase mixture β-FeB/CrB-type structure. Particle size and shape obtained from **(d)** FAULTS and **(e)** Le Bail refinements.

The largest disagreement between the experimental pattern and the herein reported FAULTS refinement arises from the peak shape. Particularly, the experimental anisotropic broadening is not well accounted in the refined pattern. FAULTS's only resource to generate anisotropic size is to limit the number of stacked layers, so to independently treat the stacking direction $[100]_\beta$ while the remaining two dimensions are treated isotropically. Hence, at most a sphere truncated in the $[100]_\beta$ direction can be modelled. In order to account for more complex morphologies, Le Bail analysis using spherical harmonics anisotropic size modelling is more suited. To enable Le Bail refinement, we have excluded the diffuse scattering area in the 36-44° region. Accurate Le Bail fitting is achieved (**Figure VI. 8b**), with final figures of merit of R_{wp} = 12.3 % and χ^2 = 6.59. Full results can be found in the **Table VI. 2**. The size modelling from spherical harmonics indeed indicates a very anisotropic shape, as shown in **Figure VI. 8e**. The $[010]_\beta$ dimension is the longest at *ca.* 77 nm, while the perpendicular *a* and *b* directions show smaller sizes of *ca.* 50 and 37 nm respectively. FAULTS best result is a sphere with average diameter 44 nm (**Figure VI. 8d**), thus demonstrating the origin of the biggest misfit between the refinement and the experimental data in the FAULTS refinement. Finally, Rietveld refinement with a phase mixture of the CrB and β-FeB as model was also performed for comparison (**Figure VI. 8c**). The difference in the modelling between Rietveld and FAULTS is evident and shows that α-FeB is an intimate intergrowth of two structure types and not simply a phase mixture.

The existence probabilities P_A, P_B, P_C and P_D and transition probabilities α_{ji} obtained from the FAULTS refinement can be converted into fractions of β-FeB and CrB domains. First, the existence probability of each binary combination of layer types (**Figure VI. 6b**) can be

Table VI. 1. A_{ji} tensor for α-FeB obtained from the FAULTS refinement. Departure layers (*j*) are in columns and arrival layers (*i*) in rows.

Layer	A	B	C	D
A	0.00	0.00	0.92	0.08
B	0.24	0.56	0.12	0.08
C	0.25	0.37	0.30	0.08
D	0.30	0.15	0.05	0.50

Table VI. 2. Crystallographic results of the refined parameters of α-FeB.

Parameter	FAULTS refinement	Le Bail refinement
a (Å)	5.49886(2)	5.4973(6)
b (Å)	2.95047(1)	2.9498(2)
c (Å)	4.06408(2)	4.0625(3)
Volume (Å^3)	65.9614(5)	65.878(1)
Average size (nm)	44.2	49.9
R_{wp} (%)	7.3	12.3
χ^2	18.7	6.6

calculated as the multiplication of the existence probability of the departure layer (P_j) times the transition probability towards the arrival layer (α_{ji}). Then, one must consider the individual contributions of each binary combinations to each structure type. The combinations yielding pure β-FeB (see **Figure VI. 6b**: A/A, B/B, C/C and D/D) and those yielding pure CrB (A/D, B/C, C/B, D/A) contribute only to β-FeB or CrB structure types, respectively. For each combination yielding mixed β-FeB/CrB (**Figure VI. 6b**), 50 % of the combination corresponds to β-FeB and 50 % to CrB-type structure. Then the β-FeB cluster fraction is evaluated as the sum of the existence probabilities of pure β-FeB combinations plus half of the existence probabilities of β-FeB/CrB combinations. The CrB cluster fraction is calculated analogously. In the end, we evaluate β-FeB and CrB fractions at 0.57 and 0.43, respectively.

We further extended the analysis to assess the distribution of β-FeB and CrB domain sizes along the stacking direction. To do so, we adapted a stochastic model reported by Serrano-Sevillano and collaborators.[120] The approach is based on the generation of a sequence of 100,000 layers according to the transition probabilities α_{ji} obtained from the FAULTS refinement, in order to obtain statistically meaningful values of average domain size. For enhanced accuracy, the calculation is repeated for 20 sequences generated independently. We obtained average domain sizes of 2.5 and 2.1 nm for the β-FeB and CrB domains, respectively. These values are consistent with the thickness of the contrasted domains observed by TEM (**Figure VI. 2**).

Synthesis of α-FeB nanostructures

After accurate modelling of the intergrown α-FeB structure, we assessed the possibility to further reduce the particle size of this material, in order to profit from the higher surface area. A common strategy to yield nanostructures is to accelerate the crystallization kinetics in order to favour nucleation over growth of crystallites.[125] One way to achieve this in the present system is to add an extra reducing agent in order to fasten the reduction of iron and boron to yield FeB. NaH was selected as reducing agent as it does not introduce further foreign elements, for which we initially tested a synthesis in a ratio $FeCl_2$:$NaBH_4$:NaH of 2:2:5 (see **Figure VI. 9a** for XRD results). The strategy does work in the sense that the crystallite size is reduced, as evidenced by the Bragg peaks broadening, but including NaH also favours the formation of Fe_2O_3 (marked with arrows in **Figure VI. 9a**). Fe_2O_3 is probably formed by oxidation of Fe^0 during the washing process. The amount of this impurity is decreased by either further increasing the NaH excess to $FeCl_2$:$NaBH_4$:NaH = 2:2:10 (**Figure VI. 9a**) or by increasing the

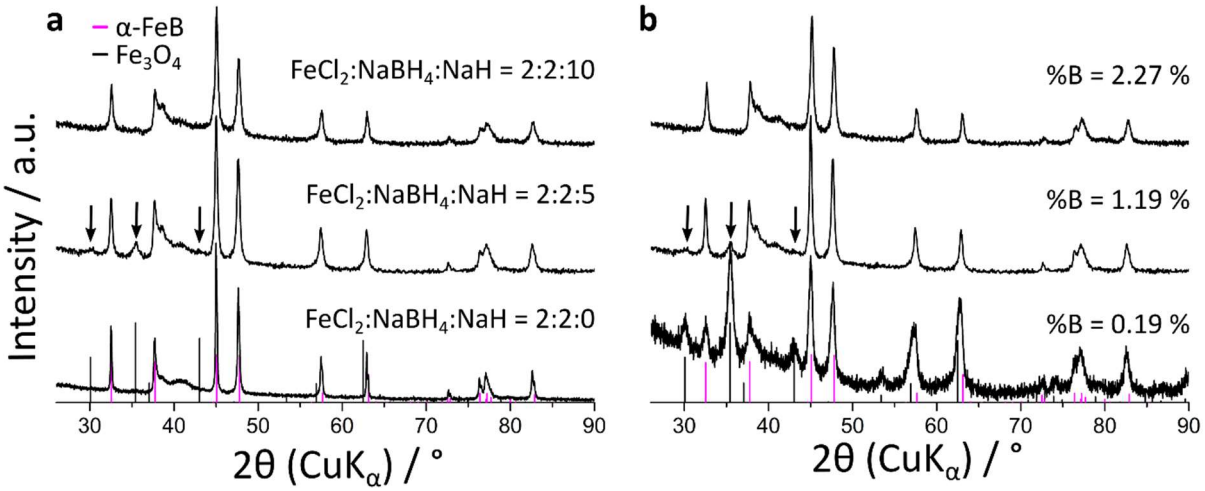

Figure VI. 9. XRD results from the synthesis conditions screening in order to yield α-FeB nanostructures. **(a)** NaH ratio screening at a fixed reagents concentration yielding a %B of 1.19 %. **(b)** Reagents concentration screening for the fixed reagents ratio of $FeCl_2$:$NaBH_4$:NaH of 2:2:5. Fe_3O_4 impurity peaks are marked with black arrows in both images.

reagents concentration at the fixed 2:2:5 reagents ratio (**Figure VI. 9b**). In all cases, the α- form of FeB is obtained as expected.

Both the $FeCl_2$:$NaBH_4$:NaH = 2:2:10 (%B = 1.19 %) and the $FeCl_2$:$NaBH_4$:NaH = 2:2:5 (%B = 2.27 %) yield pure nanocrystallites, with similar morphologies and particle size distribution (not shown). Given the similarities in both products qualities, the $FeCl_2$:$NaBH_4$:NaH = 2:2:5 (%B = 2.27 %) conditions were chosen for further experimentation, as the higher NaH excess presents combustion danger during the washing step. For these conditions, the synthesis temperature was also screened to further optimize the particle size distribution. XRD results are shown in **Figure VI. 10**, from which we deduce that the temperature can be decreased down to 500 °C without compromising the crystallinity of the product.

In order to characterize the morphology of the synthesized nanoparticles, TEM images were acquired and a higher quality XRD diffractogram of the same sample was analysed. The TEM images (**Figure VI. 11**) show rounded nanoparticles of average diameter 42 nm. The XRD analysis on the other hand was performed by both the FAULTS and Le Bail algorithms (**Figure VI. 12a** and **b** respectively). The resulting crystallographic parameters are summarized in **Table VI. 3**. Both refinements coincide in mean isotropic crystallite size of 9 and 11 nm for the FAULTS and Le Bail refinements respectively. The discrepancy with TEM data indicates that each particle is formed by several crystallites. The FAULTS refinement yields very similar transition and existence probabilities to the bulk α-FeB. Transition probabilities are summarized

in the A_{ji} tensor (**Table VI. 4**) and the existence probabilities are: P_A = 0.22, P_B = 0.34, P_C = 0.32 and P_D = 0.12. This suggests that regardless of the synthesis conditions, the faulted scheme in α-FeB remains roughly intact, supporting the idea that the distribution of stacking faults is relatively reproducible among different α-FeB morphologies.

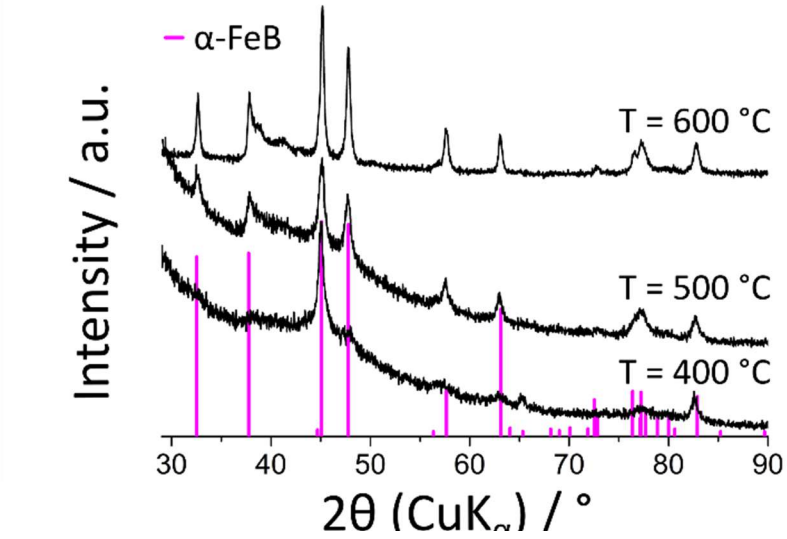

Figure VI. 10. XRD results of the synthesis temperature screening of α-FeB nanoparticles for the conditions of $FeCl_2$:$NaBH_4$:NaH = 2:2:5 (%B = 2.27 %).

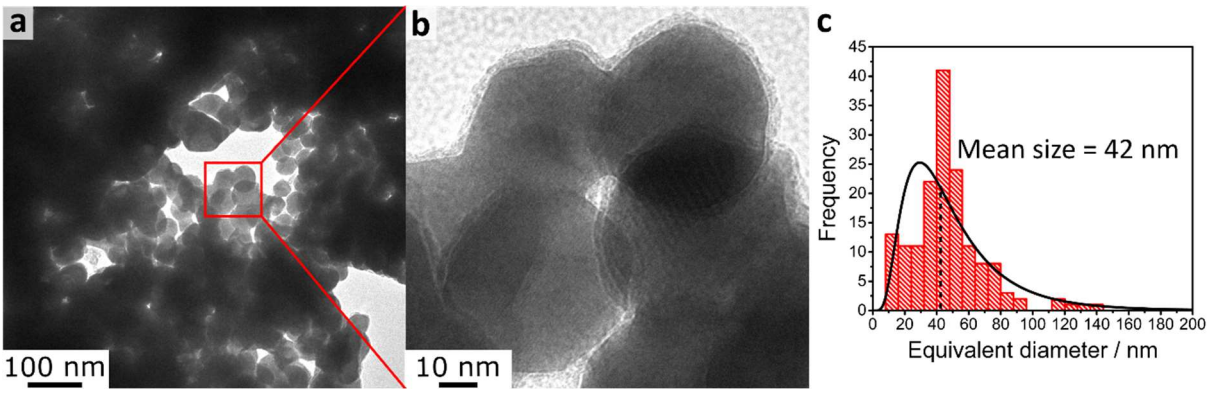

Figure VI. 11. **(a)** and **(b)** TEM images of the synthesized α-FeB nanoparticles **(c)** Size distribution histogram performed over 83 nanoparticles.

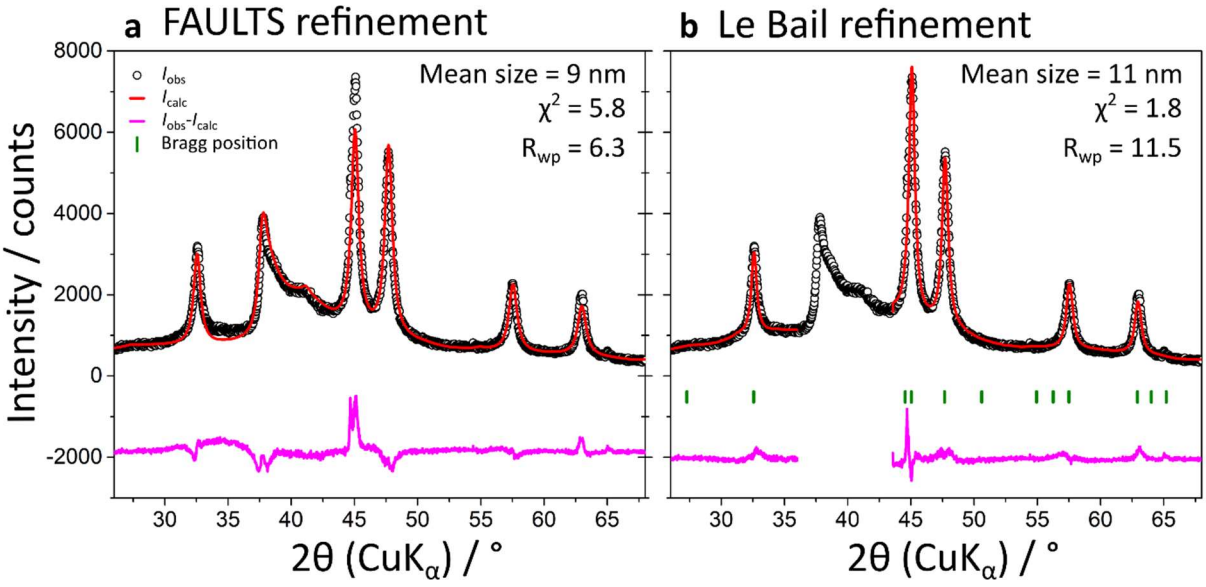

Figure VI. 12. α-FeB nanoparticles XRD analysis by the **(a)** FAULTS and **(b)** Le Bail refinement methods.

Table VI. 1. Crystallographic results of the refined parameters of the α-FeB nanostructures.

Parameter	FAULTS refinement	Le Bail refinement
a (Å)	5.4954(1)	5.4953(2)
b (Å)	2.95223(5)	2.9523(3)
c (Å)	4.06574(6)	4.0651(1)
Volume (Å^3)	65.9365(5)	65.952(4)
Average size (nm)	9.3	10.8
R_{wp} (%)	5.6	11.5
χ^2	6.2	1.8

Table VI. 2. A_{ji} tensor for the α-FeB nanostructures obtained from the FAULTS refinement. Departure layers (*j*) are in columns and arrival layers (*i*) in rows.

Layer	A	B	C	D
A	0.00	0.00	0.88	0.12
B	0.28	0.55	0.13	0.04
C	0.25	0.37	0.28	0.1
D	0.35	0.26	0.00	0.39

Electrocatalytic properties for water splitting

The electrocatalytic activity of the FeB samples in hydrogen and oxygen evolution reactions (HER and OER respectively) were investigated in 0.5 M H_2SO_4 and O_2-saturated 0.1 M KOH, respectively. For these purposes, hybrid films made of the samples, Nafion and carbon black particles was deposited on a glassy carbon substrate. Although the electrocatalytic activity would be enhanced by using carbon or Ni foam substrates,[126] this configuration enables the direct comparison of the activities normalized *versus* the catalyst mass loading and electrode surface. For comparison, the electrochemical response of a blank substrate and a carbon black/Nafion mixture were also recorded, along with the standard references for each reaction: 20 % *wt*. Pt/C for HER and IrO_2 for OER. In both cases, cyclic voltammograms (CVs) were recorded at 20 $mV \cdot s^{-1}$. The results for the first cycle are summarized in **Figure VI. 13a** (HER) and **Figure VI. 13b** (OER).

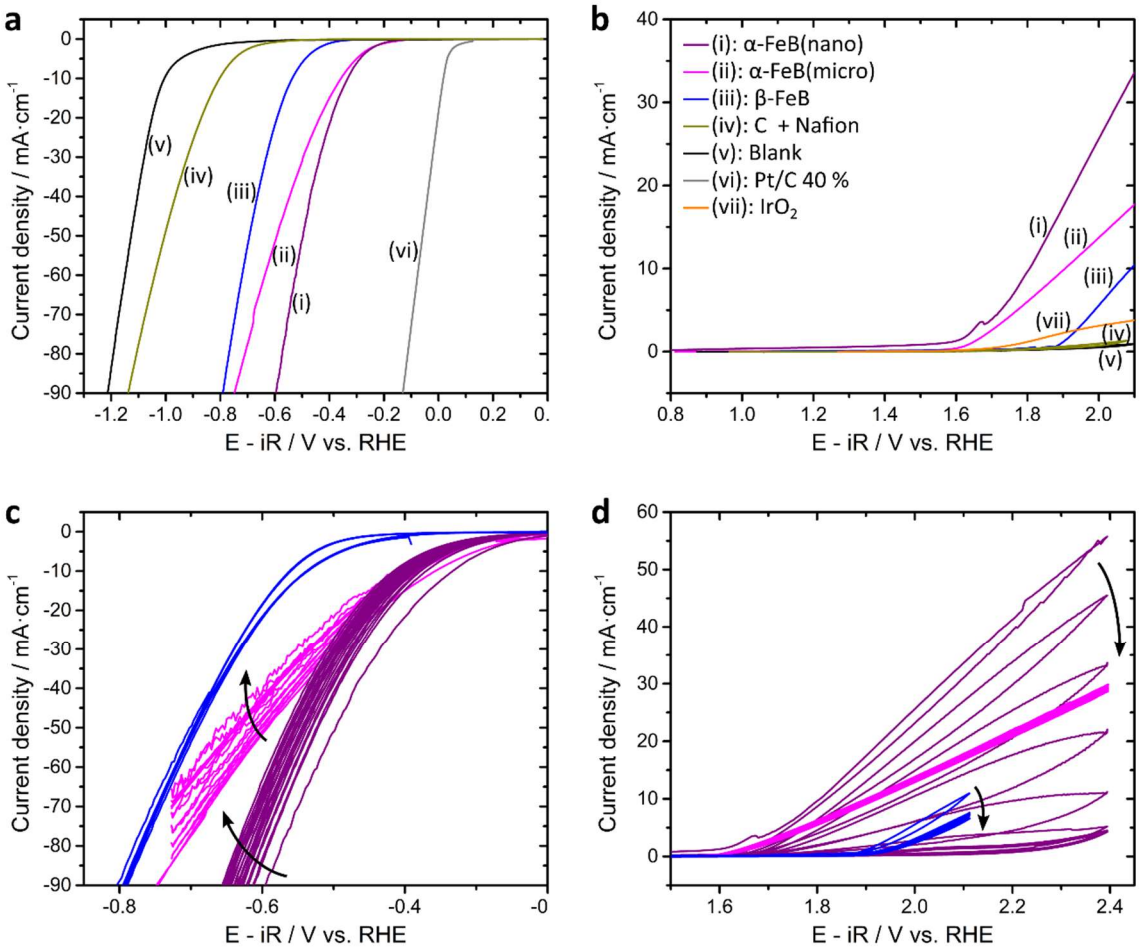

Figure VI. 13. Catalytic activity for FeB. **(a)** First CV for HER in H_2SO_4 0.5 M. **(b)** First CV for OER in O_2-saturated KOH 0.1 M. **(c)** 10 CVs cycles for HER in H_2SO_4 0.5 M. **(d)** 10 CVs cycles for OER in O_2-saturated KOH 0.1 M.

Interestingly, while the compositions of bulk β-FeB, bulk α-FeB and α-FeB nanoparticles are identical, their activities highly differed in both half-reactions of water splitting. For HER, α-FeB presents an overpotential 178 mV (at 10 $mA \cdot cm^{-1}$) smaller than β-FeB for similar particles sizes. This activity was further enhanced for the α-FeB nanoparticles, which is associated to the increase of the surface area due to the smaller size. Different activities for similar compositions and particle sizes point at a possible favourable impact of the faulted structure of α-FeB on the catalytic activity. Indeed, atoms located at structural stacking faults can act as preferential catalytically active sites because of their distorted local environment.[127] Specifically, for metal borides, the boron chains have been recognized to play a key role in the H atoms adsorption and thus in the overall activity of the material.[128] This hypothesis will be further explored by DFT calculations, which are currently underway.

Correspondingly, the overpotential was also reduced for the OER half-reaction, in the order α-FeB(nano) < α-FeB(micro) < β-FeB, as shown **Figure VI. 13b**. Here however, and as it has been repeatedly shown in the literature for metal borides, the active species are not the boride itself, but the metal oxides/oxohydroxides formed at its surface, after an oxidation wave at *ca*. 1.65 V/RHE.[129] So, the difference of activities suggest that different oxohydroxo species result from different boride local structures.

The cyclability of the catalysts was assessed by performing 10 CVs as a preliminary test, which showed that the activity drops during HER for α-FeB in both morphologies (**Figure VI. 13c**) and only for the α-FeB nanoparticles in the case of OER (**Figure VI. 13d**). Electrochemical impedance spectroscopy (EIS) was then conducted to assess charge transport in the electrodes and at the electrode-electrolyte prior and after electrocatalysis, we focused this analysis solely for the HER semi-reaction. An equivalent circuit with three main components of solution

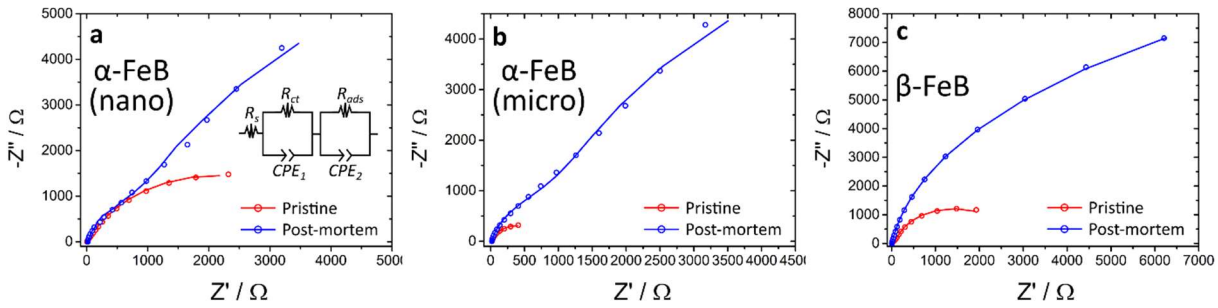

Figure VI. 14. Electrochemical impedance spectra of the pristine and post-mortem FeB samples before and after HER electrocatalysis. The graphs show the behaviorfor **(a)** α-FeB(nano), **(b)** α-FeB(micro) and **(c)** β-FeB. All spectra are fitted to the equivalent circuit shown in the inset of **(a)**.

resistance (R_s), charge transfer resistance (R_{ct}) and mass transfer resistance related to reaction intermediates adsorbed at the electrode surface (R_{ads}) was used to fit the experimental curves, as schematized in the inset of **Figure VI. 14a**.[130,131] The drop of activity is in line with the increase of the resistance during reaction according to EIS in **Figure VI. 14**.

To get deeper insights into the evolution of the materials during electrocatalysis, the surface state of the materials was investigated before and after reaction *via* X-ray photoelectron spectroscopy (XPS). The pristine materials showed very similar surface state, with components at low binding energies for Fe 2p (707 eV) and B 1s (188 ev) spectra (**Figure VI. 15**), which were ascribed to the close-to-metallic states of the elements into the boride.[132] The Fe region revealed a mixed-valence oxidized surface with at least 3 components, can be ascribed to Fe^{2+} and Fe^{3+} states at 711 eV and 724 eV, which is consistent with the mixed-valence oxyhydroxides that are usually observed at the surface of metal borides exposed to air and/or water.[129] Boron showed only one oxidized component at 192 eV, matching well with boron oxide references such as B_2O_3.[133] The fraction of oxidized boron at the surface increased from microscale α-FeB (51 % *at.*) to nanoscale α-FeB(nano) (67 % *at.*), in line with the

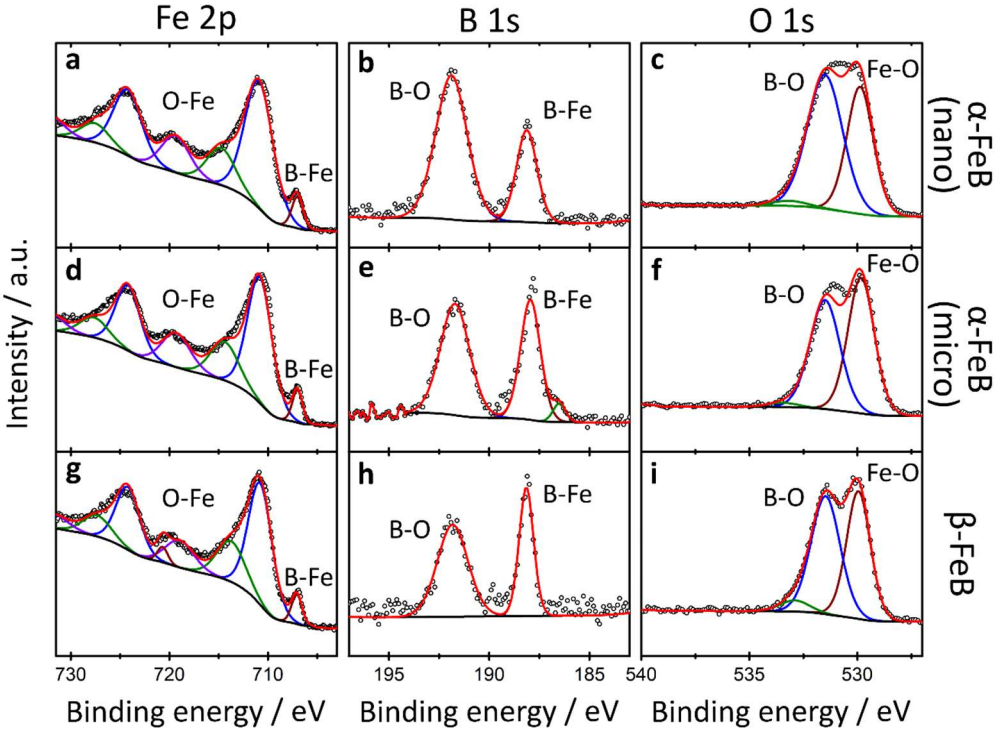

Figure VI. 15. XPS spectra for the pristine FeB samples: α-FeB(nano) spectra of **(a)** Fe 2p, **(b)** B 1s and **(c)** O 1s; α-FeB(micro) spectra of **(d)** Fe 2p, **(e)** B 1s and **(f)** O 1s; β-FeB spectra of **(g)** Fe 2p, **(h)** B 1s and **(i)** O 1s.

enhanced surface area. For the oxygen 1s spectra, a major component for Fe-O and another one for B-O were identified.[133,134]

Post mortem XPS analysis (**Figure VI. 16**) of the α-FeB samples after HER revealed a strong signal lost for Fe and B, which indicates that the samples have detached from the electrode, or have been dissolved, which is consistent with the activity loss. Although β-FeB suffers several surface changes, it does withstand the process according to XPS, in line with its maintained activity upon cycling. The signals of unoxidized Fe and B are lost, meaning that FeB has been oxidized at least on the surface. This is in line with the lower activity of β-FeB with respect to α-FeB. While the latter is more reactive and initially more active than β-FeB, especially for the nanostructures, it is also more prone to degradation by the medium. β-FeB presents less activity but more durability. This specific behavior of α-FeB raised by the destabilization of atoms in planar defects can serve as a model for taking advantage of the stacking faults in other materials exhibiting similar defects like $ThMoB_4$ or $YCrB_4$.[135] Note however that more analyses are required to decipher between the dissolution and detachment mechanisms of deactivation in order to support this conclusion.

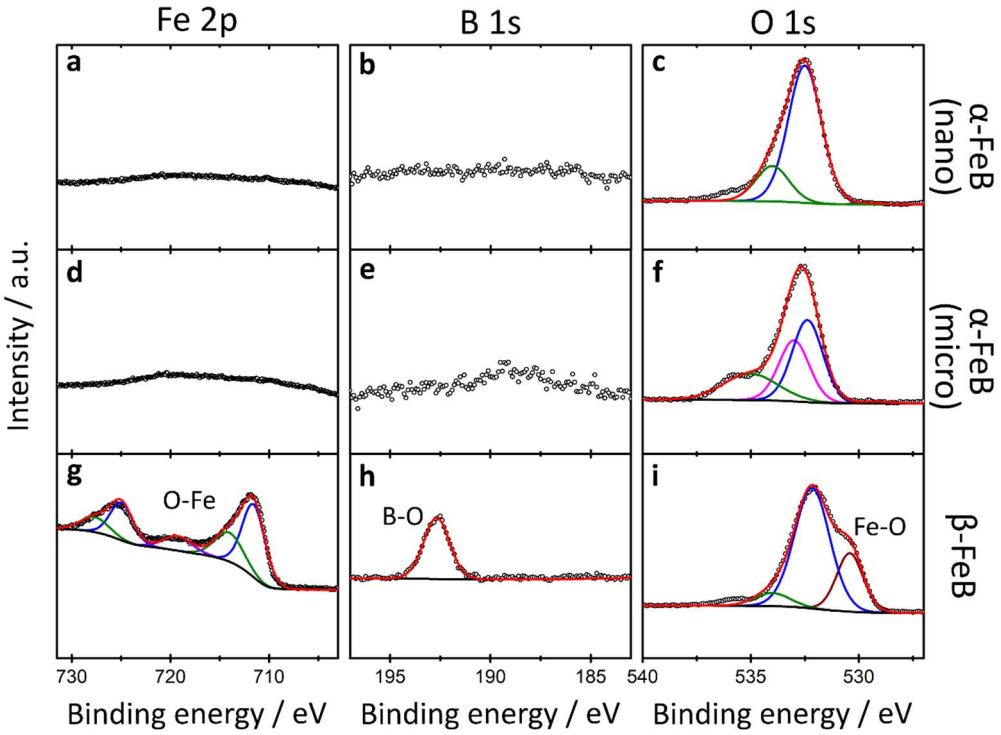

Figure VI. 16. XPS spectra for the *post mortem* FeB samples: α-FeB(nano) spectra of **(a)** Fe 2p, **(b)** B 1s and **(c)** O 1s; α-FeB(micro) spectra of **(d)** Fe 2p, **(e)** B 1s and **(f)** O 1s; β-FeB spectra of **(g)** Fe 2p, **(h)** B 1s and **(i)** O 1s.

VI.4 Partial Conclusions

Two structural modifications of FeB, α-FeB and β-FeB, have been selectively synthesized in molten salts at moderate and high temperature, respectively. While the high temperature structure (β-FeB) is well known, the α-form structure was unknown. We critically evaluated the main hypotheses present in the literature to explain the structure of α-FeB, demonstrating unambiguously that α-FeB is an intergrowth of nanodomains of β-FeB and CrB structure types. We modelled this intergrowth as a set of stacking between four different layer types, whose stochastic intermixing renders either the β-FeB or the CrB-type nanodomains. The β-FeB and CrB domains are *ca*. 2 nm-thick slabs stacked along a common crystallographic axis and separated by stacking faults. By using an extra reducing agent (NaH), we could further isolate the α-FeB phase in the form of nanoparticles of ≈ 42 nm mean diameter. These particles retain roughly the same stacking proportion and domain size of the two structure types as in bulk α-FeB. All FeB modifications exhibited catalytic activity in the water splitting reaction. The α-FeB modification systematically showed higher activity with respect to β-FeB for both HER and OER half-reactions. This higher activity may be linked to the higher reactivity of the atoms lying in the stacking faults. This higher reactivity however, also makes the α-FeB material less stable upon cyclability, and it ends up dissolving in the media, which is not the case for β-FeB. Overall the synthesis of the FeB material could be controlled to deliver two structural modifications in different morphologies. This study will be of importance for its use as a template towards Fe_2AlB_2 in the next chapter.

Chapter VII: Fe_2AlB_2 synthesis and delamination approach

VII.1 Introduction

For this last experimental chapter, we will focus on the synthesis and manipulation of the ternary MAB phase Fe_2AlB_2. The interest of this phase, as any other MAB phase, is its possible delamination by Al etching to render bidimensional MBenes (boridenes). The particular case of the hypothetical Fe_2B_2 boridene has been studied from a theoretical point of view. DFT calculations suggest that bidimensional Fe_2B_2 would exhibit small Li diffusion energy barrier and high Li storage capacity on one side, and close-to-null adsorption free energy of hydrogen on the other side. These features are relevant for electrodes of Li-ion batteries and electrocatalysis of the hydrogen evolution reaction, respectively.[58] Despite this high interest, no study has shown any advance towards the exfoliation of Fe_2AlB_2. A major hurdle setting back Fe_2AlB_2 research is its synthesis, which requires high temperatures (> 1000 °C), long reaction times (> 24 h), and still presents poor reproducibility.[84] In the present chapter, we will expose the synthesis of the ternary Fe_2AlB_2 compound in molten salts, by insertion of Al in the FeB precursor described in the previous chapter. The reaction still takes place under the templating context underlying this thesis, although rather from an atomic point of view than from the previous microstructural sense, as a topochemical transformation will be at play. In a second stage, we will show our approaches towards the delamination of the material through various methods.

VII.8 Materials and methods

All reagents were stored and handled under an argon-filled glove box. For the final synthesis, FeB starting material was obtained as described in **Section 0**, with the exception that a H_2O washed product was used instead of a MeOH washed. $FeCl_2$ (99.5 %, Alfa Aesar), $NaBH_4$ (98 % min., Alfa Aesar), $NaAlCl_4$ (99.9 %, Alfa Aesar) and $GaCl_3$ (99.999 %, Siga-Aldrich) were used as Al and Ga sources, respectively. NaH (90 %, Aldrich) was used as reducing reagent. A eutectic mixture of LiCl (99.9% Alfa Aesar)/KCl (99.9% Sigma Aldrich) (45:55 *wt*. %) was used as solvent for the synthesis of the MAB phases. $CuCl_2$ (99.9 %, Siga-Aldrich), $CoCl_2$ (99.9 %, Siga-Aldrich)/NaCl (99 %, Merck) (57:43 *wt*. %), $FeCl_2$ (99.5 %, Alfa

Aesar)/NaCl (99 %, Merck) (63:37 *wt*. %), $CdCl_2$ (99.9 %, Sigma-Aldrich)/NaCl (99 %, Merck) (13:87 *wt*. %), and $ZnCl_2$ (99.99 %, Alfa Aesar)/NaCl (99 %, Merck) (17:83 *wt*. %) were used as delaminating agents. HCl 38 % (Sigma) and deionized H_2O were used for washing steps.

Synthesis procedures

Impregnation of FeB. In order to optimize the reactivity of FeB particles, they were pre-dispersed in the eutectic salt mixture before melting. To do so, 62 mg (0.925 mmol) of FeB (either the α or β modifications) were placed in a Schlenk tube and connected to a Schlenk like. 1 mL of methanol was added and the suspension sonicated for 20 min to assure proper dispersion. Then, 2.55 g of previously ground LiCl/KCl were added abruptly. The mixture was then evacuated under vacuum, first at room temperature and then in a stepwise heating to 50, 75, 100, 120 and finally 150 °C. Each heating step was maintained until the vacuum pressure dropped below 10^{-2} mbar, the final step (150 °C) was maintained until the vacuum pressure dropped below $1.0 \cdot 10^{-3}$ mbar.

Final mixing and synthesis of Fe_2AlB_2 or $Fe_2Al_{1-x}Ga_xB_2$.

All ionic-reagents synthesis. The reagents $FeCl_2$ (0.925 mmol), $NaAlCl_4$ (0.463 mmol), $NaBH_4$ (0.930 mmol), and NaH (2.31 mmol) were mixed with 5.1 g of the eutectic LiCl/KCl mixture. **FeB-based synthesis.** Impregnated FeB and LiCl/KCl were mixed with of 266 mg $NaAlCl_4$ (1.388 mmol), 111 mg of NaH (4.625 mmol) and 2.55 g more of LiCl/KCl eutectic mixture. Reagents ratios variation for screening purposes will be specified in the **Results and Discussion** section. For both synthesis types, the solids were finely ground together at 20 Hz for 2 min in a Retsch MM400 ballmiller (airtight vials of 50 mL, one steel ball of 62.3 g and a diameter of 23 mm). The solid mixture was later placed in a Mo crucible (Ø15 mm × H200 mm), which was placed into a quartz tube. The quartz tube was connected to a Schlenk line under Ar flow and placed inside a vertical oven. A heating ramp of 10 °C·min^{-1} was used up to 1000 °C, followed by a dwell time of 1 h. After dwelling, the sample was let to cool down naturally and subsequently washed in sequences of solvent mixing, sonication (1 min), centrifugation at 21000 RPM for 2 min and separation of the solid, until the conductivity of the supernatant dropped below 50 μS·cm^{-1}. The powder was dried under vacuum at 60 °C overnight. In the case of the Ga-doped samples ($Fe_2Al_{1-x}Ga_xB_2$), $GaCl_3$ was used as Ga source. $GaCl_3$ must be weighted and ground on top of cool surfaces to avoid its evaporation. The following quantities of $NaAlCl_4$ and $GaCl_3$ were used for each sample: 239 mg $NaAlCl_4$ (1.249

mmol) + 24 mg $GaCl_3$ (0.139 mmol), 186 mg $NaAlCl_4$ (0.972 mmol) + 73 mg $GaCl_3$ (0.416 mmol) and 133 mg $NaAlCl_4$ (0.694 mmol) + 122 mg $GaCl_3$ (0.694 mmol) for the $Fe_2Al_{1-x}Ga_xB_2$ samples with x = 0.1, 0.3 and 0.5 respectively. The remaining reagents quantity and procedure remained identical to the pure Fe_2AlB_2 synthesis.

Acidic-washing purification. As obtained Fe_2AlB_2 or $Fe_2Al_{1-x}Ga_xB_2$ were washed in a 1:1 v/v dilution of HCL 38 % in deionized water. For this, the entire batch of a synthesis (approximately 120 mg) were placed in a centrifuge tube. 5 mL of acid were added and shook for 30 s. Past this time the supernatant (containing suspended material) was separated and diluted with 300 mL of H_2O. The suspended solid was separated magnetically and mixed with the remaining solid at the centrifuge tube. The product was further washed in 5 sequences of 30 mL H_2O mixing, shaking and centrifuging at 21000 RPM for 2 min.

Molten-salts or direct sublimation delamination. The delaminating salts and Fe_2AlB_2 were mixed in a molar ratio Fe_2AlB_2:MCl_2 of 2:3. Approximately 15 mg of Fe_2AlB_2 were taken for the preparation of each mixture. The mixing was performed by grinding the powders with a mortar and pestle inside an argon flow glove box for 20 min. The mixtures were then stored directly on the quartz capillaries intended to perform their heat treatment with. For the direct sublimation delamination, no salt was added and the Fe_2AlB_2 or $Fe_2Al_{1-x}Ga_xB_2$ were placed directly in the capillary. The heat treatments were performed with the *in-situ* oven developed by the team at either ID11 beamline at the ESRF. For more details on this experiment, see the **Appendix AI**.

VII.3 Results and discussion

Synthesis of Fe_2AlB_2

Fe_2AlB_2 synthesis has been achieved in the literature only in the bulk state. Such reactions require high temperatures (> 1000 °C), long dwell times (> 24 h), and reproducibility is a common struggle.[84] In the present work we have explored the synthesis of Fe_2AlB_2 by using molten salts. We initially formulated the hypothesis that the high mobility of metal ions solubilized in a salt solvent at high temperature would favour the rapid crystallization of Fe_2AlB_2 from solubilized constitutive elements, thus enabling its formation at lower temperature with limited grain growth. In view of the lack of success of this strategy, as explained below, we have used FeB as precursors that would transform easily, hence with low

energy input, into Fe_2AlB_2 upon reaction with an Al source, due to the similarities of the structures that ensure a topotactic reaction. These two molten-salts strategies will be discussed as well as the parameters that play a key role in the present synthesis.

First attempts with all-ionic precursors

Initially, the ionic $FeCl_2$, $NaAlCl_4$ and $NaBH_4$ reagents were chosen as element sources. Particularly, $NaAlCl_4$ was selected among other ionic Al sources for its low volatility. The targeted stoichiometry of Fe:Al:B = 2:1:2 does not match the redox reaction if only $NaBH_4$ is used as reducing agent. Indeed, by supposing a final oxidation number of 0 for all the elements, still 5 equivalents of negative charge are required to equilibrate the redox reaction ($5H^-$ equivalents in **Equation VII. 1**). These remaining charges would forbid the reaction to occur completely unless an extra reducing agent is added. For this reason, 5 equivalents of NaH were further included in the reaction medium. Solid NaH decomposes at ~ 380 °C,[136] so the salt solvent was chosen such that it possess a lower melting point, in order to enable the reaction in the molten state. Consequently, the eutectic mixture of LiCl/KCl (T_f = 342 °C) was used.[137] Finally, we doubled the stoichiometric quantity of $NaAlCl_4$ as numerous reports recognize the need of an excess of Al.[69,73,82,84] So the final reagents ratio used was $FeCl_2$:$NaAlCl_4$:$NaBH_4$:NaH = 2:2:2:5.

$$5\ H^-(sol) + 2\ Fe^{2+}(sol) + Al^{3+}(sol) + 2\ BH_4^-(sol) \rightarrow Fe_2AlB_2(s) + 6.5\ H_2(g) \quad \textbf{Equation VII. 1}$$

Several parameters were screened under this scheme, most notably the reaction temperature and time. The recovered crystalline phases are summarized in the **Table VII. 1**. Although the targeted phase was not retrieved as a major product for any of the tested conditions, two important observations were made: **(i)** FeB is formed at low temperature despite the presence of aluminium in the medium, meaning that it is an intermediate to the Fe_2AlB_2 formation. **(ii)**

Table VII. 1. Conditions screening and retrieved phases for the synthesis of Fe_2AlB_2 through all-ionic precursors.

t (h) / T (°C)	0.5	1	3
600	FeB > amorphous	FeB > amorphous	FeB > amorphous
800	FeB > FeAl > Al_2O_3 > $Al_{2.67}O_4$	FeB > FeAl > Al_2O_3 > $Al_{2.67}O_4$	FeB > Al_2O_3 > $Al_{2.67}O_4$
1000	FeB > Al_2O_3 > $Al_{2.67}O_4$ > **Fe_2AlB_2**	FeB > Al_2O_3 > $Al_{2.67}O_4$ > **Fe_2AlB_2**	FeB > Al_2O_3 > $Al_{2.67}O_4$ > **Fe_2AlB_2**

The Fe_2AlB_2 crystallization is achieved only at the highest temperature of 1000 °C. These clues are what triggered the exploration of the synthesis from the as-synthesized FeB compound in the next section.

FeB-based synthesis

Impregnation

In order to favour the Al incorporation, the FeB surface needs to be accessible, which is not the case in the as-synthesized product due to the particle's aggregation. To solve this issue, an impregnation protocol was developed, where the particles were dispersed in a non-binding solvent (toluene in principle) and then abruptly mixed with previously ground LiCl/KCl salt in order to avoid re-aggregation. The solvent excess was later evacuated by applying vacuum. A scheme of the procedure is depicted in the **Figure VII. 1**.

In order to be able to compare directly to the all-ionic reagents synthesis, the reagents and ratios used were identical (α-FeB:$NaAlCl_4$:NaH = 2:2:5). This time, the Fe_2AlB_2 phase was indeed retrieved as a major phase, along with Al_2O_3 impurities from the Al excess and unreacted FeB. Albeit, the synthesis showed poor reproducibility, and the purity varied from 40 to 70 % *wt.* between batches. The origin of this irreproducibility was traced to the dispersibility of the particles during the impregnation process. Toluene indeed does not yield a stable suspension of the α-FeB particles, probably due to the poor compatibility between the apolar solvent and charged surface groups of α-FeB after its washing. Therefore, a test with methanol as dispersing solvent was made to evaluate the difference. Methanol being a coordinating solvent, it could

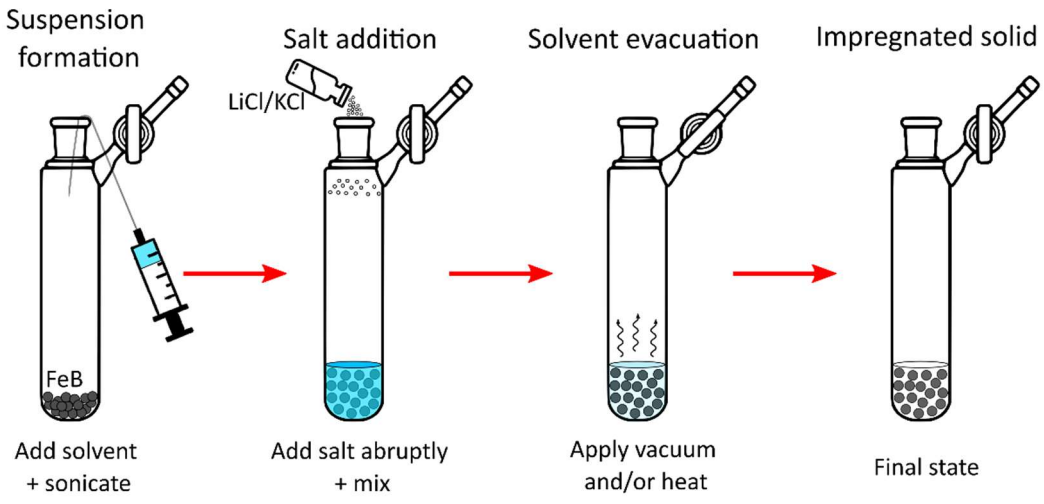

Figure VII. 1. Salt-impregnation procedure scheme.

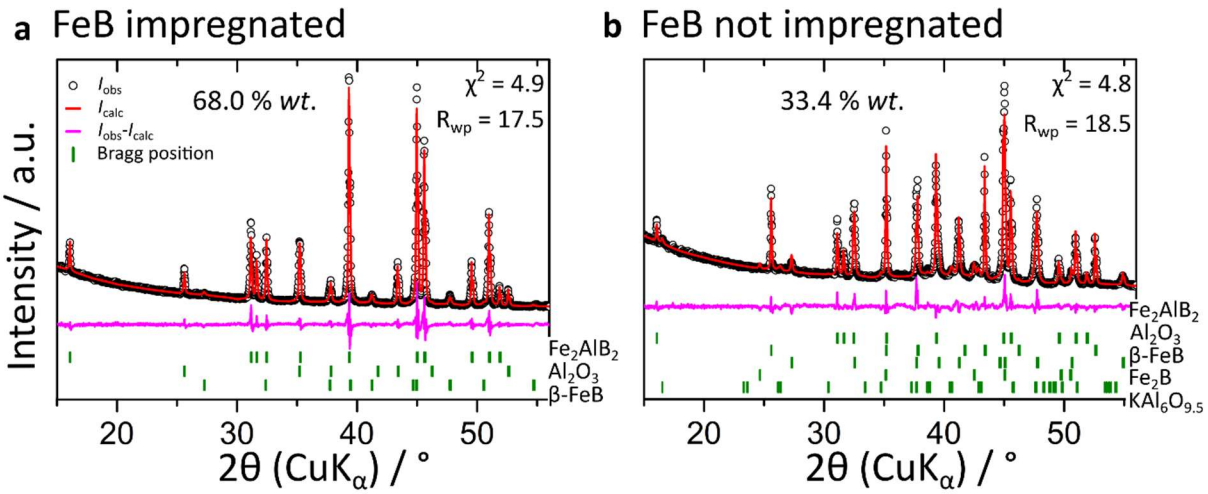

Figure VII. 2. Fe_2AlB_2 synthesis from α-FeB with **(a)** and without **(b)** employing the impregnation procedure.

not be completely removed by typical Schlenk line vacuum levels (10^{-3} mbar), so the mixture needed to be heated up to 150 °C, which may in principle have caused oxidation risks. Still, the use of methanol indeed allowed to retrieve a relatively acceptable and repeatable product purity (see the Rietveld refinement in **Figure VII. 2a**), although still a significant amount of Al_2O_3 and FeB is recovered. The importance of the impregnation step was further recognized by performing a blank reaction where the impregnation is bypassed while keeping the rest of the parameters equal (α-FeB:$NaAlCl_4$:NaH = 2:2:5). The XRD results and corresponding Rietveld refinement shown in **Figure VII. 2b** exposes how the purity was reduced to less than half when FeB is not impregnated. This proved the importance of the impregnation and of the solvent used for this purpose to assure the formation of a stable suspension.

Optimization through the excess of Al source and purification

The fact that both FeB and Al_2O_3 were recovered after the reaction indicated that the reaction was not completed. A possible hypothesis to force completion is to further provide Al excess to displace the equilibrium towards the products. The way to provide this Al input excess actually depends on the mechanism of the reaction. Either a higher amount of $NaAlCl_4$ could be introduced, which is a direct way to provide extra Al but in oxidation state 3+. Alternatively, if the NaH excess is increased, that would favour Al^{3+} reduction to Al^0 and thus serve as an Al^0 excess provider. One or the other strategy would work depending on which specie is actually inserted into the FeB structure. Ultimately, both strategies can be combined. These parameters have been screened and the XRD results are summarized in **Figure VII. 3**.

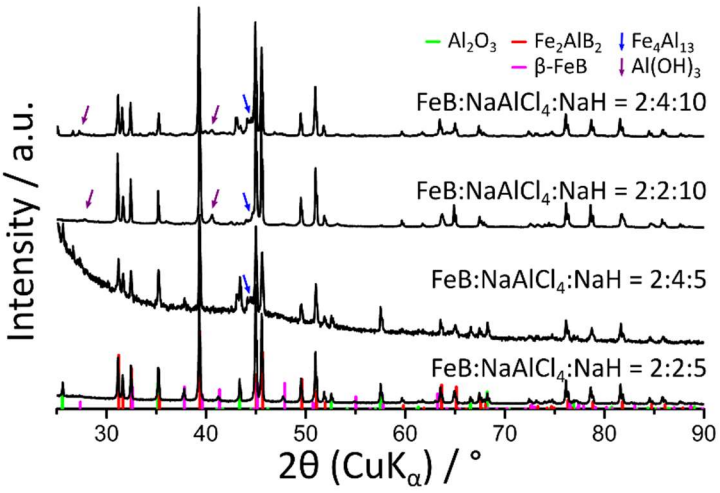

Figure VII. 3. Synthesis of Fe_2AlB_2 from α-FeB with different variations of the $NaAlCl_4$ and NaH excess input.

Further Al^{3+} excess alone (FeB:$NaAlCl_4$:NaH = 2:4:5) did not affect significantly the product purity, with still FeB and Al_2O_3 retrieved as impurities along with Fe_4Al_{13}. Adding a NaH excess alone (FeB:$NaAlCl_4$:NaH = 2:2:10) resulted in complete reaction of FeB. Some Al-rich by-products are retrieved, notably Fe_4Al_{13} and $Al(OH)_3$, but also traces of Fe_3Al and $LiAl_5O_8$ (not marked in **Figure VII. 3**). Combining excesses of $NaAlCl_4$ and NaH (FeB:$NaAlCl_4$:NaH = 2:4:10) delivered a similar product purity but larger yield.

In the end, the reagents ratio was optimized to FeB:$NaAlCl_4$:NaH = 2:3:10 showing the highest yield at similar purity levels. Even though the purity was lower than for the FeB:$NaAlCl_4$:NaH = 2:2:5 synthesis (60 % *vs*. 68 % *wt*. as shown in **Figure VII. 4a**), the Fe_4Al_{13}, $Al(OH)_3$, Fe_3Al

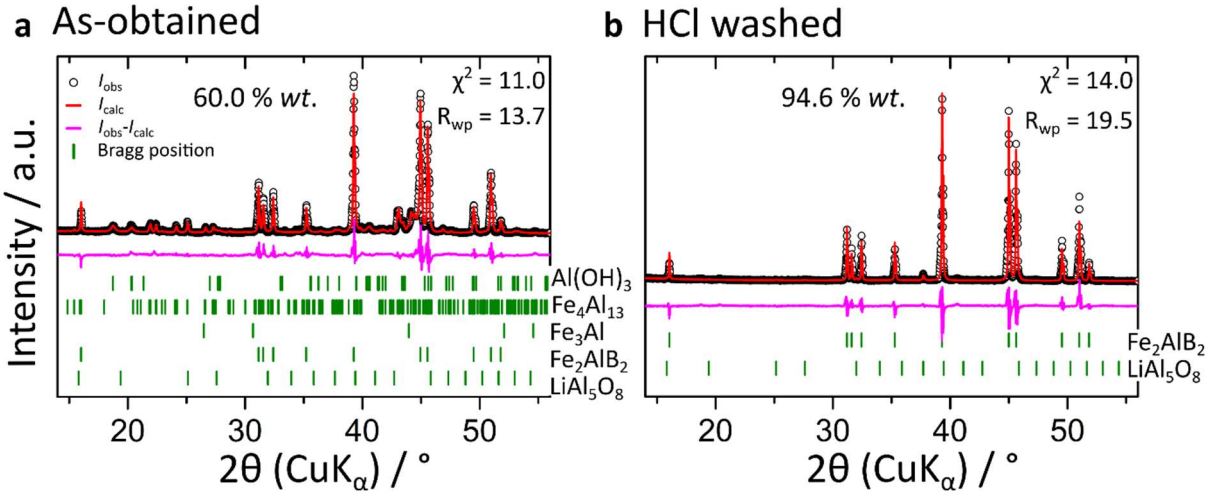

Figure VII. 4. Rietveld refinement of the Fe_2AlB_2 product as synthesized from the reagents α-FeB:$NaAlCl_4$:NaH = 2:3:10. **(a)** As-synthesized product. **(b)** Product after HCl washing.

and $LiAl_5O_8$ impurities are soluble in acidic conditions, contrary to Al_2O_3. Albeit, so is the Fe_2AlB_2 phase, although at a slower rate than the other products and at a faster rate than FeB, as evidenced by a washing test with a sample containing both compounds (not shown). This last point again pleads in favour of the FeB:$NaAlCl_4$:NaH = 2:3:10 ratio in order to consume all the FeB precursor. Washing was performed with a 1:1 v/v dilution of HCl 38 %. A high purity product (94.6 % *wt*.) was retrieved after washing, as shown by the Rietveld refinement in **Figure VII. 4b**. However, washing also partially dissolved the Fe_2AlB_2 phase, as in average it dissolved 88 % of the product, thus resulting in only a small amount (10 – 18 mg) of product. Attempts to perform a softer washing by using more diluted HCl proved unsuccessful as they do not dissolve the impurities.

Structural evolution of Fe_2AlB_2 in molten salts: design of an *in-situ* oven

To screen delamination conditions and study the structural evolution of Fe_2AlB_2 while counting with *circa* 15 mg of sample per batch, standard *ex-situ* experiments were not viable timewise. Instead, we decided to approach the upcoming studies with synchrotron-based *in-situ* X-ray diffraction, for which a large amount of information can we withdrawn out of ~ 2 mg of sample per experiment. Synchrotron-based *in-situ* and *operando* experiments are nowadays at their zenith, and so is the sample environment technology required to carry them out.[138,139] In the field of synthetic chemistry, great advances have been made in mimicking laboratory tools in such a way that is compatible with synchrotron beamlines. In 2008, Chupas *et al*. introduced a horizontal flow furnace where both sample atmosphere and temperature could be controlled.[140] The system proved very fruitful in identifying new metastable phases in ternary sulphides. *In-situ* XRD monitoring of the reaction between Cu or Sn with K_2S_3 or K_2S_5 led to the discovery of reaction intermediates that were actually new phases: $K_3Cu_4S_4$, $K_6Sn_2S_7$, $K_4Sn_2S_6$ and $K_5Sn_2S_8$.[141] Beyond the isolation of novel compounds, *in-situ* measurements can also serve to elucidate reaction mechanisms. More recently, the furnace design was adapted to operate vertically and thus stand metal fluxes. Weiland and collaborators used a vertical adaptation of this oven adaptation to probe the evolution of a Ce-Co-Ge-Sn melt towards the $A_{n+1}M_nX_{3n+1}$ homologous series.[142] Albeit, all of the above examples require vessel sealing in order to keep an inert atmosphere.

One essential piece of equipment for synthetic chemistry that still does not count with a sample-environment analogue when it comes to temperatures beyond 300 °C is the Schlenk line, or inert-gas line, which is key for performing the studies in the Fe_2AlB_2 phase delamination.

Indeed, as Al^0 is volatile above 500 °C, operating in an open vessel, under a controlled flow of inert atmosphere appears essential in order to control the elimination of Al species from the vessel. More generally, being able to mimic as close as possible lab scale syntheses and then avoid artefacts due to changes of setup from the lab to the *in-situ* experiments, often at large scale facilities like synchrotron beamlines, is a long-sought objective of the materials synthesis community. This approach has never been reported to study reactions in molten salts under controlled atmosphere. Besides, the low amount of initial product we could achieve is an obstacle in screening reaction conditions and in using standard characterization methods. For

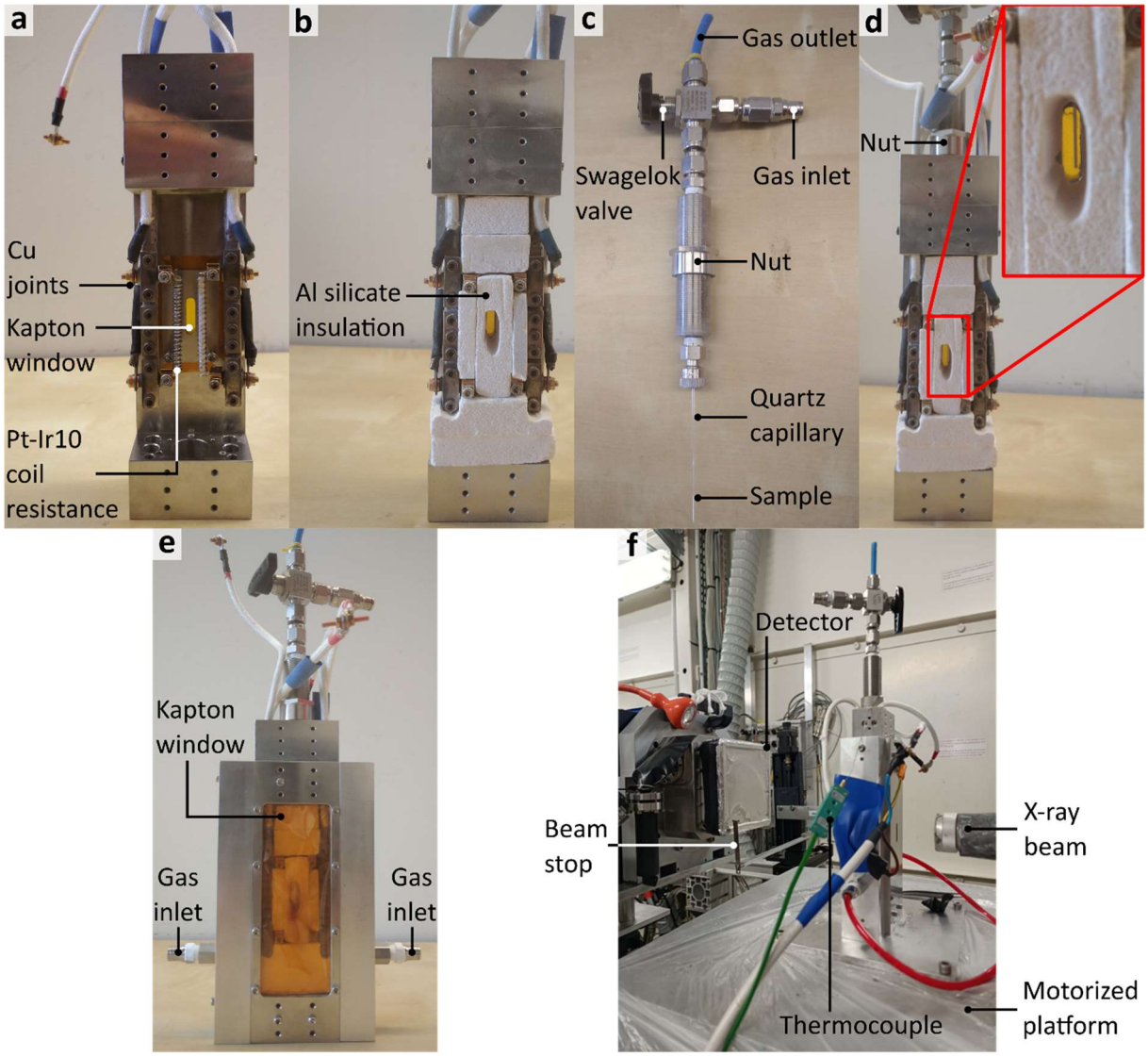

Figure VII. 5. Sample environment mimicking a Schlenk line for *in-situ* synchrotron experiments. The inside of the oven is shown in **(a)** and in **(b)** after adding the thermal insulation. The sample holder is shown independently in **(c)** and within the oven in **(d)**, where the inset shows the positioning of the sample in the aperture for the beam path. **(e)** shows the assembled oven with the side walls and front Kapton window. **(f)** depicts the oven ready for use in the ID11 beamline of ESRF.

all these reasons, we have embarked in the design of our own sample environment to reproduce Schlenk line conditions within a synchrotron beamline.

The skeleton of the sample environment was built in stainless-steel (**Figure VII. 5a**), with a base and a capping piece held together by four vertical pieces. The two pieces destined to be placed through the X-ray beam path contain Kapton windows to diminish spurious signal while keeping a closed atmosphere altogether. The beam entrance window is a narrow vertical slit (**Figure VII. 5a**) to restrict heat loss and allow vertical scanning of the capillary during heating. The exit window is broad (**Figure VII. 5e**) in order to allow collection of a broad angular range. The heating elements are two Pt-Ir10 coil resistances connected in series and powered by a proportional electrical supply, which is controlled through a PID feedback loop temperature programmer using a type K thermocouple to measure the temperature close to the capillary. Heat losses are diminished by surrounding the heating elements and the sample by aluminium silicate insulating material, as shown in **Figure VII. 5b**. In order to restrict the heat dissipation from the Pt-Ir10 coils to oven body, the coils are connected to the external wiring of the oven by copper connectors, for their high thermal and electrical conductivity that minimize Joule effect.

The sample is placed in a quartz capillary of 1.5 mm diameter, itself inserted in a vertical sample holder shown in **Figure VII. 5c**. The shape and size of the sample holder permits its facile loading inside a glove box. In the upper aperture of this sample holder, a 3-way valve allows gas flow in or vacuum atmosphere, gas flow out, and connection to the capillary. This valve can either isolate the sample for ensuring an inert transfer from the glove box to the *in-situ* oven, connect all three conduits for gas flow conditions including purging, or connect just the inlet and sample conduits for vacuum atmosphere. Once inserted in the oven, the sample lies in the aperture destined for the beam path (**Figure VII. 5d** inset). The height of the sample can be regulated by a nut sited in the sample holder's column (**Figure VII. 5c** and **d**) that locks the vertical position at the oven's upper entrance (**Figure VII. 5d**). Finally, the two side vertical walls of the oven (**Figure VII. 5e**) consist of insulating material-filled aluminium walls to further isolate the environment. Two bottom apertures are intentionally left in these side walls in order to provide an inert atmosphere to the inside of the oven. This minimizes the risks of oxidation of the copper connectors. Depending on the X-ray energy and hence the diffuse scattering of the media, He, N_2 or Ar can be used for this purpose. The oven placed and

connected in the ID11 beamline of the ESRF is shown in **Figure VII. 5f**. The data discussed below have been obtained at ID11 with an incident energy of 93.3159 keV.

An issue in adapting lab-scale syntheses to new setups, especially to a much smaller scale, like in a capillary, is the reproducibility of the thermal profiles. The linearity of the heating (cooling) and the accuracy of the temperature within the sample with respect to the measured temperature in the oven must be questioned. This issue is not trivial since for our in-house ovens, the temperature is calibrated for each type of crucible used by placing a thermocouple within the crucible during the calibration. This is not feasible for the *in-situ* oven as a thermocouple inserted into the reaction media would be corroded by the molten salts. Hence, the oven thermocouple was placed next to the capillary, at a height where the sample was present. In order to validate the heating profile, an experiment was performed by heating an MgO standard,

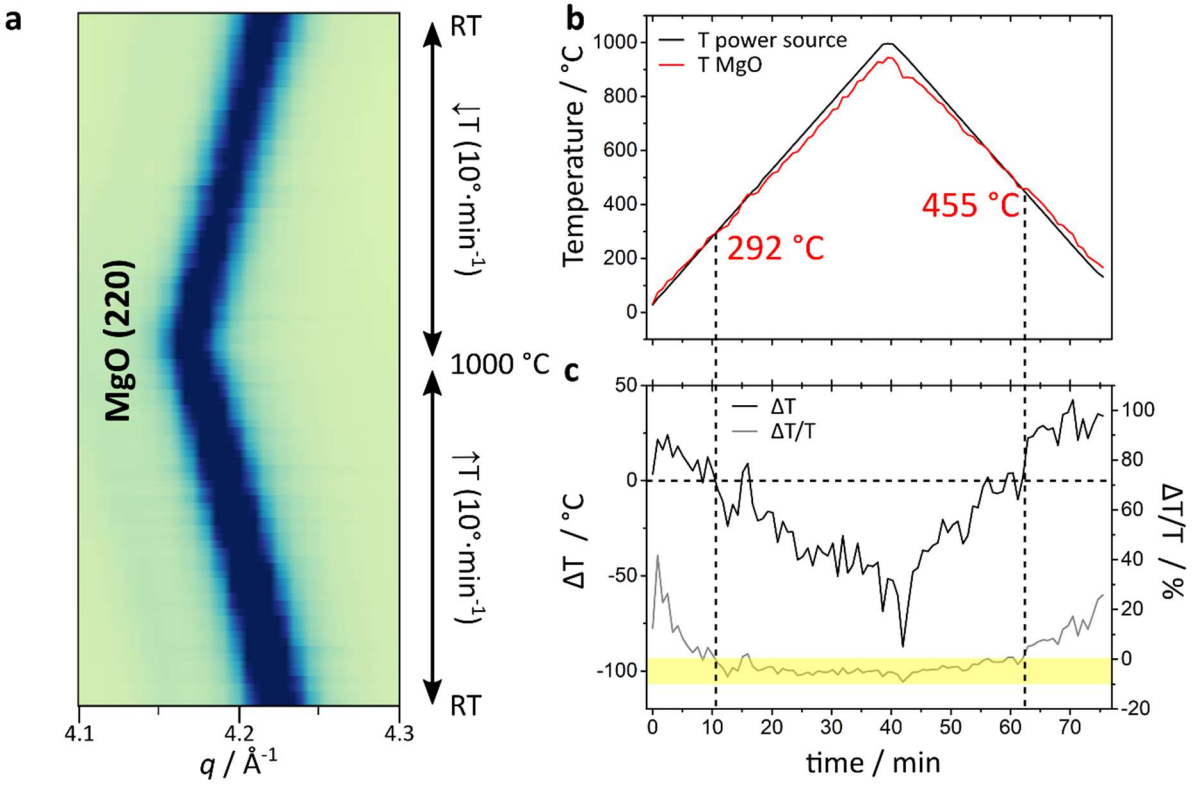

Figure VII. 6. Validation study for the temperature profile delivered by the oven within the sample. **(a)** (220) MgO reflection showing the diffraction peaks shift used to quantify the compound's volume and ultimately the real temperature against the temperature measured by the power supply. **(b)** Power source and MgO temperatures as a function of time. **(c)** Absolute – $\Delta T = T_{MgO} - T_{power\ source}$ – and relative – $\Delta T/T = (T_{MgO} - T_{power\ source})/T_{MgO}$ – temperature difference as a function of time. In yellow a fringe of relative difference of (-5 ± 5) % is marked, while the vertical dotted lines indicate the limits within which the relative difference lies within such range. Horizontal dotted line marks a null difference of temperature.

whose volumetric thermal expansion coefficient evolves from $31.1 \cdot 10^{-6}$ K^{-1} at 27 °C to $47.7 \cdot 10^{-6}$ K^{-1} at 1027 °C.[143–145] The thermal expansion (contraction) upon heating (cooling) was evidenced by the peaks shift as exemplified for the (220) reflection in **Figure VII. 6a**. Sequential Le Bail refinement for all the acquired patterns allowed to retrieve MgO cell volume as function of the temperature, which could be correlated to the temperature of MgO according to the thermal expansion equation (**Equation VII. 2**).

$$\alpha_V = \frac{\Delta V}{V_0 \Delta T}$$ **Equation VII. 2**

α_V	Volumetric thermal expansion coefficient
ΔV	Volume change
V_0	Initial volume
ΔT	Temperature change

The results suggest that the heating system does assure a linear heating (cooling) profile for the standard 10 °C·min^{-1} ramp, as shown in **Figure VII. 6b** and **VII. 7**. There is a slight discrepancy between the temperatures measured next to capillary and inside, which goes from slightly positive ΔT ($\Delta T = T_{MgO} - T_{power\ source}$) at low temperatures to increasingly negative for the highest temperatures. However, past a threshold of temperature, the relative difference of temperature (ΔT/T) stabilises at a very low value of (-5 ± 5) %, as marked in yellow in **Figure VII. 6c**. This threshold is of 292 °C during heating and 455 °C upon cooling. This is at the same

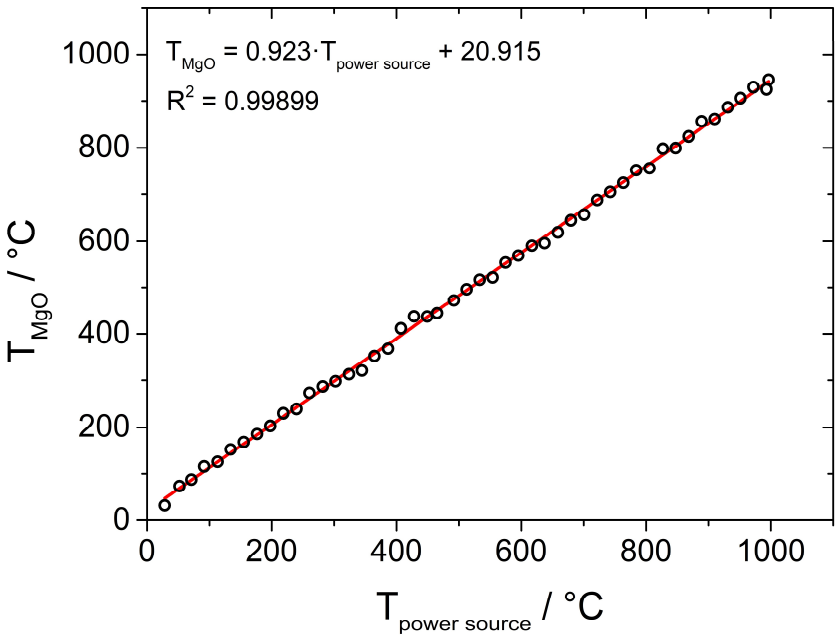

Figure VII. 7. Temperature calibration of the *in-situ* oven.

point where the difference of temperature ΔT becomes negative, which may indicate that a regime limited by heat transfer becomes operative at that point, and thus governs the error. The temperature threshold increases when cooling probably due to thermal inertia. All in all, the oven allows to work safely in a linear regime for the temperature range from *ca*. 300 °C to at least up to 1000 °C. The imposed temperature and the actual one in the sample differ by only 5 % for the high temperatures, which is in fact the range of temperatures for which the oven is designed. This difference can be easily corrected by the determined $T_{power\ source}$ / T_{MgO} calibration as depicted in **Figure VII. 7**. Furthermore, since we are going to work mostly with molten salts as solvent, the melting point can serve as internal standard for the temperature, albeit providing a single point calibration point, so still the external calibration is needed. The absolute temperature is not needed for internal comparison between *in-situ* experiments, but it is essential for extrapolating and comparing to in-house synthesis.

Fe_2AlB_2 formation mechanism and α-FeB vs. β-FeB as precursor

The successful results on the synthesis of Fe_2AlB_2 from α-FeB motivated us to gain more insights in the reaction mechanism towards the ternary compound. The literature reports how using β-FeB and Al as precursors towards Fe_2AlB_2 instead of the individual elements has improved yield, purity and reproducibility.[84,146] The rationale underlying the use of β-FeB was pre-mixing of Fe and B in the right stoichiometry within a compound bearing several structural similarities with Fe_2AlB_2. Still, the synthesis of β-FeB itself requires temperatures above 1100 °C, much higher than α-FeB, which forms already at 400 °C. To the best of our knowledge, α-FeB has not been explored as a precursor to Fe_2AlB_2, probably because of the lack of structural insight into α-FeB.

We firstly assessed the mechanism of transformation of α-FeB to Fe_2AlB_2. For this purpose, we employed synchrotron-based *in-situ* X-ray diffraction to monitor the species formed as a function of the temperature, by acquiring an XRD pattern every minute in transmission mode through the reaction medium with a composition identical to the lab-scale synthesis. The diagrams are plotted against the reaction time as a heatmap in **Figure VII. 8**. The low concentration of reagents and the diffuse scattering of the molten medium hindered peaks' signal, although they were indeed observable. Interestingly, Al^0 formation was detected upon the disappearance of the NaH peaks at *ca*. 380 °C, when the salt completely melted. α-FeB remained up to ~ 845 °C, when the Fe_2AlB_2 peaks appeared. The peak position mismatch to the reference was attributed to thermal dilatation. No signs of the characteristic reflections of

β-FeB (absent in α-FeB) were detected, thus indicating a direct reaction from α-FeB to Fe_2AlB_2. These results support the hypothesis that Al^0 is firstly formed *in situ* before being inserted inside α-FeB to yield Fe_2AlB_2, according to **Equations VII. 3** and **VII. 4**. This is also in line with the fact that higher NaH excess rather than $NaAlCl_4$ excess led to completion of the reaction, as discussed above.

$$NaAlCl_4(s) + 3\ NaH(s) \rightarrow Al(s) + 4\ NaCl(s) + 1.5\ H_2(g) \qquad \textbf{Equation VII. 3}$$

$$2\ \alpha\text{-FeB}\ (s) + Al(s) \rightarrow Fe_2AlB_2(s) \qquad \textbf{Equation VII. 4}$$

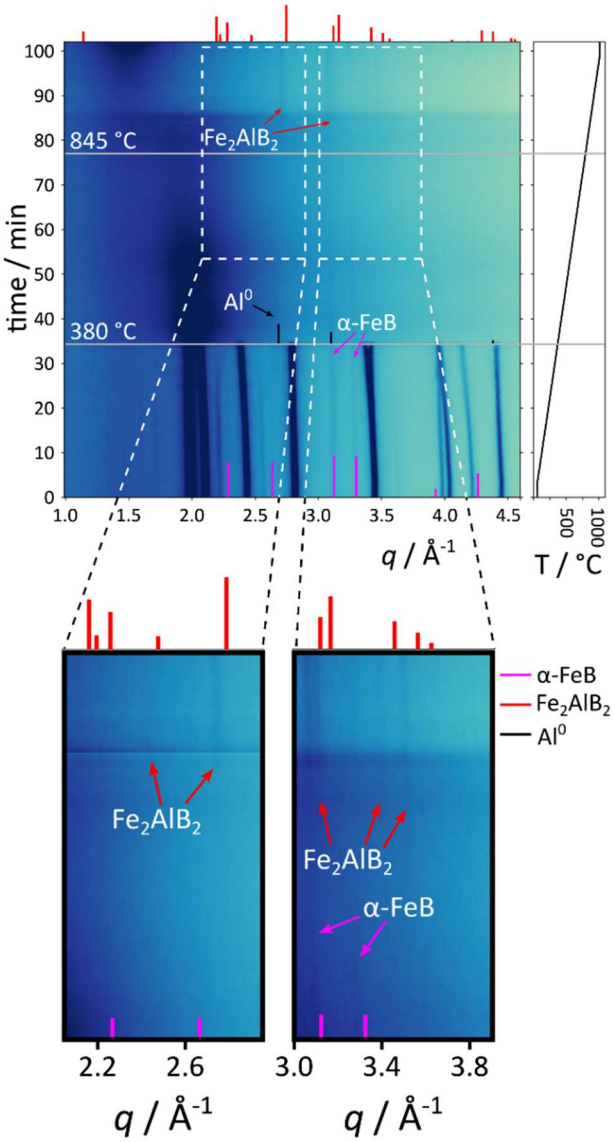

Figure VII. 8. Synchrotron *in-situ* XRD study of the α-FeB → Fe_2AlB_2 transformation.

β-FeB was reacted following the same protocol as the optimized one for α-FeB, that is FeB:$NaAlCl_4$:NaH = 2:3:10, heating at 1000 °C for 1 h. The XRD diagram of the recovered powder is shown in **Figure VII. 9a**. The product of both exhibits the reflections of Fe_2AlB_2 as major phase, although with a significantly lower purity of 42.8 % *wt*. *vs*. 60.0 % *wt*. when α-FeB was used. This can be linked to the structural similarity of the CrB-type component of the α-FeB intergrowth to the Fe_2AlB_2 product, which ensures a topotactic transformation of these domains. The *in-situ* study with β-FeB showed an identical reaction sequence to the α-FeB reaction (**Figure VII. 9b**), with similar temperatures of structural transitions. This indicates that the β-FeB nanodomains in α-FeB are the limitans in the Al incorporation, as they

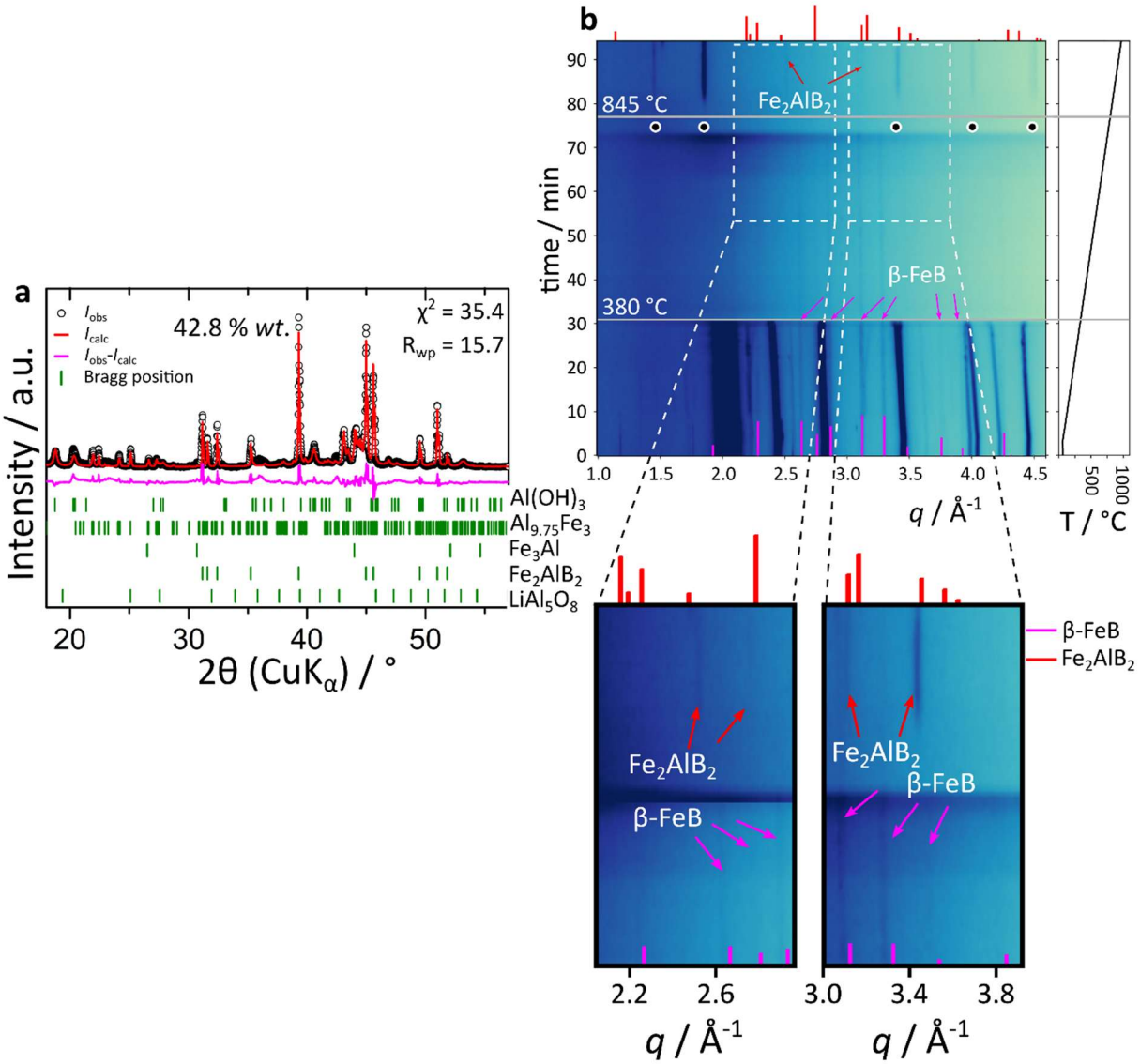

Figure VII. 9. Synthesis of Fe_2AlB_2 from β-FeB. **(a)** XRD diagram of the recovered powder. **(b)** Synchrotron XRD *in-situ* study. SiO_2 impurities coming from the quartz capillary crystallization in the presence of NaH are marked with black dots.

require a larger structural rearrangement to render the Fe_2AlB_2 structure. Consequently, α-FeB could replace advantageously β-FeB as a precursor to produce Fe_2AlB_2, since it ensures higher Fe_2AlB_2 purity and can be produced at 400 °C, against 1100 °C for β-FeB, thus ensuring lower energy consumption. Noteworthy, during the *in-situ* scan, SiO_2 crystallization from the quartz capillary is observed at higher temperatures (marked with black dots in **Figure VII. 9b**), which is an artifact due to the interaction of the capillary with NaH decomposition products.

Delamination of Fe_2AlB_2 in molten salts

Classical delamination of Fe_2AlB_2 by acidic washing was attempted without satisfactory results. HCl or HF washing either completely dissolved the compound, or did not trigger noticeable structural changes. Alternative delamination paths were then explored. We proposed the use of the molten-salts delamination method first reported by M. Li[17] and Y. Li[53] for MAX phases, as described in **Chapter V**.

According to the guidelines offered by Y. Li with respect to the choice of the delaminating salt (see **Figure V. 6** in **Chapter V**), Cu^{2+}, Ni^{2+}, Ag^{+}, Co^{2+}, Fe^{2+}, Cd^{2+}, Mn^{2+} and Zn^{2+} would all provide a sufficiently elevated reducing potential to trigger Al oxidation. $CuCl_2$ was first used as it provides the highest reducing potential of those listed as plausible candidates. Fe_2AlB_2 was then mixed with $CuCl_2$ at a ratio Fe_2AlB_2:$CuCl_2$ = 2:3, which matches the stoichiometric ratio of the envisioned reaction (**Equation VII. 5**).

$$2\ Fe_2AlB_2(s) + 3\ CuCl_2(l) \rightarrow 2\ Fe_2B_2(s) + 3\ Cu(s) + 2\ AlCl_3(g)\uparrow \qquad \textbf{Equation VII. 5}$$

The mixture was then heated in the *in-situ* oven and XRD diffractograms were recorded as a function of the temperature at the ID11 beamline of ESRF. It must be noted that this experiment was performed in September 2021, at that time the synthesis and washing of Fe_2AlB_2 was not completely optimized, so Al_2O_3 and FeB impurities were still present. In **Figure VII. 10a**, the results of this experiment are shown as a heatmap against temperature for the restricted range 400 – 800 °C for clarity. $CuCl_2$ was reduced, as metallic Cu was detected past the 400 °C, as expected. The reduction of $CuCl_2$ was accompanied by oxidation of Fe_2AlB_2, especially of the Fe atoms, as $FeCl_2$ was detected. Note that this redox reaction occurred even before $CuCl_2$ had melted (T_m = 498 °C). Overall, the oxidative power of $CuCl_2$ was too strong to enable selective etching of Al. Above 500 °C, Fe_2AlB_2 began to decomposes to Fe_2B.

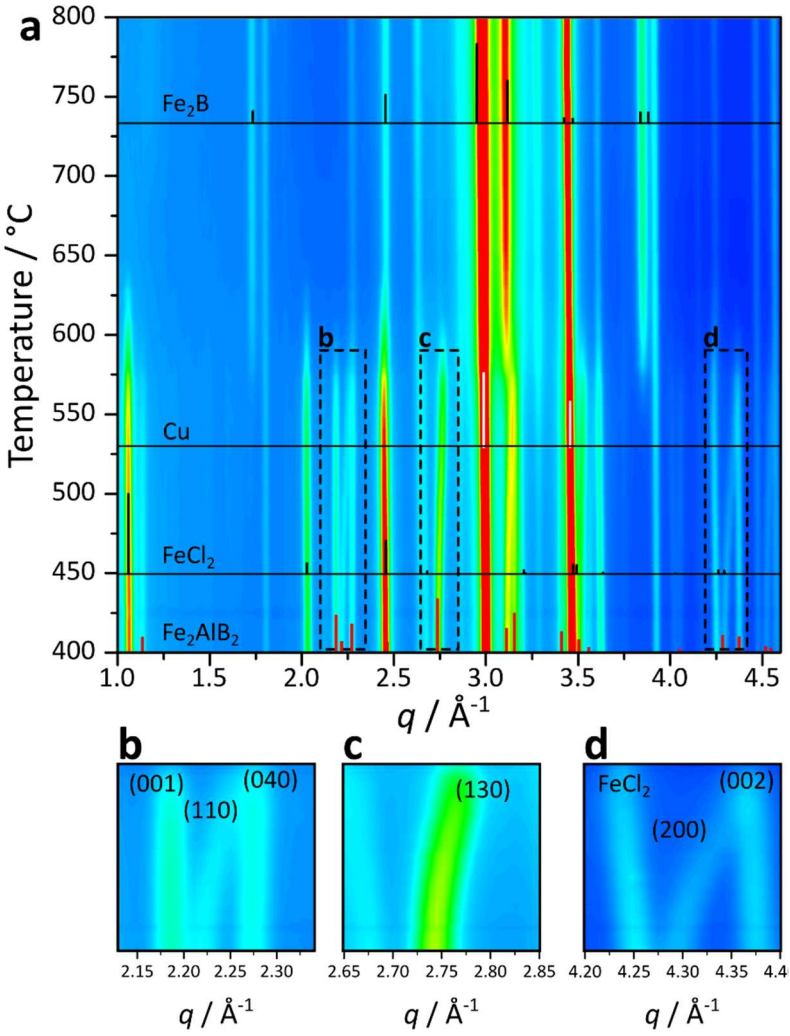

Figure VII. 10. *In-situ* XRD study of Fe_2AlB_2 delamination attempt with $CuCl_2$ **(a)** and blank experiment without delaminating salt **(b)**. **(c)**, **(d)** and **(e)** show the magnification areas marked in **(a)**.

Noteworthy, between 400 and 600 °C some Bragg peaks from Fe_2AlB_2 shifted to higher *q* values while the temperature was increasing, contrary to what would be expected from conventional thermal expansion. This point will be discussed in details in the following section. As $CuCl_2$ is a too strong oxidant for Fe_2AlB_2, we explored less oxidative salts: $CoCl_2$, $FeCl_2$, $CdCl_2$ and $ZnCl_2$. Also, since Fe_2AlB_2 is subject to structural changes above 500 °C as observed for the Fe_2AlB_2:$CuCl_2$ experience, we sought to lower the salts melting point by mixing with an inert salt that would form a eutectic at a given composition. We chose NaCl as it forms eutectic mixtures with all the listed divalent chlorides and allows to lower significantly the salts melting point: $CoCl_2$ (from 798 to 359 °C), $FeCl_2$ (from 671 to 372 °C), $CdCl_2$ (from 564 to 325 °C) and $ZnCl_2$ (from 313 to 249 °C).[137] The mixtures were prepared such that they yield the Fe_2AlB_2:MCl_2 (M = divalent cation) ratio of 2:3 and the MCl_2:NaCl ratio corresponding to

the eutectic composition. The samples were heated up to 600 °C. The results of the *in-situ* scans are shown in **Figure VII. 11**.

Some of the mixtures were reactive even before heating, during the ball-milling process used to homogenize the mixtures. For instance, $CoCl_2$ may have contained moisture from the start, as the initial mixture reacted to form Al_2O_3, $Na_{0.5}Al_{0.5}ClO_{0.5}$ and $Al_2BO_{4.5}$. Also, $ZnCl_2$ reacted at room temperature with NaCl to form Na_2ZnCl_4. Other mixtures formed stoichiometric compounds upon heating, like $FeCl_2 + 6NaCl \rightarrow Na_6FeCl_8$, $CdCl_2 + 2NaCl \rightarrow Na_2CdCl_4$, $Na_2CdCl_4 + CdCl_2 \rightarrow 2NaCdCl_3$. $ZnCl_2$ showed a phase transition from tetragonal (*t*-$ZnCl_2$) to

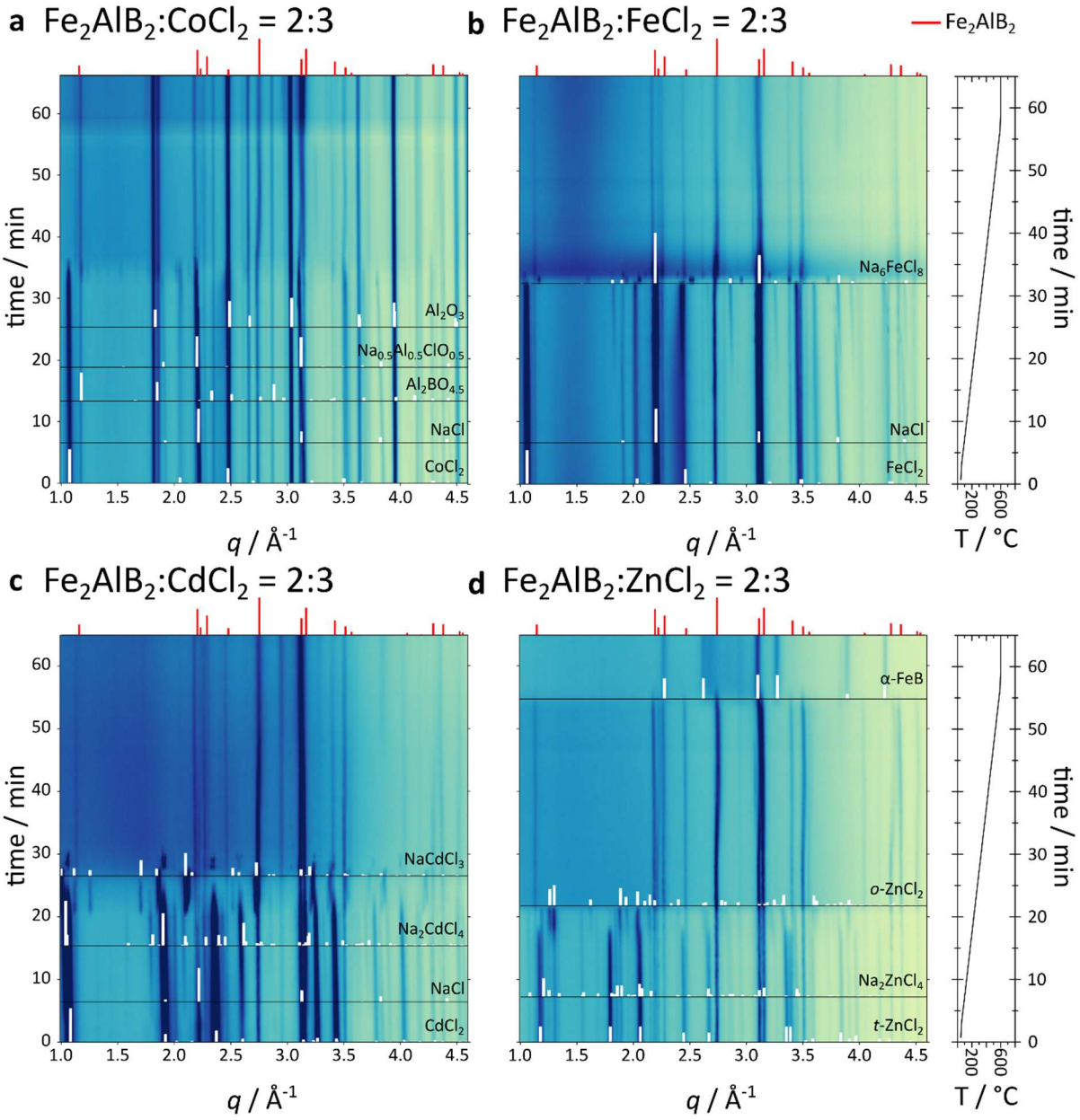

Figure VII. 11. *In-situ* XRD of Fe_2AlB_2 delamination attempt with MCl_2/NaCl eutectic salts in Fe_2AlB_2:MCl_2 ratio of 2:3 for M = Co **(a)**, Fe **(b)**, Cd **(c)**, Zn **(d)**.

orthorhombic $ZnCl_2$ (*o*-$ZnCl_2$). All these transformations occurred at relatively low temperature and before the melting point, without noticeable impact on the peaks attributed to Fe_2AlB_2. At higher temperature, none of the mixtures showed evidence of delaminating Fe_2AlB_2, as the corresponding (020) peak at q = 1.14 $Å^{-1}$ was not significantly altered. Instead and in all cases, Fe_2AlB_2 only showed the previously described shrinkage of the *a* axis between 500 and 600 °C. Only the Fe_2AlB_2:$ZnCl_2$ experiment exhibited a distinct behavior, where Fe_2AlB_2 decomposed to α-FeB near 600 °C. This could indicate that Al was etched out of the ternary structure and that the remaining Fe_2B_2 transformed to the more stable α-FeB polymorph. We attempted to evidence if an intermediate state between Fe_2AlB_2 and α-FeB could contain the 2D-Fe_2B_2 polymorph, without success though. At this point we attempted to explain the shrinkage of the *a* axis behavior as this seems to precede the phase's decomposition and may be linked to a possible delamination or structural transformation.

Thermal behavior of Fe_2AlB_2

***In-situ* studies**

Between 400 and 600 °C, a peak shift to higher q values for Fe_2AlB_2 reflections with $h \neq 0$ (**Figure VII. 10b-d**) was observed in all *in-situ* experiments. In contrast, the peaks with $h = 0$ seem to follow conventional thermal expansion (**Figure VII. 10b** and **d**). This denotes an anisotropic shrinkage of the unit cell, particularly involving the *a* axis. This result was unexpected, because it is not in agreement with previous reports that indicate that Fe_2AlB_2 is stable under argon up to at least 1200 °C[75] or decomposes directly to FeB, depending on the synthetic origin of the compound.[147–149] Besides, a conventional positive expansion coefficient has already been reported for Fe_2AlB_2.[147] As the only major difference between our sample and that in the literature is the surface state, we can propose the hypothesis that this is responsible for the unique behavior of our Fe_2AlB_2 compound. Indeed, the surface of Fe_2AlB_2 is oxidized due to the water washing, these surface oxides could react with the sample at high temperature.

In light of the systematic observation of the lattice shrinkage, particularly in the *a* direction, we decided to characterize more deeply this behavior. To get deeper insights into the transformation, we performed an *in-situ* thermal treatment of the Fe_2AlB_2 alone, but now with a sample without Al_2O_3 nor FeB impurities. In a first experiment, we monitored the thermal behavior up to 550 °C with a 10 min plateau, followed by heating to 600 °C with a 25 min

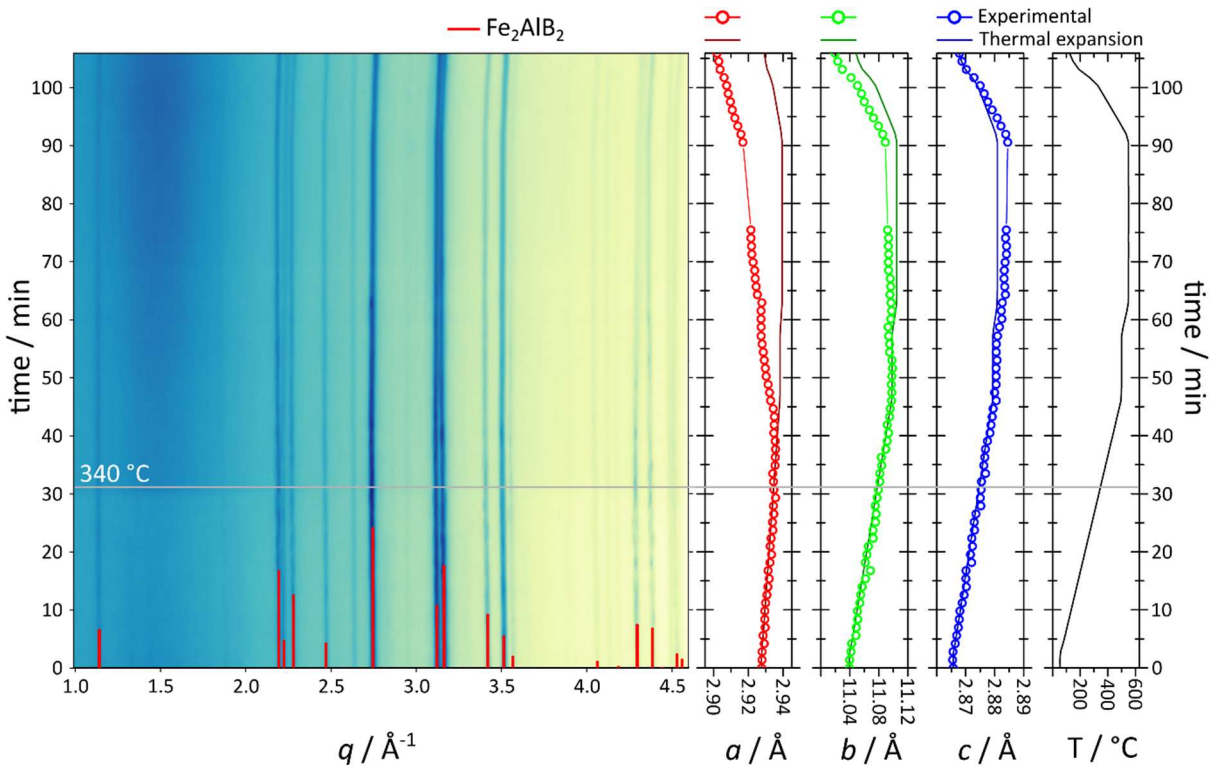

Figure VII. 12. *In-situ* XRD study of Fe_2AlB_2 along with the empirical temperature profiles and the refined lattice parameters from sequential Rietveld refinement. In each lattice parameter plot, the refined parameters are plotted as a scatter + line, and compared to the lattice parameters expected from thermal expansion in straight line.

plateau. After cooling down, we could recover the sample for further *ex-situ* analysis. We then performed sequential Rietveld refinements for all the diagrams to monitor structural changes. The refined *a*, *b* and *c* parameters are plotted in **Figure VII. 12** together with the expected values according to the reported linear anisotropic thermal expansion coefficients – $\alpha_a = 8.1(1)\cdot10^{-6}$ K^{-1}, $\alpha_b = 11.9(2)\cdot10^{-6}$ K^{-1}, $\alpha_c = 10.7(3)\cdot10^{-6}$ K^{-1} –.[147] Refinement confirms that the *a* lattice parameter shrinks above 340 °C. Since the complete decomposition of the compound was avoided and the material could be recovered, we demonstrate that the shrinkage is non-reversible, thus confirming the hypothesis that negative thermal expansion is not responsible. Interestingly, the *b* axis also shrinks to a certain extent, although not as much as the *a* value, which by the end of the thermal treatment is contracted by 0.93 %. The *c* axis seems to expand beyond the thermal expansion prediction, which can be explained by the fact that α for Fe_2AlB_2 actually increases with temperature.[150] The thermal expansion coefficient we used is a mean value measured only up to 500 °C, which probably underestimates values at higher temperatures. The anisotropic α is not reported, so we could not use a more refined model. In the end, the combination of the lattice parameters change gives a volume contraction of 0.99 %.

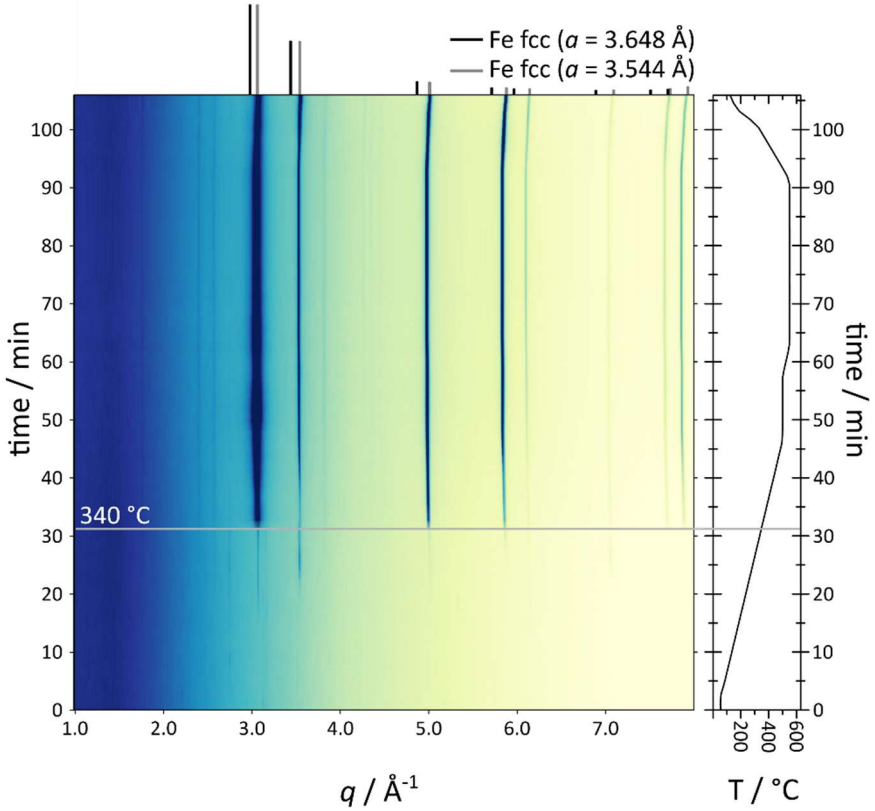

Figure VII. 13. *In-situ* XRD study of Fe_2AlB_2 thermal treatment probing 5 mm above the sample position.

Because the design of the *in-situ* oven enables to probe the homogeneity of the reaction medium, we have at the same time collected the diffraction patterns 5 mm above the sample position probed in **Figure VII. 13** in an attempt to detect possible expelled atoms responsible for the lattice shrinkage. Indeed, we detected the appearance of a crystalline phase at the same time as Fe_2AlB_2 begins to contract, as shown in **Figure VII. 13**. This phase corresponds to iron fcc, although not with the reported lattice parameter of 3.648 Å,[151] but with a smaller lattice parameter of 3.544 Å. This suggests that this Fe phase might be partially substituted by a smaller element. Out of the elements present in the system, boron is the most likely candidate as its atomic radius of 85 pm is smaller than that of Fe (126 pm), contrary to Al (143 pm).[152] Boron has already shown to be able to form substitutional alloys with Fe up to at least 10 % *at*. in boron.[153] This observation indicates that Fe and B atoms are expelled from the structure upon heating, which explains the lattice shrinkage of Fe_2AlB_2.

To further evidence the nature of the structural change on Fe_2AlB_2, we performed an experiment up to 1000 °C to trigger full decomposition (**Figure VII. 14**). Interestingly, above 900 °C a phase of stoichiometry $Fe_3Al_2B_2$ begins to form. To characterize the transformation, we also performed sequential Rietveld refinement for the whole dataset, paying special attention to the

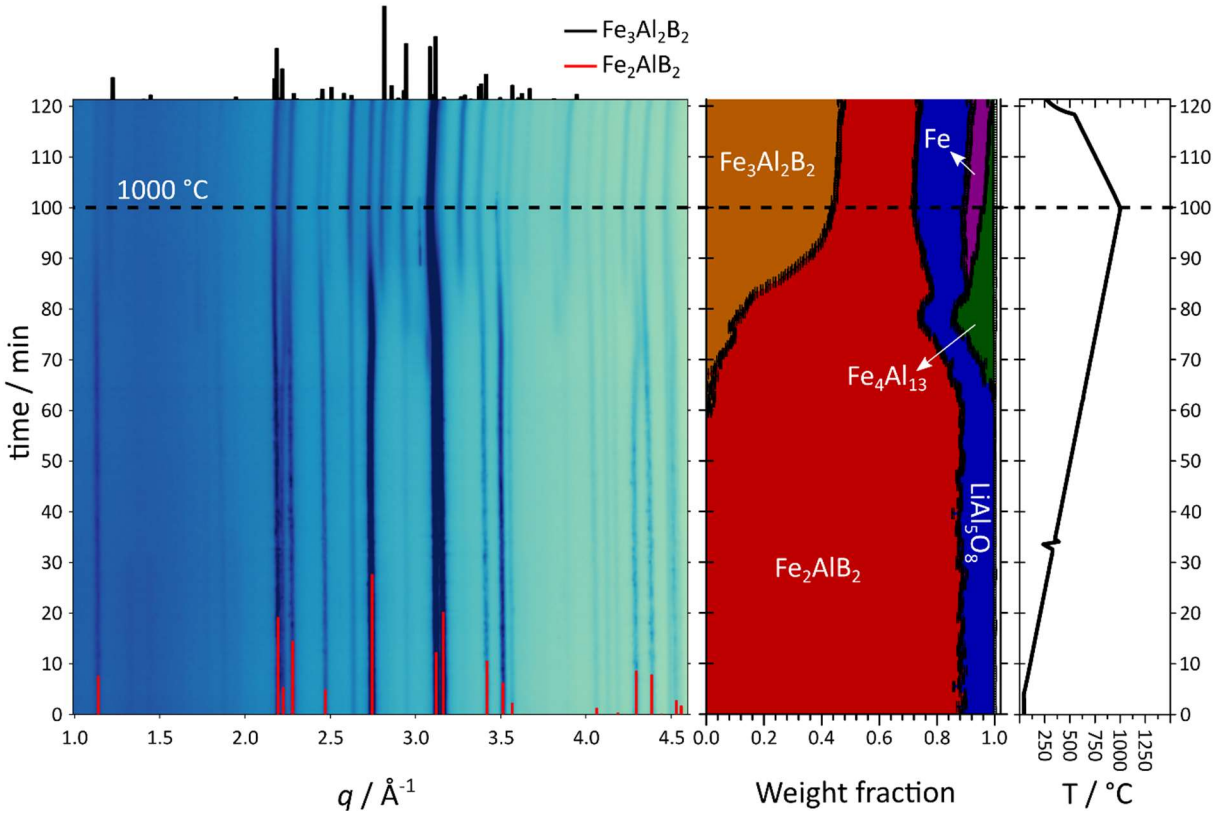

Figure VII. 14. *In-situ* XRD of Fe_2AlB_2 thermal treatment up to 1000 °C along with the empirical temperature profiles and the refined phase fraction against time from sequential Rietveld refinement.

phase fraction distribution throughout the heat treatment. By doing so, we observe that $Fe_3Al_2B_2$ forms at the expense of Fe_2AlB_2. We also detect Fe (fcc) forming during this transformation, in line with the previous results on the structural shrinkage at lower temperature. A possible equation for the transformation is described in **Equation VII. 6**.

$$2Fe_2AlB_2(s) \rightarrow Fe_3A_2lB_2(s) + FeB_\delta(s) + (2-\delta)B(s) \qquad \textbf{Equation VII. 6}$$

This reaction would explain the detection of Fe as a by-product, and the fact that this possesses smaller lattice parameters than conventional Fe fcc, as it would be partially substituted by boron atoms, also expelled from the structure to conceive **Equation VII. 6**. This could also explain the appearance of Fe_2B in the previous experiments of Error! Reference source not found.**10**, as the presence of FeB impurities in that case could change the nature of the by-product to a stoichiometric boride instead of a B-substituted Fe structure. Note that elemental boron is not volatile at such temperatures. Hence, instead of formally B in **Equation VII. 6**, it is possible that oxygenated species may form from the oxidized species at the surface of pristine Fe_2AlB_2, forming B_2O_3, which is volatile above ~700 °C.

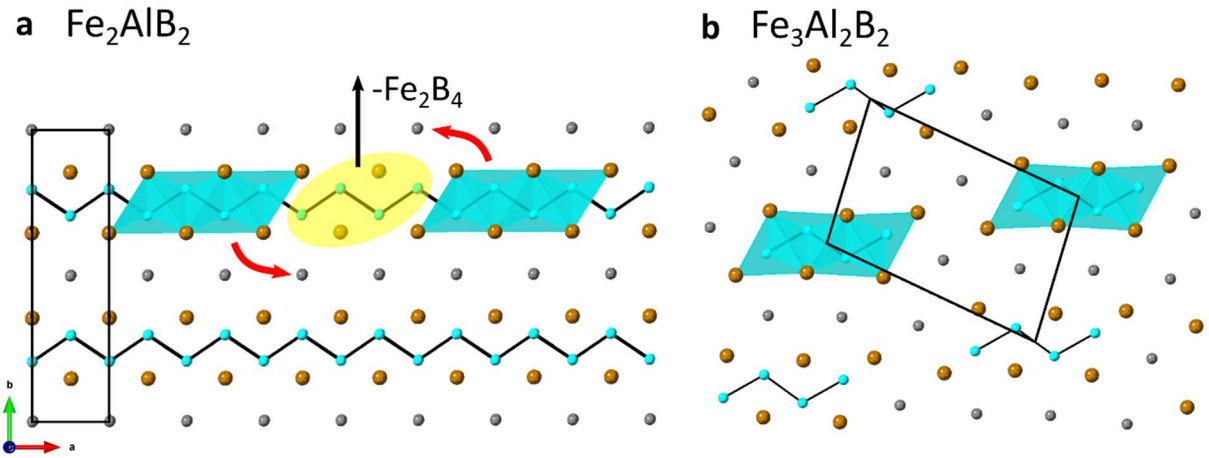

Figure VII. 15. Comparison of structures of Fe_2AlB_2 **(a)** and $Fe_3Al_2B_2$ **(b)**.

We then compare the Fe_2AlB_2 and $Fe_3Al_2B_2$ structures (**Figure VII. 15**) to understand structural transformations underlying **Equation VII. 6**. As we have already discussed, Fe_2AlB_2 consists of infinite layers of Fe_2B_2, stacked along the *b* axis and separated by a layer of Al atoms. Each Fe_2B_2 layer contains zig-zag B chains, coordinated to Fe atoms lying to the exterior of the layers. $Fe_3Al_2B_2$ on the other hand contains isolated portions of the Fe_2B_2 layers that extend to only 4 B atoms chain-length. These units are shifted out-of-plane compared to Fe_2AlB_2. In order to transform Fe_2AlB_2 into $Fe_3Al_2B_2$, firstly the Fe_2B_2 layers must be cut every other Fe_2B_4 moiety as marked in **Figure VII. 15a**. Eliminating such portions already yields the final stoichiometry, but the remaining portions must still follow the movement marked with red arrows in **Figure VII. 15a** in order to reproduce the mismatch in the $Fe_3Al_2B_2$ structure. This movement affects mostly distances in the *a* direction of Fe_2AlB_2, by contracting it, while leaving *b* and *c* practically unaltered. This movement would in fact explain the repeatedly observed shrinkage of Fe_2AlB_2 in the *a* direction, as characterized in the experiment displayed in **Figure VII. 12**. The observed shrinkage of the *a* lattice parameter would then indicate a transient state between Fe_2AlB_2 and $Fe_3Al_2B_2$, where Fe-B vacancies are being generated, which can exist up to a certain extent before leading to the transition towards $Fe_3Al_2B_2$.

Ex-situ studies

In light of the evidence of the *in situ* studies on the thermal behaviour of the synthesized Fe_2AlB_2, we pursued further characterization on the transient state between Fe_2AlB_2 and $Fe_3Al_2B_2$, which can be described as a defective Fe_2AlB_2 containing a significant amount of Fe and B vacancies. To do so, we have reproduced the thermal treatment *ex situ*. In order to account for temperature differences between the *in situ* oven and the in-house ovens (as previously

explained), we performed the *ex situ* study at 550 °C to ensure similar temperature inside the sample. The corresponding XRD pattern and its Rietveld refinement are shown in **Figure VII. 16a**. The refinement further supports the hypothesis of the faulted structure formed upon thermal treatment and demonstrates that it can be recovered at room conditions. First, the trend of lattice parameters is once again observed, especially with the *a* axis shrunk from 2.92806(6) to 2.90932(8) Å, that is a 0.64 % shrinkage, which is a typical amount for the formation of vacancies.[154] Secondly, the peaks widths are enlarged, in part due to a decrease in the crystallite size from 260 to 151 nm and in part because of the appearance of microstrains ($\Delta d/d$ of $1275 \cdot 10^{-6}$). Both effects are in line with Fe and B being expelled from the structure thus engendering point defects that increase the local strain and even probably divide some of the crystallites. Finally, the refined site occupancies are 0.91 and 0.82 for Fe and B respectively. Metallic iron is also recovered in the treated sample, in line with the *in situ* experiments. This time though it is bcc iron and not fcc, which is consistent as the former is the stable phase of iron at room temperature while the fcc arrangement is only thermodynamically stable above

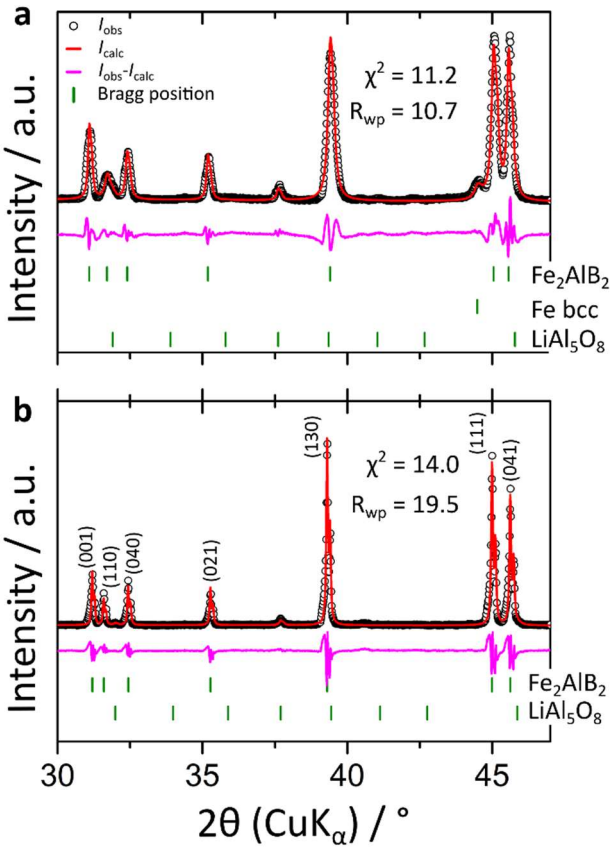

Figure VII. 16. Rietveld refinement of the heat treated Fe_2AlB_2 sample at 550 °C **(a)** in comparison to the pristine Fe_2AlB_2 sample before heat treatment **(b)**.

900 °C and metastable below this temperature.[155] All the retrieved crystallographic information is summarized in the **Table VII. 2**.

Table VII. 2. Crystallographic results of the refined parameters of the Fe_2AlB_2 pristine and heat treated at 550 °C samples.

Parameter	Fe_2AlB_2 pristine	Fe_2AlB_2 heat treated (550 °C)
a (Å)	2.92806(6)	2.90932(8)
b (Å)	11.0333(2)	11.01623(3)
c (Å)	2.86493(6)	2.86658(7)
Volume (Å^3)	92.555(5)	91.873(5)
Average size (nm)	260	151
Microstrain $\Delta d/d$ ($\cdot 10^6$)	0	1275
Fe occupancy	1.0	0.91
Al occupancy	1.0	1.0
B occupancy	1.0	0.82
R_{wp} (%)	14.0	11.2
χ^2	19.5	10.7

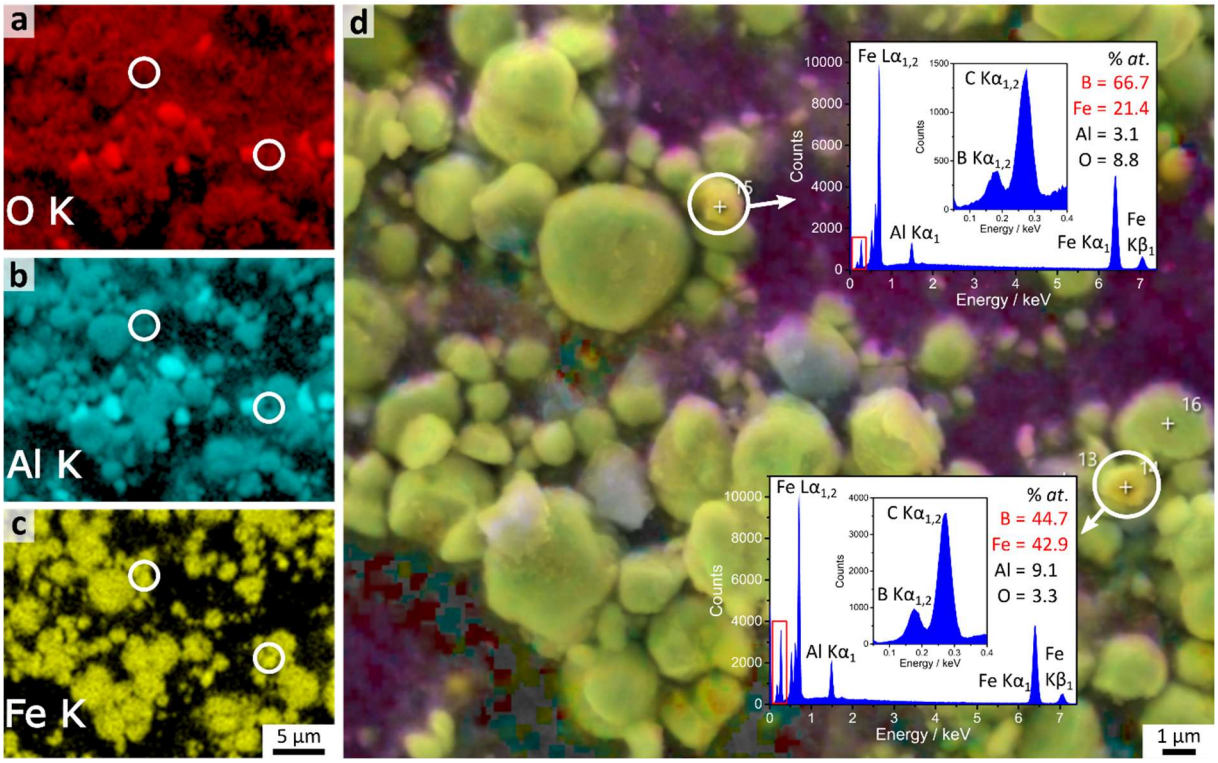

Figure VII. 17. EDX mapping of the heat treated Fe_2AlB_2 sample at 550 °C. O, Al and Fe K lines mapping are depicted in **(a)**, **(b)** and **(c)** respectively. Overlapped lines mapping is shown in **(d)** with the results of punctual EDX analysis in Fe/B particles inserted as insets.

We further analysed the *ex-situ* heated sample with scanning electron microscopy. SEM-EDX mapping (**Figure VII. 17**) highlight the expelled Fe/B particles from the contrast in the Al K and Fe K lines mapping (**Figure VII. 17a** and **b** respectively). Punctual EDX analysis in these particles, shown in the insets of **Figure VII. 17d**, revealed a rich though variable composition in both boron and iron and some minor inclusions of Al. Even if boron is a difficult element to discern by EDX due to its low Z number, magnifications of the punctual EDX scans (**Figure VII. 17** insets) show that high B concentrations allow to detect it unambiguously.

Doping of the A site

In view of the lack of successful results in regards to the Fe_2AlB_2 exfoliation in molten salts and its instability under thermal treatment, we explored another strategy. As discussed previously, the exfoliation easiness depends on the energy difference between the M-B and the M-A bonds.[58,59] In 2020, based on DFT calculations, Edirisuriya and collaborators proposed a way to manipulate these bonding energies.[156] The formation energy was found to be inversely correlated to the exfoliation energy with respect to the A site size, the latter notably decreasing in the order A = Al > Ga > In > Tl. This suggests that substituting Al for any of the other listed elements would facilitate exfoliation. At the same time the formation energy increases and so does the atom size mismatch, so Al becomes more difficult to substitute for Tl than for In and then Ga. Ga substitution in Fe_2AlB_2 has indeed already been achieved, where up to an 8.3 % of substitution was evidenced.[157] There is no record of substitution for the

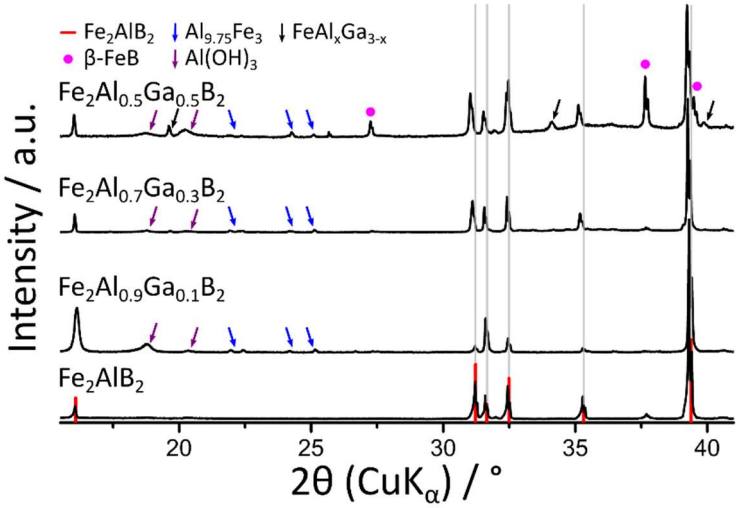

Figure VII. 18. XRD patterns for the synthesis of $Fe_2Al_{1-x}Ga_xB_2$ for x = 0.1, 0.3 and 0.5. Pure Fe_2AlB_2 pattern is also shown for comparison. The vertical grey lines drawn as continuation of the reference Bragg position are intended as visual aid.

other listed elements. We herein explored both Ga and In substitution, where only the former showed evidence of insertion in the structure, so only this case will be discussed. XRD results for $Fe_2Al_{1-x}Ga_xB_2$ input stoichiometries of x = 0.1, 0.3 and 0.5 are shown in **Figure VII. 18**, along with an Fe_2AlB_2 pattern for comparison.

While no major lattice change is observed for the reagent's ratio corresponding to 10 % Ga substitution, this indeed becomes evident starting from 30 % Ga substitution. Further Ga input yields β-FeB and $FeAl_xGa_{3-x}$ impurities, which indicates that the solubility limit is surpassed, so the $Fe_2Al_{0.7}Ga_{0.3}B_2$ targeted stoichiometry is selected for further studies. We performed a thermal treatment on this sample and followed it with *in-situ* XRD to compare its thermal behavior to that of pure Fe_2AlB_2, which is shown in **Figure VII. 19**. Unfortunately, we did not observe evidence of the stacking direction being altered throughout the treatment, as the (020) peak again follows the conventional thermal expansion. However, the compound showed a much higher thermal stability than the undoped one. The *a* axis did not begin to shrink until 780 °C and even then, the compound remains stable in the temperature range studied up to

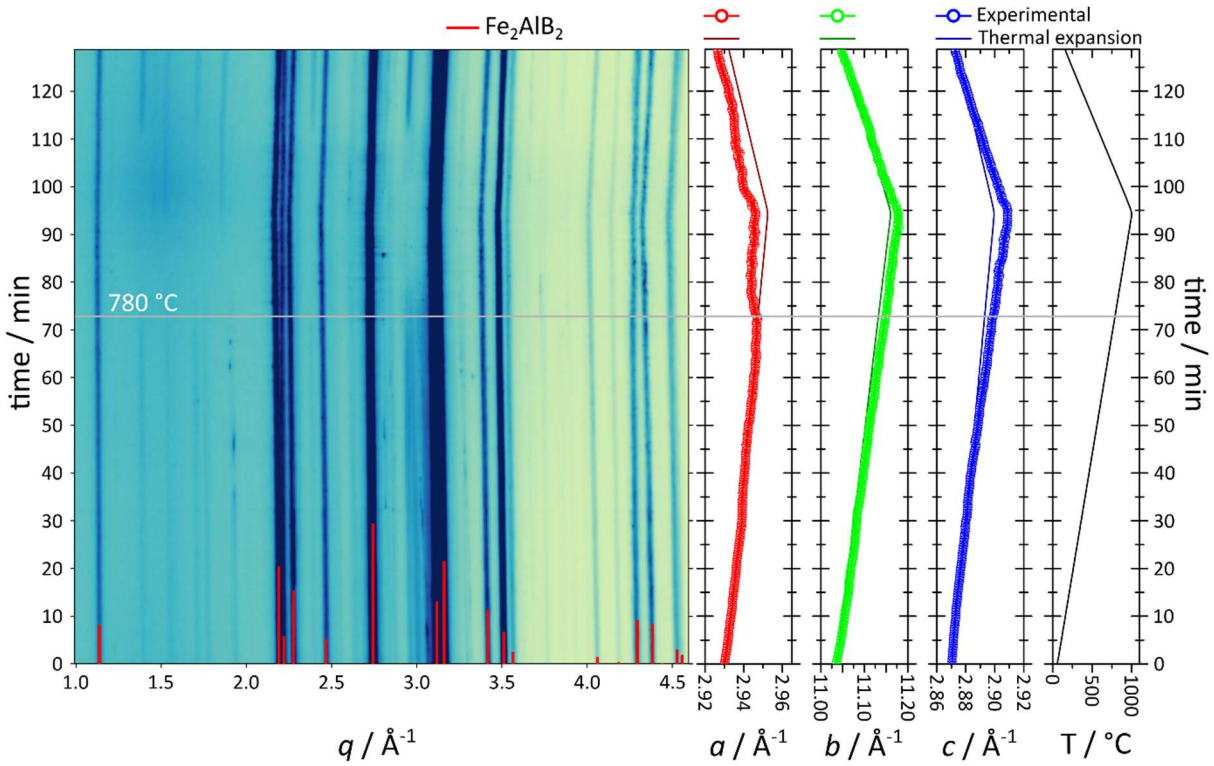

Figure VII. 19. *In-situ* XRD study of $Fe_2Al_{0.7}Ga_{0.3}B_2$ along with the empirical temperature profiles and the refined lattice parameters from sequential Rietveld refinement. In each lattice parameter plot, the refined parameters are plotted as a scatter + line, and compared to the lattice parameters expected from thermal expansion in straight line.

1000 °C. Once the sample was returned to room temperature, only a 0.24 % contraction of the *a* parameter was measured, against 0.93 % for Fe_2AlB_2 exhibited previously, and 0.26 % volumetric contraction against 0.99 % for Fe_2AlB_2. The two remaining axes follow conventional thermal expansion. The different behavior of the Ga doped sample can be interpreted as the fact that Ga inclusions, being larger than Al, act as pinning points and impede the structural rearrangement needed to release Fe and B atoms. So instead of volatilizing, Ga acts as a trapped pillar for the structure. This however could open possibilities to force the oxidation of the A elements with a molten salt at higher temperatures, as the Ga inclusion can stabilize the MAB structure in a higher temperature range than for Fe_2AlB_2. This is an interesting perspective to explore in the future.

VII.4 Partial conclusions

We studied the synthesis and delamination of Fe_2AlB_2 and derived compounds. The synthesis of this phase was achieved in molten salts by using α-FeB as starting material. Al could be inserted inside the α-FeB structure thanks to the use of a high NaH excess that yields metallic Al as intermediate. Impurities formed as by-products could be removed by acidic washing. The Al formation as an intermediate reaction was confirmed through *in-situ* X-ray diffraction. The sequence of reaction was also shown to be identical for the α and β-FeB polymorphs as starting materials. α-FeB yielded a higher purity product, which demonstrates its interest for Al inclusion towards Fe_2AlB_2, a point that has been raised before in the literature. The *in-situ* XRD studies were performed thanks to the development of a synchrotron sample environment that permits to work in inert conditions mimicking the operation conditions of a laboratory Schlenk line. The performances of this *in-situ* oven was characterized in terms of temperature stability, precision, and exactitude, with a linear response and minor errors or variations with respect to the measured temperature. This system also allowed to explore the exfoliation of Fe_2AlB_2 with molten salts. While $CuCl_2$ and $ZnCl_2$ lead to full decomposition of the layered structure, other salts did not prove major reactivity. However, Fe_2AlB_2 exhibited an abnormal lattice contraction with the temperature, which was associated to the formation of Fe/B vacancies that ultimately lead to its transformation to the $Fe_3Al_2B_2$ compound beyond 900 °C. The inclusion of Ga as a dopant of Al hinders this decomposition and pins the elements to the structure, in turn enhancing its thermal stability beyond 700 °C. The latter point could open the door to perform Fe_2AlB_2 delamination at higher temperatures with molten salts that were not reactive below 600 °C.

References for Part Two

[1]: M. W. Barsoum, *Prog. Solid State Chem.*, 2000, **28**, 201–281.
[2]: M. W. Barsoum and T. El-Raghy, *J. Am. Ceram. Soc.*, 1996, **79**, 1953–1956.
[3]: M. W. Barsoum, L. Farber, I. Levin, A. Procopio, T. El-Raghy and A. Berner, *J. Am. Ceram. Soc.*, 1999, **82**, 2545–2547.
[4]: Z. M. Sun, *Int. Mater. Rev.*, 2011, **56**, 143–166.
[5]: M. W. Barsoum, *Prog. Solid State Chem.*, 2000, **28**, 201–281.
[6]: M. Sokol, V. Natu, S. Kota and M. W. Barsoum, *Trends Chem.*, 2019, **1**, 210–223.
[7]: L. Fu and W. Xia, *Adv. Eng. Mater.*, 2021, **23**, 2001191.
[8]: A. Zhou, Y. Liu, S. Li, X. Wang, G. Ying, Q. Xia and P. Zhang, *J. Adv. Ceram.*, 2021, **10**, 1194–1242.
[9]: X. He, Y. Bai, C. Zhu and M. W. Barsoum, *Acta Mater.*, 2011, **59**, 5523–5533.
[10]: N. J. Lane, M. Naguib, J. Lu, L. Hultman and M. W. Barsoum, *J. Eur. Ceram. Soc.*, 2012, **32**, 3485–3491.
[11]: T. H. Scabarozi, J. D. Hettinger, S. E. Lofland, J. Lu, L. Hultman, J. Jensen and P. Eklund, *Scr. Mater.*, 2011, **65**, 811–814.
[12]: C. Hu, C. C. Lai, Q. Tao, J. Lu, J. Halim, L. Sun, J. Zhang, J. Yang, B. Anasori, J. Wang, Y. Sakka, L. Hultman, P. Eklund, J. Rosen and M. W. Barsoum, *Chem. Commun.*, 2015, **51**, 6560–6563.
[13]: H. Fashandi, M. Dahlqvist, J. Lu, J. Palisaitis, S. I. Simak, I. A. Abrikosov, J. Rosen, L. Hultman, M. Andersson, A. Lloyd Spetz and P. Eklund, *Nat. Mater. 2017 168*, 2017, **16**, 814–818.
[14]: H. Zhang, T. Hu, X. Wang, Z. Li, M. Hu, E. Wu and Y. Zhou, *Sci. Reports 2015 51*, 2015, **5**, 1–10.
[15]: J. Etzkorn, M. Ade and H. Hillebrecht, *Inorg. Chem.*, 2007, **46**, 7646–7653.
[16]: Q. Tao, J. Lu, M. Dahlqvist, A. Mockute, S. Calder, A. Petruhins, R. Meshkian, O. Rivin, D. Potashnikov, E. N. Caspi, H. Shaked, A. Hoser, C. Opagiste, R. M. Galera, R. Salikhov, U. Wiedwald, C. Ritter, A. R. Wildes, B. Johansson, L. Hultman, M. Farle, M. W. Barsoum and J. Rosen, *Chem. Mater.*, 2019, **31**, 2476–2485.
[17]: M. Li, J. Lu, K. Luo, Y. Li, K. Chang, K. Chen, J. Zhou, J. Rosen, L. Hultman, P. Eklund, P. O. Å. Persson, S. Du, Z. Chai, Z. Huang and Q. Huang, *J. Am. Chem. Soc.*, 2019, **141**, 4730–4737.
[18]: Y. Li, M. Li, J. Lu, B. Ma, Z. Wang, L. Z. Cheong, K. Luo, X. Zha, K. Chen, P. O. Å. Persson, L. Hultman, P. Eklund, C. Shen, Q. Wang, J. Xue, S. Du, Z. Huang, Z. Chai and Q. Huang, *ACS Nano*, 2019, **13**, 9198–9205.
[19]: Y. Li, J. Lu, M. Li, K. Chang, X. Zha, Y. Zhang, K. Chen, P. O. Å. Persson, L. Hultman, P. Eklund, S. Du, J. S. Francisco, Z. Chai, Z. Huang and Q. Huang, *Proc. Natl. Acad. Sci. U. S. A.*, 2020, **117**, 820–825.
[20]: Z. Liu, J. Wang, E. Wu, Y. Qian, H. Xiang, X. Li, Q. Jin, G. Sun, X. Chen, J. Wang and M. Li, *Acta Mater.*, 2014, **73**, 186–193.
[21]: J. Lu, A. Thore, R. Meshkian, Q. Tao, L. Hultman and J. Rosen, *Cryst. Growth Des.*, 2017, **17**, 5704–5711.
[22]: M. Ade and H. Hillebrecht, *Inorg. Chem.*, 2015, **54**, 6122–6135.
[23]: H. Zhang, F. Z. Dai, H. Xiang, X. Wang, Z. Zhang and Y. Zhou, *J. Mater. Sci. Technol.*, 2019, **35**, 1593–1600.
[24]: Y. Wang, L. X. Yang, R. J. Liu, H. J. Liu, C. L. Zeng, S. L. Zhu and C. Fu, *Powder Technol.*, 2021, **387**, 354–362.
[25]: L. T. Alameda, P. Moradifar, Z. P. Metzger, N. Alem and R. E. Schaak, *J. Am. Chem. Soc.*, 2018, **140**, 8833–8840.
[26]: L. T. Alameda, R. W. Lord, J. A. Barr, P. Moradifar, Z. P. Metzger, B. C. Steimle, C. F. Holder, N. Alem, S. B. Sinnott and R. E. Schaak, *J. Am. Chem. Soc.*, 2019, **141**, 10852–10861.
[27]: W. Jung and K. Petry, *Zeitschrift für Krist.*, 1988, **182**, 153–154.
[28]: W. Jung and K. Schweitzer, *Zeitschrift für Krist.*, 1986, **174**, 109–110.
[29]: Y. Zhou, H. Xiang, F. Z. Dai and Z. Feng, *J. Am. Ceram. Soc.*, 2018, **101**, 2459–2470.
[30]: Y. Zhou, H. Xiang, F. Z. Dai and Z. Feng, *J. Mater. Sci. Technol.*, 2018, **34**, 1441–1448.
[31]: A. A. Rezaie, Z. Yan, J. P. Scheifers, J. Zhang, J. Guo and B. P. T. Fokwa, *J. Mater. Chem. A*, 2020, **8**, 1646–1651.
[32]: V. Gvozdetskyi, G. Bhaskar, M. Batuk, X. Zhao, R. Wang, S. L. Carnahan, M. P. Hanrahan, R. A.

Ribeiro, P. C. Canfield, A. J. Rossini, C. Z. Wang, K. M. Ho, J. Hadermann and J. V. Zaikina, *Angew. Chemie - Int. Ed.*, 2019, **58**, 15855–15862.
[33]: J. Wang, T.-N. Ye, Y. Gong, J. Wu, N. Miao, T. Tada and H. Hosono, *Nat. Commun.*, 2019, **10**, 2284–2292.
[34]: X. Zhao, C. Zhou, K. Bao, P. Zhu, Q. Tao and T. Cui, *Inorg. Chem.*, 2022, **61**, 11046–11056.
[35]: J. Zhou, J. Palisaitis, J. Halim, M. Dahlqvist, Q. Tao, I. Persson, L. Hultman, P. O. Å. Persson. and J. Rosen, *Science*, 2021, **373**, 801–805.
[36]: M. Dahlqvist, J. Zhou, I. Persson, B. Ahmed, J. Lu, J. Halim, Q. Tao, J. Palisaitis, J. Thörnberg, P. Helmer, L. Hultman, P. O. Å Persson, J. Rosen, M. Dahlqvist, J. Zhou, I. Persson, B. Ahmed, J. Lu, J. Halim, Q. Tao, J. Palisaitis, J. Thörnberg, P. Helmer, L. Hultman, P. O. Å Persson, J. Rosen and J. Rosen Materials Design, *Adv. Mater.*, 2021, **33**, 1–10.
[37]: Z. Guo, L. Zhu, J. Zhou and Z. Sun, *RSC Adv.*, 2015, **5**, 25403–25408.
[38]: M. Naguib, M. Kurtoglu, V. Presser, J. Lu, J. Niu, M. Heon, L. Hultman, Y. Gogotsi and M. W. Barsoum, *Adv. Mater.*, 2011, **23**, 4248–4253.
[39]: B. Anasori, M. R. Lukatskaya and Y. Gogotsi, *Nat. Rev. Mater.*, 2017, **2**, 16098.
[40]: V. N. Naguib, M. W. Mochalin, M. W. Barsoum and Y. Gogotsi, *Adv. Mater.*, 2014, **26**, 992.
[41]: M. Ghidiu, M. Naguib, C. Shi, O. Mashtalir, L. M. Pan, B. Zhang, J. Yang, Y. Gogotsi, S. J. L. Billinge and M. W. Barsoum, *Chem. Commun.*, 2014, **50**, 9517–9520.
[42]: M. Naguib, J. Halim, J. Lu, K. M. Cook, L. Hultman, Y. Gogotsi and M. W. Barsoum, *J. Am. Chem. Soc*, 2013, **135**, 15966–15969.
[43]: M. Naguib, O. Mashtalir, J. Carle, V. Presser, J. Lu, L. Hultman, Y. Gogotsi and M. W. Barsoum, *ACS Nano*, 2012, **6**, 1322–1331.
[44]: M. Naguib, M. Kurtoglu, V. Presser, J. Lu, J. Niu, M. Heon, L. Hultman, Y. Gogotsi and M. W. Barsoum, *Adv. Mater.*, 2011, **37**, 4248–4253.
[45]: H. W. Wang, M. Naguib, K. Page, D. J. Wesolowski and Y. Gogotsi, *Chem. Mater.*, 2015, **28**, 349–359.
[46]: M. Naguib, R. R. Unocic, B. L. Armstrong and J. Nanda, *Dalt. Trans.*, 2015, **44**, 9353–9358.
[47]: M. Ghidiu, M. R. Lukatskaya, M. Q. Zhao, Y. Gogotsi and M. W. Barsoum, *Nature*, 2014, **516**, 78–81.
[48]: P. Urbankowski, B. Anasori, T. Makaryan, D. Er, S. Kota, P. L. Walsh, M. Zhao, V. B. Shenoy, M. W. Barsoum and Y. Gogotsi, *Nanoscale*, 2016, **8**, 11385–11391.
[49]: W. Sun, S. A. Shah, Y. Chen, Z. Tan, H. Gao, T. Habib, M. Radovic and M. J. Green, *J. Mater. Chem. A*, 2017, **5**, 21663–21668.
[50]: T. Li, L. Yao, Q. Liu, J. Gu, R. Luo, J. Li, X. Yan, W. Wang, P. Liu, B. Chen, W. Zhang, W. Abbas, R. Naz and D. Zhang, *Angew. Chemie Int. Ed.*, 2018, **57**, 6115–6119.
[51]: S. Yang, P. Zhang, F. Wang, A. G. Ricciardulli, M. R. Lohe, P. W. M. Blom and X. Feng, *Angew. Chemie*, 2018, **130**, 15717–15721.
[52]: H. Shi, P. Zhang, Z. Liu, S. W. Park, M. R. Lohe, Y. Wu, A. Shaygan Nia, S. Yang and X. Feng, *Angew. Chem. Int. Ed. Engl.*, 2021, **60**, 8689.
[53]: Y. Li, H. Shao, Z. Lin, J. Lu, L. Liu, B. Duployer, P. O. Å. Persson, P. Eklund, L. Hultman, M. Li, K. Chen, X. H. Zha, S. Du, P. Rozier, Z. Chai, E. Raymundo-Piñero, P. L. Taberna, P. Simon and Q. Huang, *Nat. Mater.*, 2020, **19**, 894–899.
[54]: J. Thörnberg, J. Halim, J. Lu, R. Meshkian, J. Palisaitis, L. Hultman, P. O. Å. Persson and J. Rosen, *Nanoscale*, 2019, **11**, 14720–14726.
[55]: X. Zhang, J. Xu, H. Wang, J. Zhang, H. Yan, B. Pan, J. Zhou and Y. Xie, *Angew. Chemie*, 2013, **125**, 4457–4461.
[56]: M. Naguib, M. W. Barsoum and Y. Gogotsi, *Adv. Mater.*, 2021, **33**, 2103393–2103393.
[57]: K. Kádas, D. Iuşan, J. Hellsvik, J. Cedervall, P. Berastegui, M. Sahlberg, U. Jansson and O. Eriksson, *J. Phys. Condens. Matter*, 2017, **29**, 1–11.
[58]: Z. Guo and Z. Sun, *J. Mater. Chem. A*, 2017, **5**, 23530–23535.
[59]: M. Khazaei, J. Wang, M. Estili, A. Ranjbar, S. Suehara, M. Arai, K. Esfarjani and S. Yunoki, *Nanoscale*, 2019, **11**, 11305–11314.
[60]: K. I. Portnoi, V. M. Romashov and L. N. Burobina, *Sov. Powder Metall. Met. Ceram.*, 1970, **9**, 577–580.
[61]: H. Zhang, H. Xiang, F. zhi Dai, Z. Zhang and Y. Zhou, *J. Mater. Sci. Technol.*, 2018, **34**, 2022–2026.
[62]: L. T. Alameda, C. F. Holder, J. L. Fenton and R. E. Schaak, *Chem. Mater.*, 2017, **29**, 8953–8957.
[63]: H. Zhang, H. Xiang, F. zhi Dai, Z. Zhang and Y. Zhou, *J. Mater. Sci. Technol.*, 2018, **34**, 2022–2026.

[64]: R. Sahu, D. Bogdanovski, J. O. Achenbach, S. Zhang, M. Hans, D. Primetzhofer, J. M. Schneider and C. Scheu, *Nanoscale*, 2021, **13**, 18077–18083.
[65]: G. Bhaskar, V. Gvozdetskyi, M. Batuk, K. M. Wiaderek, Y. Sun, R. Wang, C. Zhang, S. L. Carnahan, X. Wu, R. A. Ribeiro, S. L. Bud'ko, P. C. Canfield, W. Huang, A. J. Rossini, C. Z. Wang, K. M. Ho, J. Hadermann and J. V. Zaikina, *J. Am. Chem. Soc.*, 2021, **143**, 4213–4223.
[66]: W. Jeitschko, *Acta Crystallogr. Sect. B Struct. Sci. Cryst. Eng. Mater.*, 1969, **B25**, 163–165.
[67]: Y. B. Kuzma and N. F. Chaban, *Izvest Akad Nauk SSSR Neorg Mater.*, 1969, **5**, 384–385.
[68]: X. Tan, P. Chai, C. M. Thompson and M. Shatruk, *J. Am. Chem. Soc.*, 2013, **135**, 9553–9557.
[69]: J. Cedervall, M. Svante, T. Sarkar, E. K. Delczeg-czirjak, L. Bergqvist, T. C. Hansen, P. Beran, P. Nordblad and M. Sahlberg, *J. Alloys Compd.*, 2016, **664**, 784–791.
[70]: J. Cedervall, M. S. Andersson, D. Iuşan, E. K. Delczeg-Czirjak, U. Jansson, P. Nordblad and M. Sahlberg, *J. Magn. Magn. Mater.*, 2019, **482**, 54–60.
[71]: J. Cedervall, L. Häggström, T. Ericsson and M. Sahlberg, *Hyperfine Interact.*, 2016, **237**, 1–8.
[72]: B. T. Lejeune, X. Du, R. Barua, J. C. Zhao and L. H. Lewis, *Materialia*, 2018, **1**, 150–154.
[73]: S. Hirt, F. Yuan, Y. Mozharivskyj and H. Hillebrecht, *Inorg. Chem.*, 2016, **55**, 9677–9684.
[74]: T. Ali, M. N. Khan, E. Ahmed and A. Ali, *Prog. Nat. Sci. Mater. Int.*, 2017, **27**, 251–256.
[75]: E. M. Levin, B. A. Jensen, R. Barua, B. Lejeune, A. Howard, R. W. McCallum, M. J. Kramer and L. H. Lewis, *Phys. Rev. Mater.*, 2018, **2**, 34403.
[76]: R. Barua, B. T. Lejeune, L. Ke, G. Hadjipanayis, E. M. Levin, R. W. McCallum, M. J. Kramer and L. H. Lewis, *J. Alloys Compd.*, 2018, **745**, 505–512.
[77]: Q. Du, G. Chen, W. Yang, Z. Song, M. Hua, H. Du, C. Wang, S. Liu, J. Han, Y. Zhang and J. Yang, *Jpn. J. Appl. Phys.*, 2015, **54**, 053003.
[78]: Q. Du, G. Chen, W. Yang, J. Wei, M. Hua, H. Du, C. Wang, S. Liu, J. Han, Y. Zhang and J. Yang, *J. Phys. D. Appl. Phys.*, 2015, **48**, 1–6.
[79]: L. H. Lewis, R. Barua and B. Lejeune, *J. Alloys Compd.*, 2015, **650**, 482–488.
[80]: P. Chai, S. A. Stoian, X. Tan, P. A. Dube and M. Shatruk, *J. Solid State Chem.*, 2015, **224**, 52–61.
[81]: A. El Boukili, N. Tahiri, E. Salmani, H. Ez-Zahraouy, M. Hamedoun, A. Benyoussef, M. Balli and O. Mounkachi, *Intermetallics*, 2019, **104**, 84–89.
[82]: M. Elmassalami, D. D. S. Oliveira and H. Takeya, *J. Magn. Magn. Mater.*, 2011, **323**, 2133–2136.
[83]: M. Dey, S. Javaid, D. Clifford, V. Sharma, R. Barua and S. Gupta, *J. Mater. Sci.*, 2022, **57**, 2436–2454.
[84]: J. Liu, S. Li, B. Yao, S. Hu, J. Zhang, W. Yu and Y. Zhou, *J. Alloys Compd.*, 2018, **766**, 488–497.
[85]: Q. Tang, Z. Zhou and P. Shen, *J. Am. Chem. Soc.*, 2012, **134**, 16909–16916.
[86]: G. Chen, Y. Bai, H. Li, Y. Li, Z. Wang, Q. Ni, L. Liu, F. Wu, Y. Yao and C. Wu, *ACS Appl. Mater. Interfaces*, 2017, **9**, 6666–6669.
[87]: C. Tsai, F. Abild-Pedersen and J. K. Nørskov, *Nano Lett.*, 2014, **14**, 1381–1387.
[88]: C. Ling, L. Shi, Y. Ouyang and J. Wang, *Chem. Mater.*, 2016, **28**, 9026–9032.
[89]: J. K. Nørskov, T. Bligaard, A. Logadottir, J. R. Kitchin, J. G. Chen, S. Pandelov and U. Stimming, *J. Electrochem. Soc.*, 2005, **152**, J23.
[90]: X. Geng, Z. Cheng, S. Wang, C. Peng, A. Ullah, H. Wang and G. Wu, *J. Mater. Sci.*, 2022, **57**, 10755–10768.
[91]: C. Li, F. Li, J. Liang, R. Cao and Z. Zhao, *Mater. Sci. Technol.*, 2019, **35**, 2013–2023.
[92]: S. Gupta, M. K. Patel, A. Miotello and N. Patel, *Adv. Funct. Mater.*, 2020, **30**, 1–28.
[93]: F. Ni, Y. Ma, J. Chen, W. Luo and J. Yang, *Chinese Chem. Lett.*, 2021, **32**, 2073–2078.
[94]: J. D. Bocarsly, E. E. Levin, S. A. Humphrey, T. Faske, W. Donner, S. D. Wilson and R. Seshadri, *Chem. Mater.*, 2019, **31**, 4873–4881.
[95]: H. Li, P. Wen, Q. Li, C. Dun, J. Xing, C. Lu, S. Adhikari, L. Jiang, D. L. Carroll and S. M. Geyer, *Adv. Energy Mater.*, 2017, **7**, 1–12.
[96]: S. Rades, A. Kornowski, H. Weller and B. Albert, *ChemPhysChem*, 2011, **12**, 1756–1760.
[97]: S. Rades, S. Kraemer, R. Seshadri and B. Albert, *Chem. Mater.*, 2014, **26**, 1549–1552.
[98]: V. A. Tsurin, Y. E. Turkhan, V. A. Kazantsev, V. V. Fedorenko, S. I. Novikov, V. A. Barinov, V. T. Surikov and G. A. Dorofeev, *J. Met. Metallogr.*, 2003, **96**, 36.
[99]: D. B. Deyoung and R. G. Barnes, *J. Chem. Phys.*, 1975, **62**, 1726–1738.
[100]: P. R. Jothi, K. Yubuta and B. P. T. Fokwa, *Adv. Mater.*, 2018, **30**, 2–7.
[101]: D. Portehault, S. Devi, P. Beaunier, C. Gervais, C. Giordano, C. Sanchez and M. Antonietti, *Angew. Chemie - Int. Ed.*, 2011, **50**, 3262–3265.

[102]: Y. Wei, Z. Liu, S. Ran, A. Xia, T. F. Yi and Y. Ji, *J. Mater. Res.*, 2017, **32**, 883–889.
[103]: C. Kapfenberger, B. Albert, R. Pöttgen and H. Huppertz, *Zeitschrift für Krist. - Cryst. Mater.*, 2006, **221**, 477–481.
[104]: G. Gouget, P. Beaunier, D. Portehault and C. Sanchez, *Faraday Discuss.*, 2016, **191**, 511–525.
[105]: S. Hirt, F. Hilfinger and H. Hillebrecht, *Zeitschrift fur Krist. - Cryst. Mater.*, 2018, **233**, 295–307.
[106]: P. M. Woodwardt, *Acta Cryst*, 1997, **53**, 32–43.
[107]: R. Fruchart, *Ann. der Chemie*, 1959, **4**, 1247.
[108]: T. Kanaizuka, *J. Solid State Chem.*, 1982, **41**, 195–204.
[109]: V. A. Barinov, G. A. Dorofeev, L. V. Ovechkin, E. P. Elsukov and A. E. Ermakov, *Phys. status solidi*, 1991, **123**, 527–534.
[110]: A. Altomare, N. Corriero, C. Cuocci, A. Falcicchio, A. Moliterni and R. Rizzi, *Cryst. Res. Technol*, 2015, **50**, 737–742.
[111]: D. Hohnke and E. Parthé, *Acta Cryst*, 1966, **20**, 582.
[112]: K. Klepp and E. Parthé, *Acta Crystallogr.*, 1980, **B36**, 3093–3094.
[113]: K. Klepp and E. Parthé, *Acta Crystallogr.*, 1981, **B37**, 1500–1504.
[114]: J. Le Roy, J. Moreau, D. Paccard and E. Parthé, *Acta Crystallogr.*, 1978, **B34**, 9–13.
[115]: E. Parthé, *Acta Crystallogr.*, 1976, **B32**, 2813–2818.
[116]: T. Kanaizuka, *Phys. Status Solidi*, 1982, **69**, 739–744.
[117]: Steffi rades. Synthese und Charakterisierung von Nanopartikeln im System Eisen-Bor. Technische Universität Darmstadt, 2012. Germany.
[118]: M. Casas-Cabanas, J. Rodríguez-Carvajal and M. R. Palacín, *Zeitschrift für Krist.*, 2006, **23**, 144–145.
[119]: M. Casas-Cabanas, M. Reynaud, J. Rikarte, P. Horbach and J. Rodríguez-Carvajal, *J. Appl. Cryst*, 2016, **49**, 2259–2269.
[120]: J. Serrano-Sevillano, V. Charbonnier, N. Madern, M. Latroche, C. Magén, V. Serin, J. Monnier, M. Casas-Cabanas and J. Zhang, *Chem. Mater*, 2022, **34**, 4568–4576.
[121]: A. J. Perez, D. Batuk, M. Saubanère, G. Rousse, D. Foix, E. McCalla, E. J. Berg, R. Dugas, K. H. W. Van Den Bos, M. L. Doublet, D. Gonbeau, A. M. Abakumov, G. Van Tendeloo and J. M. Tarascon, *Chem. Mater.*, 2016, **28**, 8278–8288.
[122]: B. Mortemard de Boisse, M. Reynaud, J. Ma, J. Kikkawa, S. ichi Nishimura, M. Casas-Cabanas, C. Delmas, M. Okubo and A. Yamada, *Nat. Commun.*, 2019, **10**, 1–7.
[123]: T. Masese, Y. Miyazaki, J. Rizell, G. M. Kanyolo, C. Y. Chen, H. Ubukata, K. Kubota, K. Sau, T. Ikeshoji, Z. D. Huang, K. Yoshii, T. Takahashi, M. Ito, H. Senoh, J. Hwang, A. Alshehabi, K. Matsumoto, T. Matsunaga, K. Fujii, M. Yashima, M. Shikano, C. Tassel, H. Kageyama, Y. Uchimoto, R. Hagiwara and T. Saito, *Nat. Commun.*, 2021, **12**, 1–16.
[124]: M. M. J. Treacy, M. W. Deem and J. M. Newsam, in *DIFFaX Manual*, 2005, pp. 48–50.
[125]: K. J. Kim, R. P. Oleksak, E. B. Hostetler, D. A. Peterson, P. Chandran, D. M. Schut, B. K. Paul, G. S. Herman and C. H. Chang, *Cryst. Growth Des.*, 2014, **14**, 5349–5355.
[126]: J. N. Hausmann, R. Beltrán-Suito, S. Mebs, V. Hlukhyy, T. F. Fässler, H. Dau, M. Driess and P. W. Menezes, *Adv. Mater.*, 2021, **33**, 1–9.
[127]: L. Dubau, J. Nelayah, S. Moldovan, O. Ersen, P. Bordet, J. Drnec, T. Asset, R. Chattot and F. Maillard, *ACS Catal.*, 2016, **6**, 4673–4684.
[128]: E. Lee and B. P. T. Fokwa, *Acc. Chem. Res.*, 2022, **55**, 56–64.
[129]: M. S. Burke, M. G. Kast, L. Trotochaud, A. M. Smith and S. W. Boettcher, *J. Am. Chem. Soc.*, 2015, **137**, 3638–3648.
[130]: D. V. Franco, L. M. Da Silva, W. F. Jardima and J. F. C. Boodts, *J. Braz. Chem. Soc.*, 2006, **17**, 446–757.
[131]: J. Qi, W. Zhang, R. Xiang, K. Liu, H.-Y. Wang, M. Chen, Y. Han and R. Cao, *Adv. Sci.*, 2015, **2**, 1500199.
[132]: D. J. Joyner, O. Johnson and D. M. Hercules, *J. Am. Chem. Soc.*, 1980, **102**, 1910–1917.
[133]: D. J. Joyner and D. M. Hercules, *J. Chem. Phys*, 1980, **72**, 1095.
[134]: N. S. McIntyre and D. G. Zetaruk, *Anal. Chem.*, 1977, **49**, 1521–1529.
[135]: K. Yubuta, T. Mori, A. Leithe-Jasper, H. Borrmann, Y. Grin, S. Okada and T. Shishido, *J. Solid State Chem.*, 2014, **219**, 274–279.
[136]: P. Adelhelm, K. P. De Jong and P. E. De Jongh, *Chem. Commun.*, 2009, **41**, 6261–6263.
[137]: www.crct.polymtl.ca/fact/documentation/FTsalt/FTsalt_Figs.html (Revised on the 05/08/2022).

[138]: K. T. Arul, H. W. Chang, H. W. Shiu, C. L. Dong and W. F. Pong, *J. Phys. D. Appl. Phys.*, 2021, **54**, 1–20.
[139]: Q. Gu, J. A. Kimpton, H. E. A. Brand, Z. Wang and S. Chou, *Adv. Energy Mater.*, 2017, **7**, 1–7.
[140]: P. J. Chupas, K. W. Chapman, C. Kurtz, J. C. Hanson, P. L. Lee and C. P. Grey, *J. Appl. Cryst*, 2008, **41**, 822–824.
[141]: D. P. Shoemaker, Y.-J. Hu, D. Young Chung, G. J. Halder, P. J. Chupas, L. Soderholm, J. F. Mitchell and M. G. Kanatzidis, 2014, **111**, 10922–10927.
[142]: A. Weiland, M. G. Frith, S. H. Lapidus and J. Y. Chan, *Chem. Mater.*, 2021, **33**, 7657–7664.
[143]: S. S. Kushwah and J. Shanker, *Phys. B Condens. Matter*, 1996, **225**, 283–287.
[144]: Y. Sumino, O. L. Anderson and I. Suzuki, *Phys Chem Miner.*, 1983, **9**, 38–47.
[145]: I. Suzuki, *J. Phys. Earth*, 1975, **23**, 145–159.
[146]: S. P. Bennett, S. Kota, H. ElBidweihy, J. F. Parker, L. A. Hanner, P. Finkel and M. W. Barsoum, *Scr. Mater.*, 2020, **188**, 244–248.
[147]: L. Verger, S. Kota, H. Roussel, T. Ouisse and M. W. Barsoum, *J. Appl. Phys.*, 2018, **124**, 1–10.
[148]: S. Kota, L. Verger, V. Natu, M. Sokol and M. W. Barsoum, *J. Am. Ceram. Soc.*, 2021, **104**, 733–739.
[149]: J. Liu, S. Li, B. Yao, J. Zhang, X. Lu and Y. Zhou, *Ceram. Int.*, 2018, **44**, 16035–16039.
[150]: Y. Bai, X. Qi, X. He, G. Song, Y. Zheng, B. Hao, H. Yin, J. Gao and A. Ian Duff, *J. Am. Ceram. Soc.*, 2020, **103**, 5837–5851.
[151]: Y. Nishihara, Y. Nakajima, A. Akashi, N. Tsujino, E. Takahashi, K. I. Funakoshi and Y. Higo, *Am. Mineral.*, 2012, **97**, 1417–1420.
[152]: J. C. Slater, *J. Chem. Phys.*, 1964, **41**, 3199–3204.
[153]: F. H. Sanchez, J. I. Budnick, Y. D. Zhang, ' A Hines, M. Choi and R. Hasegawa, *Phys. Reviex B*, 1986, **34**, 4738–4743.
[154]: Z. Y. Pu, J. Q. Lu, M. F. Luo and Y. L. Xie, *J. Phys. Chem. C*, 2007, **111**, 18695–18702.
[155]: W. Pepperhoff and M. Acet, *Constitution and Magnetism of Iron and its Alloys*, Springer, Berlin, 2001.
[156]: E. M. D. Siriwardane, R. P. Joshi, N. Kumar and D. Çaklr, *ACS Appl. Mater. Interfaces*, 2020, **12**, 29424–29431.
[157]: R. Barua, B. T. Lejeune, B. A. Jensen, L. Ke, R. W. McCallum, M. J. Kramer and L. H. Lewis, *J. Alloys Compd.*, 2019, **777**, 1030–1038.
[158]: H. Zhang, T. Hu, X. Wang and Y. Zhou, *J. Mater. Sci. Technol.*, 2020, **38**, 205–220.
[159]: S. Yang, P. Zhang, A. S. Nia and X. Feng, *Adv. Mater.*, 2020, **32**, 1907857–1907857.
[160]: T. Kanai and Z. U. Ka, *J. Solid State Chem.*, 1982, **41**, 195–204.

Chapter VIII: General Conclusions and Perspectives

Boron-based nanomaterials are very promising for several structural and functional applications. As this scientific field advances towards more complex compositions, structures and morphologies, so must synthetic methods evolve to cope with these requisites. Topochemical transformation and nanotemplating are processes that have flourished as ways to manipulate matter into complex forms otherwise unreachable. Throughout the course of this thesis work, we have developed this concept for the chemistry of boron-based nanomaterials, namely boron carbide nanoceramics and the layered metal boride Fe_2AlB_2.

For boron carbide, we developed the use of a newly discovered nanotemplate: NaB_5C. This compound was synthesized as *circa* 5 nm edge nanocrystals. We showed by a combination of techniques, including powder X-ray diffraction, ^{11}B and ^{23}Na solid-state NMR spectra combined to DFT modelling that contrary to the reported bulk compound, the nanocrystals contained Na vacancies and carbon over stoichiometry enabling to fulfil electron counting rules with the formula $Na_{1-x}B_{5-x}C_{1+x}$. These structural deviations from the bulk could be related to the ability of the nano-objects to accommodate larger strain, and originates from the excess of carbon used during the synthesis. Notwithstanding, the excess amount of carbon input did prove to be a key parameter for controlling its later transformation to the actual compound of interest: boron carbide nanostructures.

The $Na_{1-x}B_{5-x}C_{1+x} \rightarrow B_{4+\delta}C$ transformation was studied by two approaches: high and room pressure. In the former case, the objective of using high pressures (up to 5 GPa), was to limit the diffusion of the atoms throughout the transformation and so **(i)** limit the grain growth and **(ii)** avoid the segregation of the atoms from $Na_{1-x}B_{5-x}C_{1+x}$, including those foreign to boron carbide, *i.e.*, Na. *Ex-situ* and *in-situ* studies were carried out with this goal, both failing to identify conditions suitable for avoiding segregation, and in turn yielding products with Na and B by-products that are detrimental for boron carbide structural applications. Future efforts towards this goal should be concentrated in using even higher pressures and as soft as possible heat treatments. Despite this difficulty, the second avenue of room pressure transformations did show the much-expected isomorphic transformation upon heating and volatilization of Na atoms. B atoms also partially segregated to yield a stoichiometry that we evaluated at *ca*. $B_{4.1}C$, close to the expected thermodynamic composition. After optimisation of reaction conditions and purification by selective oxidation and dissolution of elemental boron, phase pure $B_{4.1}C$

could be obtained by maintaining the size of the original $Na_{1-x}B_{5-x}C_{1+x}$ nanocrystals. The resulting boron carbide nanopowders were an ideal platform to study their crystal defects. We highlighted thanks to ^{11}B and ^{13}C NMR coupled to DFT modelling two main defects related to the CBC chains within the structure, namely the rhombi-like BBBB and linear CBC-B. Moreover, the nanopowders could be processed into dense monoliths thanks to spark-plasma sintering at high pressures (5 GPa), which in turn enabled the evaluation of the mechanical properties of the sample. We obtained hardness and amorphization resistance overcoming state-of-the-art boron carbide materials.

For the second part of the work, FeB was investigated as a nanotemplate towards Fe_2AlB_2. Again, FeB exhibited characteristic defects absent in its bulk counterpart. Indeed, two FeB structural modifications could be isolated: the low and high temperature α- and β-modifications, respectively. While bulk β-FeB could be obtained with its well-known crystal structure, we also obtained nano and micro-scale α-FeB, the structure of which was still under debate. We succeeded for the first time in providing an adequate and quantitative structural model that consists of a faulted structure formed by nanometer-thick β-FeB and CrB-type layers separated by stacking faults that form an intergrowth between these structures.

We then questioned the relative reactivities of α-FeB and β-FeB towards the formation of Fe_2AlB_2. After optimisation of the conditions of reaction between FeB, an aluminium source, and a hydride reductant into molten salts, we studied the synthesis of Fe_2AlB_2 by *in-situ* and *ex-situ* XRD. We evidenced that both modifications undergo the same reaction pathway towards Fe_2AlB_2. Nonetheless, the α-FeB phase resulted in a higher purity product. This higher reactivity was ascribed to the closer structural relationship between α-FeB, its CrB-type component, and Fe_2AlB_2, which ensures a topochemical transformation. The elucidation of the intergrowth structure of α-FeB and the demonstration of its higher performance as a reagent showed the potential use of this otherwise undermined compound.

After recovery of high purity Fe_2AlB_2, we have examined the possibility to delaminate this MAB phase by conventional acidic washing, molten salts selective oxidation and direct sublimation. The former was too corrosive as it systematically dissolved the whole sample. $CuCl_2$ and $ZnCl_2$ molten salts oxidation did show evidence of delamination, although both being also too strong and completely targeting the transition of the Fe_2B_2 bidimensional phase to more stable 3D compounds. Softer salts did not prove sufficiently reactive to cause structural changes. Direct sublimation in inert atmosphere showed evidence of structural changes with

the temperature, as the most oxidizing salts before decomposition of the MAB phase. The anomalous lattice contraction with temperature was correlated to the loss of Fe and B before transition to $Fe_3A_2lB_2$. Especially, the dry Fe_2AlB_2 powder undergoes Fe and B loss with lattice contraction from 500 °C to 1000 °C before transformation into $Fe_3A_2lB_2$. This indicates that Fe_2AlB_2 can accommodate a large amount of Fe and B vacancies, with a significant impact on local strains. Because this non-stoichiometric compound can be recovered at room temperature, it could provide an original material to study the role of crystal defects on catalytic properties, in future studies. We finally attempted to trigger the sublimation of Al by partially replacing it by the more volatile Ga atom. This was achieved, although Ga atoms acted as pinning points for the crystal framework, thus hindering the formation of strains. This is an interesting aspect to explore in the future as it could open the door to delamination at higher temperatures, where undoped Fe_2AlB_2 is unstable.

All in all, the same concept of synthesis by templating effect was developed for two different systems, yet in analogous ways. Boron carbide and layered Fe_2AlB_2 could be produced and investigated thanks to the transformation from their respective templates. In both cases the template material was optimized and fully characterized, showing distinct structural features due to the nanostructuration or the synthesis pathways. We could corelate these deviations *versus* bulk materials to specific defects, from atomic substitutions to stacking faults and vacancies. This proves the interest of performing multi-step reactions that exploit the characteristics of the starting material as a way to manoeuvre matter into more complex and performing forms.

Appendix AI: Characterizations

Powder X-ray diffraction (XRD)

Room-pressure produced powders were analyzed by powder XRD in a Bruker D8 Advance diffractometer in the Bragg-Brentano θ-θ geometry. The X-ray source consisted of a sealed Cu anode with emission lines sited at $K_{\alpha1}$ = 1.5406 Å, $K_{\alpha2}$ = 1.5443 Å, with an acceleration tension of 40 kV and a current of 30 mA. Diffracted intensity was detected using a LynxEye linear detector. Powder patterns were collected in the 2θ range 10-120° with a step defined as the FWHM/10 of the thinnest peak of the diffractogram and 5 s/step.

X-ray diffractograms of the pelletized compacts retrieved from high-pressure experiments obtained in a Rigaku MM07HF diffractometer equipped with a microfocus Mo rotating anode ($K_{\alpha1}$ = 0.709319Å, $K_{\alpha2}$ = 0.713609 Å) and a RAXIS4++ image plate detector. The sample was mounted in the head of a rotating goniometer and a 15 min phi scan with angular amplitude of 40 ° and rotation speed of 20 °·s^{-1} was performed. A LaB_6 NIST standard sample was measured in the same experimental conditions to calibrate the Fit2D program, the image processing software used to integrate the intensities around the Debye-Scherrer rings and to get the 1D patterns.[1]

The reference crystallographic structures were taken from either the ICSD or the PDF databases: NaB_5C (ICSD #408930), B_4C (ICSD #79958), H_3BO_3 (ICSD #24711), *h*-BN (ICSD #241875), $NaBH_4$ (ICSD #244142), $HNa_3(CO_3)_2{\cdot}2H_2O$ (ICSD #35191), $Na_2B_4O_7{\cdot}5H_2O$ (ICSD #36362), β-FeB (ICSD #11084), Fe_2B (ICSD #391330), Fe_3O_4 (ICSD #26410), Fe_2AlB_2 (ICSD #230159), Al_2O_3 (ICSD #160607), $KAl_6O_{9.5}$ (ICSD #66471), Fe_4Al_{13} (ICSD #290494) $Al(OH)_3$ (ICSD #25433), $LiAl_5O_8$ (ICSD #10480), $FeCl_2$ (ICSD #4059), Cu (ICSD #2124986), $Na_{0.5}Al_{0.5}ClO_{0.5}$ (PDF #04-009-7221), $Al_2BO_{4.5}$ (PDF #04-012-8918), NaCl (ICSD #29929), $CoCl_2$ (ICSD #44398), Na_6FeCl_8 (PDF #04-006-8320), $CdCl_2$ (ICSD #86440), Na_2CdCl_4 (ICSD #69344), $NaCdCl_3$ (PDF #04-063-8324), *t*-$ZnCl_2$ (PDF #04-005-4407), Na_2ZnCl_4 (PDF #04-007-4696), *o*-$ZnCl_2$ (PDF #04-005-4434), Fe fcc (ICSD #185758), $Fe_3Al_2B_2$ (ICSD #433027).

Rietveld and Le Bail refinements were performed using either the FullProf suite of programs,[2] or the GSAS-II program.[3] Stacking faults modelling and refining was performed using the FAULTS software.[4,5]

Synchrotron *in-situ* angular X-ray diffraction

The experiment was carried out at the ESRF synchrotron, on the ID11 beamline, in transmission mode at a fixed energy (wavelength) of 93.3159 keV (0.1329 Å). A Double Crystal Monochromator equipped with two Si(1 1 1) crystals was used to tune the energy and the beamsize was set to 300x300 microns. The detector was a Frelon4M 2048x2048 16Bit fast CCD Camera. We used a homemade capillary oven. In brief, it enables performing transmission X-ray diffraction *in situ* during controlled heating of the reaction mixture in a 1.5 mm-diameter quartz capillary opened under argon flow, to mimic the conditions of *ex-situ* lab synthesis.

Field Emission Gun – Scanning Electron Microscopy (SEM – FEG)

The scanning electron microscopy images were taken on a SEM-FEG HITACHI SU-70 microscope by David Montero at the Institut des Matériaux of Paris Centre.

Transmission electron microscopy (TEM)

Transmission electron microscopy analyses were performed in a Tecnai Spirit 2 apparatus, equipped with a LaB_6 electron gun, operating at 120 kV. Samples were dispersed by sonication on ethanol and deposited on top of Cu grids covered with a carbon membrane.

Solid-state Magic Angle Spinning – Nuclear Magnetic Resonance (SS–NMR)

Solid-state MAS NMR spectra were acquired on a Bruker AVANCE III 700 spectrometer based on a 16.4 T superconducting solenoid operating at ν_0 = 224.68 and *176.01* MHz for ^{11}B and ^{13}C respectively and using *a 3.2 mm Bruker probe*. Powder samples were transferred to ZrO_2 rotors and spun at a MAS rate of 20 kHz. ^{13}C and ^{11}B chemical shifts were referenced to TMS and $BF_3 \cdot OEt_2$, respectively.

Nuclear Magnetic Resonance modelling - $Na_{1-x}B_{5-x}C_{1+x}$ (Chapter III)

Different models were obtained starting from the crystalline structure of NaB_5C[6] and using 2×2×2 and 3×3×3 supercells in which carbon atoms were randomly positioned in substitution of one or two borons among B_6 octahedra. In addition, Na vacancies were introduced in some cases as described more precisely later in the text. All atomic positions were then relaxed with the VASP (Vienna Ab-initio Simulation Package) code[7] based on the Kohn-Sham Density Functional Theory (DFT) and using a plane-wave pseudopotential approach. The cells parameters were fixed to X-ray diffraction parameters during geometry optimizations. The NMR parameters were then calculated within the Kohn-Sham DFT using the QUANTUM-ESPRESSO code,[8] keeping the atomic positions equal to the values previously calculated with VASP. The PBE generalized gradient approximation[9] was used and the valence electrons were described by norm conserving pseudopotentials[10] in the Kleinman Bylander form.[11] The shielding tensor was computed using the Gauge Including Projector Augmented Wave (GIPAW) approach,[12] which enables the reproduction of the results of a fully converged all electron calculation. The isotropic chemical shift δ_{iso} is defined as $\delta_{iso} = -[\sigma - \sigma_{ref}]$ where σ is the isotropic shielding and σ_{ref} is the isotropic shielding of the same nucleus in a reference system. In the present case, the comparison between the experimental δ_{iso} and calculated σ_{iso} ^{11}B chemical shift values for B_2O_3 (δ_{iso} = 14.6 ppm) (ICSD #16021) was used for ^{11}B while for ^{23}Na, σ_{ref} was fixed so that the average sum of experimental and calculated shifts of a series of sodium phosphates and silicates coincide.[13] The principal components V_{xx}, V_{yy}, and V_{zz} of the electric field gradient (EFG) tensor were obtained by diagonalisation of the calculated tensor giving access to the quadrupolar coupling constant C_Q and the asymmetry parameter η_Q, which are defined as : $C_Q = eQV_{zz}/h$ and $\eta_Q = (V_{yy} - V_{xx})/V_{zz}$ (e is the proton charge, h Planck's constant and Q the quadrupole moment of the considered nucleus). The Q value reported by Pyykkö[14] was used in the calculations for ^{11}B (40.5 mb) and ^{23}Na (104 mb). Calculated spectra were then plotted using the DMFit program.[15]

Nuclear Magnetic Resonance modelling – $B_{4+\delta}C$ (Chapter IV)

Two basic B_4C models were obtained starting from the crystalline structure of B_4C (i) (ICSD #79958) the polar *B11Cp-CBC* model was obtained using a CBC chain and $B_{11}C$ icosahedra, the C atom being substituted in a polar site while (ii) the polar *B11Ce-CBC* model was obtained using a CBC chain and $B_{11}C$ icosahedra, the C atom being substituted in an equatorial site. In

addition, more complex models proposed by K. Rasim et al.[16] (in which one CBC chain motif was modified) were also investigated. They are composed of 2×2×1 hexagonal supercells containing initially 180 atoms which corresponds to 12 chain-icosahedron building blocks (B_{12}+CBC i.e $B_{156}C_{24}$) in which different local atomic arrangements (chain defects) were introduced (either the chain contains four instead of three atoms, or the boron atoms of the chain are located out of the three-fold axis, forming bent chains CBC or rhombi CB_2C). We investigated more specifically energetically favourable structures namely (iii) *CBC-Ba* with an additional boron position on top of the chain (iv) *BBcBcB* with two additional borons in the center chain and no more carbon in the chain and (v) *CBcBcB-Ba* with two additional borons in the center chain and one boron above the chain which keeps just one carbon. To get closer to a B_4C composition and limit the charge of the models in view of the NMR calculations, a boron in polar position was replaced in each icosahedron by a carbon.

The NMR parameters were then calculated for all these models within Kohn-Sham DFT using the QUANTUM-ESPRESSO code.[8] The PBE generalized gradient approximation[9] was used and the valence electrons were described by norm conserving pseudopotentials[10] in the Kleinman Bylander form.[11] The shielding tensor was computed using the Gauge Including Projector Augmented Wave (GIPAW) approach,[12] which enables the reproduction of the results of a fully converged all electron calculation. The isotropic chemical shift δ_{iso} is defined as $\delta_{iso} = -[\sigma - \sigma_{ref}]$ where σ is the isotropic shielding and σ_{ref} is the isotropic shielding of the same nucleus in a reference system. In the present case, the comparison between the experimental σ_{iso} and calculated σ_{iso} ^{11}B and ^{13}C chemical shift values for B_2O_3 (ICSD #16021) and amino acids[17] were used as previously described. The principal components V_{xx}, V_{yy}, and V_{zz} of the electric field gradient (EFG) tensor were obtained by diagonalisation of the calculated tensor giving access to the quadrupolar coupling constant C_Q and the asymmetry parameter η_Q, which are defined as: $C_Q = eQV_{zz}/h$ and $\eta_Q = (V_{yy} - V_{xx})/V_{zz}$ (e is the proton charge, h Planck's constant and Q the quadrupole moment of the considered nucleus). The Q value reported by Pyykkö[14] was used in the calculations for ^{11}B (40.59 mb). Calculated spectra were then plotted using the DMFit program.[15]

Vicker's microhardness measurements

For performing Vicker's hardness characterization, the compressed pellets were first embedded in an acrylic resin of methyl methacrylate for polishing. The composite was thoroughly polished

using SiC polishing paper up to grit sizes of P2000. Surface flatness was confirmed by optical microscopy.

Vickers hardness measurements have been performed using a microhardness tester (Duramin-20, Struers) under the load from 0.49 to 19.6 N. At least ten indentations were performed for each data point to provide good statistics. The radial cracks observed at the loads of 10 and 20 N allowed us to calculate the reliable load-independent value of fracture toughness by the method that was previously used for other superhard materials.[18]

Density determination by the Archimedes method

The density of the sintered samples was measured using Archimedes method with distilled water as a liquid medium. The values for the relative densities were calculated assuming a theoretical density of B_4C, that is 2.52 $g \cdot cm^{-3}$.

Raman microscopy

Raman spectroscopy of $Na_{1-x}B_{5-x}C_{1+x}$ powders were performed on a Kaiser Optical System Raman Analyzer RX1 Microprobe with a 785 nm laser diode.

Raman spectra of mechanically tested $B_{4+\delta}C$ samples were acquired using a Jobin-Yvon/Horiba HR-460 spectrometer equipped with a monochromator with 1500 $grooves \cdot mm^{-1}$ and an Andor CCD. An Argon laser operating at 514.5 nm was focused on the sample with an optical lens and the backscattered Raman spectra in the Raman shift 470 – 1900 cm^{-1} range were collected with a laser power of ~ 50 µW and averaged from 3 accumulations, each with a collection time of 300 s.

Raman cartography

Raman cartography maps were recorded using a Renishaw InVia spectrometer equipped with a 785 nm Renishaw diode laser. The laser was focused on the sample using a DM2500 Leica microscope with a 50× objective (NA = 0.55) to obtain a planar resolution of ~ 5 μm^2. The laser power at the sample surface was set at around 1 mW using neutral density filters to avoid damages due to laser-induced heating. The signal was filtered by edge filters and dispersed by a diffraction grating with 1200 $grooves \cdot mm^{-1}$ and the signal was analyzed with a RENCAM

CCD (charge-coupled device) detector. The spectrometer was calibrated using a silicon standard. Spectra were collected using the software WIRE 4.1 provided by Renishaw. Mosaics were compiled from 40 112 Raman spectra over a 1240 × 1300 μm^2 surface with a step size of 6 μm in the x-direction and 6.2 μm in the y-direction. The laser power at the sample surface was set at around 0.5 $mW \cdot \mu m^{-2}$ when using the line-scanning mode.

X-ray photoelectron spectroscopy

XPS spectra were recorded on an Omicron spectrometer using an Al Kα source (1486.7 eV) as the source energy. The binding energies were referenced *versus* the aliphatic C1s peak (284.8 eV).

Specific area determination

The specific area was evaluated by applying the BET method to a nitrogen sorption isotherm recorded at 77 K using a BELSORB-max apparatus after degassing the sample at 150 °C for 15 h.

Electrocatalytic water splitting properties

Working electrode preparation. Two types of working electrode substrates were used for different measurements. A glassy carbon (GC) rotating disk electrode (RDE) with a diameter of 5 mm was used for cyclic voltammetry (CV). A GC sheet was used for chronopotentiometry (CP) measurements. The catalyst film was prepared by drop casting. 3.5 mg of catalyst was sonicated in 480 μL absolute ethanol for 30 min, followed by adding 20 μL of Nafion solution (5% in alcohols and water, Sigma-Aldrich) for another 30 min of ultrasonication. 7 μL of the well-dispersed ink was then dropped-casted onto the as-polished RDE or the GC sheet substrate to obtain a catalyst loading of 350 $\mu g_{catalyst} \cdot cm^{-2}_{electrode}$, and then the coating was dried under air for 30 min.

Measurements of OER properties. Electrochemical measurements were performed with a typical three-electrode configuration which includes the working electrode, a carbon rod as counter electrode and an Ag/AgCl in saturated KCl electrode as reference electrode. 0.1 M KOH was used as electrolyte (pH = 13). Before measurements, the electrolyte was bubbled by O_2 for 20 min. The rotating disk electrode rotated at 1600 rpm. Cyclic voltammograms were

recorded in the potential range of 0 to 1.2 V vs. Ag/AgCl reference electrode at a scan rate of 20 $mV \cdot s^{-1}$. The measured potentials were converted by the equation: $E_{RHE} = E_{measured} + 0.197 + 0.0591 \times pH$, where pH = 13.

Measurements of HER properties. The same configuration as for OER studies was used. 0.5 M H_2SO_4 was used as electrolyte (pH = 0.3). Before measurements, the electrolyte was bubbled by Ar for 20 min. The rotating disk electrode rotated at 1600 rpm. The potential was cycled in the range of -1.2 to -0.3 V vs. Ag/AgCl reference electrode at a scan rate of $mV \cdot s^{-1}$. The measured potentials were converted by the equation: $E_{RHE} = E_{measured} + 0.197 + 0.0591 \times pH$, where pH = 0.3.

Appendix AII: Models and analyses detailed information

Table AII. 1. Crystallographic data of sodium borocarbide obtained by refinement of the structure from the X-Ray powder diffraction data at room temperature, according to model **III** (**Chapter III**, **Figure III. 3g**).

Space group	$Pm\bar{3}m$
***a, b, c* (Å)**	4.0878(2)
***α, β, γ* (°)**	90
Volume (Å^3)	68.3062(4)
R_{Bragg} **(%)**	0.66
R_{WP} **(%)**	5.41
χ^2	6.31

Table AII. 2. Atoms information retrieved from the Rietveld refinement of the structure from the X-Ray powder diffraction data at room temperature, according to model **III** (**Chapter III**, **Figure III. 3g**).

Atom	**Wyckoff**	***x***	***y***	***z***	B_{iso} **(Å^2)**	**Occupation**
Na1	1*a*	0	0.0000	0.0000	3.84(9)	0.816(2)
B1	6*f*	½	0.5000	0.8006(4)	2.93(5)	0.803(2)
C1	6*f*	½	0.5000	0.8006(4)	2.93(5)	0.197(2)

Table AII. 3. XPS quantification table for $Na_{1-x}B_{5-x}C_{1+x}$ nanocrystals from **Figure III. 6** of **Chapter III**.

Deconvoluted peaks		BE (eV)	Relative ratio (*at.* %)
B 1s	B-B	187.02	29
	B-C	188.13	20
	B-O	192.68	19
C 1s	C-B	283.06	6
	C-C	284.81	11
	C-O	286.80	3
	C=O	289.04	1
Na 1s	sodium salt	1071.57	11

Table AII. 4. Crystallographic data of the **1Crandom222** model for $Na_{1-x}B_{5-x}C_{1+x}$ nanocrystals from **Chapter III** (occupancy is 1 for all atoms).

Space group	*P1*
***a, b, c* (Å)**	8.1848
***α, β, γ* (°)**	90

Atom	***x***	***y***	***z***
B1	0.41567923	0.74877276	0.25844785
B2	0.11362724	0.24805481	0.74825343
B3	0.26368005	0.25134904	0.89674660
B4	0.41658274	0.24992639	0.74843991
B5	0.25942187	0.40062633	0.74459778
B6	0.26092943	0.74950168	0.10896587
B7	0.11281897	0.74806665	0.25814057
B8	0.25828437	0.75327947	0.41201448
B9	0.74648637	0.89648115	0.74818651

B10	0.26151212	0.90080020	0.25746276
B11	0.73557069	0.39698255	0.24864831
B12	0.08813966	0.75690838	0.75084005
B13	0.24281487	0.60655958	0.74826239
B14	0.24464921	0.75307547	0.90213276
B15	0.39131434	0.75606960	0.74935149
B16	0.24528155	0.90977610	0.75137830
B17	0.73559335	0.24754956	0.09922501
B18	0.58056283	0.25031425	0.24876948
B19	0.26343755	0.24886892	0.59894115
B20	0.73530937	0.09820252	0.24864056
B21	0.75411426	0.24693577	0.59973514
B22	0.74637364	0.74752175	0.89673752
B23	0.74734867	0.59859051	0.74825689
B24	0.59668760	0.74905982	0.74534722
B25	0.74752725	0.74755350	0.59894985
B26	0.75341263	0.89525446	0.24881542
B27	0.90639577	0.74412637	0.25043144
B28	0.75678234	0.74685857	0.39790926
B29	0.75317487	0.59773290	0.24887044
B30	0.24266133	0.40997587	0.25233277
B31	0.75601922	0.74693980	0.09972925
B32	0.75725919	0.39547566	0.74863162
B33	0.90710186	0.24407293	0.74869764
B34	0.75398194	0.24695003	0.89757775
B35	0.75610093	0.09749135	0.74865222
B36	0.24265321	0.25541433	0.09919182
B37	0.08287637	0.25613927	0.24878567
B38	0.24169427	0.10608591	0.24935907
B39	0.24216631	0.25328213	0.39839974
B40	0.73584644	0.24751038	0.39792823
C1	0.61412814	0.74476389	0.25144510
C2	0.26184056	0.60725046	0.25973228

C3	0.37999548	0.25661684	0.24914952
C4	0.87688308	0.24954851	0.24866533
C5	0.88869223	0.75000417	0.74626745
C6	0.24373003	0.75554713	0.60863191
C7	0.61487804	0.24511733	0.74850685
C8	0.26041506	0.10739938	0.74662314
Na1	0.50656418	0.99108187	0.99842819
Na2	0.50694671	0.50350787	0.98721665
Na3	0.51311516	0.99687065	0.50005098
Na4	0.99485082	0.49786866	0.99262505
Na5	0.98944568	0.49208753	0.50412743
Na6	0.99424268	0.99814700	0.00469745
Na7	0.98910387	0.00293471	0.49235125
Na8	0.51329439	0.49711729	0.50969718

Table AII. 5. Crystallographic data of the **0C-2Crandom222** model for $Na_{1-x}B_{5-x}C_{1+x}$ nanocrystals from **Chapter III** (occupancy is 1 for all atoms).

Space group	*P1*
***a, b, c* (Å)**	8.1848
***α, β, γ* (°)**	90

Atom	***x***	***y***	***z***
B1	0.41187720	0.74492394	0.25804653
B2	0.11242339	0.24650157	0.74852633
B3	0.26266035	0.25023722	0.89710000
B4	0.41525855	0.24882842	0.74857669
B5	0.26022834	0.39933435	0.74519320
B6	0.25926697	0.74849759	0.10835420
B7	0.11072882	0.74405678	0.25902902
B8	0.25876262	0.75216839	0.41302401

B9	0.74604843	0.89469193	0.74786253
B10	0.25963411	0.89961364	0.25781434
B11	0.73455604	0.40866331	0.24877533
B12	0.10125467	0.75649936	0.74866425
B13	0.25153598	0.60592194	0.74900965
B14	0.25225846	0.75221465	0.90136226
B15	0.39933484	0.75500569	0.74922154
B16	0.25348875	0.90815132	0.75201016
B17	0.73563074	0.25524922	0.09892092
B18	0.57954631	0.25819730	0.24902432
B19	0.26244276	0.24805321	0.59921549
B20	0.73498614	0.10575432	0.24871536
B21	0.75298097	0.24704045	0.60028063
B22	0.89791262	0.74826861	0.74502538
B23	0.74651755	0.74307858	0.89656238
B24	0.74700323	0.59538708	0.74790785
B25	0.59875509	0.74644401	0.74539334
B26	0.74640408	0.74316242	0.59851728
B27	0.75240000	0.89630730	0.24863227
B28	0.90173876	0.74440662	0.25084393
B29	0.74880229	0.74451871	0.39832105
B30	0.24195276	0.40917174	0.25252012
B31	0.74888364	0.74420197	0.09882141
B32	0.75263061	0.39405750	0.74868089
B33	0.90445158	0.24272258	0.74887980
B34	0.75274660	0.24703247	0.89728221
B35	0.75088949	0.09593671	0.74866500
B36	0.24236494	0.25446895	0.09943979
B37	0.08270611	0.25899943	0.24901975
B38	0.24064954	0.10577733	0.24979710
B39	0.24183531	0.25258676	0.39880808
B40	0.73592937	0.25515924	0.39861099
C1	0.61109246	0.74501095	0.25057126

C2	0.26054441	0.60535718	0.25969931
C3	0.37937360	0.25798695	0.24939557
C4	0.87708578	0.25889397	0.24886064
C5	0.75105060	0.60569771	0.24884313
C6	0.25265881	0.75424267	0.60934413
C7	0.61261275	0.24435873	0.74862069
C8	0.26161749	0.10633508	0.74695543
Na1	0.50638675	0.99007868	0.98670774
Na2	0.50188830	0.50434089	0.97105559
Na3	0.51212583	0.99581465	0.51104737
Na4	0.00077493	0.50111186	0.96905867
Na5	0.99553712	0.49582163	0.52725643
Na6	0.99249361	0.99083717	0.98519891
Na7	0.98755228	0.99500459	0.51145093
Na8	0.50772722	0.49781465	0.52547884

Table AII. 6. Crystallographic data of the **1Crandom333** model for $Na_{1-x}B_{5-x}C_{1+x}$ nanocrystals from **Chapter III** (occupancy is 1 for all atoms).

Space group	*P1*
***a, b, c* (Å)**	12.2772
***α, β, γ* (°)**	90

Atom	***x***	***y***	***z***
B1	0.16437790	0.93206549	0.49240358
B2	0.40731945	0.83503852	0.16399885
B3	0.16001447	0.17206294	0.93624598
B4	0.94283528	0.15678575	0.83202604
B5	0.16338624	0.50157663	0.40889285
B6	0.16000271	0.26841789	0.82973985
B7	0.60354277	0.17997699	0.16064547

B8	0.50095545	0.16242808	0.40109484
B9	0.59872164	0.50527322	0.49514391
B10	0.50265886	0.50222367	0.59745662
B11	0.50182816	0.40134710	0.49689944
B12	0.40013459	0.50055993	0.50235508
B13	0.50587253	0.73501794	0.16800923
B14	0.49492609	0.59873739	0.16550360
B15	0.59055934	0.49239894	0.16474640
B16	0.49658809	0.27431290	0.16865258
B17	0.49071770	0.49951291	0.26805094
B18	0.38641330	0.50171091	0.16692981
B19	0.48858997	0.49818555	0.06467602
B20	0.50270706	0.26388639	0.49831689
B21	0.59841731	0.15671908	0.50236411
B22	0.49893648	0.16921487	0.60326327
B23	0.50439075	0.84164617	0.26471606
B24	0.39996031	0.16423528	0.49963799
B25	0.15860080	0.50634492	0.26984244
B26	0.26432864	0.17372730	0.83852013
B27	0.05727321	0.50685512	0.82121445
B28	0.50086649	0.50044939	0.73542973
B29	0.39648125	0.50032019	0.83122557
B30	0.49749303	0.39764547	0.83582890
B31	0.60854917	0.83339138	0.16857230
B32	0.59799181	0.49713411	0.83902076
B33	0.50022488	0.59980341	0.83879881
B34	0.49555603	0.82951274	0.74120890
B35	0.39987769	0.82432860	0.84258850
B36	0.50312208	0.82813826	0.94171972
B37	0.59874287	0.83180634	0.83621324
B38	0.49648930	0.92976004	0.84372464
B39	0.16697620	0.26415834	0.50451081
B40	0.50824198	0.93585474	0.15572840

B41	0.84058052	0.15260719	0.73311295
B42	0.74219632	0.16356921	0.83716135
B43	0.83848669	0.05757870	0.83779893
B44	0.60315138	0.16807002	0.84342955
B45	0.15662251	0.50676764	0.06524653
B46	0.49871859	0.06908914	0.84495512
B47	0.15506988	0.40596026	0.82519891
B48	0.15665134	0.50790928	0.92536735
B49	0.25848883	0.50486904	0.82810631
B50	0.50032414	0.84467873	0.40160506
B51	0.15796029	0.60786551	0.82368584
B52	0.15767720	0.40653968	0.16837630
B53	0.16397595	0.83744476	0.73399954
B54	0.06646991	0.83582611	0.83501210
B55	0.50099307	0.17426912	0.94184269
B56	0.16568065	0.82352896	0.93195402
B57	0.26465923	0.82594453	0.83369604
B58	0.16904604	0.93094817	0.83974728
B59	0.05740879	0.50646883	0.16780993
B60	0.50210363	0.16809023	0.74222252
B61	0.40111593	0.17211215	0.84188380
B62	0.83863441	0.60298560	0.50193259
B63	0.49849564	0.74050289	0.49591915
B64	0.49679778	0.83368626	0.60293830
B65	0.06593218	0.16637160	0.49643630
B66	0.16672279	0.82538720	0.39946754
B67	0.60056438	0.84196034	0.50342461
B68	0.16426935	0.92964615	0.16544592
B69	0.16788128	0.82770474	0.26441516
B70	0.82733474	0.49729439	0.72451009
B71	0.73498280	0.49480220	0.83330137
B72	0.83935544	0.39616016	0.82470063
B73	0.84243097	0.49631526	0.92449760

B74	0.83273639	0.59735402	0.82501444
B75	0.16277353	0.16094757	0.59904007
B76	0.83863926	0.84151609	0.73493582
B77	0.73412901	0.83132144	0.82984837
B78	0.83490032	0.73364904	0.82812497
B79	0.82916669	0.82919134	0.93269905
B80	0.93263048	0.83247211	0.83747966
B81	0.16232418	0.06607835	0.49452185
B82	0.16797995	0.82519723	0.06659307
B83	0.06831863	0.82652678	0.16534352
B84	0.16461348	0.73352897	0.50669083
B85	0.26938964	0.83321303	0.16389399
B86	0.26427015	0.16193839	0.49974083
B87	0.49655205	0.94032491	0.50644153
B88	0.83038813	0.82847798	0.06709025
B89	0.73438852	0.15616149	0.49900659
B90	0.83647757	0.15908158	0.59653197
B91	0.93208801	0.16847063	0.49327350
B92	0.82804038	0.26414322	0.50265903
B93	0.16492016	0.83806920	0.59900730
B94	0.83909107	0.49272563	0.06271292
B95	0.73122087	0.48529177	0.16251376
B96	0.83823580	0.39080388	0.16247784
B97	0.83465357	0.49103221	0.26428743
B98	0.82556894	0.59069198	0.16445141
B99	0.16084261	0.17031528	0.07345240
B100	0.83963190	0.49954365	0.40146610
B101	0.73451884	0.50649565	0.49490772
B102	0.82916231	0.40132683	0.50274427
B103	0.26738831	0.83499701	0.49998521
B104	0.83148782	0.17047531	0.39576668
B105	0.16434110	0.26970589	0.17370046
B106	0.16442548	0.06800136	0.17139607

B107	0.94210874	0.16542832	0.16459995
B108	0.83048825	0.72782455	0.16643601
B109	0.83598271	0.83026341	0.26508371
B110	0.93266047	0.82399229	0.16423295
B111	0.83615879	0.92886607	0.16381946
B112	0.49662180	0.60259242	0.49466751
B113	0.26500245	0.16891032	0.16879926
B114	0.84024669	0.83657996	0.40037124
B115	0.74226750	0.84269374	0.50200692
B116	0.84282542	0.74141035	0.50561312
B117	0.84512968	0.84781873	0.59976181
B118	0.84379990	0.94240215	0.49491711
B119	0.16712001	0.16879929	0.27402655
B120	0.84618805	0.16488170	0.05753561
B121	0.74183309	0.17263019	0.15304542
B122	0.83811224	0.06622150	0.15944897
B123	0.83580754	0.16689155	0.25837467
B124	0.93202213	0.49801412	0.50916506
B125	0.84555851	0.25858004	0.82813919
B126	0.50668577	0.07478846	0.15561186
B127	0.40185189	0.16993649	0.16557194
B128	0.16286107	0.59911284	0.51020495
B129	0.26509295	0.50113903	0.50609138
B130	0.16700301	0.39963069	0.50693696
B131	0.50414798	0.16654674	0.26382835
B132	0.06630119	0.49770231	0.51310722
B133	0.16177254	0.60645164	0.16760147
B134	0.16501191	0.16319106	0.73604047
B135	0.17053057	0.06794437	0.84064607
C1	0.73944555	0.83071767	0.16760654
C2	0.49534385	0.07041172	0.50559746
C3	0.49556191	0.49909915	0.40182460
C4	0.40222441	0.83940826	0.50066736

C5	0.49998911	0.17999217	0.07068511
C6	0.48669588	0.40402253	0.16637548
C7	0.50170088	0.26533103	0.84002732
C8	0.49265798	0.49627040	0.93186903
C9	0.50194309	0.73305070	0.84275797
C10	0.07188784	0.16237553	0.83538976
C11	0.16309806	0.50399680	0.72947455
C12	0.92678733	0.49798028	0.16529635
C13	0.16146544	0.73796442	0.82613698
C14	0.07024254	0.83461804	0.49801801
C15	0.16700807	0.49943753	0.60343474
C16	0.16527509	0.16890983	0.40507069
C17	0.17039775	0.73587058	0.16646839
C18	0.50873946	0.82945228	0.07125525
C19	0.25270743	0.50333136	0.16687968
C20	0.07137218	0.16935090	0.17411182
C21	0.84649101	0.26090036	0.15857964
C22	0.83997962	0.07161803	0.49202394
C23	0.82853689	0.50123852	0.59468419
C24	0.94055275	0.83949412	0.49794876
C25	0.83431836	0.92693764	0.84028479
C26	0.92788596	0.50085482	0.81812736
C27	0.84640159	0.16331011	0.92744180
Na1	0.99934649	0.99626197	0.32201229
Na2	0.66731631	0.00061080	0.99831650
Na3	0.67036457	0.66841121	0.33793488
Na4	0.67920933	0.65846729	0.99763717
Na5	0.33435045	0.67127600	0.33779580
Na6	0.32810964	0.66829037	0.00003070
Na7	0.99526530	0.66255681	0.33698996
Na8	0.99137228	0.67303210	0.99821452
Na9	0.66634100	0.67239806	0.66142683
Na10	0.66565555	0.32694159	0.66166442

Na11	0.66145293	0.99941242	0.67328484
Na12	0.00763083	0.33998876	0.99428406
Na13	0.34267724	0.66848338	0.66166733
Na14	0.33760588	0.32455572	0.66072618
Na15	0.32863425	0.00317296	0.67813021
Na16	0.99250306	0.67858152	0.66632388
Na17	0.99596761	0.31746153	0.65760209
Na18	0.00953286	0.00164930	0.66957722
Na19	0.66970008	0.32737088	0.34145813
Na20	0.33142146	0.32532662	0.34388148
Na21	0.31313716	0.33141592	0.99692526
Na22	0.99951464	0.33885049	0.34935508
Na23	0.32595532	0.99983047	0.00008149
Na24	0.00687643	0.98432007	0.00604735
Na25	0.33433961	0.99925506	0.32154274
Na26	0.67900162	0.33534753	0.99318032
Na27	0.66606554	0.00495338	0.32726952

Table AII. 7. Crystallographic data of the **1-Na-1C-2Crandom222** model for $Na_{1-x}B_{5-x}C_{1+x}$ nanocrystals from **Chapter III** (occupancy is 1 for all atoms).

	Space group	*P1*	
	***a, b, c* (Å)**	8.1848	
	***α, β, γ* (°)**	90	
Atom	***x***	***y***	***z***
B1	0.41178098	0.74584135	0.25821610
B2	0.11250925	0.24616120	0.74766357
B3	0.26269827	0.25224894	0.89677322
B4	0.41512868	0.24627215	0.74865854
B5	0.26179394	0.40086788	0.74473655
B6	0.25965865	0.74984185	0.10823417
B7	0.11089391	0.74616109	0.25939959
B8	0.25757343	0.75532429	0.41282312
B9	0.25925759	0.90105299	0.25769866

B10	0.73459851	0.41035805	0.24812460
B11	0.10159438	0.76003227	0.74809016
B12	0.25362899	0.60865870	0.74825900
B13	0.25260653	0.75482942	0.90108866
B14	0.39942741	0.76087529	0.74915950
B15	0.25209649	0.91135764	0.75004045
B16	0.73521636	0.25525409	0.09863692
B17	0.57942636	0.25986118	0.24856329
B18	0.26226978	0.24920642	0.59856044
B19	0.73492153	0.10761888	0.24918060
B20	0.75283284	0.23743707	0.59958593
B21	0.89800844	0.74889624	0.74532011
B22	0.74634150	0.74300648	0.89615955
B23	0.74646234	0.59298696	0.74818842
B24	0.59965055	0.74910554	0.74566100
B25	0.74723134	0.74280286	0.59890512
B26	0.75263193	0.89969075	0.24961435
B27	0.90231448	0.74726706	0.25170954
B28	0.75001666	0.75000487	0.39783285
B29	0.24157082	0.41034495	0.25184159
B30	0.74899545	0.74959753	0.09961520
B31	0.75203865	0.38547794	0.74876255
B32	0.90534628	0.23470431	0.74786554
B33	0.75189712	0.23739598	0.89733677
B34	0.75527719	0.08254988	0.74654119
B35	0.24209065	0.25606579	0.09925194
B36	0.08246085	0.25867970	0.25019613
B37	0.24029642	0.10702976	0.25006907
B38	0.24126893	0.25336737	0.39839760
B39	0.73601543	0.25526886	0.39867941
C1	0.74892680	0.88580020	0.74673386
C2	0.61087986	0.74640195	0.25059599
C3	0.26060705	0.60656171	0.25902262

C4	0.37931835	0.25982001	0.24875351
C5	0.87668155	0.25939105	0.24937921
C6	0.75082303	0.60844655	0.24818837
C7	0.25195165	0.75763502	0.60882206
C8	0.61219412	0.23408030	0.74882916
C9	0.26064060	0.10825117	0.74603597
Na1	0.49361886	0.99826489	0.00004762
Na2	0.49611609	0.49959622	0.97759224
Na3	0.50155359	0.00422092	0.49805845
Na4	0.00813391	0.49472529	0.97451200
Na5	0.00218938	0.48750429	0.52088059
Na6	0.00683051	0.99814724	0.99659052
Na7	0.50215472	0.49264660	0.51906378

Table AII. 8. Crystallographic data of the **3-Na-1C-2Crandom333** model for $Na_{1-x}B_{5-x}C_{1+x}$ nanocrystals from **Chapter III** (occupancy is 1 for all atoms).

	Space group	*P1*	
	***a, b, c* (Å)**	12.2772	
	***α, β, γ* (°)**	90	
Atom	***x***	***y***	***z***
B1	0.16524991	0.93156059	0.49505602
B2	0.40757383	0.83562452	0.16256814
B3	0.15981314	0.17085158	0.93693295
B4	0.94188951	0.15698573	0.83343528
B5	0.16564610	0.49384992	0.40895530
B6	0.15949327	0.26863256	0.83169576
B7	0.60353065	0.18025049	0.16200234
B8	0.50033317	0.16044296	0.40258591
B9	0.59874965	0.50770937	0.49291071
B10	0.50399606	0.50101075	0.59806812
B11	0.50334607	0.40195296	0.49750796

B12	0.40088588	0.49804748	0.50423444
B13	0.50646023	0.73551224	0.16634911
B14	0.49558927	0.59955132	0.16527577
B15	0.59065981	0.49333014	0.16749953
B16	0.49692734	0.27452002	0.16983251
B17	0.49134433	0.50239560	0.26928012
B18	0.38722733	0.50177653	0.16684448
B19	0.49015459	0.49871612	0.06493379
B20	0.50356325	0.26403882	0.49883780
B21	0.59830113	0.15529174	0.50390477
B22	0.49815657	0.17086778	0.60498787
B23	0.50510260	0.84101280	0.26395572
B24	0.40009158	0.16803851	0.50160680
B25	0.15970139	0.50438427	0.27068677
B26	0.26390028	0.17443105	0.83897388
B27	0.05704489	0.50692548	0.82122800
B28	0.50070021	0.49882070	0.73543135
B29	0.39655943	0.50004250	0.83141434
B30	0.49628244	0.39780830	0.83570184
B31	0.60884861	0.83301436	0.16815358
B32	0.59763800	0.49724251	0.83875467
B33	0.50024500	0.60002560	0.83653813
B34	0.49735111	0.83332093	0.73252725
B35	0.40019430	0.82428582	0.83425610
B36	0.50266496	0.82936458	0.93510354
B37	0.59909987	0.83254454	0.82886372
B38	0.49692462	0.93126181	0.83734668
B39	0.50880223	0.93615500	0.15422522
B40	0.83973048	0.15357999	0.73417399
B41	0.74124720	0.16357098	0.83730860
B42	0.83678833	0.05787320	0.83790629
B43	0.60236433	0.16813260	0.84355916
B44	0.15470732	0.50777955	0.06584624

B45	0.49853729	0.07028516	0.84335970
B46	0.15471986	0.40550495	0.82712103
B47	0.15544760	0.50845039	0.92581782
B48	0.25829327	0.50422156	0.82879128
B49	0.50265226	0.84409173	0.40339949
B50	0.15753529	0.60732510	0.82339022
B51	0.15758748	0.40670141	0.16743860
B52	0.16199830	0.83637381	0.73453182
B53	0.06635913	0.83550513	0.83702435
B54	0.50070887	0.17439534	0.94227743
B55	0.16757163	0.82383087	0.93221782
B56	0.26468646	0.82587901	0.83143434
B57	0.16884772	0.93089122	0.83886168
B58	0.05753463	0.50681866	0.17111426
B59	0.50162656	0.17054636	0.74299745
B60	0.40047845	0.17352561	0.84266716
B61	0.83990829	0.60335507	0.49501647
B62	0.49741069	0.74125887	0.49971975
B63	0.06627685	0.16902133	0.49631321
B64	0.16905937	0.82486887	0.40085131
B65	0.60094145	0.84232337	0.50463553
B66	0.16448750	0.93012724	0.16706111
B67	0.16927915	0.82806106	0.26551802
B68	0.82745009	0.49683475	0.72120231
B69	0.73448053	0.49506413	0.83136521
B70	0.83887283	0.39635573	0.82425672
B71	0.84123747	0.49695644	0.92392552
B72	0.83297334	0.59746858	0.82337828
B73	0.16262965	0.16340329	0.60026243
B74	0.84050751	0.84165867	0.73549300
B75	0.73437645	0.83186131	0.82800541
B76	0.83499371	0.73374682	0.82774074
B77	0.82795242	0.82819593	0.93309465

B78	0.93249406	0.83242690	0.83983658
B79	0.16302905	0.06757093	0.49827652
B80	0.16839040	0.82589053	0.06735356
B81	0.06854967	0.82686746	0.16666859
B82	0.16560225	0.72984230	0.50674283
B83	0.26989442	0.83377939	0.16410936
B84	0.26473737	0.16600891	0.50073213
B85	0.49537173	0.94103686	0.50960752
B86	0.82994733	0.82684304	0.06776690
B87	0.73459307	0.15495619	0.50026168
B88	0.83660433	0.16047288	0.59785584
B89	0.93223886	0.17174381	0.49437922
B90	0.82652199	0.26449470	0.50141562
B91	0.16383553	0.83530683	0.60018343
B92	0.83746211	0.49357306	0.06454740
B93	0.73121885	0.48634200	0.16370612
B94	0.83866180	0.39148409	0.16531069
B95	0.82598984	0.59157267	0.16883721
B96	0.16109448	0.16980466	0.07466114
B97	0.83755503	0.49965033	0.39337299
B98	0.73386919	0.50900027	0.48814819
B99	0.82692961	0.40110186	0.49644109
B100	0.26803603	0.83382313	0.50392399
B101	0.83207399	0.16911897	0.39698300
B102	0.16449650	0.27043065	0.17395482
B103	0.16439586	0.06865978	0.17441877
B104	0.94213739	0.16616890	0.16568417
B105	0.82992728	0.72836962	0.17018708
B106	0.83449908	0.83185546	0.26625206
B107	0.93251661	0.82417150	0.16553623
B108	0.83612814	0.92891206	0.16289270
B109	0.49538517	0.60316732	0.49786688
B110	0.26541723	0.16970322	0.16946448

B111	0.83875450	0.83841142	0.40126313
B112	0.74282952	0.84298597	0.50512954
B113	0.84329630	0.74160301	0.50342680
B114	0.84664112	0.84703260	0.60072213
B115	0.84459230	0.94289095	0.49770370
B116	0.16775647	0.17159749	0.27510901
B117	0.84594016	0.16701270	0.05857039
B118	0.74172156	0.17331482	0.15451978
B119	0.83808249	0.06700713	0.15932009
B120	0.83610116	0.16619211	0.25996365
B121	0.93229327	0.49575860	0.50156277
B122	0.84482561	0.25890828	0.82932408
B123	0.50705124	0.07502093	0.15559917
B124	0.40223383	0.17042918	0.16616197
B125	0.16328186	0.59192413	0.50979420
B126	0.26616223	0.49318089	0.50826500
B127	0.16778968	0.39080893	0.50724554
B128	0.50393339	0.16547073	0.26492640
B129	0.06650133	0.49008772	0.51115238
B130	0.16220279	0.60682827	0.16922120
B131	0.16429257	0.16658890	0.73716767
B132	0.16958315	0.06814092	0.83966077
C1	0.16732816	0.25979067	0.50656141
C2	0.49933739	0.83600261	0.59905204
C3	0.83288468	0.49179992	0.26002906
C4	0.73931397	0.83051962	0.16851266
C5	0.49415225	0.07072544	0.50952126
C6	0.49559827	0.50237672	0.40268710
C7	0.40307191	0.84005602	0.50272379
C8	0.50022310	0.18033540	0.07144685
C9	0.48717195	0.40449016	0.16743839
C10	0.50019492	0.26613264	0.84107388
C11	0.49377275	0.49769703	0.93199580

C12	0.50192493	0.73343450	0.83622722
C13	0.07087430	0.16229073	0.83660276
C14	0.16300904	0.50028496	0.73011720
C15	0.92616995	0.49816178	0.16676065
C16	0.16128261	0.73759303	0.82634540
C17	0.07105214	0.83374678	0.49842892
C18	0.16676775	0.49210735	0.60405979
C19	0.16562697	0.16911747	0.40681292
C20	0.17093595	0.73633642	0.16764578
C21	0.50814061	0.83046761	0.06799603
C22	0.25249240	0.50332381	0.16677415
C23	0.07139971	0.17004383	0.17534046
C24	0.84628057	0.26195544	0.16245644
C25	0.84195714	0.07222922	0.49483381
C26	0.82925669	0.50064499	0.58785280
C27	0.94092486	0.83955334	0.49823502
C28	0.83361788	0.92687673	0.84031314
C29	0.92769257	0.50080106	0.81731492
C30	0.84593794	0.16478684	0.92857556
Na1	0.99441099	0.99251995	0.31943038
Na2	0.66523844	0.00004753	0.99085266
Na3	0.67458853	0.66394654	0.99465947
Na4	0.33787350	0.66819524	0.33607629
Na5	0.33075654	0.66876029	0.99775049
Na6	0.99835693	0.67073124	0.34030072
Na7	0.99402455	0.67751775	0.99540077
Na8	0.67299165	0.66723174	0.66064755
Na9	0.65948932	0.32216831	0.66353334
Na10	0.00933601	0.33686646	0.98967517
Na11	0.34038423	0.65549119	0.66584489
Na12	0.33330989	0.01466156	0.68677006
Na13	0.99122494	0.67852234	0.66700906
Na14	0.98733028	0.32065550	0.66437272

Na15	0.00319999	0.99917568	0.67621014
Na16	0.66158987	0.32089523	0.34843780
Na17	0.34251990	0.32866112	0.34317194
Na18	0.31711590	0.33219416	0.99045383
Na19	0.99812953	0.33525969	0.34740593
Na20	0.32880722	0.00057589	0.99698042
Na21	0.00522840	0.98367332	0.00468655
Na22	0.33966988	0.00003701	0.31385679
Na23	0.67318997	0.33169058	0.98802365
Na24	0.66840004	0.00405148	0.32731438

Table AII. 9. Calculated ^{11}B and ^{23}Na NMR parameters in the NaB_5C structure (single cell) in which the B3 atom is in line with the C atom.

	δ_{iso} (ppm)	C_Q (MHz)	η
B1	5.4	1.74	0.56
B2	5.4	1.74	0.56
B3	12.3	0.44	0.00
B4	5.4	1.74	0.56
B5	5.4	1.74	0.56
Na	-15.2	-0.62	0.0

Table AII. 10. Calculated ^{11}B NMR parameters in the $Na_8(B_5C)_8$ model **1Crandom222**.

	δ_{iso} (ppm)	C_Q (MHz)	η		δ_{iso} (ppm)	C_Q (MHz)	η
B1	3.3	-1.09	0.53	B21	7.1	-1.67	0.39
B2	-4.3	-1.55	0.21	B22	5.0	-1.73	0.59
B3	3.1	-1.75	0.50	B23	6.3	-1.71	0.55
B4	5.7	1.08	0.95	B24	13.1	-1.52	0.01

B5	19.7	-1.56	0.26	B25	5.8	-1.80	0.32
B6	-6.1	-1.59	0.38	B26	3.7	-1.63	0.59
B7	-7.1	-1.55	0.47	B27	12.7	-1.54	0.19
B8	7.3	-1.18	0.59	B28	8.7	-1.80	0.29
B9	8.5	-1.79	0.29	B29	5.9	-1.75	0.29
B10	14.7	-1.61	0.17	B30	2.8	-0.95	0.61
B11	5.3	-1.79	0.32	B31	7.0	-1.76	0.55
B12	4.5	-1.07	0.67	B32	4.5	-1.72	0.60
B13	-8.9	-1.59	0.25	B33	13.0	-1.57	0.14
B14	14.3	-1.62	0.02	B34	7.6	-1.71	0.38
B15	-4.7	-1.57	0.31	B35	6.5	-1.83	0.32
B16	4.4	-1.09	0.83	B36	1.1	-1.73	0.20
B17	5.5	-1.76	0.46	B37	16.0	-0.70	0.34
B18	16.4	-0.81	0.02	B38	-9.2	-1.52	0.55
B19	3.6	-1.80	0.21	B39	3.1	-1.74	0.38
B20	3.8	-1.70	0.62	B40	4.2	-1.71	0.46

Table AII. 11. Calculated ^{11}B NMR parameters in the $Na_8(B_5C)_6(B_4C_2)(B_6)$ model **0C-2Crandom222**.

	δ_{iso} (ppm)	C_Q (MHz)	η		δ_{iso} (ppm)	C_Q (MHz)	η
B1	1.0	-0.72	0.78	B21	5.8	-1.61	0.47
B2	-4.8	-1.51	0.33	B22	4.0	-1.40	0.04
B3	3.4	-1.76	0.48	B23	3.1	-1.17	0.25
B4	6.8	-1.08	0.82	B24	8.6	-1.47	0.19
B5	19.0	-1.53	0.27	B25	7.8	-1.51	0.02
B6	-4.3	-1.70	0.36	B26	4.4	-1.23	0.11
B7	-9.7	-1.27	0.49	B27	16.1	-1.80	0.41

B8	9.1	-1.32	0.53	B28	16.1	-1.83	0.24
B9	9.1	-1.46	0.31	B29	12.5	-2.28	0.13
B10	14.1	-1.67	0.30	B30	2.9	-0.95	0.33
B11	3.8	-0.80	0.73	B31	10.7	-2.26	0.12
B12	5.2	-1.89	0.26	B32	8.7	-1.86	0.55
B13	-7.2	-1.47	0.39	B33	13.7	-1.43	0.02
B14	15.0	-1.47	0.11	B34	6.2	-1.65	0.44
B15	10.7	-1.95	0.23	B35	7.8	-1.94	0.20
B16	5.9	1.09	0.80	B36	1.5	-1.73	0.19
B17	5.1	-1.87	0.31	B37	16.1	-0.67	0.23
B18	15.2	-0.95	0.17	B38	-10.2	-1.49	0.75
B19	3.9	-1.81	0.22	B39	3.5	-1.75	0.38
B20	-9.3	-1.29	0.94	B40	4.1	-1.84	0.30

Table AII. 12. Calculated ^{11}B NMR parameters in the $Na_{27}(B_5C)_{27}$ model **1Crandom333**.

	δ_{iso} (ppm)	C_Q (MHz)	η		δ_{iso} (ppm)	C_Q (MHz)	η		δ_{iso} (ppm)	C_Q (MHz)	η
B1	2.3	-1.84	0.18	B46	16.6	-1.58	0.12	B91	6.7	-1.73	0.23
B2	-5.6	-1.54	0.38	B47	-7.9	-1.56	0.45	B92	16.2	-1.56	0.11
B3	4.6	-1.55	0.10	B48	2.0	-1.36	0.03	B93	2.7	-1.80	0.54
B4	5.2	-1.18	0.20	B49	-10.9	-1.62	0.18	B94	4.1	-1.41	0.39
B5	6.1	-1.30	0.10	B50	4.8	-1.75	0.48	B95	13.4	-1.42	0.45
B6	5.5	-1.54	0.41	B51	4.3	-1.25	0.69	B96	5.5	-1.09	0.77
B7	5.2	-1.50	0.32	B52	-8.6	-1.58	0.18	B97	4.8	-1.66	0.27
B8	6.0	-1.71	0.52	B53	6.5	-1.71	0.28	B98	-5.1	-1.62	0.39
B9	5.9	-1.80	0.42	B54	6.6	-1.82	0.41	B99	-4.8	-1.46	0.20
B10	18.9	-1.54	0.30	B55	6.5	-1.13	0.58	B100	15.9	-1.54	0.10

B11	6.2	-1.70	0.23	B56	6.4	-1.66	0.52	B101	3.6	-1.80	0.32
B12	6.2	-1.79	0.37	B57	5.0	-1.65	0.35	B102	8.8	-1.66	0.17
B13	2.0	-1.62	0.35	B58	15.7	-1.56	0.06	B103	14.6	-0.69	0.24
B14	13.3	-1.77	0.12	B59	17.2	-1.01	0.25	B104	5.8	-1.61	0.51
B15	-5.2	-1.43	0.15	B60	-9.2	-1.53	0.39	B105	5.0	-1.61	0.39
B16	4.3	-1.02	0.70	B61	5.9	-1.71	0.28	B106	3.0	-1.66	0.30
B17	-5.4	-1.02	0.56	B62	6.7	-1.47	0.62	B107	3.5	-1.10	0.33
B18	3.4	-0.94	0.75	B63	-7.4	-1.51	0.55	B108	4.6	-1.64	0.26
B19	-5.6	-0.94	0.68	B64	3.9	-1.62	0.40	B109	5.5	-1.74	0.25
B20	16.5	-1.56	0.35	B65	4.6	-1.75	0.30	B110	17.8	-1.62	0.07
B21	5.4	-1.57	0.28	B66	2.3	-1.83	0.43	B111	5.0	-1.61	0.56
B22	5.3	-1.62	0.35	B67	19.2	-1.40	0.11	B112	7.0	-1.56	0.71
B23	16.2	-1.64	0.32	B68	17.7	-1.48	0.22	B113	15.2	-1.66	0.04
B24	4.3	-1.64	0.15	B69	5.5	-1.64	0.14	B114	4.5	-1.90	0.47
B25	3.7	-1.65	0.48	B70	5.8	-1.23	0.65	B115	8.3	-1.35	0.15
B26	18.2	-1.60	0.24	B71	15.8	-1.58	0.04	B116	-7.9	-1.55	0.54
B27	2.6	1.24	0.89	B72	5.9	-1.53	0.44	B117	4.0	-1.82	0.53
B28	16.2	-1.72	0.26	B73	-10.2	-1.43	0.33	B118	7.6	-1.33	0.92
B29	4.9	-1.66	0.23	B74	5.8	-1.73	0.17	B119	6.1	-1.12	0.70
B30	-2.2	-0.97	0.72	B75	19.6	-1.54	0.10	B120	4.5	-1.14	0.65
B31	5.9	-1.18	0.66	B76	6.1	-1.57	0.41	B121	-9.3	-1.42	0.59
B32	4.4	-1.74	0.58	B77	3.7	-1.81	0.47	B122	12.5	-1.65	0.22
B33	-2.2	-0.94	0.91	B78	17.4	-1.55	0.26	B123	-5.7	-1.60	0.35
B34	-6.0	-1.49	0.96	B79	6.2	-1.73	0.28	B124	2.5	-1.62	0.26
B35	3.3	-1.68	0.34	B80	4.7	-1.79	0.32	B125	-8.4	-1.52	0.59
B36	7.6	-1.18	0.28	B81	5.7	-1.70	0.40	B126	-9.6	-1.37	0.19
B37	6.0	-1.79	0.40	B82	5.9	-1.61	0.31	B127	5.7	-1.68	0.32
B38	15.5	-1.54	0.02	B83	4.1	-1.75	0.34	B128	6.9	-1.74	0.38
B39	5.4	-1.72	0.34	B84	2.7	-1.77	0.67	B129	3.5	-1.89	0.44

B40	3.3	-1.48	0.14	B85	5.1	-1.68	0.53	B130	6.5	-1.82	0.55
B41	15.3	-1.69	0.11	B86	3.5	-1.73	0.44	B131	16.3	-1.66	0.14
B42	-8.1	-1.46	0.50	B87	6.7	-1.17	0.45	B132	3.7	-1.72	0.40
B43	2.8	-1.18	0.38	B88	6.2	-1.71	0.37	B133	3.9	-1.13	0.70
B44	5.4	-1.54	0.64	B89	3.9	-1.66	0.26	B134	4.8	-1.68	0.38
B45	1.8	-1.54	0.45	B90	5.0	-1.61	0.32	B135	6.9	-1.72	0.31

Table AII. 13. Calculated ^{11}B NMR parameters in the $Na_7(B_5C)_7(B_4C_2)$ model **1-Na-1C-2Crandom222**.

	δ_{iso} (ppm)	C_Q (MHz)	η		δ_{iso} (ppm)	C_Q (MHz)	η
B1	-0.4	-0.67	0.84	B21	4.9	-1.74	0.21
B2	-3.7	-1.52	0.26	B22	0.9	-1.54	0.36
B3	1.9	-1.71	0.53	B23	17.7	-1.53	0.32
B4	4.6	-0.96	0.77	B24	3.6	-1.73	0.35
B5	17.1	-1.48	0.45	B25	4.9	-1.65	0.47
B6	-5.5	-1.66	0.35	B26	17.0	-1.94	0.55
B7	-8.6	-1.31	0.54	B27	19.4	-1.94	0.28
B8	9.8	-1.42	0.60	B28	10.3	-2.24	0.17
B9	14.8	-1.67	0.34	B29	2.1	-0.93	0.38
B10	1.4	-0.73	0.66	B30	6.9	-2.09	0.10
B11	4.4	-1.77	0.21	B31	-7.2	-1.45	0.73
B12	-10.6	-1.45	0.26	B32	14.7	-1.60	0.05
B13	16.8	-1.49	0.18	B33	4.0	-1.69	0.27
B14	4.8	-1.71	0.30	B34	7.3	-1.20	0.60
B15	6.3	1.08	0.95	B35	-0.2	-1.68	0.23
B16	3.7	-1.82	0.33	B36	16.8	-0.71	0.25
B17	14.4	-0.91	0.18	B37	-9.4	-1.53	0.75

B18	5.3	-1.84	0.17	B38	5.0	-1.81	0.37
B19	-7.2	-1.33	0.92	B39	5.0	-1.86	0.26
B20	6.4	-1.74	0.38				

Table AII. 14. Calculated ^{11}B NMR parameters in the $Na_{24}(B_5C)_{24}(B_4C_2)_3$ model **3-Na-1C-2Crandom333**.

	δ_{iso} (ppm)	C_Q (MHz)	η		δ_{iso} (ppm)	C_Q (MHz)	η		δ_{iso} (ppm)	C_Q (MHz)	η
B1	-1.7	-1.61	0.15	B45	16.8	-1.51	0.18	B89	-1.0	-1.45	0.36
B2	-6.9	-1.52	0.43	B46	-6.5	-1.59	0.29	B90	15.4	-1.56	0.07
B3	5.1	-1.49	0.08	B47	1.5	-1.29	0.09	B91	3.3	-1.89	0.36
B4	4.1	-1.12	0.17	B48	-9.1	-1.66	0.18	B92	17.9	-1.71	0.11
B5	3.9	-1.35	0.05	B49	17.6	-2.06	0.35	B93	17.5	-1.87	0.50
B6	7.2	-1.64	0.45	B50	3.8	-1.24	0.93	B94	3.1	-1.47	0.13
B7	5.2	-1.47	0.35	B51	-7.3	-1.58	0.20	B95	-3.5	-2.05	0.14
B8	1.2	-1.61	0.65	B52	7.0	-1.70	0.25	B96	-1.1	-1.54	0.11
B9	7.1	-1.78	0.30	B53	7.6	-1.83	0.40	B97	13.1	-0.45	0.49
B10	19.3	-1.61	0.19	B54	3.6	-0.97	0.80	B98	5.6	-2.00	0.34
B11	8.6	-1.72	0.42	B55	5.1	-1.64	0.57	B99	5.8	-1.66	0.17
B12	5.5	-1.76	0.43	B56	4.5	-1.65	0.37	B100	12.0	-0.51	0.64
B13	4.4	-1.70	0.44	B57	15.3	-1.56	0.06	B101	4.2	-1.55	0.48
B14	15.7	-1.85	0.18	B58	12.7	-0.65	0.53	B102	5.4	-1.67	0.37
B15	-7.2	-1.21	0.25	B59	-5.0	-1.63	0.27	B103	2.8	-1.70	0.22
B16	3.7	-0.98	0.81	B60	5.6	-1.67	0.22	B104	4.4	-1.11	0.47
B17	-4.8	-1.20	0.63	B61	6.0	-1.55	0.68	B105	1.7	-1.44	0.24
B18	3.3	-0.83	0.75	B62	-5.9	-1.94	0.18	B106	7.4	-1.79	0.18
B19	-6.0	-1.03	0.53	B63	3.9	-2.06	0.18	B107	17.1	-1.56	0.02
B20	19.7	-1.56	0.24	B64	1.1	-1.86	0.41	B108	4.4	-1.52	0.57

B21	9.2	-1.62	0.24	B65	24.4	-1.99	0.04	B109	2.4	-1.39	0.73
B22	11.4	-1.88	0.28	B66	17.5	-1.45	0.23	B110	17.5	-1.75	0.03
B23	13.9	-1.35	0.45	B67	4.7	-1.60	0.11	B111	5.3	-1.96	0.60
B24	0.6	-1.48	0.39	B68	8.1	-1.10	0.73	B112	8.8	-1.22	0.26
B25	2.8	-1.67	0.39	B69	17.5	-1.69	0.05	B113	-6.8	-1.53	0.56
B26	22.0	-1.75	0.20	B70	6.2	-1.62	0.31	B114	4.2	-1.92	0.43
B27	1.2	1.20	0.82	B71	-12.8	-1.17	0.51	B115	7.7	1.35	0.95
B28	18.8	-1.78	0.19	B72	7.0	-1.80	0.05	B116	2.4	0.90	0.79
B29	6.3	-1.65	0.38	B73	20.6	-2.05	0.02	B117	4.3	-1.29	0.79
B30	-0.8	-1.12	0.75	B74	8.6	-1.63	0.34	B118	-8.2	-1.50	0.61
B31	8.4	-1.34	0.79	B75	6.0	-1.82	0.36	B119	16.1	-1.68	0.19
B32	2.4	-1.67	0.53	B76	16.0	-1.47	0.23	B120	-5.9	-1.69	0.36
B33	-3.2	0.94	0.96	B77	3.4	-1.67	0.37	B121	-2.3	-1.55	0.38
B34	-3.2	1.41	0.13	B78	2.3	-1.69	0.41	B122	-9.6	-1.44	0.55
B35	1.2	-1.66	0.21	B79	16.8	-1.96	0.25	B123	-9.6	-1.37	0.11
B36	0.2	-1.00	0.30	B80	6.1	-1.61	0.37	B124	5.3	-1.62	0.29
B37	7.3	-1.92	0.37	B81	3.6	-1.76	0.30	B125	-3.2	-1.46	0.49
B38	17.2	-1.70	0.05	B82	5.0	-1.66	0.78	B126	5.7	-2.02	0.29
B39	2.3	-1.47	0.22	B83	6.0	-1.72	0.54	B127	3.8	1.05	0.75
B40	17.7	-1.74	0.11	B84	6.3	-2.17	0.19	B128	15.9	-1.65	0.19
B41	-6.2	-1.55	0.59	B85	5.3	-1.56	0.21	B129	0.4	-1.73	0.40
B42	4.3	-1.28	0.57	B86	3.4	-1.70	0.30	B130	4.0	-1.16	0.57
B43	5.5	-1.55	0.75	B87	10.2	-1.78	0.22	B131	1.0	-1.47	0.53
B44	1.8	-1.57	0.55	B88	7.4	-1.72	0.24	B132	5.1	-1.70	0.23

Table AII. 15. Calculated ^{23}Na NMR parameters in the $Na_8(B_5C)_8$ model **1Crandom222**, $Na_8(B_5C)_6(B_4C_2)(B_6)$ model **0C-2Crandom222** and $Na_7(B_5C)_7(B_4C_2)$ model **1-Na-1C-2Crandom222**.

	1Crandom222			**0C-2Crandom222**			**1-Na-1C-2Crandom222**		
	δ_{iso} (ppm)	C_Q (MHz)	η	δ_{iso} (ppm)	C_Q (MHz)	η	δ_{iso} (ppm)	C_Q (MHz)	η
Na1	-11.9	0.70	0.77	-10.2	1.07	0.11	-12.1	-0.92	0.31
Na2	-11.7	0.81	0.33	-4.6	1.23	0.39	-6.7	1.01	0.11
Na3	-9.2	0.58	0.16	-8.4	0.93	0.77	-11.1	-0.69	0.38
Na4	-12.7	0.47	0.92	-8.4	1.01	0.73	-11.3	0.69	0.93
Na5	-11.6	0.89	0.46	-7.4	-1.09	0.79	-10.7	-0.82	0.85
Na6	-13.2	0.47	0.55	-12.7	0.76	0.61	-13.5	0.51	0.92
Na7	-12.3	0.91	0.49	-11.7	1.05	0.61	-6.1	0.88	0.46
Na8	-9.1	0.73	0.41	-3.0	-1.09	0.93			

Table AII. 16. Calculated ^{23}Na NMR parameters in the $Na_{27}(B_5C)_{27}$ model **1Crandom333** and $Na_{24}(B_5C)_{24}(B_4C_2)_3$ model **3Na-1C-2Crandom333.**

	1Crandom333			**3Na-1C-2Crandom333**		
	δ_{iiso} (ppm)	C_Q (MHz)	η	δ_{iiso} (ppm)	C_Q (MHz)	η
Na1	-11.4	0.48	0.30	-9.4	0.43	0.80
Na2	-11.3	-0.47	0.48	-11.3	-0.46	0.29
Na3	-15.4	0.57	0.76	-13.9	0.53	0.86
Na4	-11.8	-0.36	0.02	-14.2	0.81	0.51
Na5	-13.7	0.53	0.60	-12.6	0.58	0.93
Na6	-11.3	-0.55	0.58	-9.4	1.17	0.06
Na7	-11.3	0.85	0.08	-7.3	-0.88	0.76
Na8	-8.9	-0.66	0.45	-15.0	-0.82	0.89
Na9	-14.9	0.55	0.79	-12.8	-0.52	0.87
Na10	-14.5	-0.47	0.87	-7.6	-0.33	0.55
Na11	-13.6	-0.48	0.32	-10.4	1.18	0.47

Na12	-8.6	-0.43	0.61	-9.9	-0.49	0.65
Na13	-11.4	-0.50	0.72	-7.5	0.69	0.79
Na14	-12.3	0.41	0.27	-6.3	0.79	0.14
Na15	-14.5	0.25	0.51	-8.2	0.75	0.65
Na16	-7.6	0.75	0.87	-6.5	-0.54	0.09
Na17	-6.3	0.57	0.67	-10.9	1.07	0.21
Na18	-8.0	0.74	0.12	-10.6	0.51	0.86
Na19	-11.1	0.55	0.59	-8.0	1.47	0.45
Na20	-12.8	0.57	0.28	-13.9	-0.41	0.90
Na21	-10.3	0.62	0.40	-9.5	-0.55	0.56
Na22	-9.5	0.56	0.81	-9.5	0.59	0.74
Na23	-13.4	-0.33	0.53	-9.5	0.99	0.35
Na24	-9.3	-0.57	0.60	-13.7	0.44	0.40
Na25	-13.0	0.23	0.14			
Na26	-7.9	1.27	0.16			
Na27	-13.6	0.38	0.78			

Table AII. 17. Crystallographic data of α-FeB layers model for FAULTS refinement.

Layer	Atom	*x*	*y*	*z*	B_{iso} (Å^2)	Occupation
A	Fe1	0.82291	0.25000	0.88012	0.004	1.0
	Fe2	0.67709	0.75000	0.38012	0.004	1.0
	Fe3	0.32291	0.25000	0.61988	0.004	1.0
	Fe4	0.17709	0.75000	0.11988	0.004	1.0
	B1	0.96370	0.25000	0.38590	0.006	1.0
	B2	0.46370	0.25000	0.11410	0.006	1.0
	B3	0.53630	0.75000	0.88590	0.006	1.0
	B4	0.03630	0.75000	0.61410	0.006	1.0
B	Fe1	0.32291	0.25000	0.61988	0.004	1.0
	Fe2	0.17709	0.75000	0.11988	0.004	1.0
	Fe3	0.82291	0.25000	0.35964	0.004	1.0
	Fe4	0.67709	0.75000	0.85964	0.004	1.0
	B1	0.46370	0.25000	0.12566	0.006	1.0
	B2	0.96370	0.25000	0.85386	0.006	1.0
	B3	0.03630	0.75000	0.62566	0.006	1.0
	B4	0.53630	0.75000	0.35386	0.006	1.0
C	Fe1	0.32291	0.25000	0.14036	0.004	1.0
	Fe2	0.17709	0.75000	0.64036	0.004	1.0
	Fe3	0.82291	0.25000	0.88012	0.004	1.0
	Fe4	0.67709	0.75000	0.38012	0.004	1.0
	B1	0.46370	0.25000	0.64614	0.006	1.0
	B2	0.96370	0.25000	0.37434	0.006	1.0
	B3	0.03630	0.75000	0.14614	0.006	1.0
	B4	0.53630	0.75000	0.87434	0.006	1.0
D	Fe1	0.82291	0.25000	0.38012	0.004	1.0
	Fe2	0.67709	0.75000	0.88012	0.004	1.0
	Fe3	0.32291	0.25000	0.11988	0.004	1.0
	Fe4	0.17709	0.75000	0.61988	0.004	1.0
	B1	0.96370	0.25000	0.88590	0.006	1.0
	B2	0.46370	0.25000	0.61410	0.006	1.0
	B3	0.53630	0.75000	0.38590	0.006	1.0
	B4	0.03630	0.75000	0.11410	0.006	1.0

Table AII. 18. Transition and existence probabilities used in the simulations of **Figure VI. 7**. The data is ordered as shown from top to bottom for each subfigure of **Figure VI. 7**.

Mixing type (Figure)	α_{AA}	α_{AB}	α_{BA}	α_{BB}	P_A	P_B
A/B (**VI. 7a**)	0	1	0	1	0	1
	0.1	0.9	0.1	0.9	0.1	0.9
	0.2	0.8	0.2	0.8	0.2	0.8
	0.3	0.7	0.3	0.7	0.3	0.7
	0.4	0.6	0.4	0.6	0.4	0.6
	0.5	0.5	0.5	0.5	0.5	0.5
	0.6	0.4	0.6	0.4	0.6	0.4
	0.7	0.3	0.7	0.3	0.7	0.3
	0.8	0.2	0.8	0.2	0.8	0.2
	0.9	0.1	0.9	0.1	0.9	0.1
	1	0	1	0	1	0
A/B (**VI. 7c**)	0	1	1	0	0.5	0.5
	0.1	0.9	0.9	0.1	0.5	0.5
	0.2	0.8	0.8	0.2	0.5	0.5
	0.3	0.7	0.7	0.3	0.5	0.5
	0.4	0.6	0.6	0.4	0.5	0.5
	0.5	0.5	0.5	0.5	0.5	0.5
	0.6	0.4	0.4	0.6	0.5	0.5
	0.7	0.3	0.3	0.7	0.5	0.5
	0.8	0.2	0.2	0.8	0.5	0.5
	0.9	0.1	0.1	0.9	0.5	0.5
	1	0	0	1	0.5	0.5
Mixing type (Figure)	α_{BB}	α_{BC}	α_{CB}	α_{CC}	P_B	P_C
B/C (**VI. 7b**)	0	1	0	1	0	1
	0.1	0.9	0.1	0.9	0.1	0.9
	0.2	0.8	0.2	0.8	0.2	0.8
	0.3	0.7	0.3	0.7	0.3	0.7
	0.4	0.6	0.4	0.6	0.4	0.6
	0.5	0.5	0.5	0.5	0.5	0.5
	0.6	0.4	0.6	0.4	0.6	0.4
	0.7	0.3	0.7	0.3	0.7	0.3
	0.8	0.2	0.8	0.2	0.8	0.2
	0.9	0.1	0.9	0.1	0.9	0.1
	1	0	1	0	1	0
B/C (**VI. 7d**)	0	1	1	0	0.5	0.5
	0.1	0.9	0.9	0.1	0.5	0.5
	0.2	0.8	0.8	0.2	0.5	0.5
	0.3	0.7	0.7	0.3	0.5	0.5
	0.4	0.6	0.6	0.4	0.5	0.5
	0.5	0.5	0.5	0.5	0.5	0.5
	0.6	0.4	0.4	0.6	0.5	0.5
	0.7	0.3	0.3	0.7	0.5	0.5
	0.8	0.2	0.2	0.8	0.5	0.5
	0.9	0.1	0.1	0.9	0.5	0.5

Table AII. 19. Summary of crystallographic parameters for the refinement of all the models studied for α-FeB. In the case of the phase mixture model, only the β-FeB structure parameters are shown.

Hypothesis:	**(i)**	**(ii)**		**(iii)**	
Model:	**Anti-site mixing**	**S.G. *Cmcm***	**S.G. *Pnca***	**Phase mixture**	**Intergrowth**
a (Å)	5.4954(2)	2.9460(4)	5.4944(4)	5.49312(3)	5.4989(2)
b (Å)	2.9492(3)	7.6100(3)	2.9491(2)	2.94817(4)	2.9505(3)
c (Å)	4.0622(2)	2.9491(2)	4.0614(3)	4.06097(5)	4.0641(2)
Volume (Å^3)	65.961(8)	66.130(10)	65.808(8)	65.766(13)	65.961(8)
R_{wp} (%)	52.8	49.9	33.3	35.1	7.3
χ^2	604.50	549.40	245.10	267.34	18.70

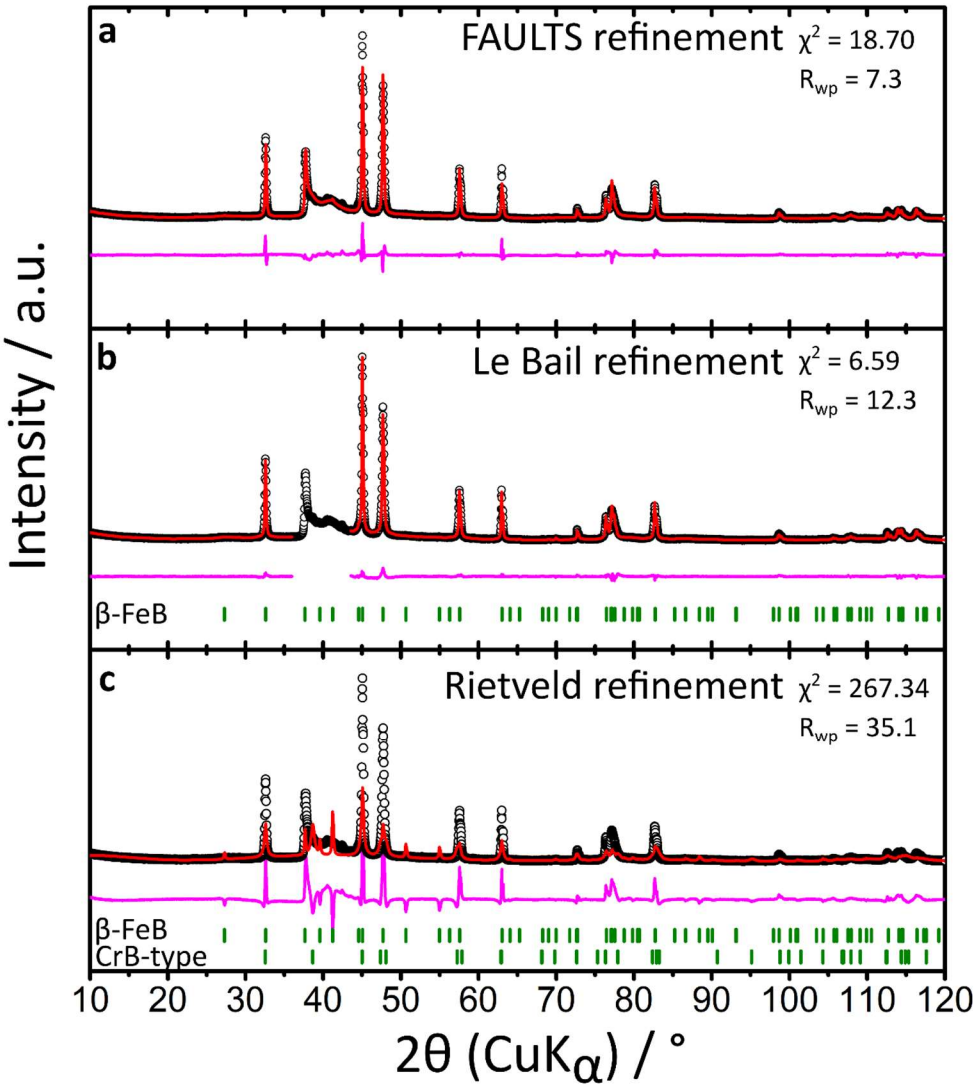

Figure AII. 1. Different refinement approaches for α-FeB in the full measured 2θ range. **(a)** FAULTS refinement with the 4-layers model proposed by Kanaizuka.[52] **(b)** Le Bail refinement assessing the anisotropic particle size. **(c)** Rietveld refinement of a phase mixture β-FeB/CrB-type structure.